

**Variations of oceanic and foraminiferal oxygen isotopes at
the present day and the Last Glacial Maximum**

Equilibrium simulations with an oceanic general circulation model

**Variationen von Sauerstoff-Isotopen im Ozean und in
Foraminiferen für heute and während des Letzten Glazial
Maximums**

Gleichgewichtssimulationen mit einem Ozeanzirkulationsmodell

Fachbereich Physik und Elektrotechnik

Der Universität Bremen

Zur Erlangung des akademischen Grades eines

Doktor der Naturwissenschaften (Dr. rer. nat.)

von

Xu Xu

Gutachter

1. Prof. Dr. Gerrit Lohmann
2. Prof. Dr. Jelle Bijma

Dissertation eingereicht am: 31.07.2012

Tag des Promotionskolloquiums: 10.10.2012

Abstract

The stable water isotopes H_2^{18}O and HDO are incorporated as passive tracers into the oceanic general circulation model MPI-OM, and simulations under present-day and last glacial maximum climate conditions are analyzed in detail.

In present-day simulation, both $\delta^{18}\text{O}$ and δD distributions at the ocean surface and deep ocean are generally consistent with available observations on the large scale. The modelled δD - $\delta^{18}\text{O}$ relations in surface waters slightly deviates from the slope of the global meteoric water line in most basins, and a much steeper slope is detected in Arctic Oceans. The simulated deuterium excess of ocean surface waters shows small variations between 80°S and 55°N , and a strong decrease north of 55°N . The model is also able to capture the quasi-linear relationship between $\delta^{18}\text{O}$ and salinity S , as well as δD and S , as seen in observational data. Both in the model results and observations, the surface δ - S relations show a steeper slope in extra-tropical regions than in tropical regions, which indicates relatively more addition of isotopically depleted water at high latitudes.

Simulated oceanic isotope distributions at the last glacial maximum (21000 years ago) show features similar to the preindustrial in most basins but the northern North Atlantic. With the exception of the ice sheet impact, the oxygen-18 content variations in the last glacial maximum at sea surface are mainly controlled by the changes in boundary isotopic fluxes in most regions, while the changes from subsurface to bottom waters are mostly due to the differences in the water mass circulations. The changes in topography at the northern high latitudes have remarkable influence on the isotopic composition in the Arctic Ocean. Simulated LGM surface water δ - S relations are similar to present day in extra-tropical regions.

The present-day and the last glacial maximum oxygen isotope compositions of calcite in the surface water and their difference are also calculated using the paleo-temperature equation. These results are compared with the observed values from different foraminifer species, and are in agreement with the observations in most

regions. Additionally, the influences of seawater carbonate chemistry and life processes of foraminifera are also included in the simulations of the calcite oxygen isotope compositions. These results suggest that sea surface temperature and seawater oxygen isotope composition are the most important controls on the oxygen isotope partitioning in foraminifera. The variations in the seawater carbonate chemistry may contribute to around 10-20% of the oxygen isotope changes in foraminiferal shell. The understanding of the 'vital effect' impacts still needs inclusion of further knowledge about the life processes of foraminifera.

Contents

<i>Abstract</i>	5
<i>Contents</i>	7
<i>List of Acronyms</i>	11
<i>List of Figures</i>	13
<i>List of Tables</i>	19
1 Introduction	21
2 Water isotopes	25
2.1 Oxygen and hydrogen isotopes	25
2.2 Fractionation processes	27
2.3 $\delta^{18}\text{O}$ and δD in the hydrosphere	30
2.3.1 Meteoric water	31
2.3.2 The Oceans	33
2.4 Oxygen isotope in biogenic carbonate	35
2.4.1 Planktic foraminifera	35
2.4.2 Oxygen isotope paleo-thermometer	36
2.5 General circulation models (GCMs)	38
3 Model description	41
3.1 The Ocean model MPI-OM	41
3.1.1 Ocean primitive equations	42
3.1.2 Ocean sub-grid-scale parameterizations	43

3.1.3	Sea ice dynamics and thermodynamics	45
3.1.4	Model grid	46
3.2	Biogeochemistry model HAMOCC	46
3.2.1	Biochemistry in upper layer	47
3.2.2	Marine carbon chemistry	49
3.2.3	Air-Sea gas exchange	50
3.3	FORAM model	50
3.3.1	Diffusion and reactions	51
3.3.2	Vital effect	52
3.4	Isotope tracers	53
4	<i>Water isotope variations at present day</i>	57
4.1	Experiment setup	57
4.2	Isotopic boundary conditions	58
4.3	Observational database of $\delta^{18}\text{O}$ and δD	62
4.4	Results	63
4.4.1	Simulated salinity and temperature distribution	63
4.4.2	Simulated distribution of water isotopes	67
4.4.3	Simulated δD - $\delta^{18}\text{O}$ relationship and d-excess variations	75
4.4.4	Simulated relations between H_2^{18}O , HDO and salinity	80
4.5	Discussion	82
5	<i>Oxygen isotope simulation at Last Glacial Maximum</i>	85
5.1	Experiment setup	85

5.2 Isotopic boundary conditions _____	86
5.3 Results _____	92
5.3.1 Comparison of simulated LGM and PD ocean _____	92
5.3.2 Simulated $\delta^{18}\text{O}$ distribution and PD-LGM comparison _____	97
5.3.3 Simulated relations between H_2^{18}O and salinity _____	107
5.4 Discussion _____	109
6 $\delta^{18}\text{O}$ composition reconstruction in the biogenic carbonate _____	113
6.1 Experiment setup _____	113
6.2 Dust conditions in LGM and present day simulation _____	114
6.3 Observational data _____	116
6.4 Results: Implications for $\delta^{18}\text{O}$ of the foraminiferal carbonates ____	126
6.4.1 $\delta^{18}\text{O}_c$ reconstruction by $\delta^{18}\text{O}_w$ and SST _____	127
6.4.2 $\delta^{18}\text{O}_c$ reconstruction from $\delta^{18}\text{O}_w$, SST and seawater carbonate chemistry conditions _____	133
6.4.3 $\delta^{18}\text{O}_c$ reconstruction from $\delta^{18}\text{O}_w$, SST and DIC conditions in the microenvironment of <i>G.sacculifer</i> _____	140
6.5 Discussion _____	144
7 Conclusions and Outlook _____	149
Acknowledgement _____	153
Bibliography _____	155

List of Acronyms

AMIP	Atmospheric Model Intercomparison Project
AMOC	Atlantic meridional ocean circulation
AGCM	atmospheric general circulation model
BBL	bottom boundary layer
C	Carbon
COSMOS	Community Earth System Models
D	Deuterium
DIC	dissolved inorganic carbon
DMS	dimethyl sulfide
DOM	dissolved organic matter
E	Evaporation
ECHAM	European Centre Hamburg Model
H	Hydrogen
HAMOCC	Hamburg Model of Ocean Carbon Cycling
GCMs	General circulation models
GEOSECS	Geochemical Ocean Section Study
GLAMAP	Glacial Atlantic Ocean Mapping
GLODAP	Global Ocean Data Analysis Project
GMWL	global meteoric water line
LGM	Last glacial maximum
Ma	Million years
MARGO	Multiproxy Approach for the Reconstruction of the Glacial Ocean surface
MPI-OM	Max-Planck-Institute Global Ocean/Sea-Ice Model
NADW	North Atlantic Deep Water
NRMSE	normalized root mean square error
P	Precipitation

PD	present day
PDB	Pee Dee Belemnite
PMIP	Paleoclimate Modelling Intercomparison Project Phase
S	Salinity
SIC	sea surface ice concentration
SSS	sea surface salinity
SST	sea surface temperature
R	correlation coefficient
T	Temperature
SMOW	Standard Mean Ocean Water
VPDB	Vienna Pee Dee Belemnite
VSMOW	Vienna Standard Mean Ocean Water
WOA	World Ocean Atlas

List of Figures

Figure 2.1: Isotopic fractionation of the remaining vapor and of the condensate as a function of the remaining fraction of vapor.	29
Figure 2.2: Fluxes for meteoric water cycle.	31
Figure 2.3: Schematic illustration of various effects on the isotopic composition and salinity of ocean surface water.	34
Figure 2.4: Microphotographs of <i>O.universa</i> and <i>G. sacculifer</i> .	36
Figure 2.5: Schematic summary of the various factors that affect the oxygen isotope ratios in foraminiferal carbonate.	38
Figure 3.1: Schematic overview of the model used in this study.	41
Figure 3.2: The scheme of BBL transport.	44
Figure 3.3: Standard MPI-OM grid set for the model simulations in this study.	46
Figure 3.4: Overview of the marine ecosystem as simulated in HAMOCC.	48
Figure 3.5: Schematic view of the symbiont bearing foraminifera in FORAM model simulation.	51
Figure 3.6: Schematic representations of the isotope tracers in model simulation.	54
Figure 4.1: Present day annual-mean precipitation rates of H ₂ O, H ₂ ¹⁸ O and HDO of ECHAM-wiso results.	59
Figure 4.2: Present day annual-mean precipitation rates of H ₂ O, H ₂ ¹⁸ O and HDO of ECHAM-wiso results.	60
Figure 4.3: Present day annual mean $\delta^{18}\text{O}$ and δD composition of precipitation obtained from ECHAM-wiso.	61
Figure 4.4: The $\delta^{18}\text{O}$ - δD relation of global precipitation at present day simulated by ECHAM-wiso.	62
Figure 4.5: Annual mean SST distribution from MPI-OM PD simulation.	63
Figure 4.6: Annual mean vertical distribution of simulated PD temperature through the Atlantic basin.	64
Figure 4.7: Annual mean SSS distributions from MPI-OM PD simulation.	64

Figure 4.8: Annual mean vertical distribution of simulated PD salinity through the Atlantic basin.	65
Figure 4.9: Differences between modeled temperature and WOA09 temperature fields.	66
Figure 4.10: Differences between modeled salinity and WOA09 salinity fields.	67
Figure 4.11: The global zonal-mean δD and $\delta^{18}O$ values of sea surface water from a MPI-OM PD simulation.	68
Figure 4.12: The simulated and observed $\delta^{18}O$ distribution in ocean surface waters.	70
Figure 4.13: The simulated and observed δD distribution in ocean surface waters.	71
Figure 4.14: Comparison of observed water isotopic values versus modeled surface isotopic values.	72
Figure 4.15: The annual zonal mean δD and $\delta^{18}O$ of the Atlantic basin of the MPI-OM PD simulation.	73
Figure 4.16: Comparison of observed water isotopic values versus modeled isotopic values below 100m depth.	74
Figure 4.17a-b: Simulated relationship between δD and $\delta^{18}O$ of surface waters in the Atlantic Ocean, the Pacific Ocean, the Southern Ocean, and the Arctic Ocean.	75
Figure 4.18: Observed and modeled δD - $\delta^{18}O$ relationship and d-excess in sea surface water.	77
Figure 4.19: The simulated global zonal mean d-excess of sea surface water.	78
Figure 4.20: The simulated annual mean d-excess distribution at sea surface.	79
Figure 4.21: Relationship between $\delta^{18}O$ and salinity for simulated and observed surface waters.	80
Figure 4.22: Relationship between δD and salinity for simulated and observed surface waters.	81
Figure 5.1: The simulated LGM annual mean precipitation rates of H_2O and the anomaly between LGM and PD simulations.	87
Figure 5.2: The simulated LGM annual mean precipitation rates of $H_2^{18}O$ and the anomaly between LGM and PD simulations.	88
Figure 5.3: The simulated LGM annual mean evaporation rates of H_2O and the	

anomaly between LGM and PD simulations.	89
Figure 5.4: The simulated LGM annual mean evaporation rates of H ₂ ¹⁸ O and the anomaly between LGM and PD simulations.	90
Figure 5.5: The simulated LGM annual mean δ ¹⁸ O values of precipitation and the anomaly between LGM and PD simulations.	91
Figure 5.6: Modeled annual mean SST distribution at LGM and the anomaly between LGM and PD simulations.	92
Figure 5.7: Modeled annual mean SIC distribution at LGM and the anomaly between LGM and PD simulations.	93
Figure 5.8: Modeled annual mean SSS distribution at LGM and the anomaly between LGM and PD simulations.	94
Figure 5.9: LGM annual mean vertical distribution of simulated salinity through the Atlantic basin and the anomaly between LGM and PD simulations.	95
Figure 5.10: The simulated AMOC at PD and LGM.	96
Figure 5.11: The global zonal -mean δ ¹⁸ O _w isotopic compositions of sea surface water from the LGM, PD, and ISOPD simulation.	97
Figure 5.12: Annual mean δ ¹⁸ O _w at ocean surface modelled in the LGM, ISOPD, and PD experiments.	98
Figure 5.13: The sea surface δ ¹⁸ O _w anomalies between different model experiments (LGM, ISOPD, and PD).	101
Figure 5.14: The annual zonal mean δ ¹⁸ O _w of the Atlantic basin from the LGM, ISOPD, and PD simulations.	102
Figure 5.15: The zonal mean δ ¹⁸ O _w anomalies in the Atlantic basin between different model experiments (LGM, ISOPD, and PD).	103
Figure 5.16: The annual zonal mean δ ¹⁸ O _w of the Pacific basin from the LGM, ISOPD, and PD simulations.	104
Figure 5.17: The zonal mean δ ¹⁸ O _w anomalies in the Pacific basin between different model experiments (LGM, ISOPD, and PD).	105
Figure 5.18: Relationship between δ ¹⁸ O and salinity S for simulated LGM and present day surface waters in tropical oceans.	107

Figure 5.19: Relationship between $\delta^{18}\text{O}$ and salinity S for simulated LGM and present day surface waters in extra-tropical oceans.	108
Figure 6.1: Simulated annual mean dust deposition fluxes for present day climate and LGM climate by the dust cycle model.	115
Figure 6.2: MARGO planktonic $\delta^{18}\text{O}_c$ late Holocene and core top data for four different species.	116
Figure 6.3: Simulated zonal mean $\delta^{18}\text{O}_c$ for the ocean surface and bottom of the euphotic zone in the PD and LGM simulations.	129
Figure 6.4: Comparison of observed $\delta^{18}\text{O}_c$ versus modelled surface $\delta^{18}\text{O}_c$ values for the present day climate.	130
Figure 6.5: Comparison of observed $\delta^{18}\text{O}_c$ versus modelled surface $\delta^{18}\text{O}_c$ values for the LGM climate.	131
Figure 6.6: Modelled $\delta^{18}\text{O}_c$ differences between LGM and PD in tropical and subtropical sea surface waters.	133
Figure 6.7: Modelled $\delta^{18}\text{O}_c$ differences between LGM and PD in the North Atlantic (north of 40°N).	134
Figure 6.8: The present day annual mean sea surface DIC distributions from the HAMOCC simulation and the GLODAP data.	135
Figure 6.9: The present day annual mean sea surface total alkalinity distributions from the HAMOCC simulation and the GLODAP data.	136
Figure 6.10: The present day annual mean $\delta^{18}\text{O}_c$ calculated from the simulated and observed SST, $\delta^{18}\text{O}_w$ and carbon chemistry conditions.	137
Figure 6.11: The LGM annual mean DIC and total alkalinity distribution at sea surface from model simulation.	139
Figure 6.12: The LGM annual mean $\delta^{18}\text{O}_c$ calculated from the SST, $\delta^{18}\text{O}_w$ and carbon chemistry conditions from the model simulation.	140
Figure 6.13: Reconstructed $\delta^{18}\text{O}_c$ differences between LGM and PD from the modelled SST, $\delta^{18}\text{O}_w$, and carbonate chemistry.	141
Figure 6.14: The reconstructed present day oxygen isotope compositions in the shell of <i>G. sacculifer</i> .	143

Figure 6.15: The reconstructed LGM oxygen isotope compositions in the shell of *G. sacculifer*._____ 144

Figure 6.16: The reconstructed LGM-PD differences of oxygen isotope compositions in the shell of *G. sacculifer*._____ 145

List of Tables

Table 2.1: Averaged natural abundances of oxygen isotopes and hydrogen isotopes.	26
Table 2.2: Averaged natural abundances of nine water isotopologues.	26
Table 2.3: Water isotope compositions of international reference standards.	27
Table 2.4: Approximate volumes and typical isotopic compositions of hydrosphere reservoirs.	31
Table 2.5: Oxygen isotopic composition of the principal deep water masses.	34
Table 3.1: Biogeochemical tracers in the HAMOCC standard simulation.	47
Table 6.1: Measured C fluxes during the life processes of planktic foraminifers <i>G. sacculifer</i> .	114
Table 6.2: Cores used for studies of oxygen isotope ratios in <i>G. ruber</i> .	118
Table 6.3: Cores used for studies of oxygen isotope ratios in <i>G. sacculifer</i> .	119
Table 6.4 Cores used for studies of oxygen isotope ratios in <i>G. bulloides</i> .	121
Table 6.5 Cores used for studies of oxygen isotope ratios in <i>N. pachyderma</i> .	122

Chapter 1

Introduction

The stable water isotopes H_2^{18}O and HDO (D = deuterium) have been considered as a useful tool in ocean and climate research since the pioneering work by Epstein and Mayeda (1953), Dansgaard (1953), as well as Friedman (1953). It was recognized that the observed ratios of water isotopes in different water samples are affected by temperature-dependent isotope fractionation occurring at any phase transition within the Earth's hydrological cycle. In addition, different freshwater fluxes into the ocean (e.g., precipitation, or river discharge) have distinctive isotopic signatures, which enables the use of water isotopes as tracers of different oceanic water masses, comparable but not identical to salinity (Craig and Gordon, 1965). A secondary parameter, deuterium excess, can be also derived from the interrelationship between hydrogen and oxygen isotope ratios (Dansgaard, 1964). It is an indication of kinetic (non-equilibrium) fractionation effects occurring during evaporation of water from oceanic area (Dansgaard, 1964). Because deuterium excess is determined by the air-sea interaction processes, the ocean surface conditions strongly affect its values in vapor and rainfall (Uemura et al., 2008). Consequently, the variations of deuterium excess in surface ocean water should go in parallel with deuterium excess variations in vapor and rainfall as well.

In modern research, measurements of water isotopes have enabled the depiction of circulation of deep water masses (Östlund and Hut, 1984; Meredith et al., 1999) and their formation processes (Toggweiler and Samuels, 1995), as well as examination of the export of local fresh water fluxes such as sea ice melt, glacial and river runoff (Bauch et al., 1995; Macdonald et al., 1999; Khatiwala et al., 1999) to the ocean. The deuterium excess records from polar ice cores have been used to reconstruct ocean surface temperature at the source region of evaporation (e.g. Ciais et al., 1994; Vimeux et al., 2001; Masson-Delmotte et al., 2005; Stenni et al., 2010).

Although the modern observational database of oxygen-18 (Schmidt et al., 1999b)

contains widespread observations over global seawater, the data coverage itself varies greatly from region to region (LeGrande and Schmidt, 2006). Measurements across boundaries between different regions, in particular around the Southern Ocean frontal region, provide insufficient coverage to well characterize the isotope distribution. In addition, there are not enough data from subsurface to bottom water, which makes it difficult to define different water masses in ocean basins. Furthermore, there are only limited observations of hydrogen isotope over global oceans, whilst a better understanding of deuterium excess at sea surface is essential for resolving ongoing issues in modelling the deuterium excess (Cappa et al., 2003; Schmidt et al., 2005). Development of explicit stable water isotopes diagnostics in general circulation models (GCMs) will enable the globally quantitative interpretation of the global relationship between water isotopes and various climate variables.

In paleo-studies, oxygen isotope ratios are also considered as an important proxy in many climate archives (e.g. marine and lacustrine sediment cores, ice cores, etc.), which among others, are established tools to reconstruct past climate conditions. The variations of calcite oxygen isotope content in sediment cores provide quantitative interpretation of past climate changes. Since oxygen isotope in organic carbonate integrates records of multiple factors (the local temperature, the global ice sheet volume, oxygen isotope content in ambient water, and ecological variations), it has potential of yielding some important information about ancient oceans such as paleo-temperature (e.g. Broecker, 1986), paleo-salinity (Duplessy et al., 1991; Sarnthein et al., 1992), past surface-water stratification (Williams and Healy Williams, 1980; Mulitza et al., 1997), and past sea level variations (Sowers and Bender, 1995; Broecker and Henderson, 1998).

Analysis of oxygen isotopes in foraminiferal calcite has been applied in most oceanic paleoclimate studies after the first measurements made in 1950s (Emiliani, 1955). The oxygen isotope compositions in foraminiferal calcite constitute one of the most important variables for the Earth climate system and are considered established means for climate studies (Wefer et al., 1999). The empirically derived paleotemperature equations based on the measured oxygen isotope composition of planktonic

foraminifera are used to constrain the past sea surface temperature (Broecker, 1986; Zachos et al., 1994; Meland et al., 2005). In these applications, oxygen isotope changes in water are either estimated by ice volume effect or by implementation of an empirical relationship (e.g., between water isotopic composition and salinity). However, local variations of oxygen isotope in sea water are affected by multiple factors (global ice volume, isotopic fluxes, and ocean circulation), which can all differ from present day. An isotope-enhanced climate model is therefore needed to acquire the sea water isotopic distribution under paleo-climate conditions. This modelling approach also enables the evaluation of the simulated climate conditions by direct comparison between modelled and observed oxygen isotope composition in planktonic foraminifera (Schmidt, 1999a; Roche et al., 2004; Tindall et al., 2010).

Apart from the impacts of temperature and oxygen isotope composition of seawater, the interpretation of oxygen-18 values in foraminiferal shells is, however, complicated by the sea water carbonate chemistry (Spero et al., 1997; Zeebe, 1999). This effect needs to be considered for instance when samples from a period which has different sea water chemistry (e.g. the last glacial maximum) as compared with present day. The biogenic ‘vital effects’ also bias the interpretation by causing the calcite to precipitate out of isotopic equilibrium. Quantitative descriptions of the influence of vital effects are needed for a better understanding.

In our study, model experiments are designed to simulate the water isotope distribution in oceans under different climate conditions. These model results are analyzed for better understanding of the above mentioned issues. In Chapter 2, we give an overview of the behavior of water isotope in the earth system. A brief introduction of the numerical models we applied in this study is given in Chapter 3.

We present the first output of the water isotopes simulation in an established ocean general circulation model MPI-OM (Marsland et al., 2003) in Chapter 4. The present-day global oceanic distributions of water isotopes and deuterium excess are simulated in this newly isotope-enhanced version of the MPI-OM. The model results are validated by available observations in order to examine the model performance in capturing the main characteristics of the water isotopic distributions at sea surface and

deep waters.¹

Hereafter, this model is applied to simulate the stable oxygen isotope in sea water and foraminiferal calcite under the present day (PD) as well as last glacial maximum (LGM) conditions in Chapter 5. The modelled oxygen isotope composition of the sea waters are used to interpret the oceanic oxygen isotope distributions under different climate conditions. Sensitivity studies are also performed to understand the factors that cause the variations of sea surface and deep water isotope content during PD and LGM. A comparison of modelled oxygen-18 values in calcite at sea surface with the available planktonic foraminiferal observations at PD and LGM examines the model performance in capturing the characteristics of oceanic changes in PD and LGM.²

Last but not least, we also show the preliminary results from the biogeochemical and the FORAM models in Chapter 6. And discuss the effects of sea water carbon chemistry and vital effects on the isotopic composition buildup of the planktic foraminiferal calcite. The methods used to reconstruct the paleo-climate changes are also compared with each other.

Conclusions are given in Chapter 7.

¹ A large part of this chapter is identical to a publication of Xu et al. (2012), which will appear in the journal 'Geoscientific Model Development'.

² Content in this chapter is prepared in discussion of the journal 'Climate of the Past'.

Chapter 2

Water isotopes

Water is omnipresent on the Earth's surface, where it plays an important role in the formation of minerals, the development of landscapes, meteorological patterns, and all life processes. Since the oxygen and hydrogen isotopes are comprised in the water molecules and constitute built-in tracers of water, they undergo large fractionations during these processes, providing a multiple isotopic tracer record of diverse phenomena. Therefore stable water isotope analyses in different archives (e.g. ice core, sediment, fossil, stalagmite etc) have been widely applied in Earth sciences. The stable water isotopes are usually considered as conservative tracers, particularly for low-temperature surface waters, but physical processes and chemical reactions with rocks and other fluids can modify their composition in natural water.

2.1 Oxygen and hydrogen isotopes

Both oxygen and hydrogen are abundant in terrestrial environment, they are important elements in isotope geochemistry studies. There are two stable hydrogen isotopes (^1H , ^2H or D); the second isotope deuterium was first detected by Urey (1932). Hydrogen isotopes have by far the largest mass difference relative to the mass of the element, thus hydrogen exhibits the largest isotopic variation in nature. Oxygen consists of three stable isotopes (^{16}O , ^{17}O , and ^{18}O); together with hydrogen isotopes, there are nine possible stable isotopologues of water: H_2^{16}O , H_2^{17}O , H_2^{18}O , HD^{16}O , HD^{17}O , HD^{18}O , D_2^{16}O , D_2^{17}O , and D_2^{18}O . The average terrestrial abundances of oxygen isotopes and hydrogen isotopes (Rosman and Taylor, 1998) in atom percent are listed in Table 2.1. The abundances of water isotopologues are determined by multiplying the average abundances of constituent isotopes (Table 2.2).

Based on the abundance of these isotopologues, only four of them have practical application in isotopic studies: H_2^{16}O , H_2^{18}O , H_2^{17}O , HD^{16}O . However, H_2^{17}O is less abundant than H_2^{18}O , but tends to parallel H_2^{18}O in the hydrological system.

Therefore, H₂¹⁶O, H₂¹⁸O, and HD¹⁶O are the primary water isotopologues of interest.

Oxygen/Hydrogen isotopes	Average abundance (%)
¹⁶ O	99.757
¹⁸ O	0.205
¹⁷ O	0.038
H	99.9885
D	0.0115

Table 2.1 Averaged natural abundances of oxygen isotopes and hydrogen isotopes.

Isotopologues of water	Average abundance (%)
H ₂ ¹⁶ O	99.73406
H ₂ ¹⁸ O	0.20495
H ₂ ¹⁷ O	0.03799
HD ¹⁶ O	0.02294
HD ¹⁸ O	0.000047
HD ¹⁷ O	0.0000087
D ₂ ¹⁶ O	0.0000013
D ₂ ¹⁸ O	0.0000000027
D ₂ ¹⁷ O	0.0000000005

Table 2.2 Averaged natural abundances of nine water isotopologues.

For quantitative expression, H₂¹⁸O and HD¹⁶O are generally measured as the proportion relative to H₂¹⁶O by mass spectrometers. Because of the small values of the isotopic ratio for ¹⁸O and D in absolute value, it is customary to refer their ratios to a standard for comparison and describe in ‰ such that:

$$\delta^{18}\text{O} = \frac{[(^{18}\text{O}/^{16}\text{O})_{\text{sample}} - (^{18}\text{O}/^{16}\text{O})_{\text{standard}}]}{(^{18}\text{O}/^{16}\text{O})_{\text{standard}}} \times 1000 \text{ ‰} \quad (2.1)$$

$$\delta\text{D} = \frac{[(\text{D}/\text{H})_{\text{sample}} - (\text{D}/\text{H})_{\text{standard}}]}{(\text{D}/\text{H})_{\text{standard}}} \times 1000 \text{ ‰} \quad (2.2)$$

The primary standards of absolute isotopic ratios used by the international stable isotope community are summarized in Table 2.3.

Standard	Ratio	Value (10^{-6})
VSMOW (Vienna Standard Mean Ocean)	D/H	155.76 ± 0.1 (Hagemann et al., 1970)
	$^{18}\text{O}/^{16}\text{O}$	2005.20 ± 0.43 (Baertschi, 1976)
VPDB (Vienna Pee Dee Belemnite)	$^{18}\text{O}/^{16}\text{O}$	2067.1 ± 2.1 (Craig, 1957)

Table 2.3 Water isotope compositions of international reference standards.

There are two different δ -scales for oxygen isotope, $\delta^{18}\text{O}$ (VSMOW) and $\delta^{18}\text{O}$ (VPDB), because of two different treatment categories in traditional oxygen isotope studies. PDB is a Cretaceous belemnite from the Pee Dee Formation and was the laboratory working standard used at the University of Chicago in the early 1950's when the paleo-temperature scale was developed. The VPDB scale is applied for low-temperature carbonate analyses. The VSMOW is Vienna standard mean ocean water scale, which is used in oxygen isotope studies of waters, silicates, phosphates, sulfates and high-temperature carbonates. The conversion of $\delta^{18}\text{O}$ (VSMOW) to $\delta^{18}\text{O}$ (PDB) and vice versa (Coplen et al. 1983) is given by:

$$\delta^{18}\text{O} (\text{PDB}) = 0.97002\delta^{18}\text{O} (\text{VSMOW}) - 29.98 \quad (2.3)$$

$$\delta^{18}\text{O} (\text{VSMOW}) = 1.03091\delta^{18}\text{O} (\text{PDB}) + 30.91 \quad (2.4)$$

2.2 Fractionation processes

The differences in atomic mass of the water isotopologues cause the partitioning of the water isotopes between two different phases. This process is called fractionation, which can be either produced by isotope exchange reactions (equilibrium) or kinetic processes (non-equilibrium). The fractionation factor (α) is used to describe the rate of fractionation, and is defined as the ratio of the isotopic ratios in two phases (R_A , R_B):

$$\alpha_{A-B} = \frac{R_A}{R_B} \quad (2.5)$$

There are several possibilities to fractionate water isotopes in nature (e.g. liquid \longleftrightarrow

gas, gas \longleftrightarrow solid and liquid \longleftrightarrow solid). However, the fractionation between liquid water and water vapor is the most important process for determination of the isotopic composition of different water masses. Compare to lighter isotopes, the heavier isotopes prefer to stay at lower energy state. Therefore, the lighter isotopologues that constitute liquid water have higher translational velocities in contrast to heavier species; consequently, H_2^{16}O preferentially escapes from the surface of the liquid into the vapor phase upon evaporation, while H_2^{18}O and HD^{16}O are preferentially removed from vapors during condensation.

In general, condensation is considered as an equilibrium process. The stable isotope fractionations associated with condensation only depend on temperature, thus the isotopic systematics of condensation processes is relatively easy to treat. The oxygen isotope liquid-vapor fractionation factor between liquid and vapor under equilibrium condition can be expressed as:

$$\alpha_{l-v} = \frac{(^{18}\text{O}/^{16}\text{O})_l}{(^{18}\text{O}/^{16}\text{O})_v} = p\text{H}_2^{18}\text{O} / p\text{H}_2^{16}\text{O} \quad (2.6)$$

Here, l and v refer to liquid and vapor, respectively; p is vapor pressure at a given temperature. The liquid-vapor fractionation factor of hydrogen is calculated in the same way, but replaces $p\text{H}_2^{18}\text{O}$ by $p\text{HD}^{16}\text{O}$. The fractionation factors determined by vapor pressure measurements are in good agreement with the values measured by exchange experiments between liquid water and water vapor.

To interpret the fractionation associated with condensation, closed-system (Batch) and open-system (Rayleigh) isotopic fractionations are frequently used. The Batch model assumes that condensation takes place isothermally in a closed system, thus a constant difference between the isotopic content of vapor and liquid obtained due to the equilibrium fractionation factor is maintained during the condensation process (Figure 2.1). In nature, condensation results in cooling, this changes the fractionation factor as the process proceeds. Therefore the isothermal system is not an appropriate approximation for fractionation between condensate and vapor in case of precipitation on Earth.

The Rayleigh model is the other fractionation model that complements the

closed-system Batch model. Under Rayleigh conditions, the condensate is no longer in contact with remaining vapor and in exchange equilibrium as in Batch model, but is continuously removed from the system forever. While the remaining vapor becomes progressively more depleted due to continuously removal of heavy isotope from the system during condensation, the newly formed condensate becomes correspondingly more and more depleted by an amount dictated by the fractionation factor at the temperature of condensation (Figure 2.1). This assumption results in large depletions of heavy isotope, particularly when the air mass has lost most of its vapor. Based on measurements over many years, the gross isotopic variation in precipitation can be expressed for the most part by Rayleigh fractionation. Nonetheless, true Rayleigh conditions are practically never met in real, since vapor and condensate coexist in clouds, and possibly undergoing exchange reactions.

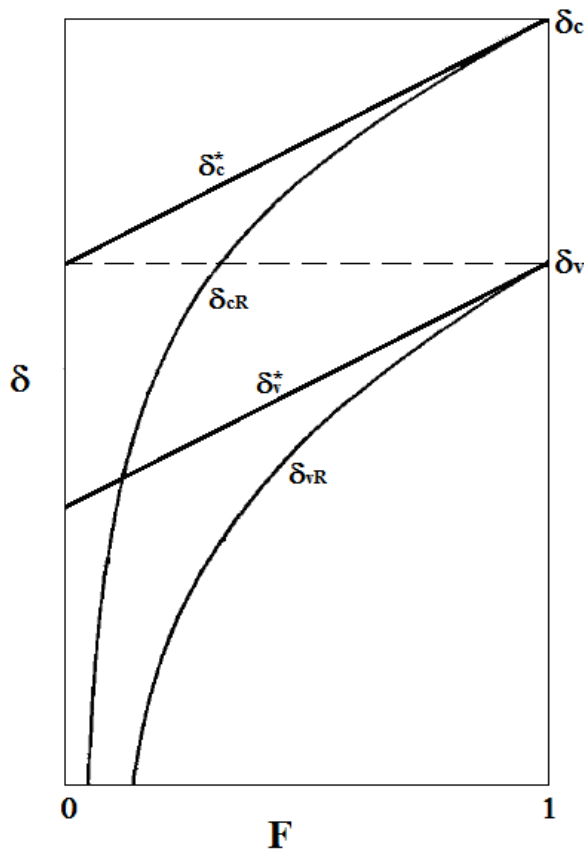


Figure 2.1 Isotopic fractionation of the remaining vapor and of the condensate as a function of the remaining fraction (F) of vapor. At $F = 1$, there is only vapor, while $F = 0$ represents all liquid. δ_c^* and δ_v^* are the trajectories of condensate and vapor under isothermal condensation. δ_{cR} and δ_{vR} are the trajectories of condensate and vapor by cooling under Rayleigh condition. (After Dansgaard, 1964)

In contrast to condensation, evaporation is more a complicated kinetic process, as it takes place in a variety of settings (clouds, large and small standing water bodies, soil,

and respiration of animals and plants). Therefore the water isotope fractionation factors existing in evaporation are affected by a number of elements. Evaporation is primarily a unidirectional process until relative humidity reaches 100%, before which the isotopic exchange between the departing vapor and the remaining liquid is restrained. Isotopic exchange between vapor and liquid acquires equilibrium when net evaporation ceases. However, over the oceans, above saturated air and inexistent wind fields are never achieved together precluding this complete isotopic exchange at interface to occur. The failure to attain equilibrium isotopic exchange between vapor and liquid results in lighter isotopic composition than that predicted for equilibrium fractionations at the given sea-surface temperature. The fractionation factors of ocean water and vapor vary with temperature and relative humidity. The typical observed value is $\alpha_{\text{liquid-vapor}} = 1.013$, which indicates 13‰ depletion of the evaporated vapor under non-equilibrium process instead of 9‰ from equilibrium assumption (Majoube, 1971). During evaporation into unsaturated air, the vapor pressure of different isotopologues, relative humidity of air, turbulence in the liquid, as well as relative diffusion rate of oxygen isotopes affect the fractionation (Craig and Gordon, 1965).

2.3 $\delta^{18}\text{O}$ and δD in the hydrosphere

The hydrosphere is described by the combined mass of water found on, under, and over the surface of the Earth. According to their different origin, these waters are defined as meteoric water, ocean water, connate water, and formation water. The present day variations of hydrogen and oxygen isotope compositions in different natural water reservoirs are expressed in Table 2.4. In general, the water isotopic ratios in large and relatively well mixed reservoirs (e.g. ocean, large lake) are more homogenous. In contrast, the isotopic composition of waters in minor abundance, especially those formed as a result of evaporation (meteoric origin), show wide variations. Over all, the meteoric and the oceanic waters are most important components of the hydrological cycle, and therefore of more interest in this study.

Reservoir	Volume (%)	$\delta^{18}\text{O}$ (‰)	δD (‰)
Ocean	97.2	0 ± 1	0 ± 5
Ice caps and glaciers	2.15	-30 ± 15	-230 ± 120
Groundwater	0.62		
Vadose water		-5 ± 15	-40 ± 70
Dilute groundwater		-8 ± 7	-50 ± 60
Brines		0 ± 4	-75 ± 50
Surface waters	0.017		
Freshwater lakes		-8 ± 7	-50 ± 60
Saline lakes and inland seas		-2 ± 5	-40 ± 60
River and stream channels		-8 ± 7	-50 ± 60
Atmospheric water	0.001	-20 ± 10	-150 ± 80

Table 2.4 Approximate volumes and typical isotopic compositions of hydrosphere reservoirs. (Criss, 1999)

2.3.1 Meteoric water

Meteoric waters include any water that participates in evaporation, condensation, and precipitation. As a component of the meteorological cycle, precipitation carries specific isotopic information about the climatic conditions of its origin. The systematic variations in $\delta^{18}\text{O}$ of precipitation elucidate the isotopic effects assigned to each part of the meteoric water cycle (Figure 2.2).

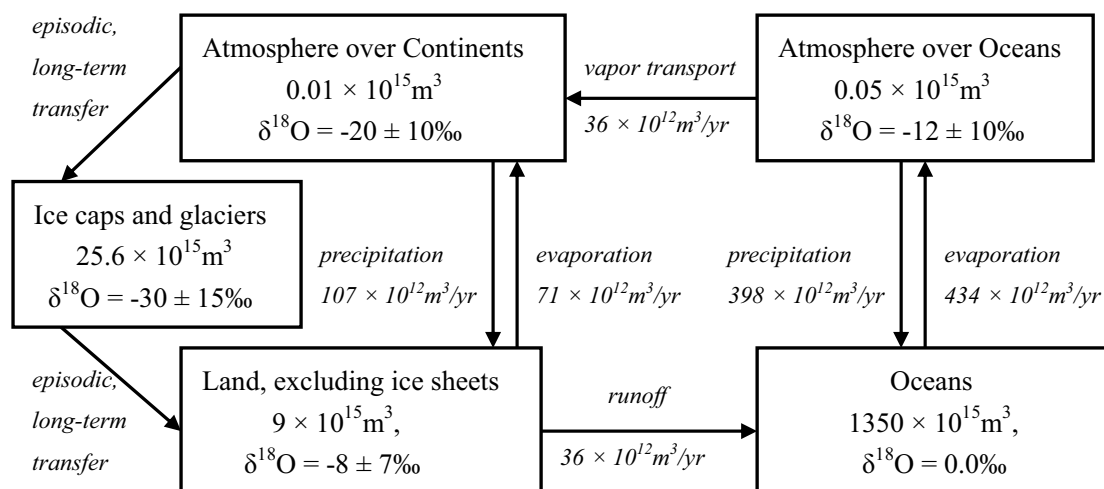


Figure 2.2 Fluxes for meteoric water cycle. (After Shape, 2007)

Variations of δD in most waters of meteoric origin are nearly in linear correlation with $\delta^{18}O$. According to a worldwide survey of precipitation, continental runoff, and polar meltwater entering the seas, a linear relationship between δD and $\delta^{18}O$ in meteoric waters was defined as (Craig, 1961):

$$\delta D = 8 * \delta^{18}O + 10 \quad (2.7)$$

It is known as the “Global Meteoric Water Line”. Later, a secondary parameter deuterium excess d ($d = \delta D - 8 * \delta^{18}O$) was introduced by Dansgaard (1964) as an index for non-equilibrium conditions. However, the coefficient, 8, and the d are not constant, but changed in response to local climatic processes.

According to an earlier study by Craig and Gordon (1965), the isotopic composition of mean global precipitation is estimated to be $\delta^{18}O = -4\text{‰}$ and $\delta D = -22\text{‰}$. But the total range of $\delta^{18}O$ in precipitation is about 4‰ to -62‰ , while the values of δD lie between 40‰ to -500‰ (Criss, 1999), and their geographic distribution is related to a number of environmental parameters, such as latitude, altitude, distance to the coast, amount of precipitation, and surface air temperature (Dansgaard, 1964). Among all of these factors, temperature and amount of precipitation are especially significant. The surface temperature strongly correlates with isotopic composition at high latitudes. Dansgaard (1964) first provided the empirical relationship between the weighted mean $\delta^{18}O$ values of precipitation in temperate climates and the mean annual surface temperature at the collection site, with the temperature coefficient of $0.7\text{‰}/^{\circ}C$. In tropical regions, the amount of monthly precipitation is negatively correlated to the $\delta^{18}O$ values; this inverse correlation is not observed in higher latitudes (Kendall and Coplen, 2001).

$\delta^{18}O$ values vary across latitudes because of the rain out effect and the temperature effect. As a result of the increase in degree of rain out and decrease in temperature with latitude, the $\delta^{18}O$ values at $0 - 20^{\circ}$ (around -2‰) are similar to ocean water, but become more depleted (around -5‰) between 20° to 40° , are even lower (around -15‰) at $40 - 90^{\circ}$ (Craig and Gordon, 1965), and the extremely low values (-62‰) are found in winter ice at the South Pole. The typical magnitude of latitude effect is approximately $0.002 \pm 0.001\text{‰}/km$ (Criss, 1999).

2.3.2 The Oceans

Oceans, as the largest reservoir of the hydrosphere, have apparently uniform isotopic composition, with most of samples having $\delta^{18}\text{O} = 0 \pm 1\text{‰}$ and $\delta\text{D} = 0 \pm 5\text{‰}$ relative to SMOW (Craig and Gordon, 1965). Values with higher variability are always confined to surface waters, where the variation is governed by fractionation during evaporation and sea-ice formation and by the isotope content of additional fresh water influx, such as precipitation, runoff and iceberg melting. The δD and $\delta^{18}\text{O}$ concentrations in sea water usually vary in parallel (Friedman, 1953).

Because similar key physical processes (evaporation and the addition of freshwater) affect the salinity and the isotopic composition of ocean water, a positive relationship between salinity and water isotopes can be expected. This almost linear correlation was first recognized by Epstein and Mayeda (1953) in the surface water of Atlantic. In an ice-free world, $\delta^{18}\text{O}$ would change by about 0.2‰ per unit change in salinity, although this will vary in accordance with the value of the added freshwater (Sharp, 2007). The factors that contribute to the variation of $\delta^{18}\text{O}$ and salinity are illustrated in Figure 2.3. Subtropical excess in evaporation enriches both $\delta^{18}\text{O}$ and salinity, whereas intense precipitation at equatorial lowers the $\delta^{18}\text{O}$ and salinity values. At high latitudes, the meltwater entering ocean has extremely low $\delta^{18}\text{O}$ values, which induces a stronger effect on isotopic ratio than salinity. Because the fractionation of oxygen isotope between ice and seawater is small (O'Neil, 1968), but almost no salt is incorporated as ice formation, the salinity of seawater increases significantly during growth of sea ice while its $\delta^{18}\text{O}$ value only decreases slightly.

Although the total variation in oxygen isotopic composition of deep ocean water is much less compared to surface (around 0.3‰), the deep waters of different ocean basins have distinct values of $\delta^{18}\text{O}$ and salinity (Table 2.5). Therefore, highly precise measurements can be used to deduce the details of oceanic circulation patterns.

It is suggested by some researchers that a large change in the $\delta^{18}\text{O}$ values of ocean water has occurred over geological time, when the $\delta^{18}\text{O}$ value of the hydrosphere is buffered by the Earth's lithosphere. A timescale of approximately 30Ma is required to circulate the entire ocean through the mid-oceanic hydrothermal systems (Gregory

and Taylor, 1981). On a shorter timescale during the Quaternary period, the fluctuations in $\delta^{18}\text{O}$ values of ocean water are approximately $\pm 1\%$. These fluctuations are considered as the reflection of the cycles of growth and melting of continental ice sheets (Savin and Yeh, 1981), and their timescale was much too fast to be offset by lithospheric buffering.

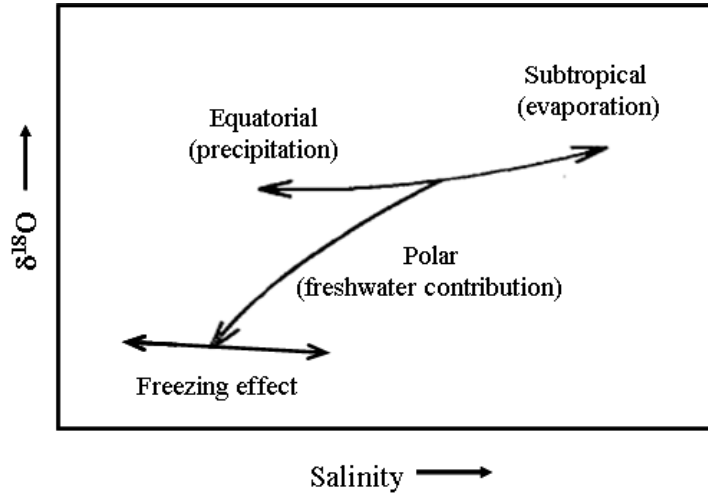


Figure 2.3 Schematic illustration of various effects on the isotopic composition and salinity of ocean surface water (After Craig and Gordon, 1965).

	Salinity	$\delta^{18}\text{O}$ (‰)
North Atlantic Deep Water	34.93	0.12
Antarctic Bottom Water	34.65	-0.45
Indian Deep Water	34.71	-0.18
Pacific Deep Water		
Pacific Antarctic (55-65°S)	34.700	-0.21
South Pacific (22-40°S)	34.707	-0.17
Equatorial Pacific (6°S-30°N)	34.692	-0.17
North Pacific (44-54°N)	34.700	-0.17
Circumpolar Water	34.69	-0.3 to -0.2

Table 2.5 Oxygen isotopic composition of the principal deep water masses (Craig and Gordon, 1965).

2.4 Oxygen isotope in biogenic carbonate

Carbonates are one of the most important archives in stable isotope geochemistry. They have preserved oxygen isotope information over almost all chronological intervals, and this information is the fundamental index to infer paleo-temperatures, circulation patterns, and ice volume. The possibility of biogenic carbonates to be employed as an indicator of paleoclimate was first recognized by Urey et al. (1948), who determined the ancient ocean temperature using the measured oxygen isotopic ratio of biogenic carbonate deposited from marine organism. Although there are a number of potential problems, this technique of determining paleo-temperatures has proven to be a valuable tool in paleoclimate reconstruction by several subsequent researchers.

2.4.1 Planktic foraminifera

Planktic foraminifera are a group of marine protozoan most of which built calcite shells of roughly 0.5mm diameter comprising of a series of chambers around a coiling axis (Berger, 1969; Signes et al., 1993). There are approximately 45 extant species which are distributed throughout the entire world oceans from the surface to depths of 1000m or more (Hemleben et al., 1989). As passive inhabitants of their environment, planktic foraminifera are distributed by water current, however, the geographic distribution of the different species is restricted to the global climate belts.

Planktic foraminifera can be divided into two general categories: species possessing calcite spines that radiate out from the shell surface (spinose species, Figure 2.4) and those without spines (non-spinose species). Most of the spinose species harbor large numbers of algae between their spines whose amount can exceed 5,000 algal cells per foraminifera (Spero and Parker, 1985).

In general, the life span of individual planktic foraminifera is short and synchronized with the lunar cycle (Spindler et al., 1979; Bijma et al., 1990). The shell reflects approximately two weeks (*G. ruber*) to four weeks (*G. sacculifer*, *O. universa*, *H. pelagica*) of calcification. Because of their short reproductive cycle and relative abundance, planktic foraminifera are a primary contributor of biogenic calcite to the

open ocean marine sediment (Bé 1977) and are considered ideal tool for reconstruction of paleo-environmental conditions.

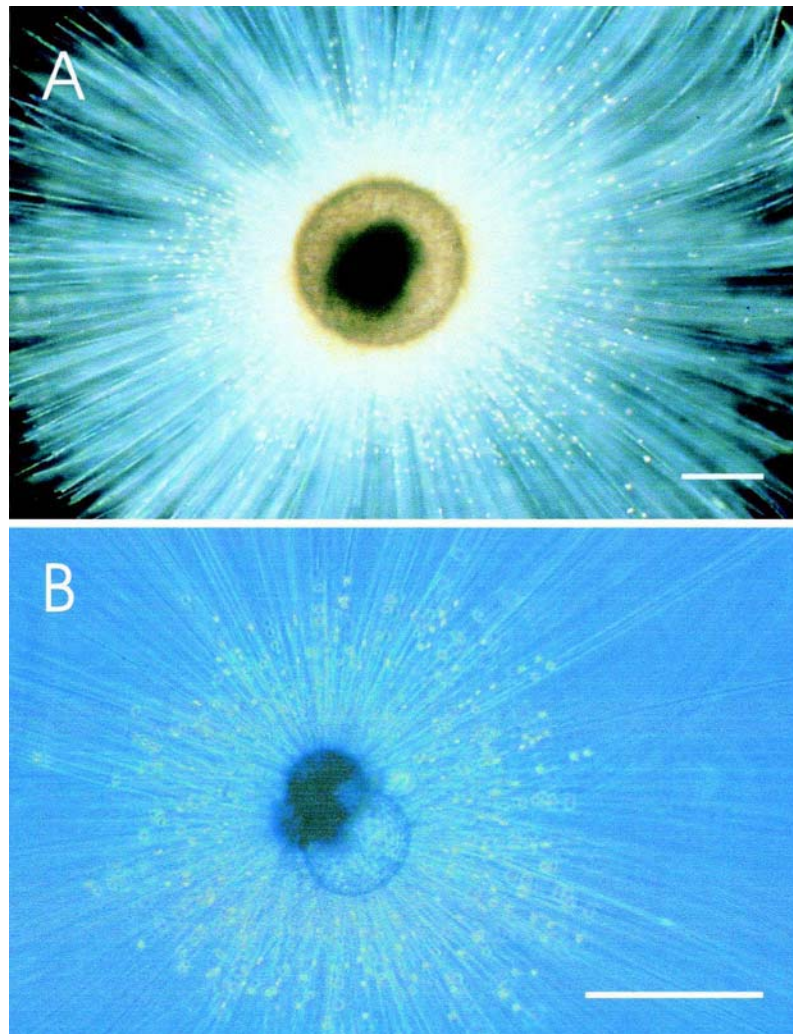


Figure 2.4 (A) Microphotograph of *O. universa* d'Orbigny with symbiotic dinoflagellates (photo: H.J. Spero; scale bar = 300 μ m). (B) Microphotograph of *G. sacculifer* (Brady) with symbiotic dinoflagellates (photo: H.J. Spero; scale bar = 300 μ m). (After Wolf-Gladrow et al., 1999)

2.4.2 Oxygen isotope paleo-thermometer

In early isotopic studies, foraminifera were used primarily for biostratigraphic analysis. The application of planktic foraminifera to paleo-oceanographic and paleo-climatic research has been propelled into the forefront of these fields after the work at the University of Chicago (McCrea, 1950; Epstein et al., 1953; Emiliani,

1954; Emiliani, 1955).

The basic idea behind the application of calcite shell of planktic foraminifera as indicator for paleo-temperature is based on the theory that the fractionation between calcite and water is a function of temperature, so the difference between $\delta^{18}\text{O}$ values of calcite and water can be used to derive the temperatures of the ocean at the time of carbonate formation. Based on oxygen isotope analyses of the carbonate samples from mollusks (e.g. belemnites), an empirical paleo-temperature equation was established (Epstein et al., 1953) derived from a best fit of the measured data to a second-order polynomial. This classic paleo-temperature equation can be rewritten to appropriate for δ_c ($\delta^{18}\text{O}$ value of calcite) and δ_w ($\delta^{18}\text{O}$ value of water) on the PDB and SMOW scales, respectively:

$$T \text{ (}^\circ\text{C)} = 15.75 - 4.3(\delta^{18}\text{O}_{\text{c-PDB}} - \delta^{18}\text{O}_{\text{w-SMOW}}) + 0.14(\delta^{18}\text{O}_{\text{c-PDB}} - \delta^{18}\text{O}_{\text{w-SMOW}})^2 \quad (2.8)$$

In this carbonate paleo-temperature equation, temperature T is estimated from the measured $\delta^{18}\text{O}$ values of carbonate and assumed $\delta^{18}\text{O}$ values of water in ancient oceans, which depend on equilibrium fractionations between water and the various carbonate species (H_2CO_3 , HCO_3^- , and CO_3^{2-}). However, the validity of this estimate relies on the variation of $\delta^{18}\text{O}$ values in the water at the time of calcite formation and deviations from equilibrium $\delta^{18}\text{O}$ in calcite caused by several processes (e.g. ‘vital effect’, Urey, 1948). A comprehensive summary of various proposed Temperature- $\delta^{18}\text{O}$ relationship was presented by Bemis et al. (1998) based on data from cultured foraminifera.

Figure 2.5 illustrates the main processes that determine the $\delta^{18}\text{O}$ values of sea waters, as well as those affecting oxygen isotopic fractionation between foraminifera carbonate and sea water. The ice volume effect exerts by far the most important control on global oceanic $\delta^{18}\text{O}$ enrichment, while the relationship between sea level and $\delta^{18}\text{O}$ value of sea water is approximately $0.012 \pm 0.001\text{‰/m}$ (Aharon, 1983; Labeyrie et al., 1987; Shackleton, 1987; Fairbanks, 1989). For planktic foraminifera, the temperature is the major control on the $\delta^{18}\text{O}$ record, and although the vital effects are considered to be species-specific it still remains largely descriptive in

understanding.

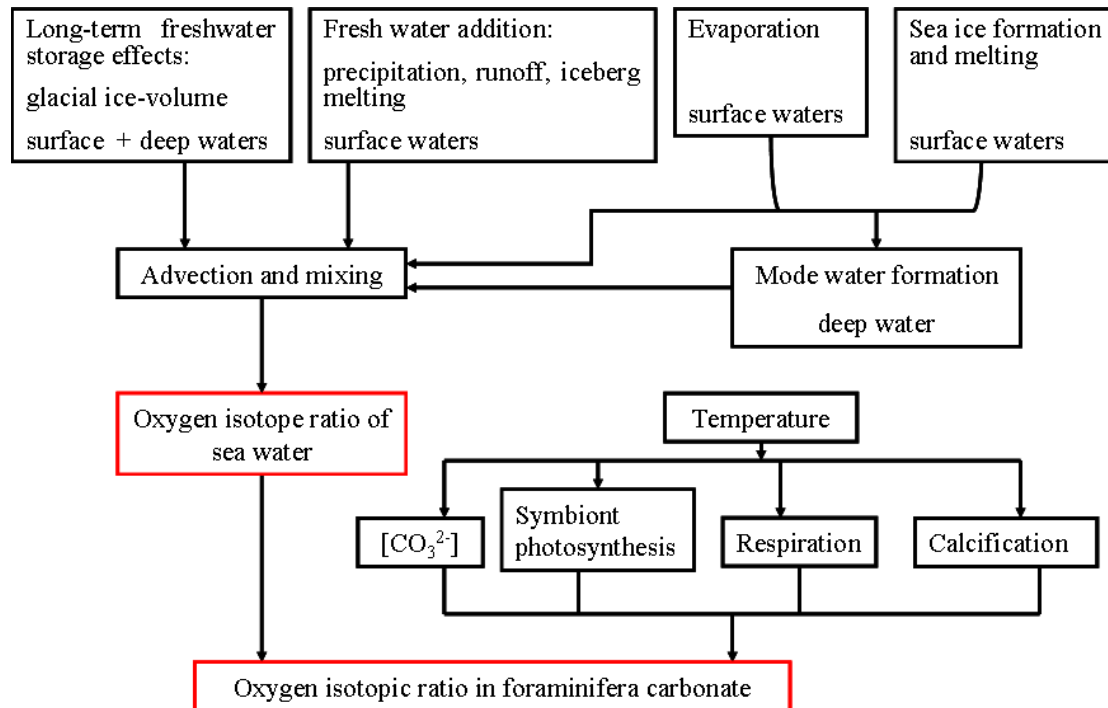


Figure 2.5 Schematic summary of the various factors that affect the oxygen isotopic ratios in foraminiferal carbonate.

2.5 General circulation models (GCMs)

For the past several years, general circulation models, which include explicit stable water isotopes diagnostics, are established tools to investigate the relationship between water isotopes and various climate variables.

Joussaume et al. (1984) pioneered the application of GCMs in isotope studies by incorporating the water isotopes as conservative tracers in an atmospheric GCM (Laboratoire de Météorologie Dynamique; LMD). Following which, water isotopes in meteorological cycle have been simulated in several atmospheric GCMs under different climatic conditions (Jouzel et al., 1987; Cole et al., 1993, Hoffmann et al., 1998; Lee et al., 2008). These previous modeling studies stressed the importance of understanding the spatial and temporal isotopic variations for a quantitative interpretation of their relationship to climate changes.

Implement of the water isotopes in ocean GCMs was started by Schmidt (1998), who

considered the water isotopes as passive tracers in the ocean circulation. Since then, the ocean GCMs are used to study the isotopic composition in the ocean, and their relationship with salinity (Paul et al., 1999; Delaygue et al., 2000; Wadley et al., 2002). For oceanic GCMs, in particular, the studies also showed the potential of $\delta^{18}\text{O}$ to characterize different water masses.

More recently, fully coupled atmosphere-ocean GCMs have become advance tools in isotopic simulation (Schmidt et al., 2007; Tindall et al., 2010). The use of a coupled model enables consistent simulation of the natural range of the variability and to link changes in the different components of the model.

Chapter 3

Model description

The results of this study are based on the simulations with three numerical models, the ocean general circulation model MPI-OM (Marsland et al, 2003), the carbon cycle model HAMOCC (Six and Maier-Reimer, 1996), and a diffusion-reaction FORAM model (Wolf-Gladow et al., 1999) for carbonate chemistry in the vicinity of symbiont bearing foraminifera. A water isotope tracer module is first implemented in MPI-OM. The salinity, temperature, and water isotope composition based on the isotope tracer included ocean model simulation, and the hydrogen iron concentration, dissolved inorganic carbon (DIC), dissolved oxygen, as well as partial pressure of CO₂ derived from HAMOCC are used as the inputs for the FORAM model to calculate the carbon chemistry. Thereafter, the resultant is used to estimate the isotopic composition in the carbonate shell of foraminifera. A schematic overview of the model application in our study is shown in Figure 3.1.

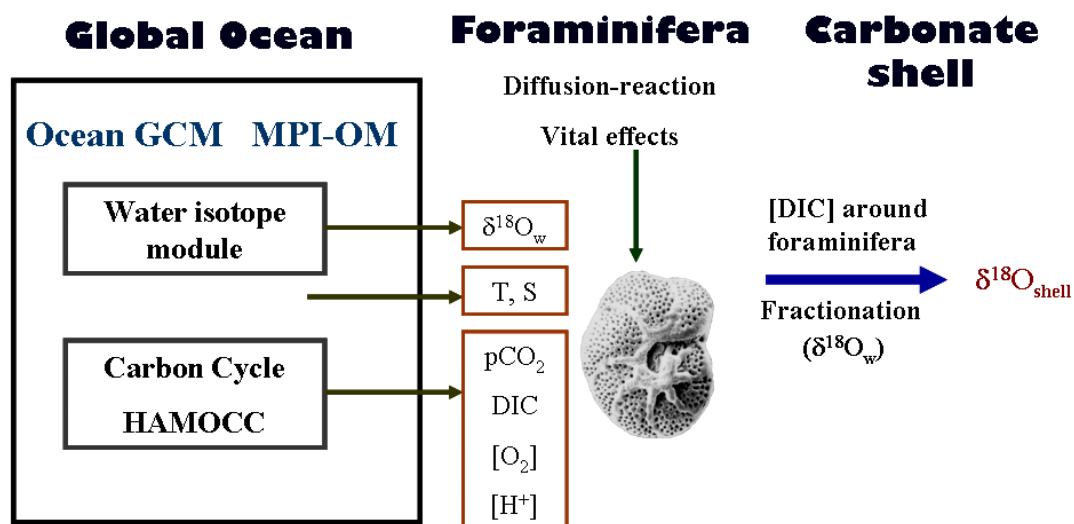


Figure 3.1 Simplified schematic overview of the model used in this study.

3.1 The ocean model MPI-OM

The Max-Planck-Institute Global Ocean/Sea-Ice Model MPI-OM (Marsland et al.,

2003) solves the primitive equations on an Arakawa C-grid (Arakawa and Lamb, 1977) while the vertical discretization is on z-level. The model has a free surface and includes sub-grid-scale parameterizations for the bottom boundary layer (BBL) flow across steep topography, horizontal and vertical viscosity, vertical and isopycnal diffusivity, and convection. As sea ice component, a viscous-plastic rheology sea ice model (Hibler, 1979) is embedded. This sea ice model includes thermodynamic sea ice growth and melt, as well as the thermohaline coupling to the ocean model by brine rejection.

3.1.1 Ocean primitive equations

The horizontal velocity (\vec{V}) of a hydrostatic Boussinesq fluid is described by the horizontal momentum balance on a rotating sphere, while the hydrostatic equation is used to close the momentum balance.

$$\frac{d\vec{V}}{dt} + f(\vec{k} \times \vec{V}) = -\frac{1}{\rho_w} [\vec{\nabla}_H(p + \rho_w g \zeta)] + \vec{F}_H + \vec{F}_V \quad (3.1)$$

$$\frac{\partial p}{\partial z} = -g\rho \quad (3.2)$$

f : Coriolis parameter ρ_w : reference density, 1025kg/m³

ζ : sea surface elevation \vec{F}_H / \vec{F}_V : horizontal/vertical eddy viscosity

Density (ρ) in equation 3.2 is a function of model pressure, temperature, and salinity according to the equation of state defined by the Joint Panel on Oceanographic Tables and Standards (UNESCO, 1983).

The change of the sea level elevation is equal the vertical velocity (w) at sea surface. This relation is used to forward integrate the ocean model surface.

$$\frac{\partial \zeta}{\partial t} = w \Big|_{z=\zeta} \quad (3.3)$$

Considering the incompressible fluid condition, the vertical velocity is derived from the continuity equation. Therefore, the vertical velocity at surface is deduced from the integration of the continuity equation through the whole depth.

$$\frac{\partial w}{\partial z} = \vec{\nabla}_H \vec{V} \quad (3.4)$$

The potential temperature (θ) and salinity (S) follows the advection and diffusion scheme.

$$\frac{d\theta}{dt} = \vec{\nabla}_H \cdot (K \vec{\nabla}_H \theta) \quad (3.5)$$

$$\frac{dS}{dt} = \vec{\nabla}_H \cdot (K \vec{\nabla}_H S) \quad (3.6)$$

3.1.2 Ocean sub-grid-scale parameterizations

In order to include the processes whose scales are smaller than the model resolution, sub-grid-scale parameterizations are applied. The coarse z-coordinate ocean model fail to resolve the ‘overflow’ (Price and Baringer, 1994) process where dense nearly bottom waters cross sills between ocean basins, therefore a BBL slope convection is formulated to overcome this problem. The BBL scheme in MPI-OM is sketched in Figure 3.2. In this scheme, a maximum BBL depth is prescribed to restrict the BBL thickness ($H_{BBL} = \min(\Delta z_s, BBL_{\max})$) in the deeper grid cell of the coarse resolution ocean model. The neutral buoyancy target cell (k_t), instead of the bottom cell (k_{bot}), is chosen based on the density in the source cell (k_s). Therefore the BBL transport and remaining advection are expressed as:

$$T_{rBBL} = u_s \Delta x, y H_{BBL} \quad (3.7)$$

$$T_r = u_s \Delta x, y (\Delta z - H_{BBL}) \quad (3.8)$$

The horizontal and vertical viscosities are treated separately. The horizontal viscosity is parameterized by a scale-dependent biharmonic formulation. A time filter applied eddy coefficient, which includes Richardson number term, background viscosity term, as well as wind mixing term, is used to parameterize the vertical viscosity.

The tracer mixing by advection is represented by isoneutral/dianeutral diffusion, after the Gent et al. (1995) parameterization. The parameterization of vertical

diffusivity is similar to the vertical viscosity, but has a cubic dependence on the Richardson number term.

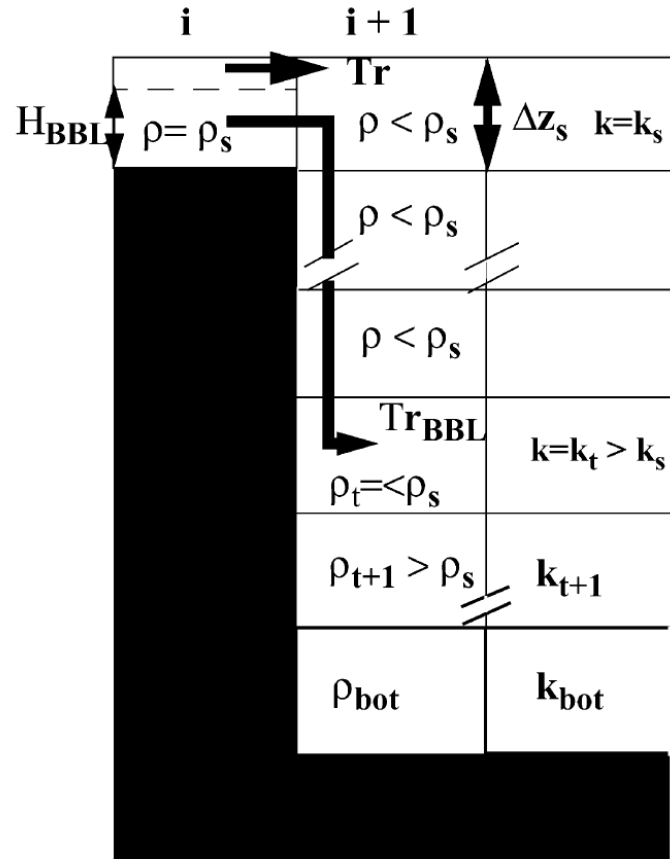


Figure 3.2 The scheme of BBL transport, where the purely horizontal transport and BBL transport are indicated by Tr and Tr_{BBL} , respectively. (Marsland et al., 2003)

There are three choices for convection parameterization. The convective adjustment follows Bryan (1969), which aims to increase the penetrative depth of convection. The penetrative plume scheme of Paluszkiwicz and Romea (1997) is able to use a much more physically based parameterization, but is computationally expensive. The third scheme parameterizes convection by greatly enhanced vertical diffusion under static instability (e.g. Klinger et al., 1996). This approach avoids the excessive intermediate mixing in the traditional adjustment scheme.

3.1.3 Sea ice dynamics and thermodynamics

The motion of sea ice is solved in a two dimensional momentum balance equation. In addition to the Coriolis force and pressure gradient, the velocity of sea ice also responds to wind, ocean current and internal ice stress (Hilber, 1979).

Thermodynamics of sea ice in this model include the local growth/melt at the base of sea ice and the local melt at the surface. At the surface, a thermodynamic equilibrium is applied at the interface between atmosphere and sea ice/snow layer, where the heat flux over sea ice equals to the conductive heat flux within the sea ice/snow layer. Since the conductive heat flux depends on the temperature gradient across the sea ice/snow layer, the sea ice/snow layer melts at the surface when the surface temperature is greater than 0°C. An interim upper layer ocean temperature is introduced to complete the sea ice thermodynamic evolution at the interface between ocean and sea ice/snow layer. New sea ice is formed at the base when the upper layer ocean temperature is lower than the freezing temperature (T_{freeze}), while melting occurs when it is above the melting temperature (T_{melt}). The effect of salinity on the freezing and melting is ignored, constant T_{freeze} (-1.9°C) and T_{melt} (0°C) values are used. Additionally, the sea ice is embedded into the upper layer of ocean by an upper-bound to the sea ice thickness.

The sea ice model is coupled to the ocean thermohaline circulation by salt and fresh water exchange at the upper layer during sea ice growth and melt. In the model, the salinity of sea ice is assumed to be a constant ($S_{ice} = 5$).

$$(S_1 + \Delta S) \Delta z'^{old} + \frac{\rho_i h_i^{old}}{\rho_w} S_{ice} = S_1 \Delta z'^{new} + \frac{\rho_i h_i^{new}}{\rho_w} S_{ice} \quad (3.9)$$

$$S_1 : \text{salinity at upper layer}; \quad \Delta z' = \Delta z_1 + \zeta - \frac{1}{\rho_w} (\rho_i h_i + \rho_s h_s)$$

Δz_1 : depth of the upper ocean layer; ρ_i : density of sea ice, 910kg/m³

ρ_s : density of snow, 330 kg/m³; h_i/h_s : ice/snow thickness

3.1.4 Model grid

The model is implemented on a bipolar orthogonal spherical coordinate system, with the poles located over Antarctica and Greenland, respectively. The second location avoids a grid singularity in the Arctic Ocean while the horizontal resolution is high in the deep-water-formation regions of the Arctic and the northern North Atlantic Oceans. Location and radius of the poles can be modified to give relatively high resolution in the region of interest. The standard MPI-OM grid set for this study is illustrated in Figure 3.3.

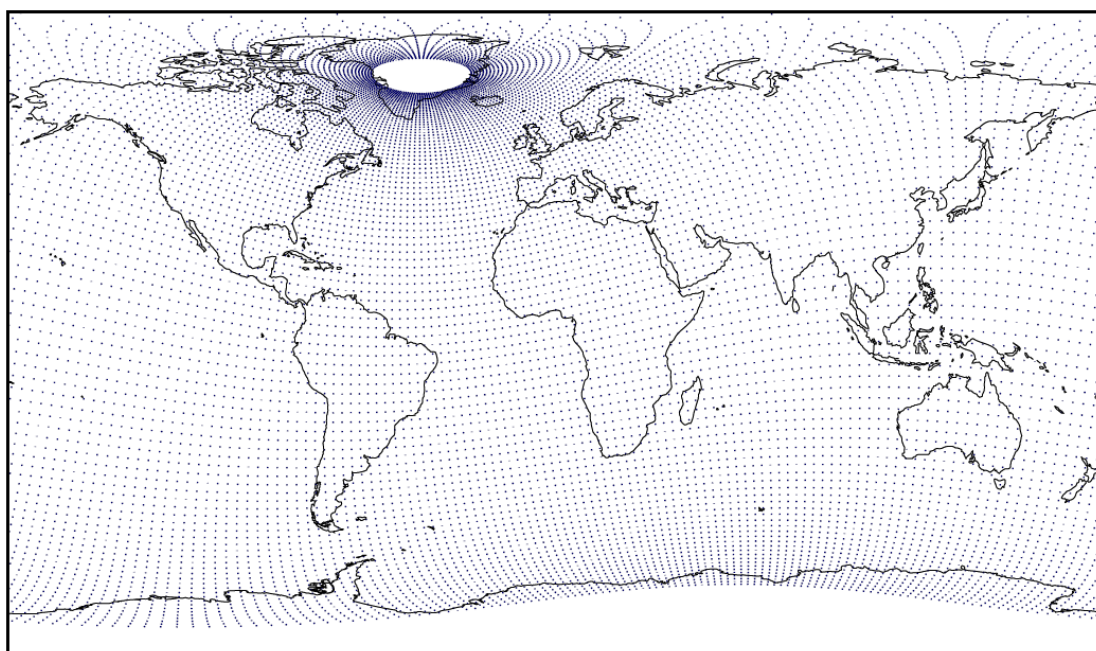


Figure 3.3 Standard MPI-OM orthogonal curvilinear grid for the model simulations in this study.

3.2 Biogeochemistry model HAMOCC

The Hamburg Oceanic Carbon Cycle Model (HAMOCC) simulates the carbon cycle in air, water and sediments, as well as the interaction between these three components (Six and Maier-Reimer, 1996). This biogeochemistry model is implemented into MPI-OM as a subroutine. It runs with the same spatial resolution and time step as defined in the ocean model. The biogeochemical tracers simulated in the standard HAMOCC set are listed in Table 3.1. These tracers are advected and diffused in the same way as salinity in the MPI-OM advection-diffusion scheme, but the isopycnal

mixing is neglected.

Symbol	Meaning	Units
C_T^{12}	Total dissolved inorganic ^{12}C	kmol C m^{-3}
A_T	Total alkalinity	kmol eq m^{-3}
PO_4	Phosphate	kmol P m^{-3}
O_2	Oxygen	kmol O m^{-3}
N_2	nitrogen	kmol N m^{-3}
NO_3	Nitrate	kmol N m^{-3}
$SI(OH)_4$	Silicate	kmol Si m^{-3}
DOM	Dissolved organic matter	kmol P m^{-3}
PHY	Phytoplankton	kmol P m^{-3}
ZOO	Zooplankton	kmol P m^{-3}
DET	Detritus	kmol P m^{-3}
$CACO_3$	Calcium carbonate shells	kmol C m^{-3}
OPAL	Opal shells	kmol Si m^{-3}
C_T^{14}	Total dissolved inorganic ^{14}C	kmol C m^{-3}
N_2O	Nitrous oxide	kmol N m^{-3}
DMS	Dimethyl sulfide	Kmol m^{-3}
FDUST	Free (non-aggregated) dust	Kg m^{-3}
FE	Dissolved iron	kmol Fe m^{-3}

Table 3.1 Biogeochemical tracers in the HAMOCC standard simulation.

To drive the model, a monthly mean dust deposition file should be obtained as the input file of HAMOCC. The size and sinking speed of all dust particles are assumed to be same in HAMOCC.

3.2.1 Biochemistry in upper layer

Since the biological processes depend on light, the photosynthesis and zooplankton

grazing are restricted to the euphotic zone (upper 100m of the water column). Therefore, only aerobic processes are simulated in this region. Below the euphotic zone, all organic matter ultimately remineralizes to nutrients. And, the rest of particulate matters fall onto the sediment. The marine ecosystem as simulated by HAMOCC is illustrated in Figure 3.4.

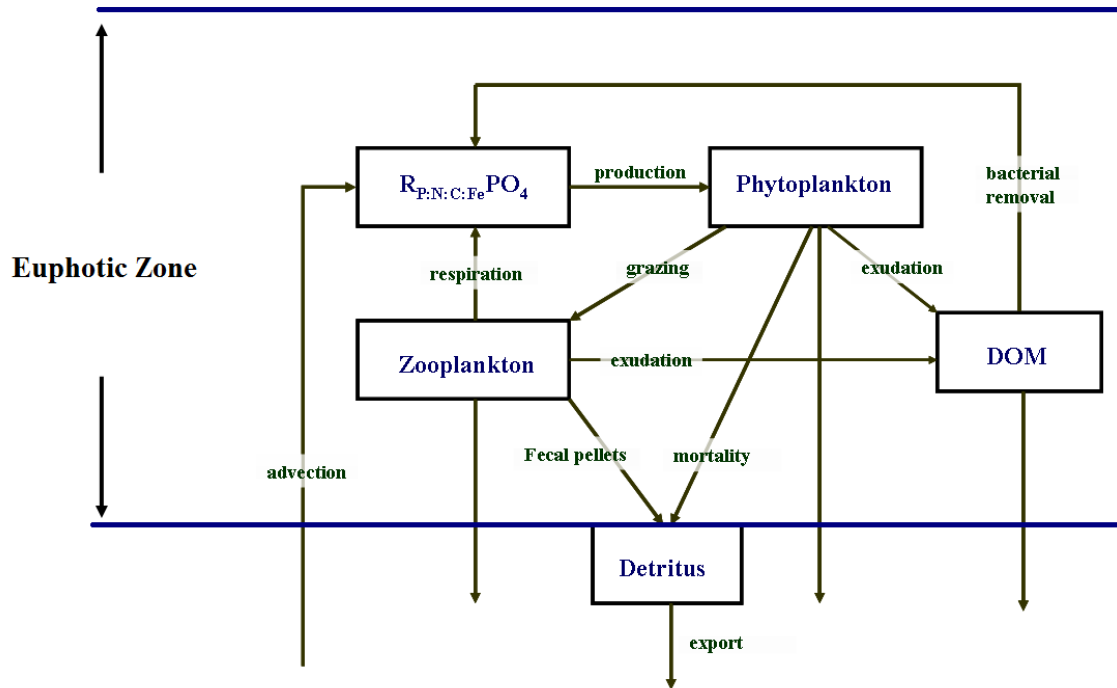


Figure 3.4 Overview of the marine ecosystem as simulated in HAMOCC. (after Wetzel, 2004)

In the model, the growth rate of phytoplankton is formulated by availability of light and nutrients. At surface, the light intensity follows the prescribed solar radiation in the ocean GCM. Below the surface, light is attenuated by water and chlorophyll through depth. The limitation of nutrients also affects the phytoplankton growth, which is taken as the least available nutrient $\left(\min \left(PO_4, \frac{NO_3}{R_{N:P}}, \frac{FE}{R_{Fe:P}} \right) \right)$. Exudation from phytoplankton is one of the sources of dissolved organic matter, and the dead phytoplankton forms detritus.

There are three different types of phytoplankton that are accounted in HAMOCC:

diatoms, coccolithophorids, and flagellates. The growth of diatoms takes precedence when silicate is available, while opal shells are formed during their growth. Because of the priority for diatoms, the fraction of calcium carbonate shells which are built by coccolithophorids depends on the concentration of silicate. Only the shell material of dead phytoplankton is accounted as opal and calcium carbonate. The growth of both diatoms and coccolithophorids regulates the DMS production, which is also controlled by water temperature.

Phytoplankton is the food for zooplankton. Part of the grazed phytoplankton leads to the growth of zooplankton, and the rest either becomes detritus as fecal pellet or be excreted as nutrient. The dead body of zooplankton is another source of detritus.

Phosphate concentration is proportional to zooplankton excretion and DOM remineralization, whereas it is reduced by photosynthesis. The nitrate dynamics and Fe fixation in the surface layer follow constant stoichiometric ratios, $R_{N:P}$ and $R_{Fe:P}$, respectively.

3.2.2 Marine carbon chemistry

The dissolved inorganic carbon chemistry and calcium carbonate dissolution are treated in the same way as described by Maier-Reimer and Hasselmann (1987). The simulated C_T and A_T in HAMOCC are defined as:

$$[C_T] = [H_2CO_3] + [HCO_3^-] + [CO_3^{2-}] \quad (3.10)$$

$$[A_T] = [HCO_3^-] + 2[CO_3^{2-}] + [B(OH)_4^-] + [OH^-] - [H^+] \quad (3.11)$$

In equation 3.10, the aqueous carbon dioxide and true carbonic acid are not chemically separated, both are represented by H_2CO_3 . The biogeochemical processes, sea-air gas exchange, as well as calcium carbonate dissolution affect the total carbon concentration.

The formation of calcium carbonate shells by coccolithophorids consumes dissolved inorganic carbon, and decrease the alkalinity as well. Furthermore, the formation and degradation of phosphorous particulates change the C_T under a constant ratio. The

associated changes in nitrate concentration also modify the A_T . Calcium carbonate is dissolved with a constant dissolution rate depending on the under-saturation of CO_3^{2-} in sea water.

3.2.3 Air-Sea gas exchange

The exchange of O_2 , N_2 , and CO_2 across air-sea interface can be calculated in two ways. One is to assume that the concentration of atmospheric tracers is constant, and the other way is to take account of the change of the atmospheric concentration due to the air-sea exchange. The air-sea gas exchange rates V_i of different gas tracers i are formulated based on the Schmidt number and piston velocity (Wanninkhof, 1992) as:

$$V_i = (1 - F_{ice}) \frac{u^2}{(Sc_i / 660)^{\frac{1}{2}}} * 0.337 \quad (3.12)$$

F_{ice} : sea ice fractionation; u : wind speed; Sc_i : Schmidt number of tracer i

Solubility (S_i) of all the gases are calculated from temperature and salinity based on Weiss (1970). Therefore, the fluxes (F_i) of these gases at sea surface are described as:

$$F_i = V_i * S_i * (pP_{i-water} - pP_{i-air}) \quad (3.13)$$

where $pP_{i-water}$ and pP_{i-air} are the partial pressures at air and water of the gas tracer i , respectively.

3.3 FORAM model

The FORAM model (Wolf-Gladrow et al., 1999; Wolf-Gladrow and Riebesell, 1997) is a species based diffusion-reaction model for the carbonate system in the microenvironment of foraminifera. A spherical geometry is assumed in the model, which is a reasonable approximation for foraminifera. In this model, two boundaries are considered, the inner boundary is the surface of the foraminifera's shell and the

outer boundary is the region where all the chemical species have the same concentrations as the bulk values ($\sim 3000\mu\text{m}$ away from shell). The concentration profiles of the chemical species are calculated as a function of the distance from the center of the shell. A schematic representation of the model is sketched in Figure 3.5.

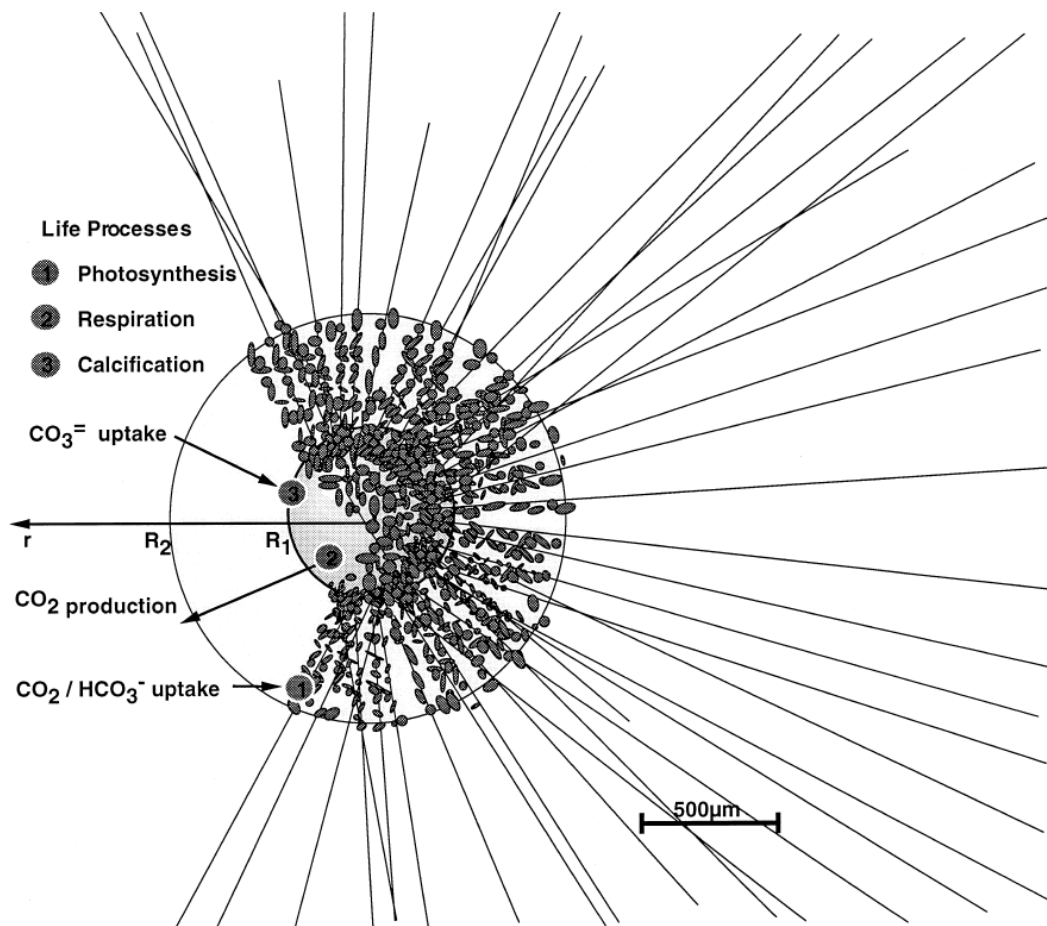


Figure 3.5 Schematic view of the symbiont bearing foraminifera. R_1 is the radius of the calcite shell. Symbionts are located in a halo between R_1 and R_2 . (Wolf-Gladrow et al., 1999)

3.3.1 Diffusion and reactions

The time scales of diffusion and reactions (~ 1 min) are very small in comparison to the time scales of calcification, respiration, and photosynthesis in the real environment (\sim hours or days). Therefore, the fluxes of those chemical species of the carbon system can be considered being in a steady state. According to this assumption,

the basic equation of the model is formulated as:

$$\frac{\partial c(r,t)}{\partial t} = \text{Diffusion} + \text{Reaction} + \text{Uptake} = 0 \quad (3.14)$$

where $c(r,t)$ is the concentration of a species of the carbon system.

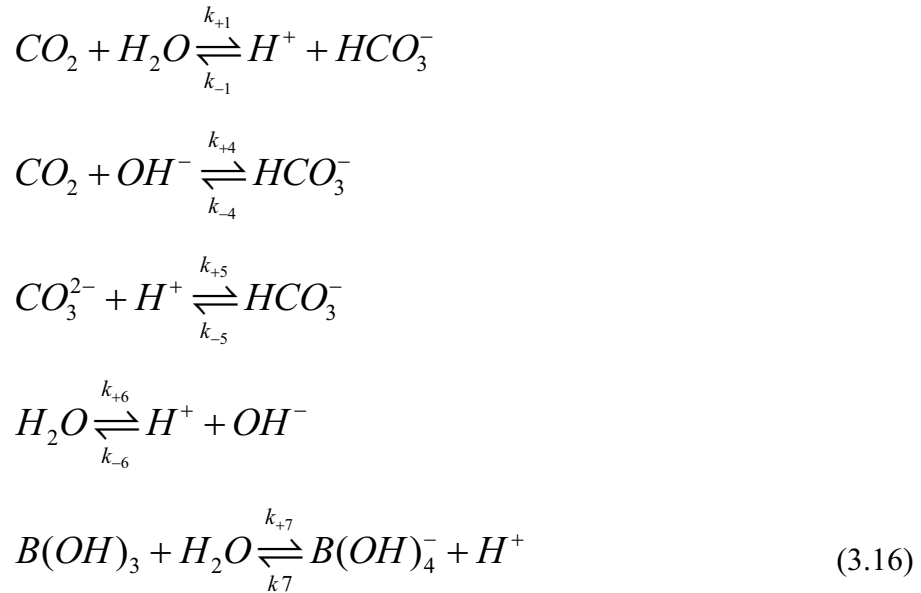
The diffusion term under spherical symmetric condition is expressed by:

$$\frac{D_c}{r^2} \frac{d}{dr} \left(r^2 \frac{d[c]}{dr} \right) \quad (3.15)$$

D_c : diffusion coefficient of a species of the carbon system

r : distance from the center of the cell

The chemical reactions simulated in the model are listed following:



where k denotes the kinetic (rate) constant. Both D_c and k are depend on temperature and salinity.

Thus, the changes in the concentration by diffusion, the reactions, as well as specific sources and sinks from the various life processes will have to be included to complete the equation 3.14.

3.3.2 Vital effect

There are three life processes involved in the model: calcification, photosynthesis and respiration. The influence of these life processes on the carbon system is considered

as constant rates based on laboratory measurement.

In general, calcification consumes CO_3^{2-} ions due to the chemical reaction:



However, HCO_3^- ions can be also used for calcite precipitation. Whereby, calcification consumes HCO_3^- and releases CO_2 at the same time. In the model, calcification can be simulated either by CO_3^{2-} uptake or by HCO_3^- uptake. Here, we used the CO_3^{2-} uptake in our simulation.

Photosynthesis is due to the life processes of the symbiotic algae. The total carbon uptake includes two parts: CO_2 and HCO_3^- . The CO_2 uptake is calculated via Michaelis-Menten kinetics, while the HCO_3^- uptake is considered as the remaining part of the total carbon uptake.

Respiration of the foraminifera produces CO_2 at the surface of the shell, which represents the inner boundary condition of CO_2 . Because the symbiotic algae exist in the whole symbiont halo, their respiration is considered as another source of CO_2 .

3.4 Isotope tracers

The stable water isotopes $H_2^{18}O$ and HDO are incorporated as conservative passive tracers into MPI-OM. They are fully advected and mixed by the ocean GCM. The isotopic variations occurring in MPI-OM primarily depend on the temperature-dependent isotope fractionation during evaporation, the isotopic composition of freshwater fluxes entering the ocean, and the oceanic advection and mixing of different water masses. The schematic of isotopic simulation is presented in Figure 3.6.

For an ocean GCM isotope simulation, the required isotopic composition of evaporation (E) and precipitation (P) fluxes can either be taken from observational data or obtained from suitable atmospheric model output. Several previous studies

applied a regression formula (Gat and Gonfiantini, 1981) to calculate the isotopic composition of precipitation (Schmidt, 1998; Wadley et al., 2002). This global regression is based on observed local temperatures and precipitation amounts over continents and some island stations. The high latitudes are underrepresented by this empirical approach, and the tropical amount effect is not well captured (Rozanski et al., 1993).

Boundary Forcing of H_2^{18}O , HD^{16}O (HDO)

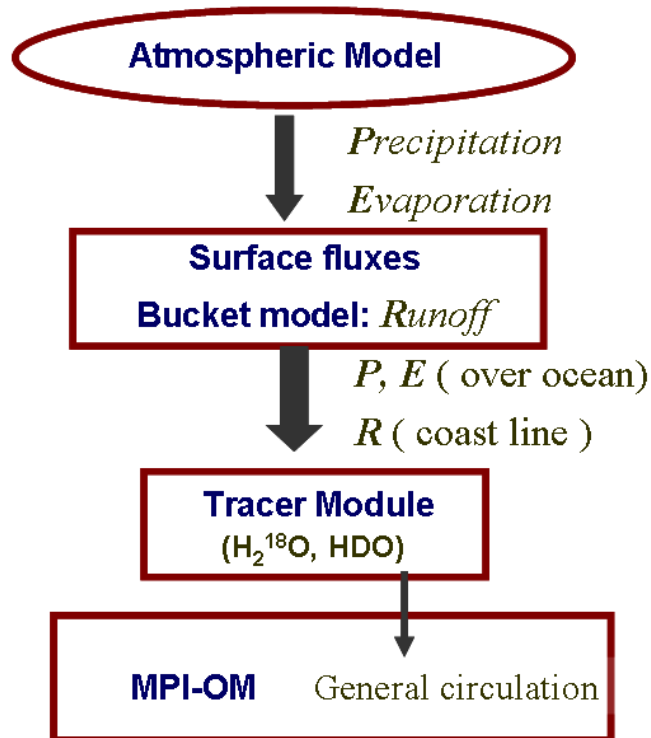


Figure 3.6 Schematic representations of the isotope tracers in model simulation.

In this study, the daily isotopic content of P and E fluxes over ocean surface stem from the atmospheric GCM ECHAM5-wiso. ECHAM5-wiso is a derivative of the ECHAM5 AGCM (Roeckner et al., 2003) enhanced by explicit water isotope diagnostics (Werner et al., 2011). This approach avoids the systematic uncertainties mentioned above.

Changes of oxygen isotopes occurring at phase transitions of water during the formation of sea ice are also included. Because sea ice formation is assumed to occur at isotopic equilibrium, the isotopic composition in sea ice is calculated by a liquid to

ice fractionation factor. For our experiments, this fractionation factor is set to 1.003, which is the average from various sources (Craig and Gordon, 1965; Majoube, 1971; Lehmann and Siegenthaler, 1991; Macdonald et al., 1995). There is no fractionation accompanied during sea ice melting due to very low rate of isotopic diffusion in sea ice.

The isotopic composition of river runoff is another boundary condition which influences the marine isotopic values, particularly in coastal regions. In this study, the amount and isotopic composition of continental runoff are calculated from a bucket model, which drains the continental freshwater fluxes simulated by ECHAM5-wiso following the topographic slope. The discharge of continental net precipitation ($P - E$) towards the ocean depends on the slope of the underlying topography, and the calculated total river runoff is based on the assumption that the global water cycle is balanced, i.e. all net precipitation over land surfaces is transported to the ocean. In our procedure, lakes are not present and the hydrological cycle is closed. This may introduce small distortions in magnitude and location of the simulated river runoff when compared with observations.

Chapter 4

Water isotope variations at present day

Here, we report first results with a new isotope-enhanced version of the ocean general circulation model MPI-OM (Marsland et al., 2003). This experiment focuses on a simulation of the present-day global oceanic distribution of $\delta^{18}\text{O}$ and δD as well as the deuterium excess d . The model results are analyzed for different ocean basins to understand the processes that lead to the simulated isotopic distribution of both oxygen-18 and deuterium at the ocean surface. A comparison of the simulation results with available observations examines the model performance in capturing the main characteristics of the present-day oceanic water isotopic distribution as well as the relationship of salinity versus $\delta^{18}\text{O}$ and δD in different ocean basins.

4.1 Experiment setup

For this experiment, the MPI-OM grid configuration GR30 with a formal horizontal resolution of $3^\circ \times 1.8^\circ$, 40 unequal vertical layers, and a time step length of 8640 seconds is chosen. The ETOPO-5 data set (Data Announcement 88-MGG-02, Digital relief of the Surface of the Earth. NOAA, National Geophysical Data Center, Boulder, Colorado, 1988) is used to create the grid-based topography and bathymetry. Initial conditions for marine temperature and salinity are interpolated from climatological fields given by Steele et al. (2001). Sea surface salinity is restored with a time scale of 39 days.

The atmospheric forcing is derived from output of an atmospheric general circulation model (AGCM) present-day control simulation in a T31 spectral resolution (about $3.75^\circ \times 3.75^\circ$) with 19 vertical levels (ECHAM5-wiso; Werner et al., 2011). Mean daily values of heat, freshwater and momentum fluxes at the air-sea interface are obtained from a 10 years simulation period. All forcing fields from the ECHAM5-wiso simulation are bilinearly interpolated to the MPI-OM grid.

The daily isotopic content of P and E fluxes over ocean surface stems from the same

ECHAM5-wiso simulation as used for obtaining the default freshwater, heat and momentum fluxing forcing.

For the initial distribution of H_2^{18}O and HDO in the ocean, a homogenous setup has been chosen with all values set to present-day $\delta^{18}\text{O}$ and δD values of 0‰ with reference to the Vienna Standard Mean Ocean Water (Baertsch, 1976; Dewit et al., 1980). No surface restoring of water isotopes is applied.

4.2 Isotopic boundary conditions

For isotope simulation, precipitated and evaporated water isotopes at air-sea interface are considered as the only fluxes of isotopes over ocean basin. These exhibit patterns are strikingly similar patterns to the distribution seen in normal precipitation and evaporation.

The daily precipitation of normal water (H_2O) and water isotopes (H_2^{18}O and HDO) are averaged over 10 years. As shown in Figure 4.1, strong precipitations are located at the equatorial Pacific Ocean, the South Pacific Convergence Zone, and the equatorial Indian Ocean. In contrast, the eastern parts of the subtropical basins in both hemispheres exhibit weak precipitation. Among these three types of precipitation, only the normal precipitation is applied in oceanic fresh water flux forcing. Because of the relatively little abundance in nature, the precipitation of H_2^{18}O ($\sim 10^{-3}$) and HDO ($\sim 10^{-4}$) are much less as compared to the normal water. Therefore, the absence of isotopic precipitation in hydrological cycle almost has no influence on the oceanic fields and ocean circulation.

As with precipitation, the evaporation is also divided into three parts: normal evaporation (H_2O), and isotopic evaporations (H_2^{18}O and HDO). Strong evaporation appears in the subtropics and western boundary system in both hemispheres, especially over the Gulf Stream and Kuroshio system (Figure 4.2). On the other hand, evaporation rate is low over the cold tongues in both the eastern equatorial Pacific Ocean and Atlantic Ocean. At high latitudes, evaporation rate is quite low due to the cold sea surface temperature. This indicates that the main factor affecting the surface isotopic composition at high latitudes is the isotope content in precipitation.

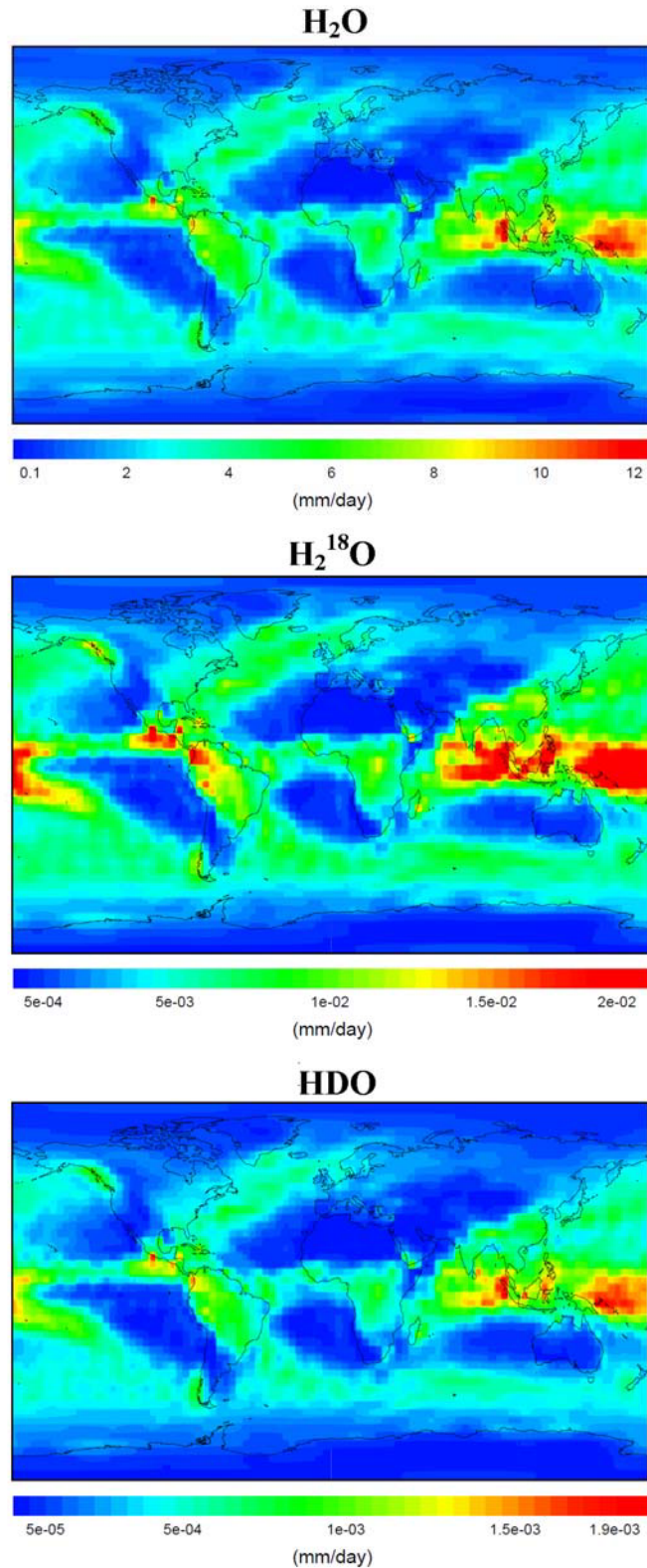


Figure 4.1 The global annual-mean precipitation rates of H_2O , $H_2^{18}O$ and HDO obtained from ECHAM-wiso (Werner et al., 2011) present-day simulation, which is used as air-sea fresh water (H_2O) and water isotope ($H_2^{18}O$ and HDO) influxes in the isotope enhanced MPI-OM.

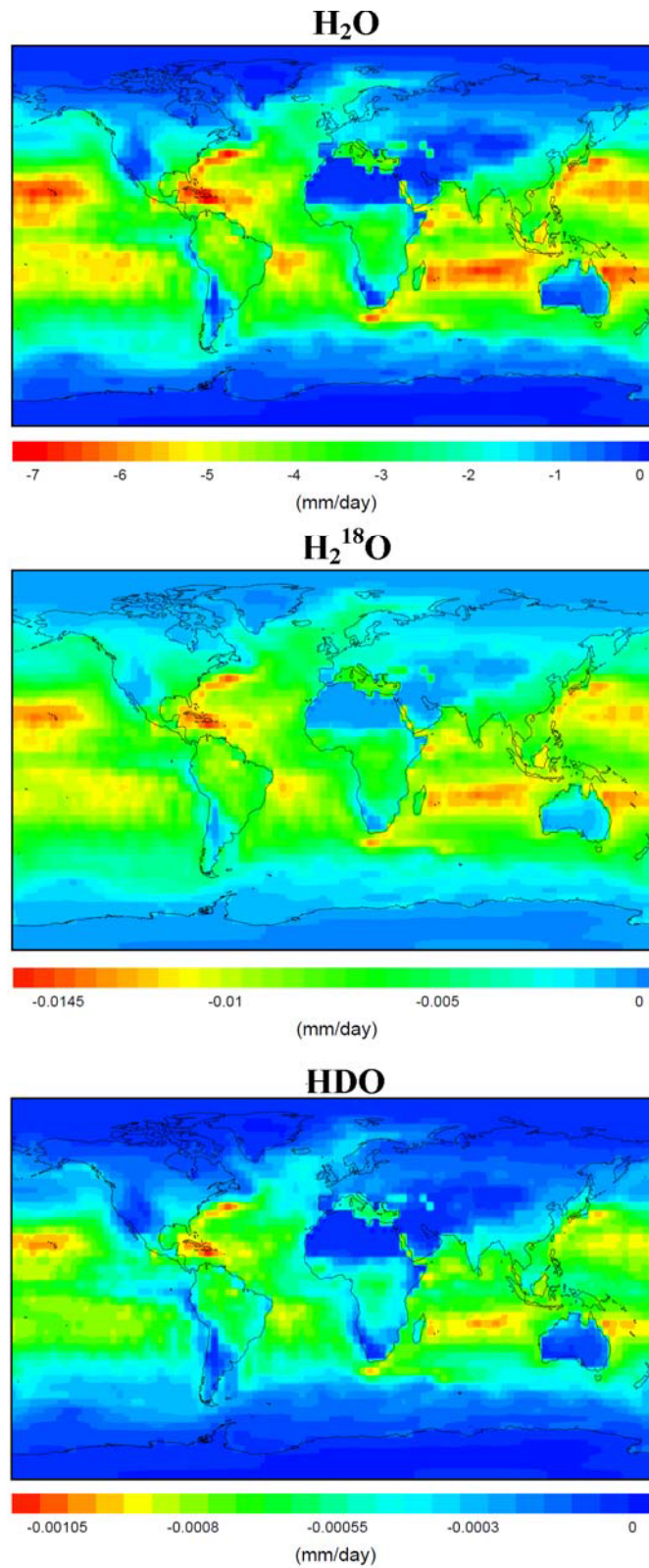


Figure 4.2 The global annual-mean evaporation rates of H_2O , $H_2^{18}O$ and HDO obtained from ECHAM-wiso (Werner et al., 2011) present-day simulation, which is used as out going fresh water (H_2O) and water isotope ($H_2^{18}O$ and HDO) at air-sea interface in the isotope enhanced MPI-OM.

The isotopic composition of precipitation is presented in Figure 4.3. Both $\delta^{18}\text{O}$ and δD values decrease with latitudes. The most depleted precipitation is found at Antarctic continent and Greenland. In general, the isotopic composition of precipitation over land is more depleted in comparison to the precipitation over ocean at the same latitude due to the rainout effect.

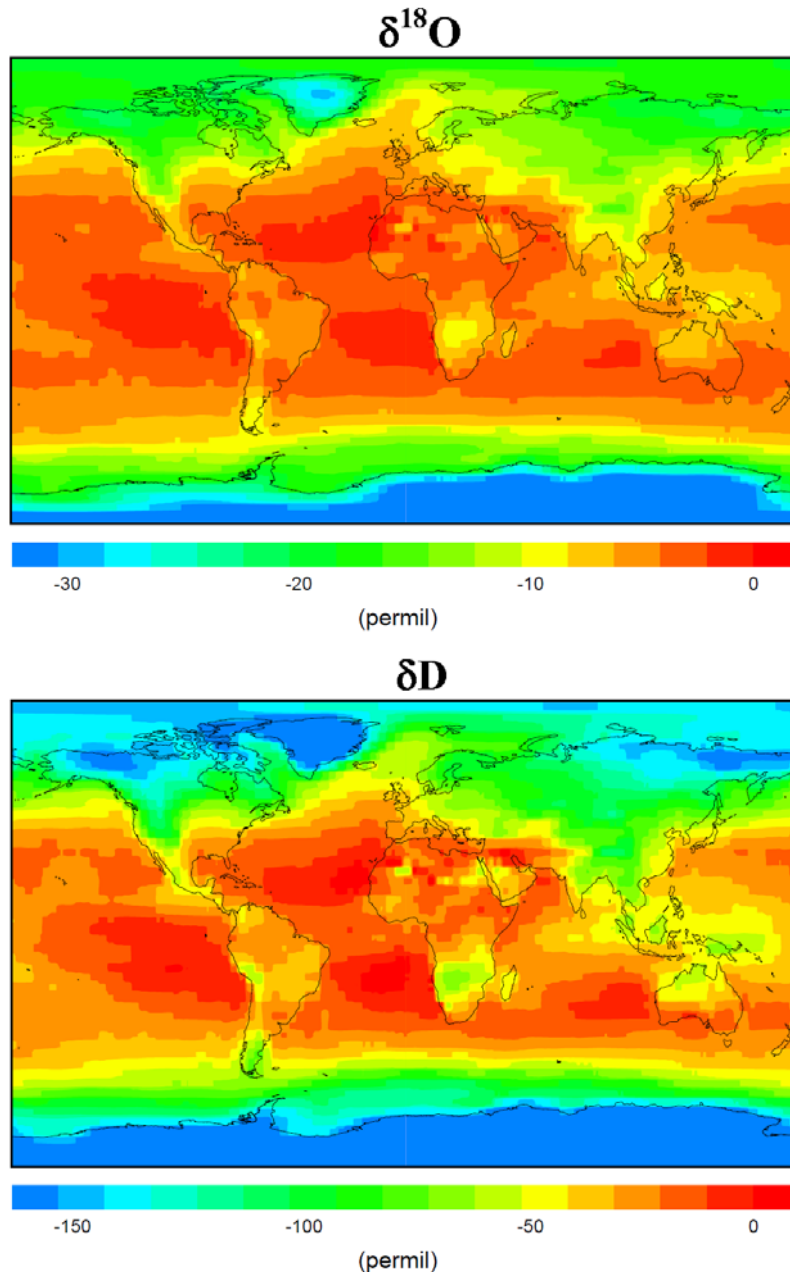


Figure 4.3 Present day annual mean oxygen-18 ($\delta^{18}\text{O}$) and deuterium (δD) composition of precipitation obtained from the ECHAM-wiso (Werner et al., 2011)

The range of $\delta^{18}\text{O}$ is about -50‰ to 0‰, while the values of δD are in the range of

-400‰ to 0‰. δD and $\delta^{18}O$ values of precipitation are highly correlated. Most of them are in agreement with the global meteoric water line, but slightly deviate from GMWL in less depleted regions.

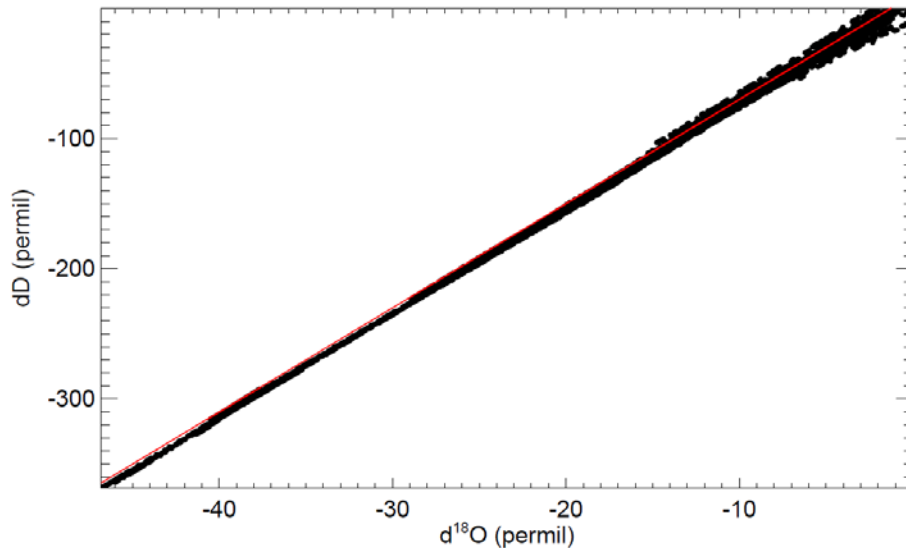


Figure 4.4 The $\delta^{18}O$ - δD relation of global precipitation at present day calculated from the $\delta^{18}O$ and δD values in the precipitation simulated by ECHAM-wiso (Werner et al., 2011). The red line is the global meteoric water line (GMWL), as defined by Craig (1961).

4.3 Observational database of $\delta^{18}O$ and δD

The Global Seawater Oxygen-18 Database (Schmidt et al., 1999b) contains a collection of over 26,000 observations since about 1950, which offers a unique opportunity to compare the observed and modeled oceanic $\delta^{18}O$ values. For the comparison with our model results, all data entries of the top 10 meters-layer are taken as representative of ocean surface water $\delta^{18}O$ values. All measurements between 100 meters depth and bottom used for model-data intercomparison at subsurface and deep ocean.

Although δD observations of ocean waters are not as widespread as $\delta^{18}O$, there are some measurements available to validate our simulations. For this study, we consider global δD measurements from the GEOSECS expeditions (Östlund et al., 1987) which are complemented with observations from the Northwest Pacific (Horibe and Ogura,

1968), the tropical West Pacific (Aharon and Chappell, 1986), the Indian Ocean (Duplessy, 1970; Delaygue et al., 2001), the Arctic Ocean (Friedman et al., 1961), the Baltic Sea (Ehhalt, 1969; Fröhlich et al., 1988), the Mediterranean (Gat et al., 1996), the Gulf of Mexico (Yobbi, 1992), and the Weddell Sea (Weiss et al., 1979). In the same way as applied for $\delta^{18}\text{O}$, the δD measurements above 10m and below 100m depth haven been chosen. The chosen surface data have been averaged over the upper 10m.

4.4 Results

The MPI-OM present-day climate control simulation has been run for 3000 years into a quasi-steady state. For the analyses we only used the mean state of the last 100 simulation years.

4.4.1 Simulated salinity and temperature distribution

First, we present the salinity and temperature fields from our simulation. Sea surface temperature decreases poleward, with the highest temperature at equatorial band (Figure 4.5). In subtropical basins, temperature is generally higher at western boundaries in contrast to the eastern. There is a cold front in the southern oceans, especially in the 40-50° latitudinal bands.

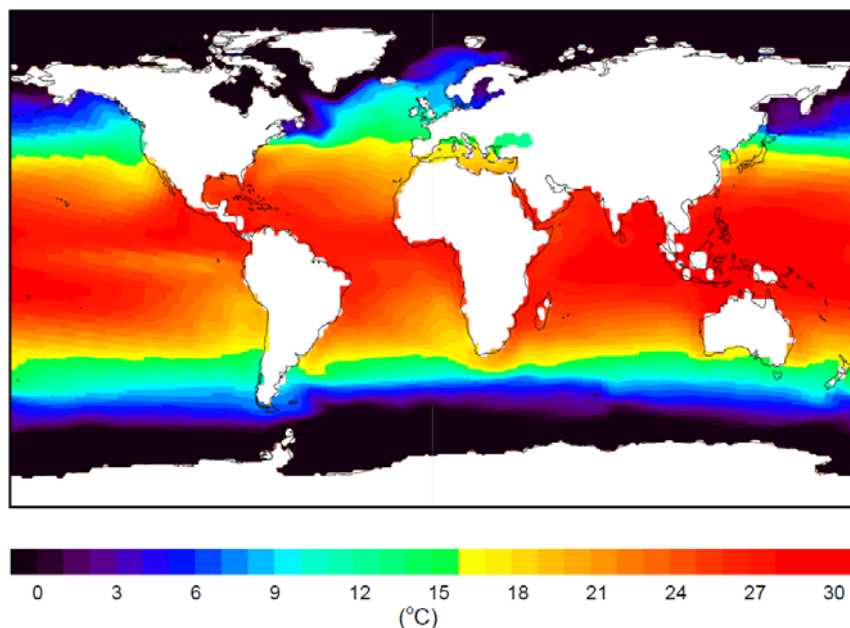


Figure 4.5 Annual mean sea surface temperature distributions from model simulation. The meridional cross-section of temperature distribution along the Atlantic basin presents bowl-shaped isothermals in the upper ocean (Figure 4.6). A cold front extends from the sea surface to the deep ocean is in the Southern Ocean.

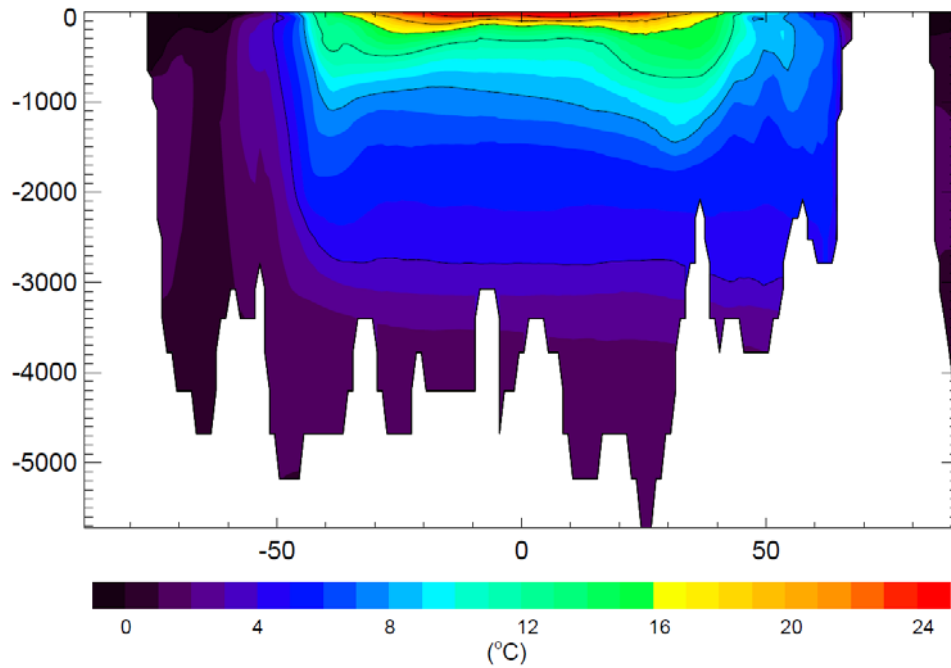


Figure 4.6 Annual mean vertical distribution of simulated temperature through the Atlantic basin.

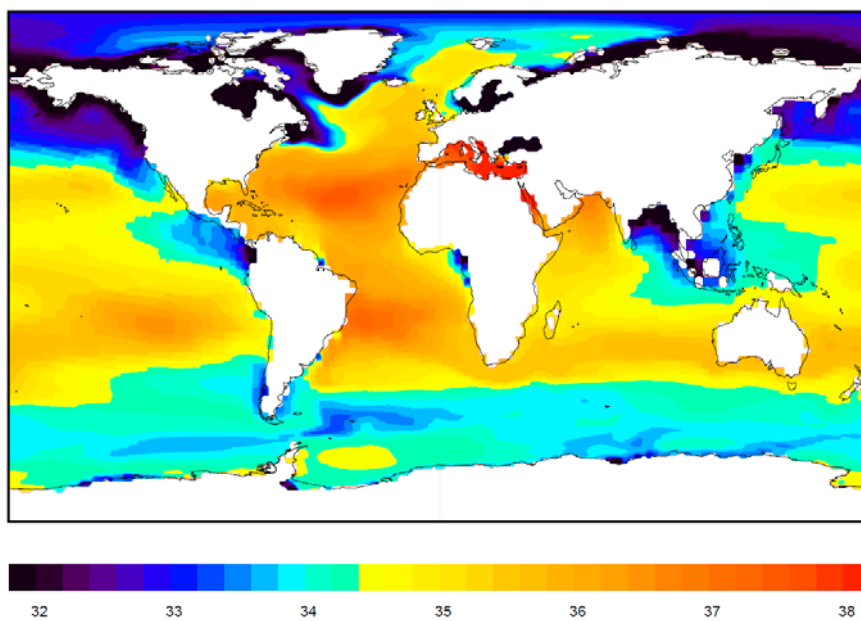


Figure 4.7 Annual mean sea surface salinity distributions from model simulation.

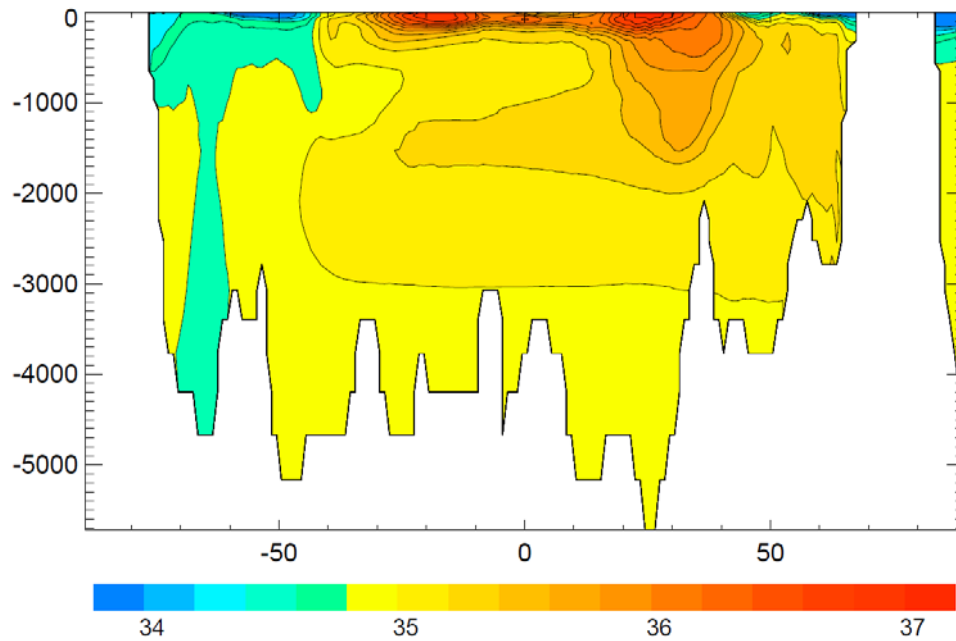


Figure 4.8 Annual mean vertical distribution of simulated salinity through the Atlantic basin.

The surface distribution and Atlantic meridional distribution of salinity are illustrated in Figure 4.7 and Figure 4.8, respectively. Sea surface salinity is high in the centers of the subtropical basins, especially in the Atlantic Ocean. In the North Atlantic Ocean, there is a high salinity branch, starting from the upper ocean and penetrating to 2km depth. This tongue-like feature extends southward and crosses equator. A similar feature, which is comparably fresh, originates from the surface at 50°S and extends to the depth of 1km.

Hereafter, we compare simulated salinity and temperature fields to the climatological fields of salinity and temperature data from World Ocean Atlas 2009 (WOA09) to ensure that the MPI-OM simulation represents a realistic present-day mean oceanic state (Figure 4.9, Figure 4.10). In general, the model reproduces the salinity and temperature fields which are known from available observations. The surface salinity and temperature pattern of most basins agrees well with the observations, with differences less than 1 psu and 2 degrees, respectively, in salinity and temperature. The simulated surface salinity of the Arctic Ocean is higher than the observational data, which may be due to the brine rejection from simulated sea ice concentrations.

Because the coarse resolution of model grid is unable to simulate the runoff effects at coastal regions, the Arctic estuarine areas are more saline in comparison with observation. The comparison of MPI-OM versus WOA09 mean vertical distribution pattern through the Atlantic basin indicates a 0.5 to 1 psu more saline and much warmer (3 to 7 degrees) simulated Antarctic Intermediate Water.

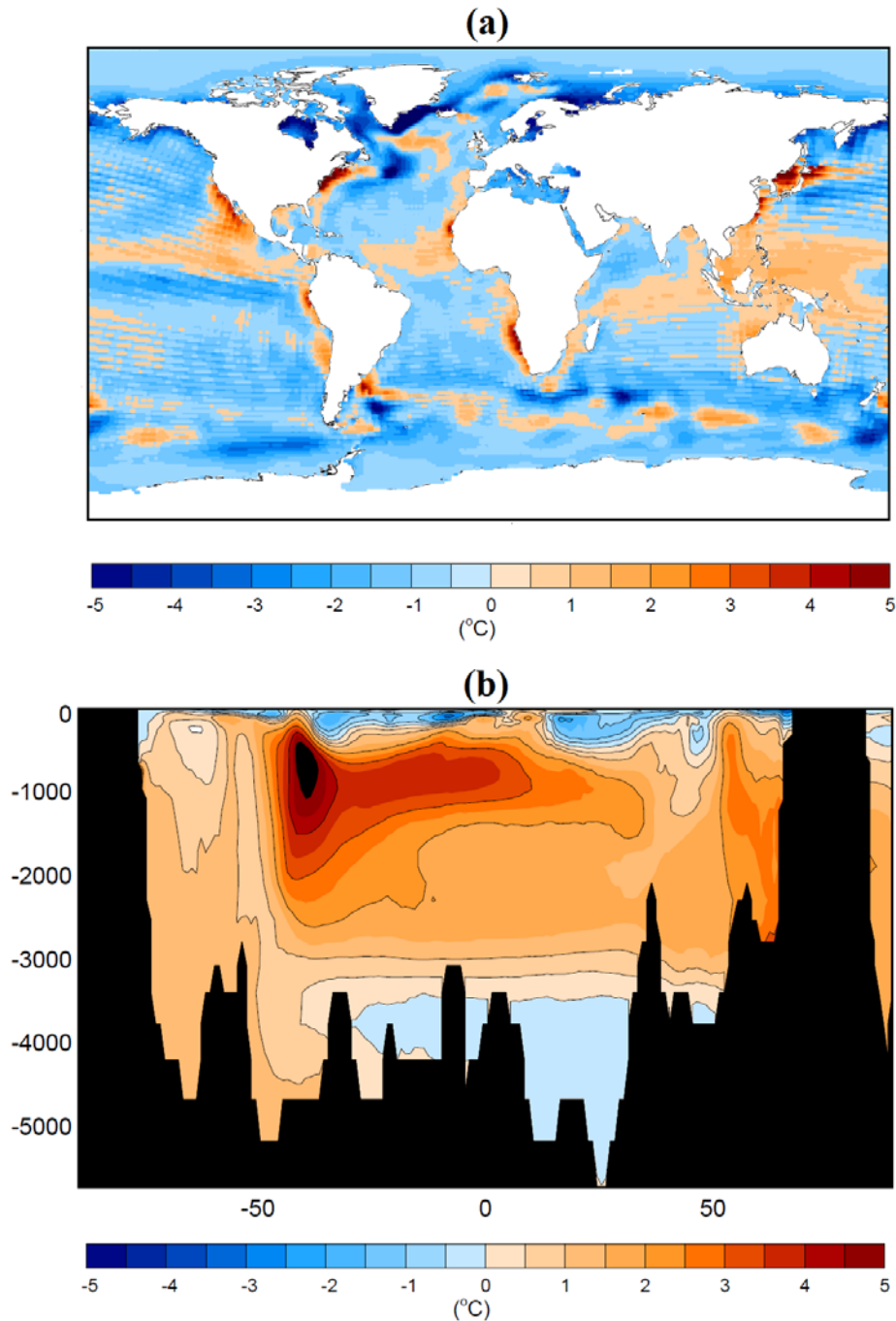


Figure 4.9 Differences between modeled temperature and WOA09 temperature fields at the ocean surface (a) and along the Atlantic basin (b).

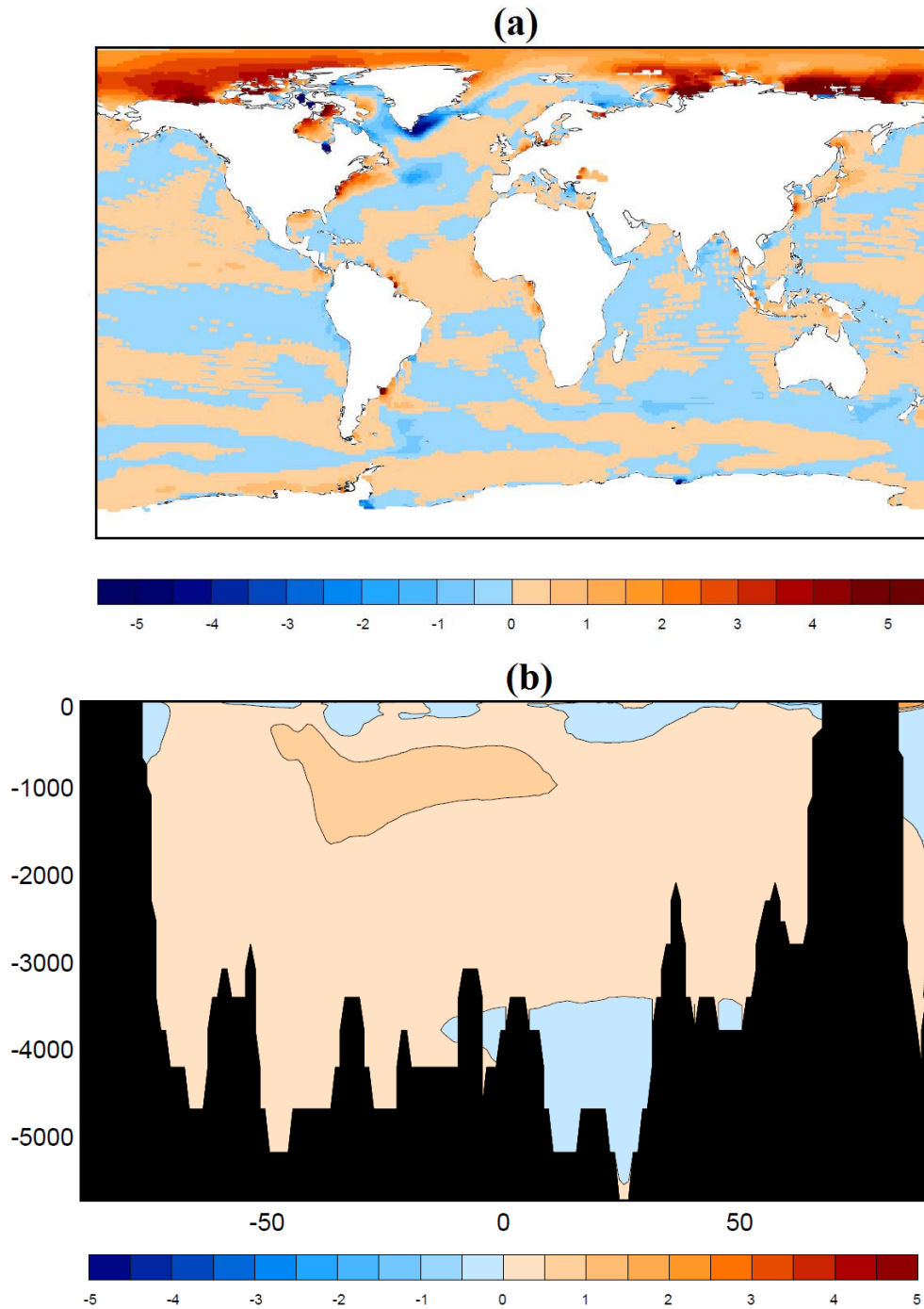


Figure 4.10 Differences between modeled salinity and WOA09 salinity fields at the ocean surface (a) and along the Atlantic basin (b).

4.4.2 Simulated distribution of water isotopes (H_2^{18}O and HDO)

For a first assessment of our simulation results, we evaluate the global zonal-mean isotopic composition of δD and $\delta^{18}\text{O}$ in ocean surface water (Figure 4.11).

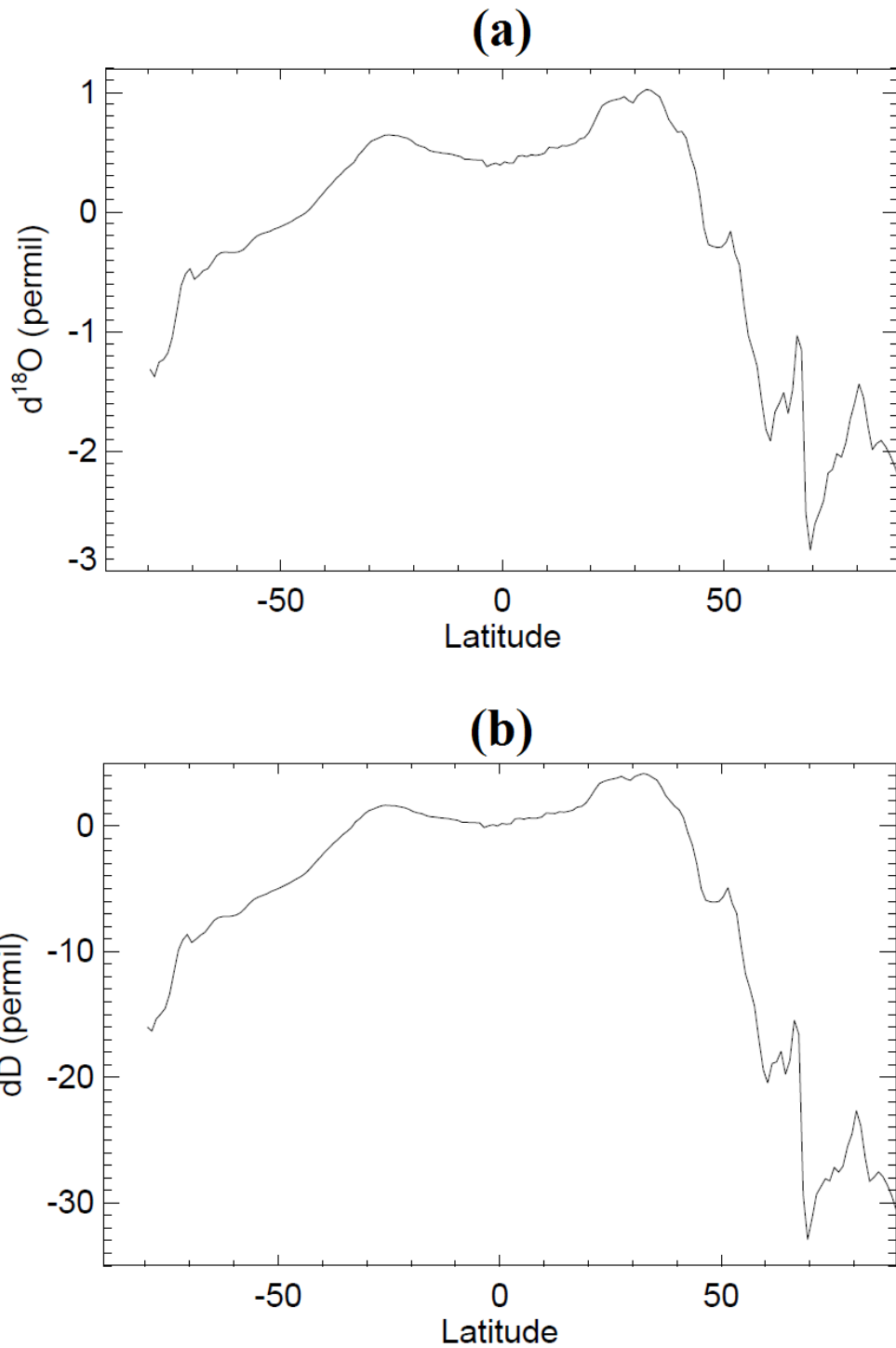


Figure 4.11 (a) The global zonal-mean HDO isotopic composition of sea surface water (δD) from a MPI-OM present-day climate control simulation. (b) The same as (a), but for H_2^{18}O ($\delta^{18}\text{O}$).

Due to the larger mass difference of the two stable isotopes relative to the mass of the element, zonal deuterium exhibits much larger absolute variations (-15‰ to +5‰) in

the isotopic composition of surface waters as compared to $\delta^{18}\text{O}$ (-3‰ to +1‰). However, as the same boundary fluxes (precipitation, evaporation, and river runoff) determine both H_2^{18}O and HDO in ocean surface waters, strikingly similar features of the zonal mean isotopic composition can be seen in most regions. Both $\delta^{18}\text{O}$ and δD decrease from mid to high latitudes as a result of the latitudinal temperature decrease and the rainout effect, similar to the trends observed in meteoric water samples (e.g. Craig and Gordon, 1965; Criss, 1999). There is a slight increase of the water isotopes concentration from equatorial regions to the subtropics, which can be related to a relative excess in evaporation over subtropical oceans. The most enriched areas are located around 30°N, where the zonal mean δD and $\delta^{18}\text{O}$ values reach almost +5‰ and +1‰, respectively. The most depleted regions are found north of 65°N, with δD values less than -20‰ and $\delta^{18}\text{O}$ values less than -1.5‰. The isotopic values in the northern hemisphere exhibit a much stronger heterogeneity as compared to the Southern Hemisphere.

For further analyses, the simulated global $\delta^{18}\text{O}$ and δD distributions at the sea surface as well as the observations are shown in Figure 4.12 and Figure 4.13, respectively. The Atlantic Ocean between 30°S and 40°N has much enriched isotopic values, especially in the Northern Hemisphere ($\delta^{18}\text{O} > 1\text{‰}$, $\delta\text{D} > 5\text{‰}$), as compared to the Pacific Ocean. The North Atlantic Current transports these enriched water to the Nordic Seas. Extremely depleted values are seen in marginal seas at high latitudes such as the Baltic Sea (-6‰ to -10‰ for $\delta^{18}\text{O}$, and -50‰ to -80‰ for δD) and estuaries of Arctic rivers (-6‰ to -14‰ for $\delta^{18}\text{O}$, and -67‰ to -118‰ for δD). The most enriched values of $\delta^{18}\text{O}$ and δD are found in the eastern Mediterranean Sea (approx. 2.8‰ and 15‰, respectively), where evaporation is the dominating influence on the isotopic composition of seawater.

The spatial structures of $\delta^{18}\text{O}$ and δD simulated by MPI-OM are similar to the available observations (Figure 4.12b, 4.13b). Both model results and observational data show strongly depleted areas ($\delta^{18}\text{O} < -5\text{‰}$, $\delta\text{D} < -20\text{‰}$) in coastal regions with continental river discharge. For a more quantitative model-data comparison, we average all observations within a specific grid cell and compare the mean value with

corresponding MPI-OM result (Figure 4.14). Analyses of the correspondence between simulated and observed fields indicate a good agreement between the two fields. The correlation coefficients (R) are 0.75 and 0.96 for $\delta^{18}\text{O}$ and δD (significant on a 95% interval), and the normalized root mean square errors (NRMSE) are 8.3% and 9.4% respectively.

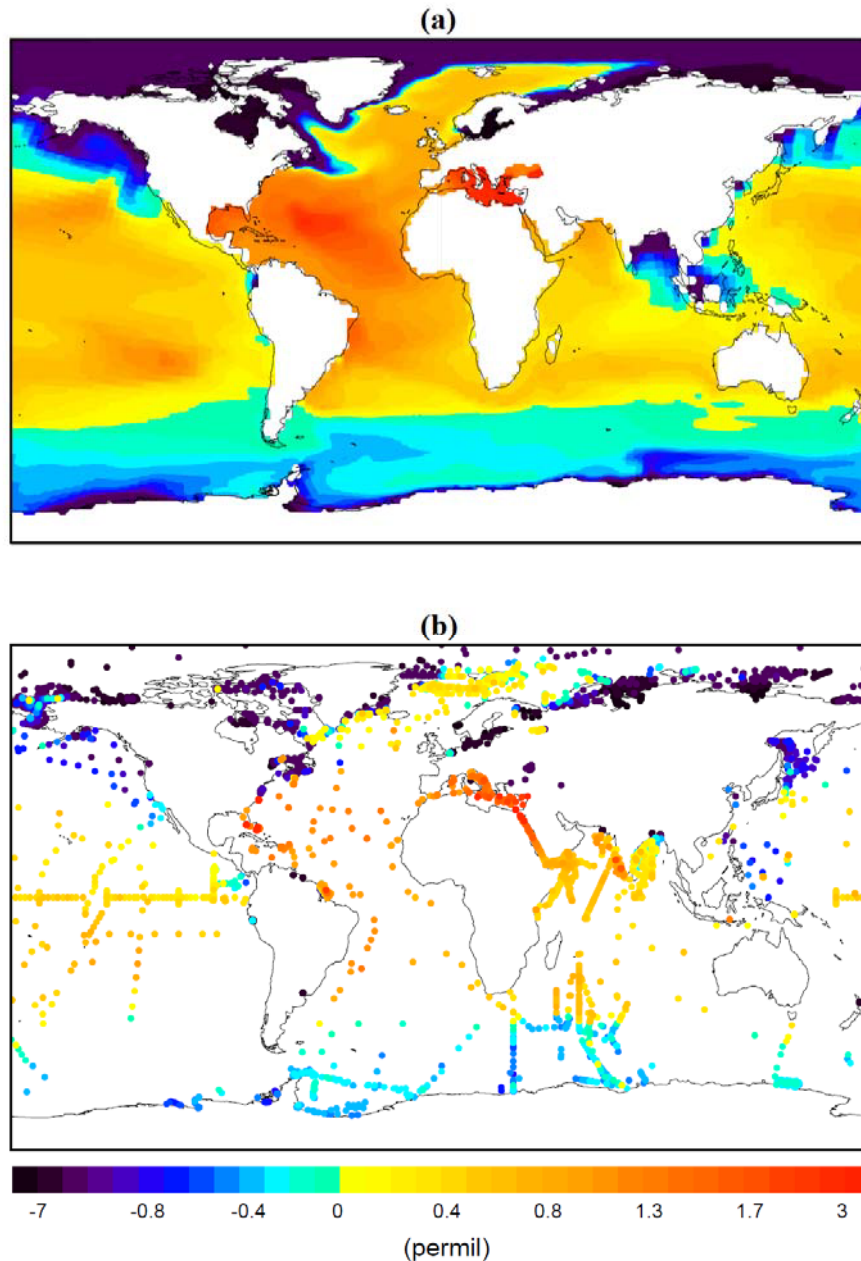


Figure 4.12 (a) The annual mean $\delta^{18}\text{O}$ distribution in ocean surface waters simulated by MPI-OM. (b) The sea surface $\delta^{18}\text{O}$ measurements included in the Global Seawater Oxygen-18 Database (Schmidt et al., 1999b).

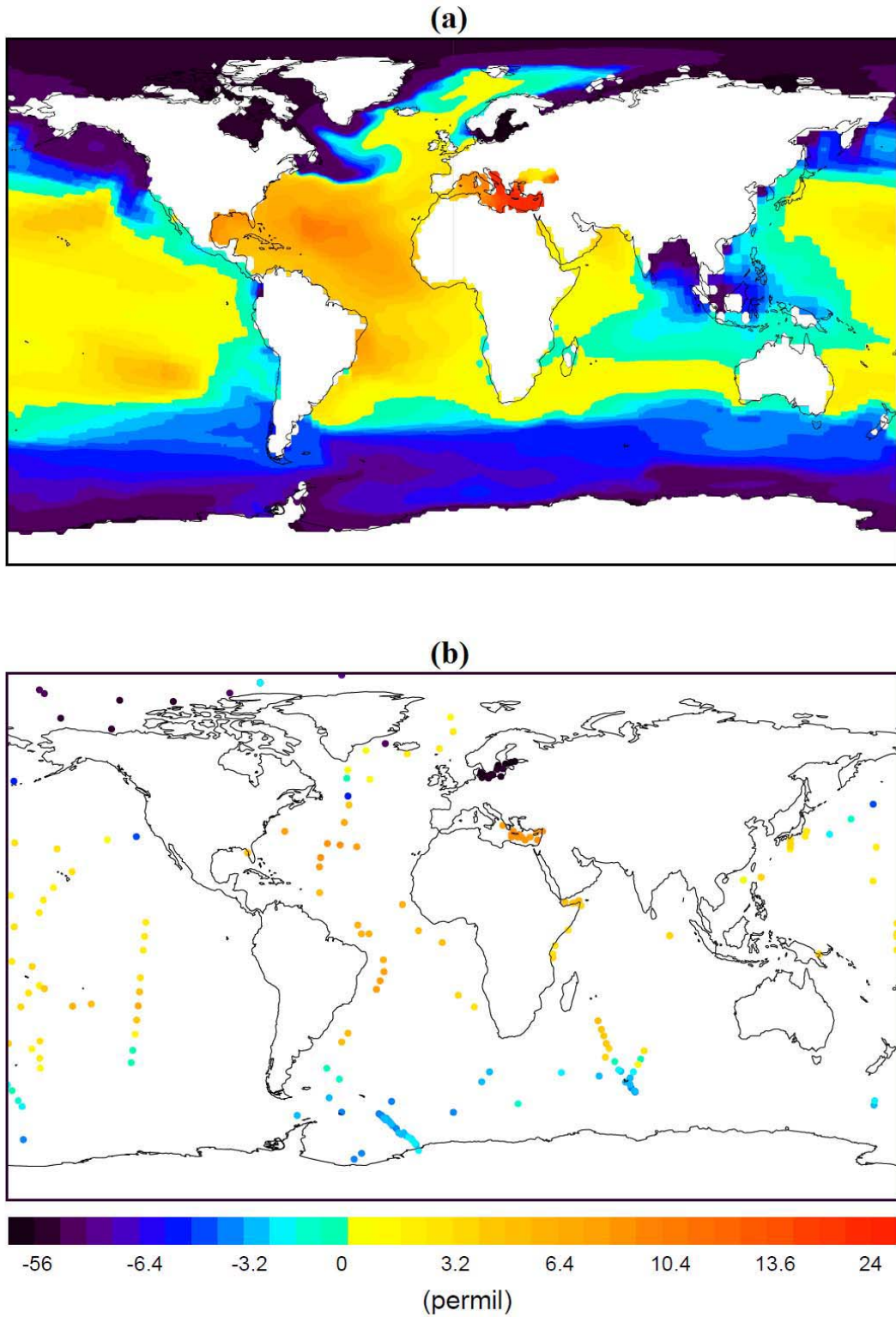


Figure 4.13 (a) The annual mean δD distribution in ocean surface waters as simulated by MPI-OM. (b) Available δD measurements from sea surface water samples (see text for details).

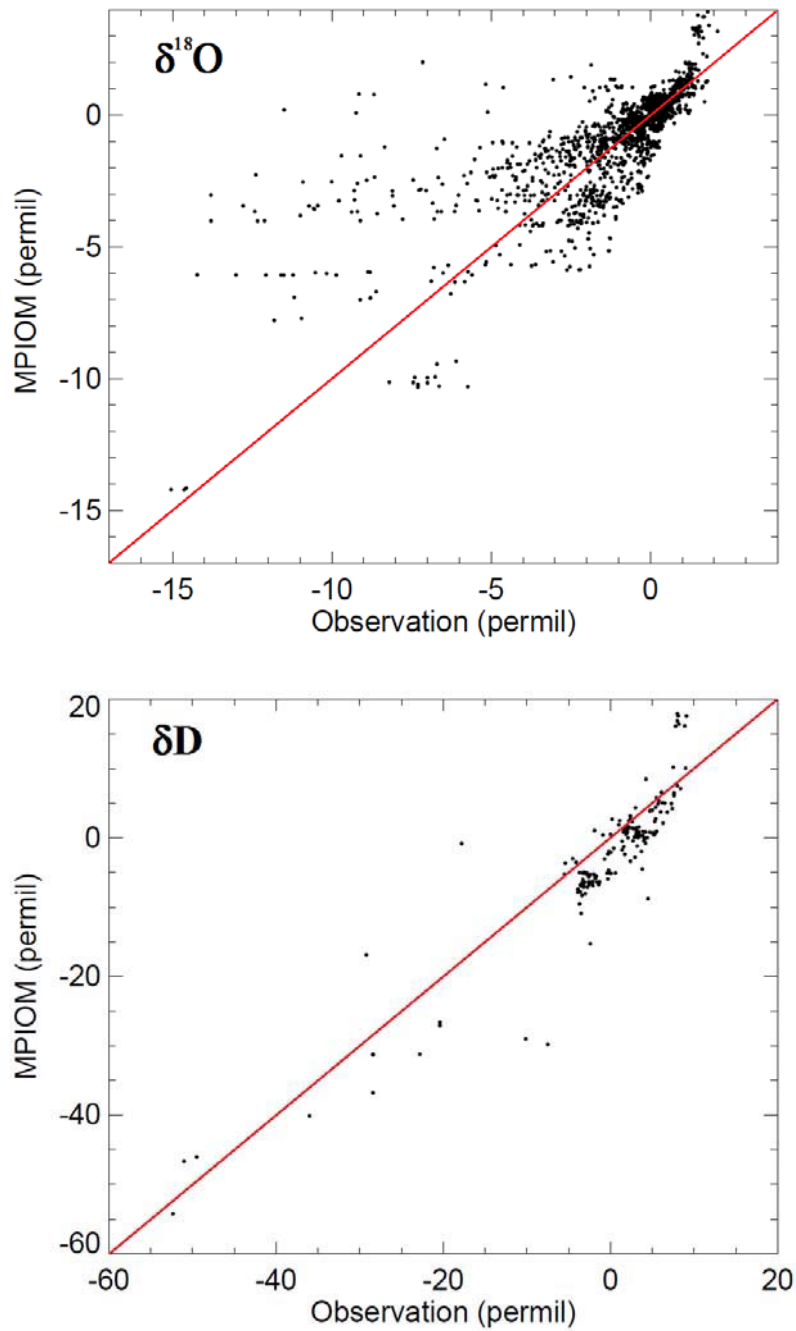


Figure 4.14 Comparison of observed water isotopic values (averaged onto the MPIOM model grid) versus modeled surface isotopic values. The 1:1 line is colored in red.

Meridional sections of $\delta^{18}\text{O}$ and δD in Atlantic subsurface and deep waters are shown in Figure 4.15. The distributions are distinctly different from the surface and more homogeneous. We find enriched values in North Atlantic and relatively depleted values in the Southern Ocean. The $\delta^{18}\text{O}$ distribution is consistent with the formation

and transport of Atlantic water masses. The North Atlantic Deep Water layer is isotopically enriched compared to the layers associated with Antarctic Intermediate Water and Antarctic Bottom Water. The meridional δD distribution along Atlantic basin exhibits features similar to $\delta^{18}O$, but larger variation. Its distribution should be very similar to $\delta^{18}O$ after an appropriate scaling.

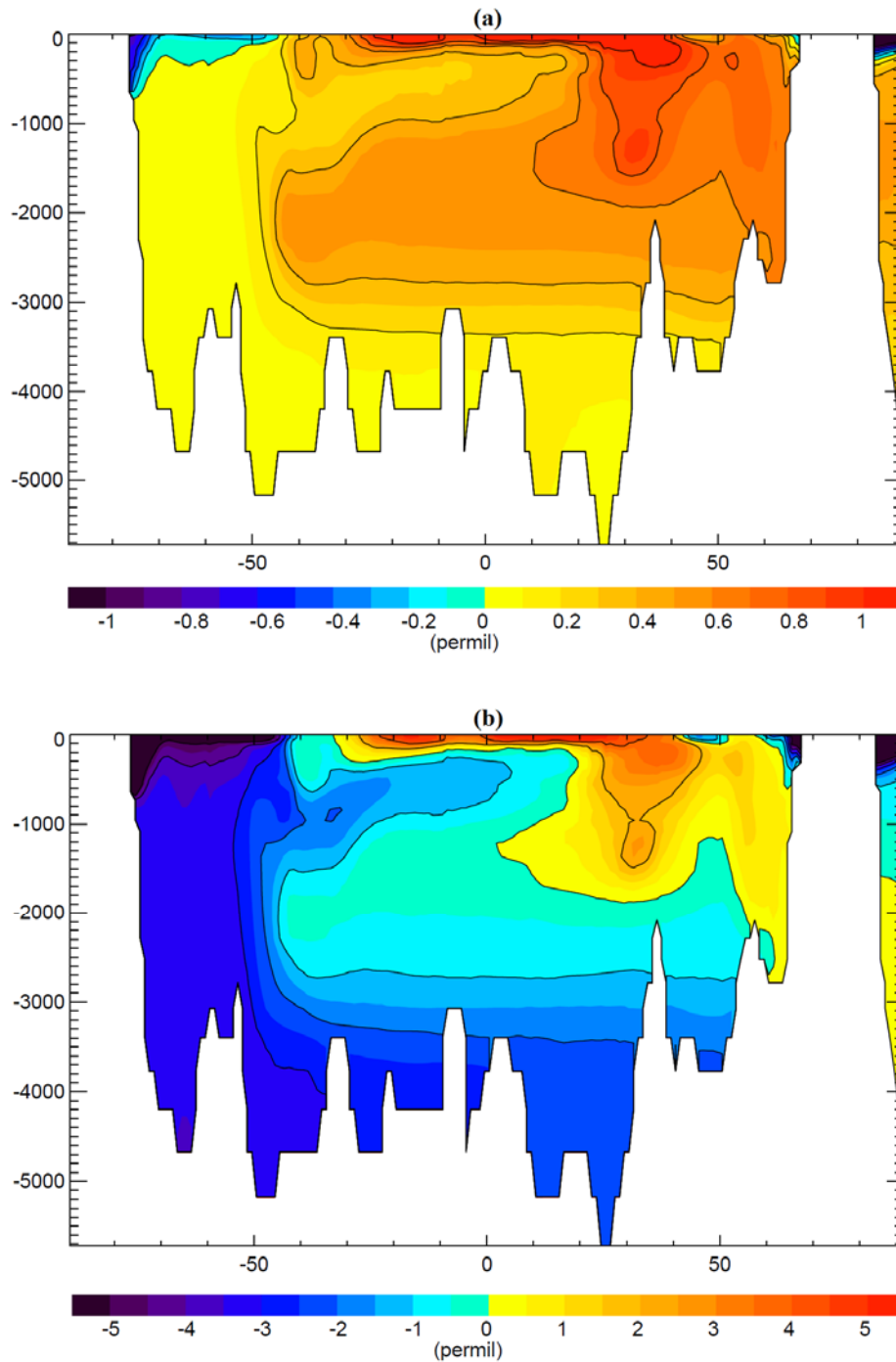


Figure 4.15 MPI-OM simulation results (a) The annual zonal mean $\delta^{18}O$ of the Atlantic basin. (b) The annual zonal mean δD of the Atlantic basin.

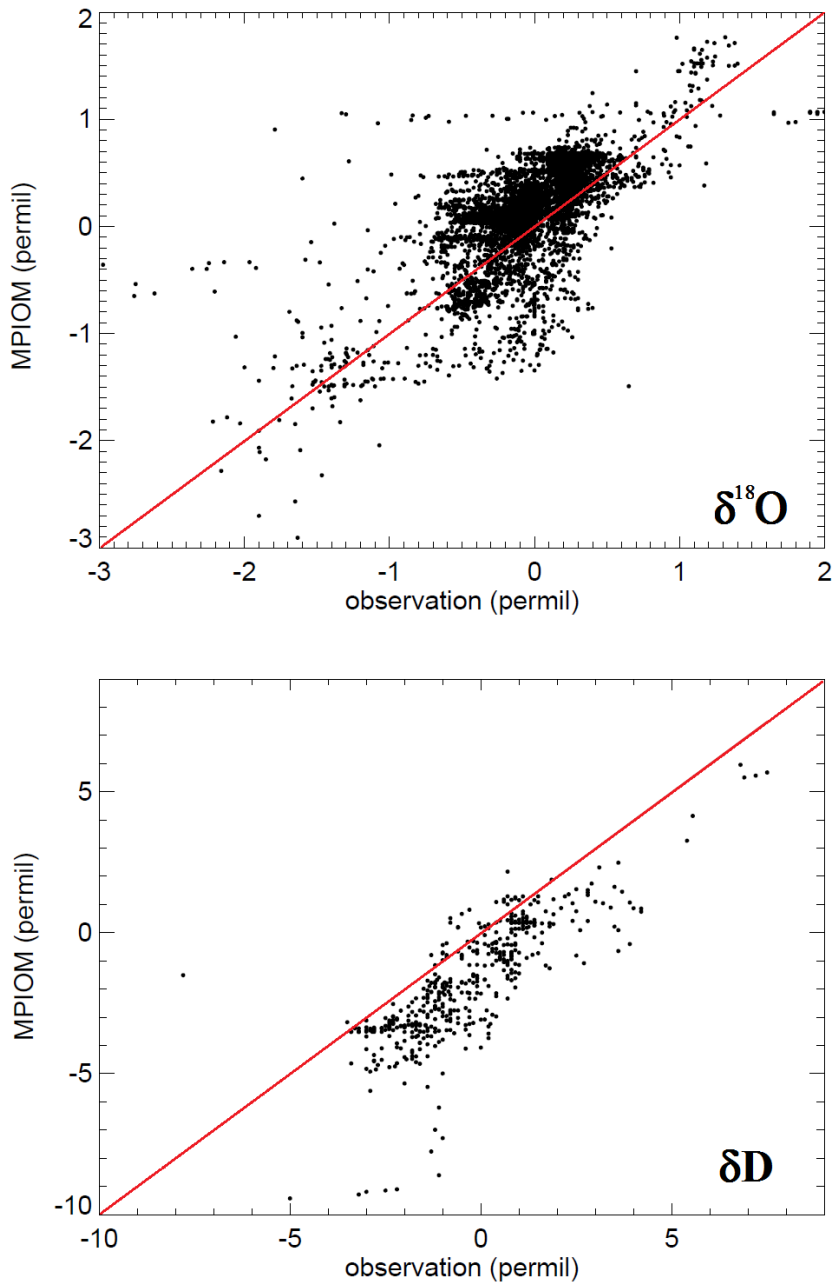


Figure 4.16 Comparison of observed water isotopic values (averaged onto the MPIOM model grid) versus modeled isotopic values below 100m depth. The 1:1 line is colored in red.

Performing the same average of observational values within different model grid cells as for the surface data, we find that the model results below 100m also agree well with the observations. The Rs are 0.76 and 0.82 for $\delta^{18}\text{O}$ and δD , and the NRMSEs are 4.6% and 13.2% respectively (Figure 4.16).

4.4.3 Simulated δD - $\delta^{18}O$ relationship and d-excess variations

Based on precipitation measurements, a linear relation between δD and $\delta^{18}O$ in precipitation was first reported by Dansgaard (1964), with $\delta D = 8 * \delta^{18}O$. This relation can be explained by a simple Rayleigh-type model of isotopic fractionation occurring during evaporation and condensation processes. As illustrated in Figure 4.17a and Figure 4.17b, a similar linear relationship between δD and $\delta^{18}O$ at sea surface is found in most basins.

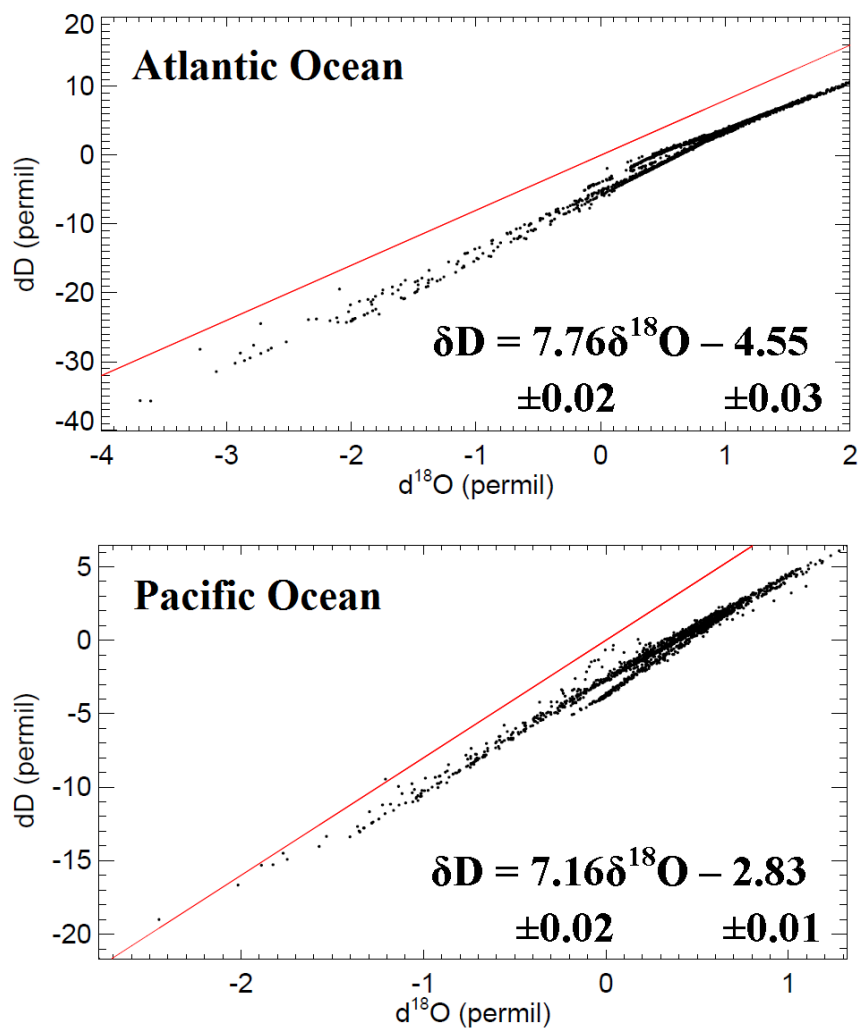


Figure 4.17a Relationship between deuterium and oxygen-18 of surface waters in the Atlantic and Pacific Ocean obtained by our model. The red line in each panel represents the linear approximation $\delta D = 8 * \delta^{18}O$.

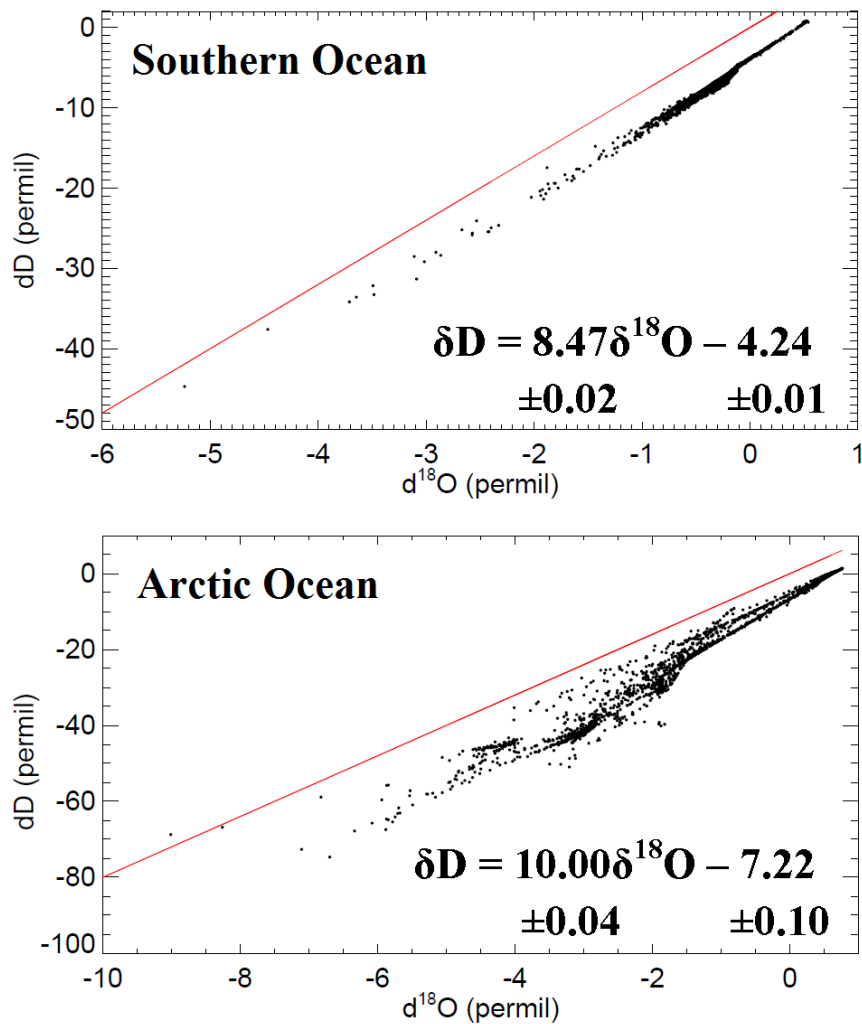


Figure 4.17b The same as Figure 4.17a, but for the Southern Ocean and the Arctic Ocean. The red line in each panel represents the linear approximation $\delta D = 8 * \delta^{18}O$.

The simulated deuterium and oxygen-18 composition in both basins are indeed highly correlated ($r > 0.98$), and the slopes of the linear fit between δD and $\delta^{18}O$ slightly deviate from the factor 8 at most basins (Atlantic Ocean: 7.76; Pacific Ocean: 7.16; Antarctic Ocean: 8.47). Largest deviations are found for the Arctic Ocean (10.00). Two separated tails in the δD - $\delta^{18}O$ relations in both Atlantic and Pacific Ocean can be detected. Compared to other basins, the δD - $\delta^{18}O$ relation shows larger variations in the Arctic Ocean. The tropical oceans show relatively flatter slopes (6.5 ~ 6.9) than the extra-tropical oceans (North Atlantic: 7.69; South Atlantic: 8.39; North Pacific: 7.53; South Pacific: 8.39). These differences in δD - $\delta^{18}O$ relations result in the separated tails at extra-tropical oceans.

Based on the simulated water isotopic compositions, the modeled ocean surface d-excess values are calculated. For oceanic regions, the d-excess in the surface waters may be affected by evaporation, precipitation, as well as mixing of different water masses. We compiled existent observational data, where both δD and $\delta^{18}O$ measurements exist at the same location, and calculated for these location the d-excess of ocean surface waters (Figure 4.18). The modeled δD - $\delta^{18}O$ relationship agrees with the observations, but a clear negative offset is detected for the simulated d-excess values. Both observations and simulation show similar ranges of d-excess variations with an increase in d-excess for water masses with stronger $\delta^{18}O$ -depletion.

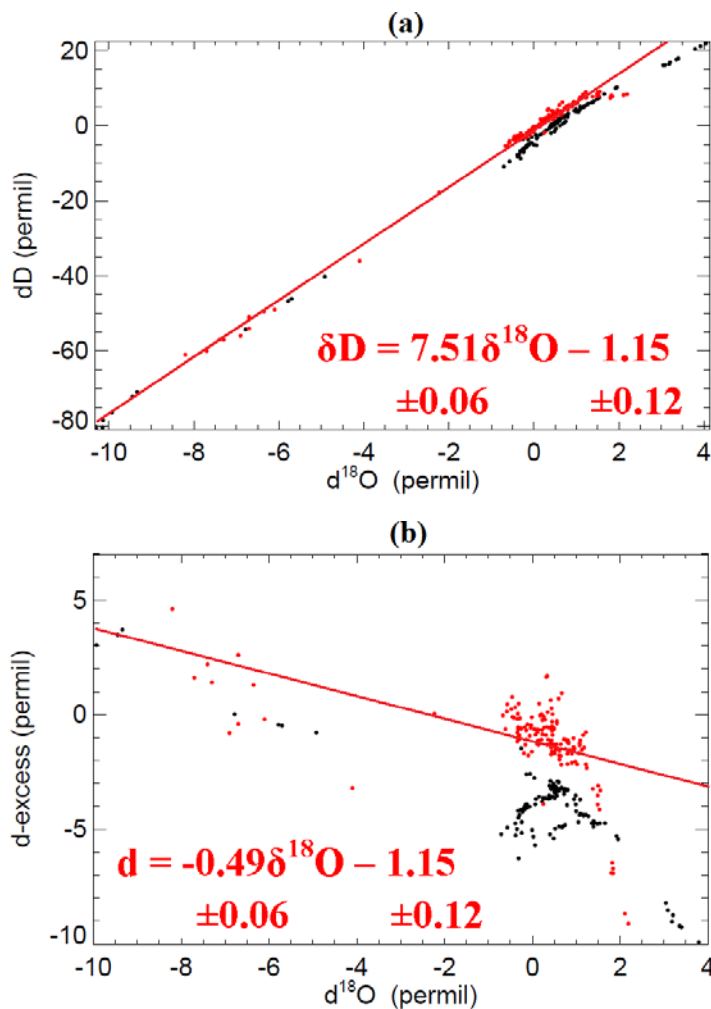


Figure 4.18 (a) Observed (red) and modeled (black) relationship between deuterium and oxygen-18 in sea surface waters. (b) Observed (red) and modeled (black) deuterium excess in sea surface waters. The regressions are calculated from measurements.

The simulated global zonal mean d-excess values of sea surface waters vary between -2‰ and -13‰, with rather small variations ($-4 \pm 1‰$) between 80°S and 55°N (Figure 4.19). These negative values are in general agreement with the enriched (positive) deuterium excess values of atmospheric water vapor simulated (and observed) in the marine boundary layer. A sharp decrease is detected at around 55°N, where the d-excess drops from approximately -3.5‰ to -13‰.

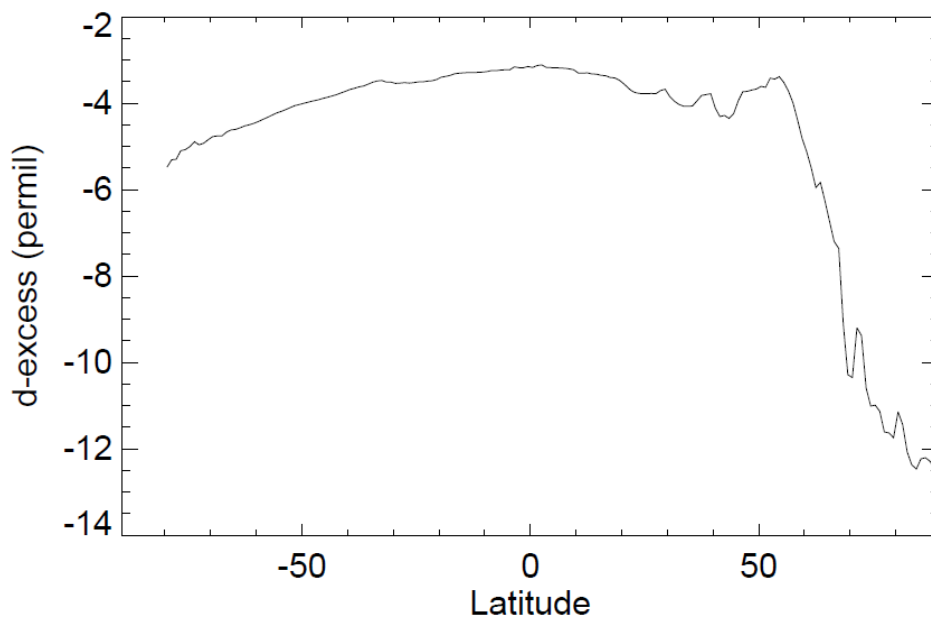


Figure 4.19 The global zonal mean d-excess of sea surface water from MPI-OM simulation.

In Figure 4.20, we illustrate the spatial variations of the d-excess values. There are few marginal seas (Baltic Sea, Bay of Bengal, James Bay) which exhibit a positive d-excess, most likely strongly influenced by river runoff. The variances of d-excess in major basins are small, but there are significant differences between the different ocean basins. The Pacific and Indian Oceans are relatively enriched in d-excess as compared to the Atlantic Ocean, and the most depleted regions are located in the Arctic Oceans. The water transported by the Labrador Current and the East Greenland Current contains much lower d-excess values than water of the Gulf Stream and the North Atlantic Drift. For the Arctic Ocean, the inflows from the North Atlantic and Pacific preserve their d-excess values from its original region. The Pacific water flow

through the Bering Strait has higher d-excess, and the North Atlantic current brings relatively lower d-excess values. In the Southern Hemisphere, the Antarctic Circumpolar Current traps the depleted water in the Southern Ocean.

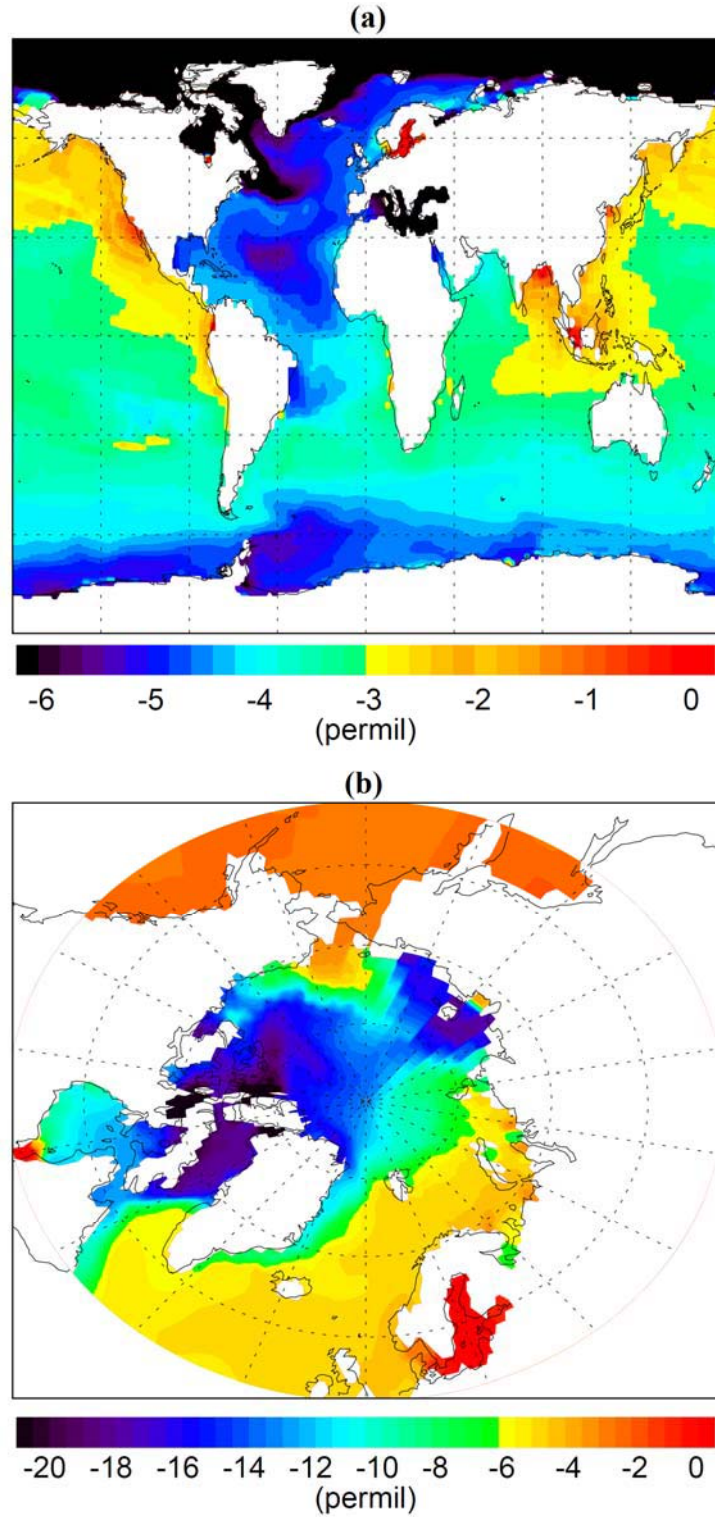


Figure 4.20 (a) Annual mean d-excess distribution at sea surface as simulated by MPI-OM. (b) The same as (a), but for the region north of 53°N.

4.4.4 Simulated relations between H₂¹⁸O, HDO and salinity

Because similar physical processes (precipitation, evaporation, and river runoff) affect the salinity and the isotopic composition of ocean waters, a positive relationship between salinity (*S*) and water isotopes can be expected, particularly for ocean surface waters.

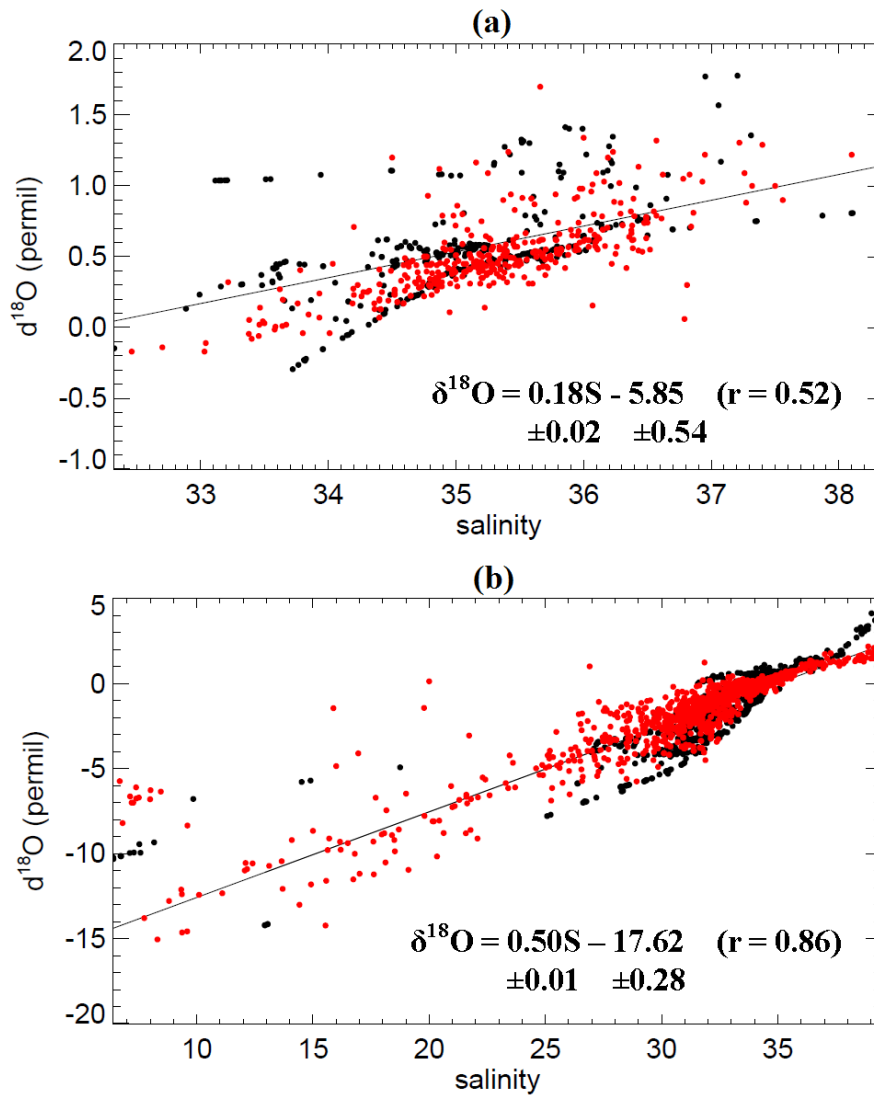


Figure 4.21 Relationship between δ¹⁸O and salinity *S* for simulated and observed surface waters. (a) tropical regions, (b) extra-tropical regions. In all panels, model results are plotted in black and observational data are plotted in red. The regressions are calculated from simulation results, the corresponding observational regressions are given in text. For the model-data comparison, only those model grid cells that contain observations are chosen. If several observed data values exist in a corresponding grid cell, the mean of all data values is used for the analyses.

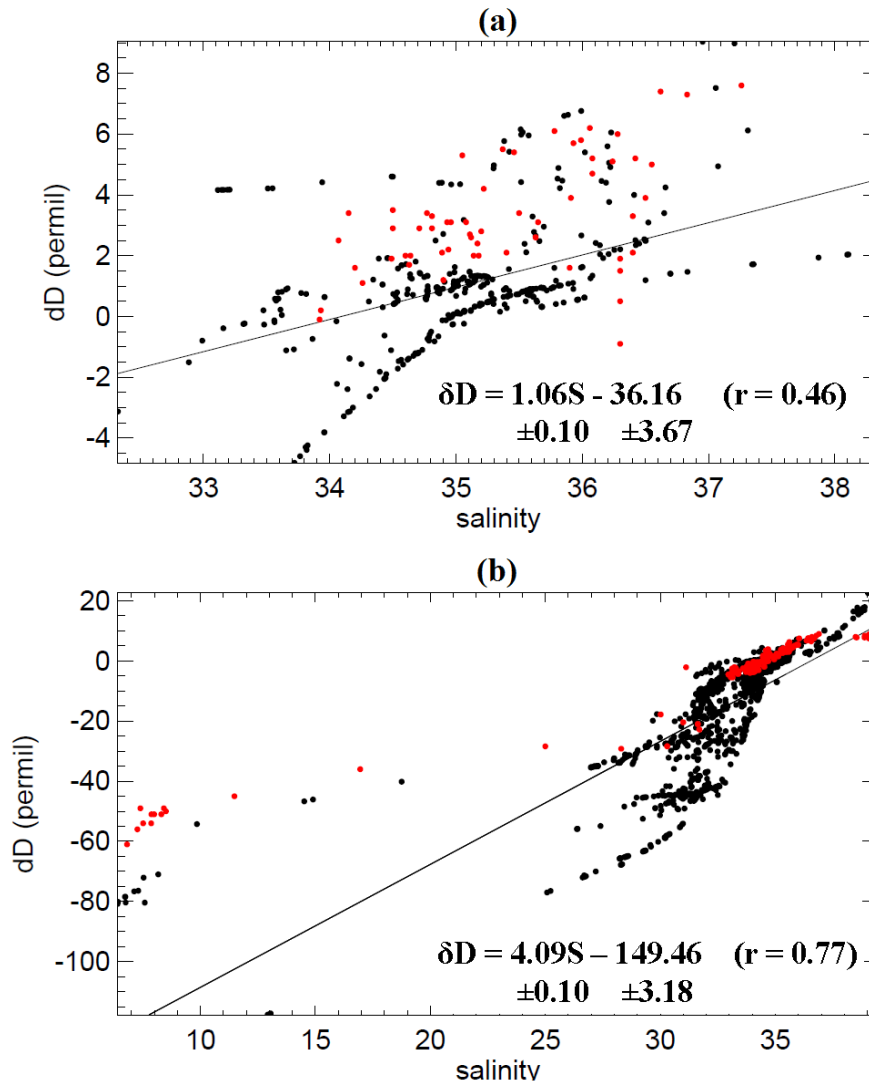


Figure 4.22 Relationship between δD and salinity S for simulated and observed surface waters. (a) tropical regions, (b) extra-tropical regions. In all panels, model results are plotted in black and observational data are plotted in red. The regressions are calculated from simulation results. Please note that the same grid cells as used in the $\delta^{18}\text{O}$ - S analyses (Fig. 4.21) have been selected to determine the δD - S relations in tropical and extra-tropical oceans (see text for further explanation).

As illustrated in Figure 4.21, the model is able to represent the general features of the observed $\delta^{18}\text{O}$ - S relation. The modelled $\delta^{18}\text{O}$ - S slope at tropical oceans is $\sim 0.18\text{‰/PSU}$, which agrees well with the observed gradient of $\sim 0.17\text{‰/PSU}$. This consistency is also maintained in the end member, where the simulated $\delta^{18}\text{O}$ value (-5.85‰) is in accordance with the observations (-5.55‰). For the extra-tropical

oceans, the model is able to represent the main features of the observations, too. Both slope (model: $\sim 0.50\text{‰}/\text{PSU}$, observations: $0.43\text{‰}/\text{PSU}$) and end member (model: -17.62‰ , observations: 14.98‰) are in fair agreement with the observations. The modeled $\delta^{18}\text{O}$ -S slopes agree also with the general latitudinal trends, with a steeper meridional gradient in high latitudes than in tropical surface waters. The correlation between $\delta^{18}\text{O}$ and salinity in tropical waters is weaker than in the extra-tropical regions, both in the observations and the simulation results.

For δD , there is a limited number of measurements, and even less investigation on the δD -S relation (Baltic Sea: $\sim 1.96\text{‰}/\text{PSU}$, Fröhlich et al., 1988; Mediterranean Sea: $\sim 1.72\text{‰}/\text{PSU}$, Gat et al., 1996). This sparse data set is not enough for a robust data-model comparison. Therefore, we have selected the same grid cells used in the $\delta^{18}\text{O}$ -S analyses to determine the δD -S relations in tropical and extra-tropical oceans (Figure 4.22). In agreement with the similarity of the basin-scale variations of deuterium and oxygen-18, we find coincident relations of $\delta^{18}\text{O}$ and δD with salinity. For δD , a slope of $\sim 1.06\text{‰}/\text{PSU}$ is found in tropical regions, and a much steeper slope of $\sim 4.09\text{‰}/\text{PSU}$ is simulated in extra-tropical regions. At both tropical and extra-tropical oceans, δD exhibits larger absolute variation compare to $\delta^{18}\text{O}$ with the same range of salinity, and shows relatively weaker correlation to salinity.

4.5 Discussion

We implemented the passive isotopic tracers H_2^{18}O and HDO into the ocean model MPI-OM. In most regions, the simulated water isotope composition of surface waters agrees well with observations. The correlation between model results and observations is higher for δD ($R = 0.96$) than for $\delta^{18}\text{O}$ ($R = 0.75$). However, this is probably an artifact which is due to the smaller number of δD observations compared to $\delta^{18}\text{O}$. If the model-data comparison for $\delta^{18}\text{O}$ is restricted to the same locations used in the δD analyses, a similar high correlation coefficient ($R = 0.97$) is calculated. The largest differences are found in some marginal seas, where river runoff has a strong effect, such as in the Baltic Sea, the Kara Sea and Laptev Sea. The deviations between data and model are likely due to the unresolved scales and processes at those marginal

areas as a result of the coarse resolution in our model simulation. Vertically, the number of observations from deeper water layers is insufficient to draw a precise global picture of the vertical distribution of water isotopes. However, the simulated vertical values of δD and $\delta^{18}O$ agree also well with the observations. There are a small number of δD values completely off the 1:1 line in Fig.6. These values are located at the costal line of the Weddell Sea. The depletion in our simulation is probably mainly due to the runoff calculation, which considers all the snowfall as river runoff into the ocean according to the mass balance. The main discrepancies in $\delta^{18}O$ as seen in the model-data comparison are found mainly in the Gulf of St. Lawrence. This mismatch may be due to our coarse model resolution, which is unable to resolve the physical processes in this region. The modeled water isotope distribution at Atlantic meridional section is consistent with the different water masses. Our model results compare reasonably well with previous results from other isotope included OGCM model studies, either by ocean only (Schmidt, 1998; Paul et al., 1999; Wadley et al., 2002) or coupled versions (Schmidt et al., 2007).

Since precipitation and evaporation are the main water fluxes affecting the isotopic composition of ocean surface water, a similar linear relation between δD and $\delta^{18}O$ as the global meteoric water line (Craig, 1961) is expected. Our simulation represents this similar relation in most oceans and consistent with the observed slope 8.1 ± 0.4 (Friedman, 1953) in the ocean as well. In addition, the unique δD - $\delta^{18}O$ relation in the Mediterranean Sea found by Gat et al (1996) is not reproduced by our model. In agreement with recent observations (Cox et al., 2011), the simulated Mediterranean relation follows the general δD - $\delta^{18}O$ relation. The reasonable δD - $\delta^{18}O$ relation enables a realistic d-excess surface field, which is necessary to model d-excess. However there are only a few studies on the d-excess in ocean waters, which makes it rather difficult to evaluate the modelled d-excess variations in sea surface waters. Based on the approach that the atmospheric d-excess signature is dominated by non-equilibrium isotope fractionation during evaporation processes from marine surface waters (Dansgaard, 1964; Gat et al., 1994), the remaining ocean surface water should have a negative d-excess value. In our simulation results, we find such

negative d-excess values in most ocean regions. Water masses with positive d-excess values are found in regions that are controlled by the river runoff, preserving a positive d-excess signal found in precipitation. Compared to the available observations, our model simulates in general too negative d-excess values. This mismatch might be related to our chosen model setup: The used isotope forcing fluxes of precipitation and evaporation stem from an ECHAM5-wiso simulation, where a constant d-excess value of 0‰ was assumed for all ocean surfaces (Werner et al., 2011). This inconsistency can be only solved in a fully coupled ocean-atmosphere system and should result in slightly higher d-excess values of ocean surface waters.

For the relation between $\delta^{18}\text{O}$ and salinity S in marine surface waters, different gradients have been obtained in various model studies. These studies suggest an extra-tropical region of 0.5 – 0.6‰/S and a tropical slope of 0.2‰/S (Schmidt, 1998; Schmidt et al., 2007; Delaygue et al., 2000; Wadley et al., 2002). Our results are in agreement with these findings. Both deuterium and oxygen-18 exhibit a linear relationship with salinity, and both $\delta^{18}\text{O}$ -S and δD -S gradients vary when different ocean basins are chosen for the calculation. Thus, for a more precise interpretation of δ -changes in terms of salinity variations, basin-scale relationships should be applied. However, the surface salinity is not a free variable in our model setup due to the surface salinity restoring, which is necessary to maintain the general MPIOM ocean state in agreement with the observations. Our relation between $\delta^{18}\text{O}$ and S is therefore not purely determined by the model, but also by the salinity data used for restoring. These inconsistencies in the δ -S relation will be overcome in future work using a fully coupled ocean-atmosphere set up.

Chapter 5

Oxygen isotope simulation at Last Glacial Maximum

In this experiment, the isotope-enhanced MPI-OM used in the Chapter 4 is applied. Here, we have simulated ocean fields as well as the $\delta^{18}\text{O}$ composition in the sea waters at LGM. The model results are compared with the corresponding PD simulation for different oceanic basins to understand the processes that lead to isotopic distribution of oxygen-18 at the sea surface and in the deep water. Sensitivity studies are used to understand the factors giving rise to the variations of $\delta^{18}\text{O}$ during present day and LGM. In paleo-studies, the relationship between $\delta^{18}\text{O}$ and salinity at LGM is assumed to be similar to $\delta^{18}\text{O}$ -S relations at present day. Therefore, the $\delta^{18}\text{O}$ -S relations of different basin are calculated to examine this assumption.

5.1 Experiment setup

The ocean model is also configured with a formal horizontal resolution of $3^\circ \times 1.8^\circ$ and 40 unequal vertical layers. For the present-day experiment, the same topography data set applied in Chapter 4 is used to create the grid-based topography and bathymetry. In the LGM simulations, the mean sea-level is lowered corresponding to the ice-sheet extent by 116 meters, in agreement with the settings of Paleoclimate Modelling Intercomparison Project Phase III (PMIP3, available at <https://pmip3.lsce.ipsl.fr/>). Therefore, the Hudson Bay and Barents Sea are covered by the main northern hemisphere ice-sheets, while the Bering Strait is closed.

Initial conditions for marine temperature and salinity in the PD simulation are interpolated from the same climatological fields (Steele et al., 2001) used in Chapter 4. Sea surface temperature (SST) and salinity for the LGM run stem from an LGM simulation of the Earth System Model COSMOS (Zhang et al., 2012). Sea surface salinity is restored at a time scale of 39 days in both PD and LGM simulation.

For the initial distribution of H_2^{18}O in the present-day ocean, a homogenous setup has been chosen with all values set to present-day $\delta^{18}\text{O}$ values of 0‰ with reference to the

VSMOW (Baertschi, 1976). In accordance with the larger ice volume at LGM, 1‰ is added to LGM $\delta^{18}\text{O}$ initial distribution (Schrag et al., 2002). No surface restoring of water isotopes is applied.

The atmospheric forcing for PD and LGM conditions are derived from the atmospheric general circulation model ECHAM5-wiso in a T31 spectral resolution (about $3.75^\circ \times 3.75^\circ$) with 19 vertical levels (Werner et al., 2011). Mean daily values of heat, freshwater and momentum fluxes at the air-sea interface are obtained from a 10 years simulation period. For PD, AMIP-conform (Gates et al., 1999) present-day boundary conditions, including monthly climatological sea surface temperatures and sea ice cover of the period 1979-1999 have been prescribed. For LGM, ECHAM5-wiso used SST and sea ice boundary conditions calculated from the difference between the PD and LGM simulations employing the climate model COSMOS under present-day and glacial conditions. We used the Earth System Model COSMOS in a coupled atmosphere-ocean-land surface model version, which has already successfully been applied for the Holocene (Wei et al., 2012; Wei and Lohmann, 2012).

The daily isotopic content of precipitation and evaporation fluxes over ocean surface stem from the same PD and LGM ECHAM5-wiso simulation which is used for obtaining the default freshwater, heat and momentum fluxing forcing.

In a sensitivity experiment, we set all boundary conditions like for the LGM simulation, except for the daily isotopic forcing, which was set to the PD values. This sensitivity experiment is named as ISOPD hereafter. It will allow us to distinguish between the impact of LGM ocean circulation changes and glacial isotopic changes in the precipitation and evaporation fluxes on the simulated isotopic composition of ocean water masses.

5.2 Isotopic boundary conditions

The LGM annual mean precipitation of H_2O and H_2^{18}O and their difference with the present day simulation are represented in Figure 5.1 and Figure 5.2, respectively.

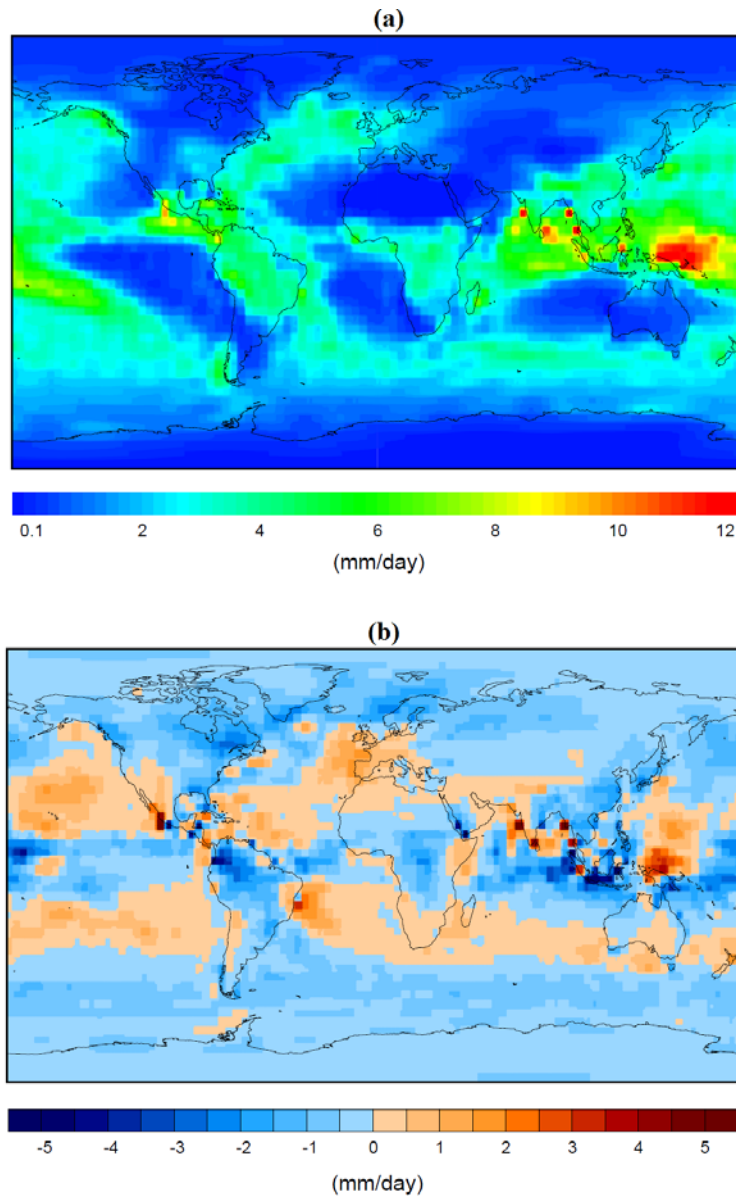


Figure 5.1 (a) The LGM global annual-mean precipitation rates of H₂O obtained from ECHAM-wiso (Werner et al., 2011) simulation under LGM climate condition. (b) The normal precipitation anomaly between the LGM and present day simulations from ECHAM-wiso.

Like in present day simulation, the normal precipitation and isotopic precipitation at LGM apparently have coincident distributions. Both of them present similar spatial patterns as present day, where the maximum precipitation locates at ITCZ (Intertropical Convergence Zone) and decreases along latitudes. In general, the precipitation over continent is less at LGM due to the drier atmosphere. Over oceans,

the amount of precipitation over equatorial and high latitudes basins is smaller in comparison to present day. At sub-tropical regions, there is slightly more precipitation at LGM, especially in the eastern basins of northern hemisphere. The North Atlantic storm tracks shift southward at LGM, which is because of the narrower LGM Hadley Cell width and an increase of sea ice cover.

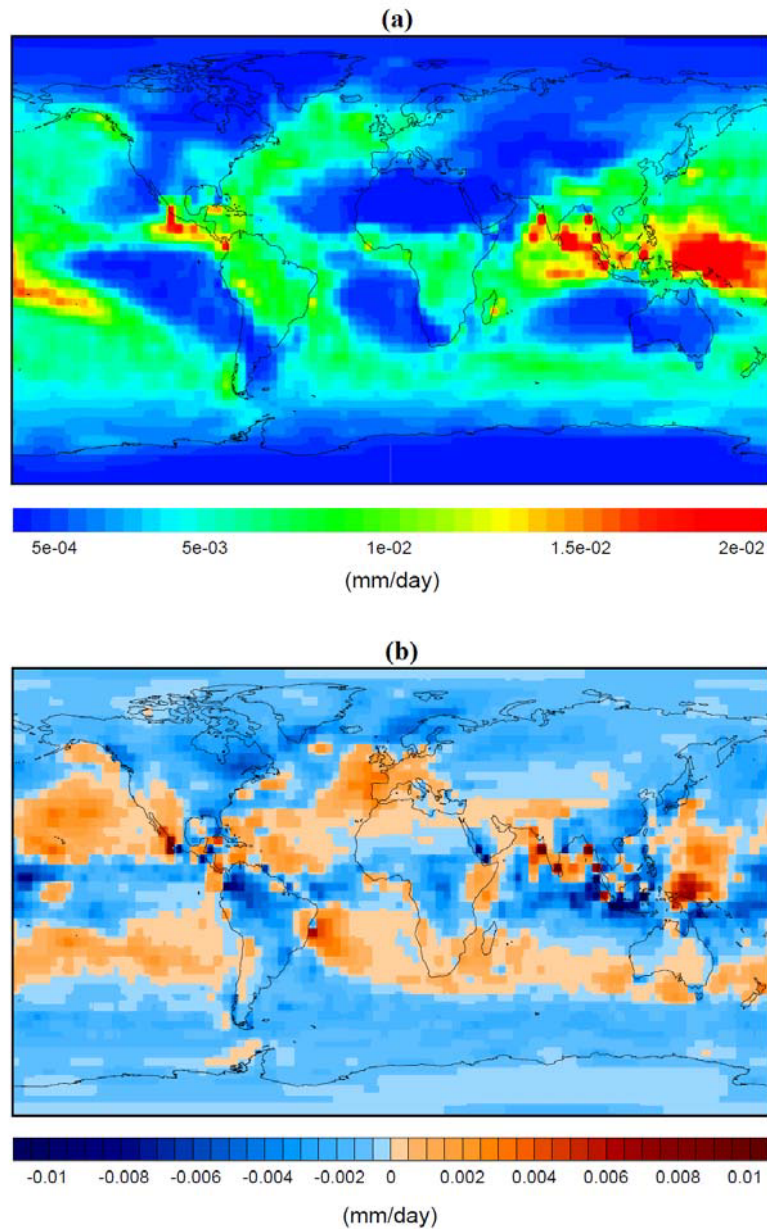


Figure 5.2 (a) The LGM global annual-mean precipitation rates of $H_2^{18}O$ from ECHAM-wiso (Werner et al., 2011) simulation. (b) The isotopic precipitation anomaly between the LGM and present day simulations from ECHAM-wiso.

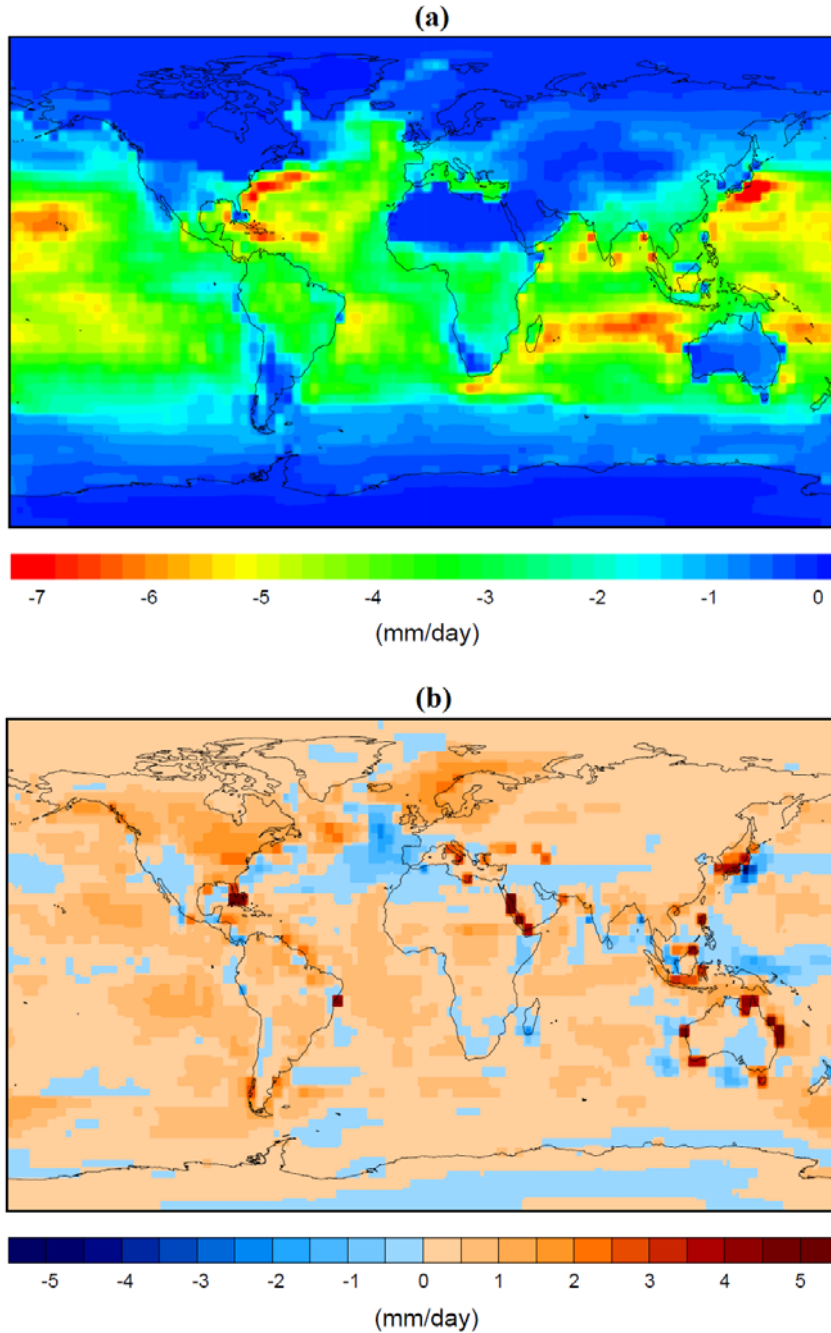


Figure 5.3 (a) The global annual-mean evaporation rates of H₂O obtained from the ECHAM-wiso (Werner et al., 2011) LGM simulation. (b) The normal evaporation anomaly between the LGM and present day simulation from ECHAM-wiso.

The LGM evaporation rates of both H₂O and H₂¹⁸O, alike present day features, with strong evaporation at tropical oceans and weak evaporation at cold regions (Figure 5.3, Figure 5.4). The evaporation rates are described as negative fluxes, so the positive anomaly between LGM and present day means less evaporation at LGM, and vice

versa. Because of the cold climate at LGM, the evaporation rates at most areas are smaller than present day. The evaporation over North American and modern Barents Sea is much less due to the ice sheet extent, where the temperatures are extremely lower as compared to present day.

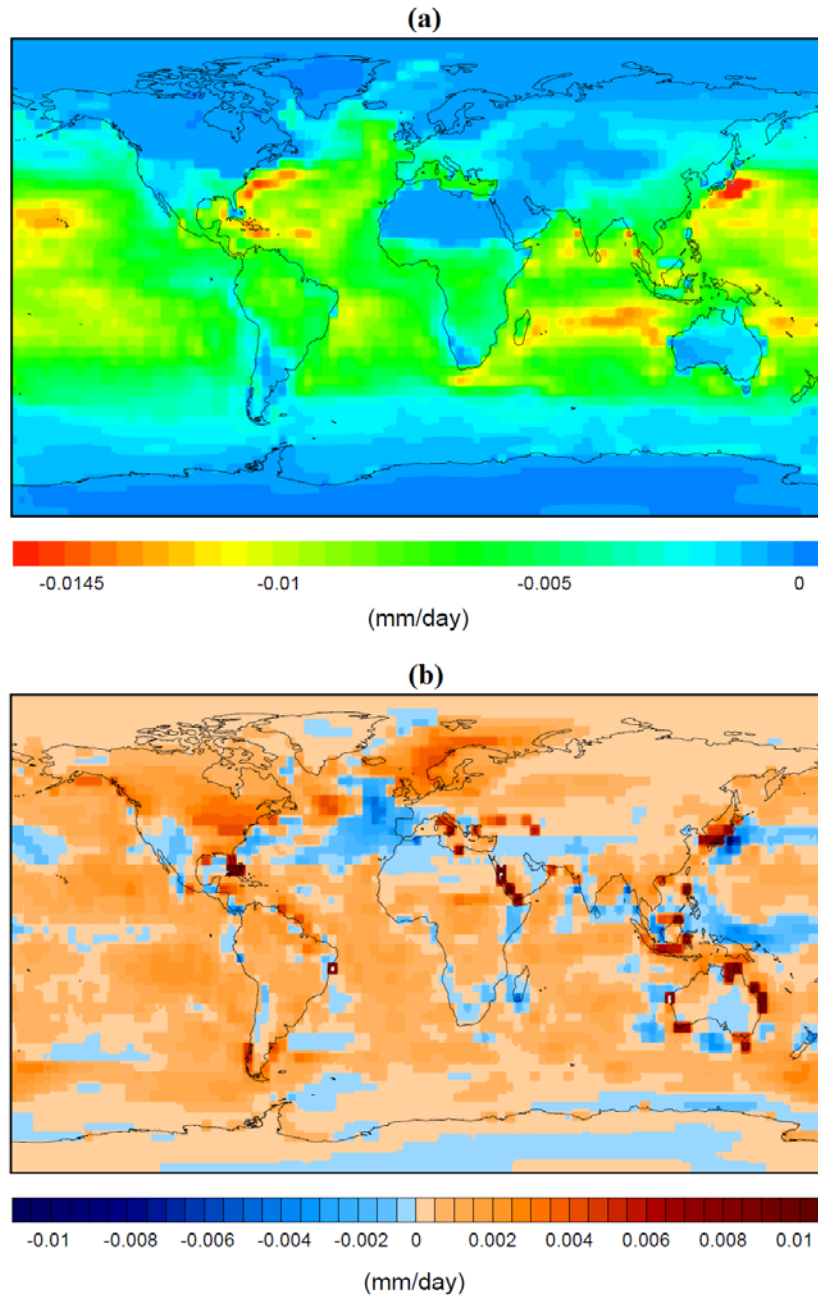


Figure 5.4 (a) The LGM global annual-mean evaporation rates of $H_2^{18}O$ from the ECHAM-wiso (Werner et al., 2011) simulation. (b) The isotopic evaporation anomaly between the LGM and present day simulation from ECHAM-wiso.

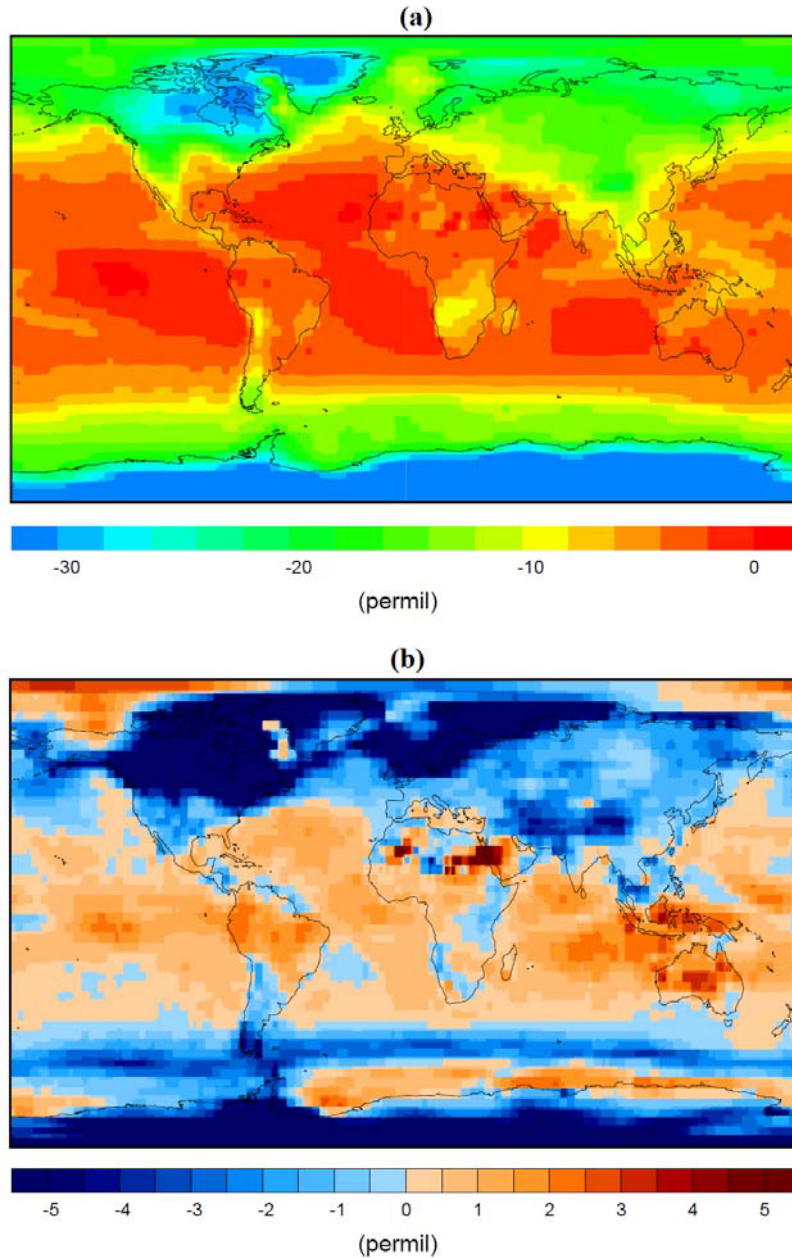


Figure 5.5 (a) The global LGM annual mean $\delta^{18}\text{O}$ values of precipitation simulated by ECHAM-wiso (Werner et al., 2011). (b) $\delta^{18}\text{O}$ anomaly between the LGM and present day simulation from ECHAM-wiso.

As shown in Figure 5.5, the isotopic composition of LGM precipitation also exhibits decreasing trend from equatorial regions to high latitudes. In comparison to present day, the LGM precipitation are more enriched at tropical to sub-tropical regions, and more depleted at most extra-tropical areas. The precipitation over glacial ice sheet is especially more depleted as compared with present day.

5.3 Results

All the simulations discussed in this chapter have been run for 3000 years into a quasi-steady state. For the analyses, we used the mean state of the last 100 simulation years.

5.3.1 Comparison of simulated LGM and PD ocean

First we present the SST, sea surface salinity (SSS), and sea surface ice concentration (SIC) in the LGM simulation and then compare them with the present day results.

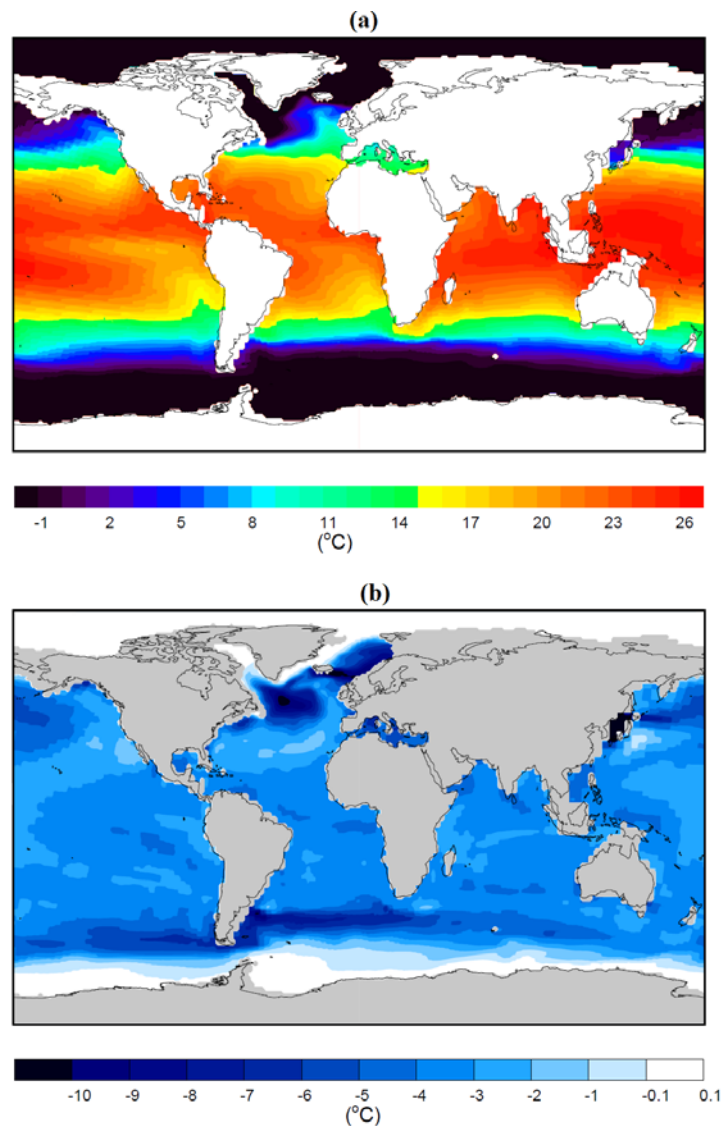


Figure 5.6 (a) Modeled annual mean sea surface temperature distributions at LGM. (b) SST anomaly between LGM and present day.

The global mean SST in LGM is approximately 2.2°C colder than present day. As illustrated in Figure 5.6, the SST distribution structures in tropical and sub-tropical regions are similar to present day. Distinct features are found in mid-to-high latitudes in both hemispheres, especially in the North Atlantic. The most pronounced SST decrease is located in the eastern basin of Nordic Seas and off the eastern coast of Laurentide ice sheet, where the cooling is more than 6°C. In the Southern Ocean, an annular cooling pattern is simulated with a strong cooling at around 40°~45°S. The tropical regions are about 3 to 4°C colder at LGM as compared to present day. In the Arctic Ocean and south of 65°S, there is not much difference between LGM and present day SST due to the permanent sea ice cover at both LGM and present day at this region.

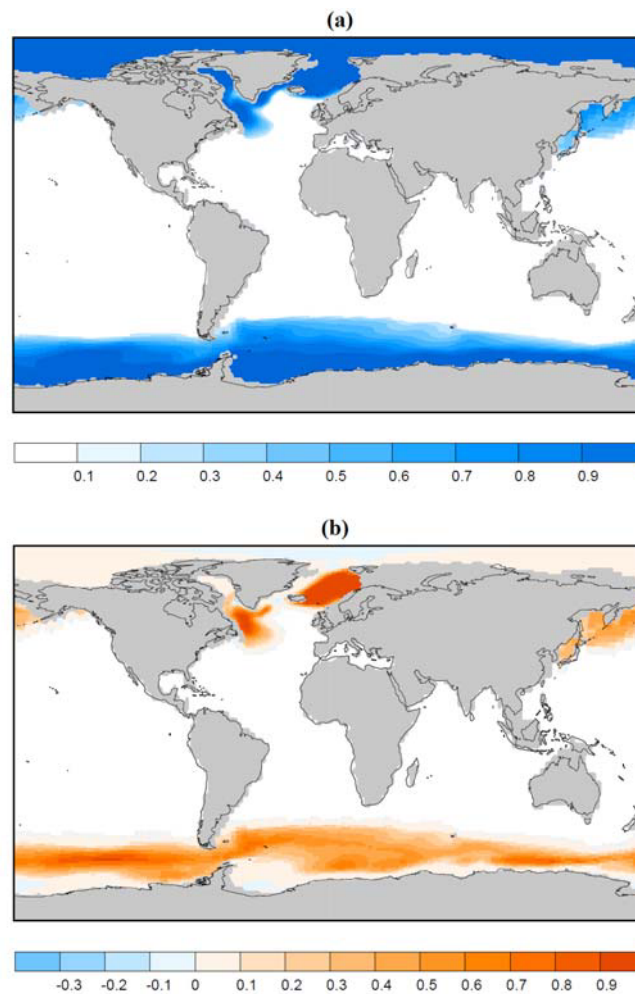


Figure 5.7 (a) Modeled annual mean surface ice concentration distributions at LGM. (b) SIC anomaly between LGM and present day.

In response to the cold climate at LGM, the sea-ice extents reach lower latitudes in both hemispheres compared with the PD simulation (Figure 5.7). The sea ice extent changes are in agreement with the SST differences between LGM and PD at high latitudes. Few variations (<10%) are found in the regions, which exhibit permanent sea ice cover at present day. In our simulation, the increase in sea ice compactness in the eastern Nordic Seas is up to 90%. There is also noticeable SIC increase around the coast of Newfoundland extending far into the Western Atlantic. The LGM sea ice coverage extends further north in the Southern Ocean compared with the PD conditions.

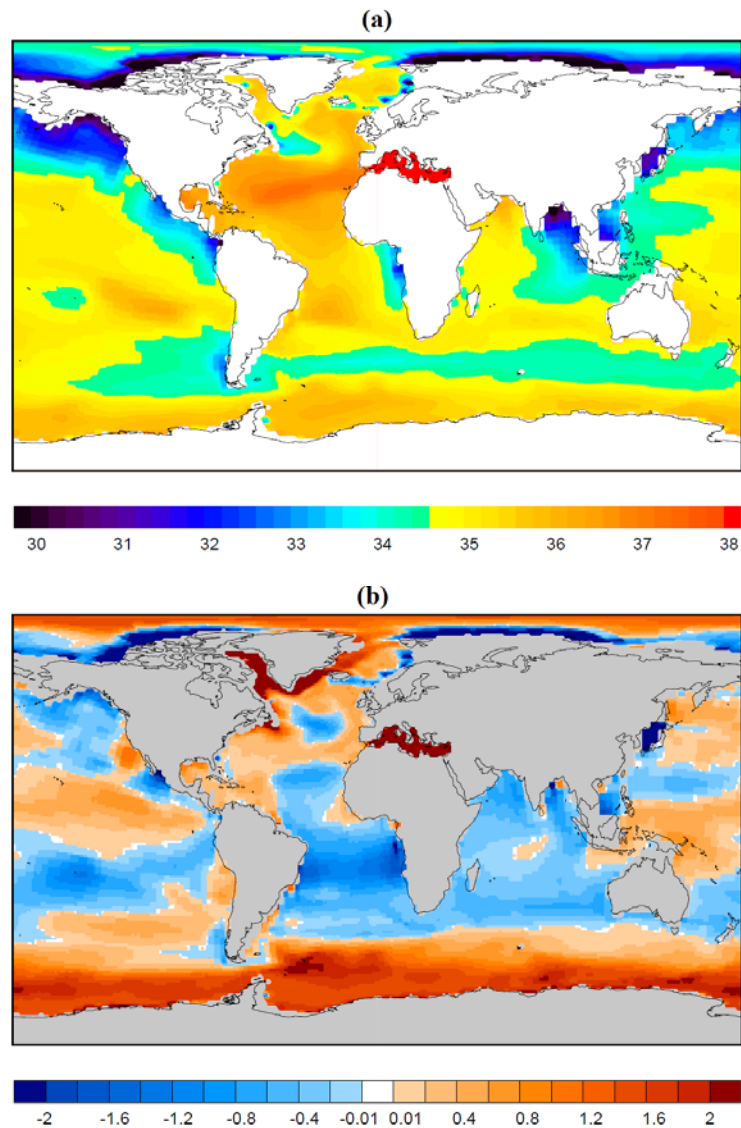


Figure 5.8 (a) Modelled annual mean sea surface salinity distributions at LGM. (b) SST anomaly between LGM and present day.

The modelled surface salinities show obvious differences at LGM when compare with present day (Figure 5.8). At most basins, except the Arctic Ocean and the Southern ocean, SSSs are generally within 1 of the present day values. The most important salinity increase represented by the simulation is in the Southern Ocean, where intensive sea ice formation increases the SSS up to 2.

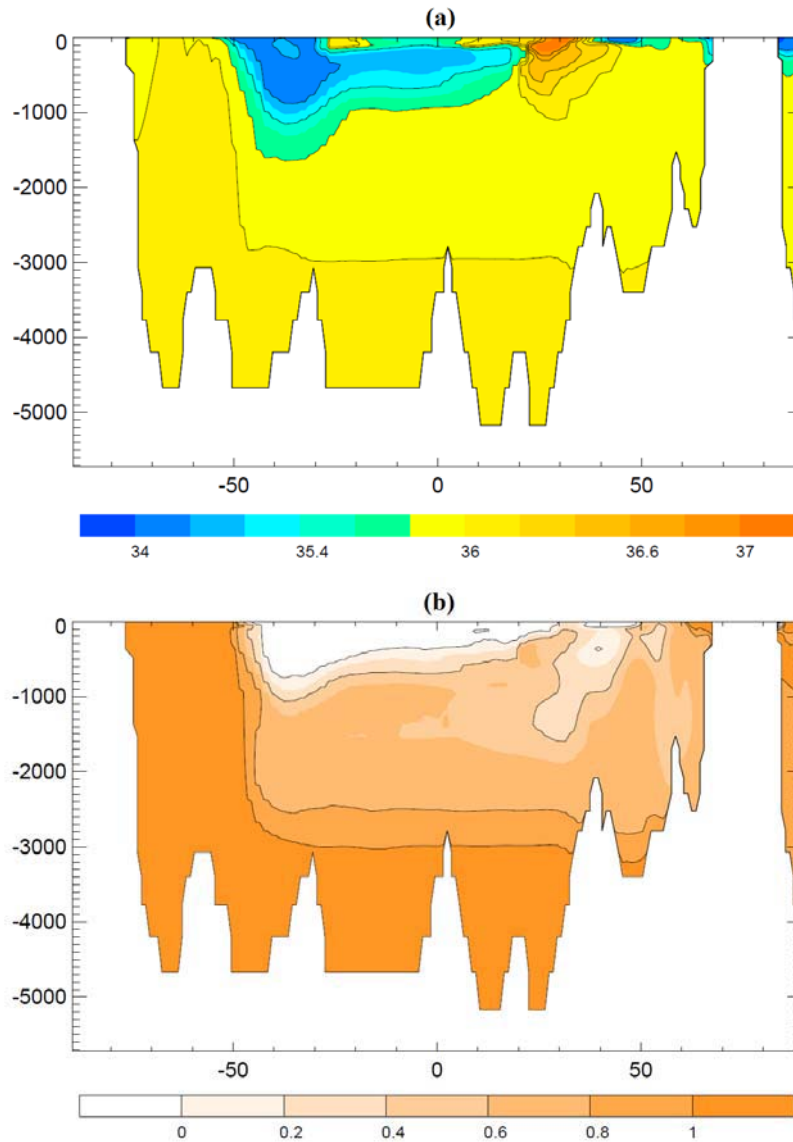


Figure 5.9 (a) LGM annual mean vertical distribution of simulated salinity through the Atlantic basin. (b) Anomaly between LGM and present day simulation.

The salinity distribution along Atlantic basin (Figure 5.9) reveals that the vertical structure of the LGM salinity is distinct from present condition. In the North Atlantic Ocean, the high salinity branch sinks to shallower depth (~1km) when compare with

present condition. Instead of the southward extension of this high salinity branch, the northwardly extending fresh water tongue that originates from 50°S is more pronounced. In contrast to present day, most saline water is at the bottom of Southern Ocean. The vertical salinity distribution is more homogenous compare to present day. With the exception of the northward extension of relatively less saline tongue in the upper 1km, the Atlantic basin is saltier than present day. The salinity increases from 0.2 to more than 1 from North Atlantic to the Southern Ocean.

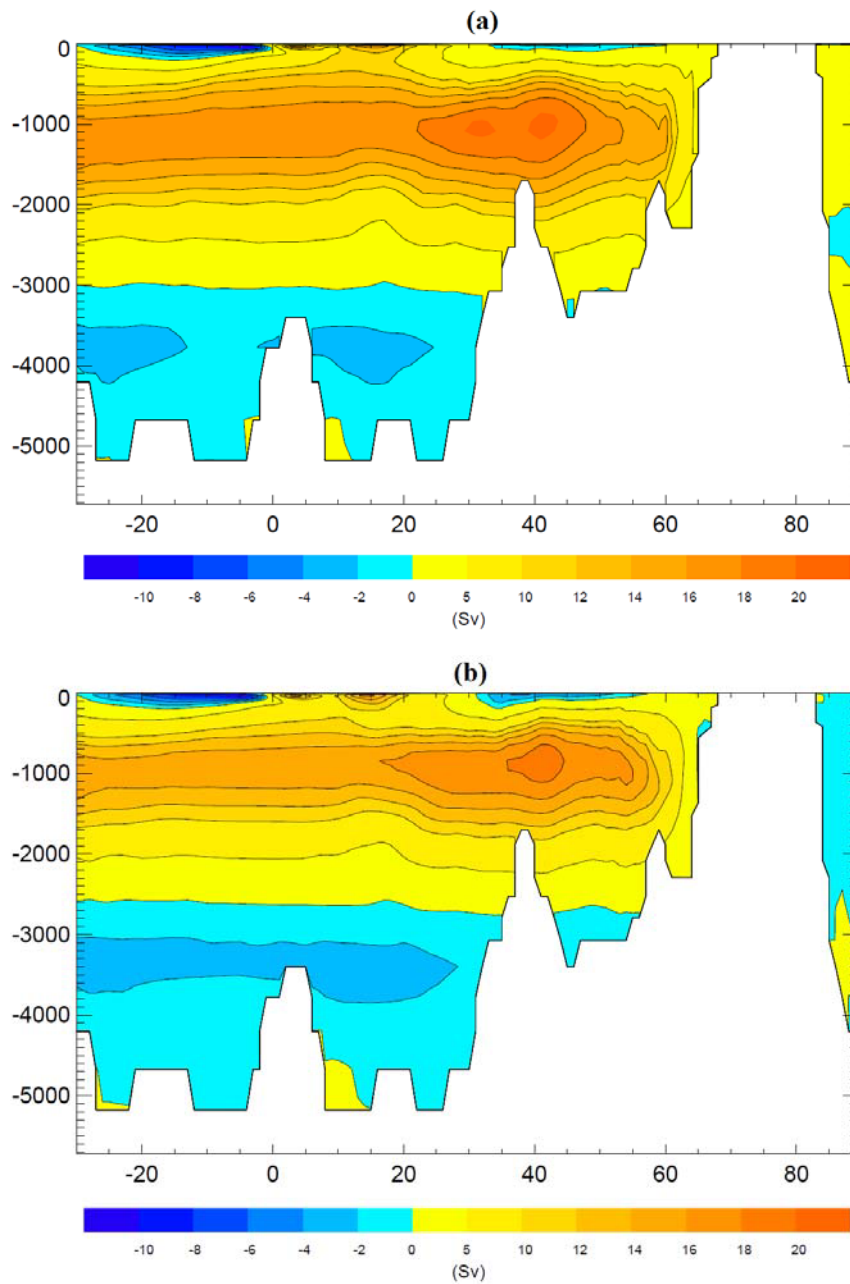


Figure 5.10 (a) The simulated Atlantic meridional ocean circulation (AMOC) at present day. (b) The AMOC at LGM.

The Atlantic meridional overturning circulation (AMOC) is one of the most important features for examining the large-scale ocean circulation. As shown in Figure 5.10, the main difference between the LGM and PD AMOC is in the characteristics of their upper cell. At LGM, the upper cell of AMOC is around 400-500 meters shallower than present day. The maximum value of this cell is centered at around 1km at both LGM and present day, and it is slightly weaker at LGM. Remarkable decrease in the strength of AMOC occurs at 2km depth, where the circulation is reduced by 4 to 5 Sv at LGM. The lower cell of the AMOC is located slightly upward at LGM and is relatively stronger due to the more pronounced Antarctic Bottom Water.

5.3.2 Simulated $\delta^{18}\text{O}$ distribution and PD-LGM comparison

Modelled isotopic distribution in LGM, PD, and ISOPD simulations present the behavior of oceanic oxygen isotope composition under different scenarios of ocean circulation and isotopic fluxes. First we evaluate the sea surface zonal-mean isotopic compositions in the modelled results.

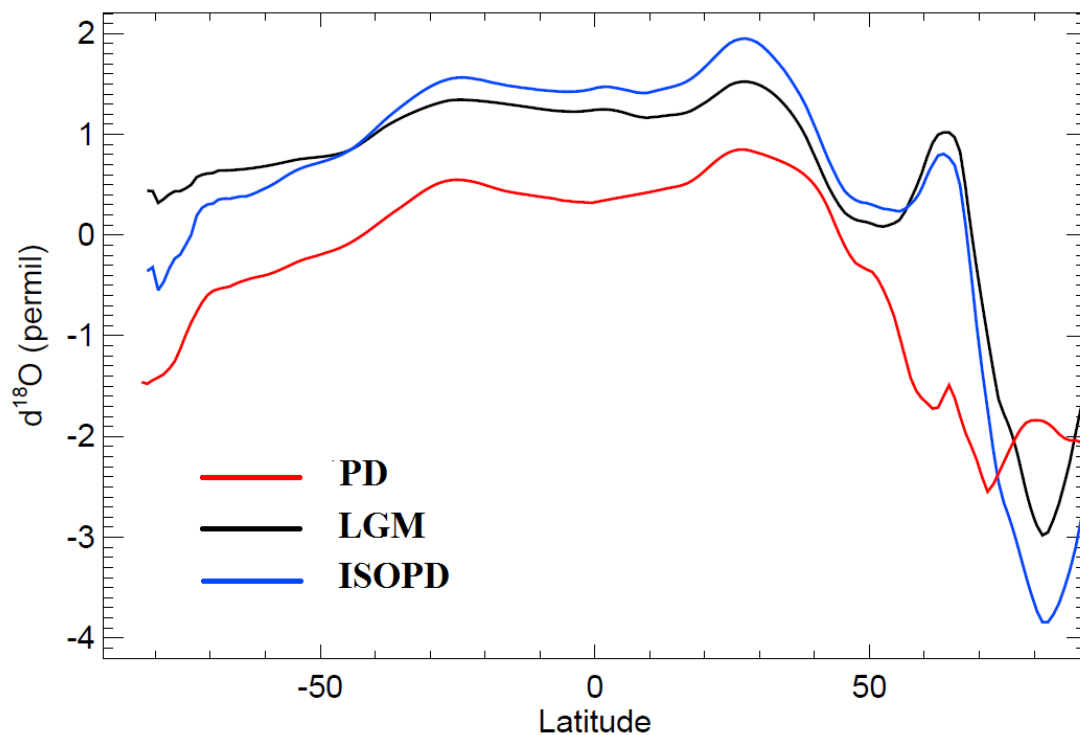


Figure 5.11 The global zonal-mean $\delta^{18}\text{O}_w$ isotopic compositions of sea surface water from the LGM, PD, and ISOPD simulation.

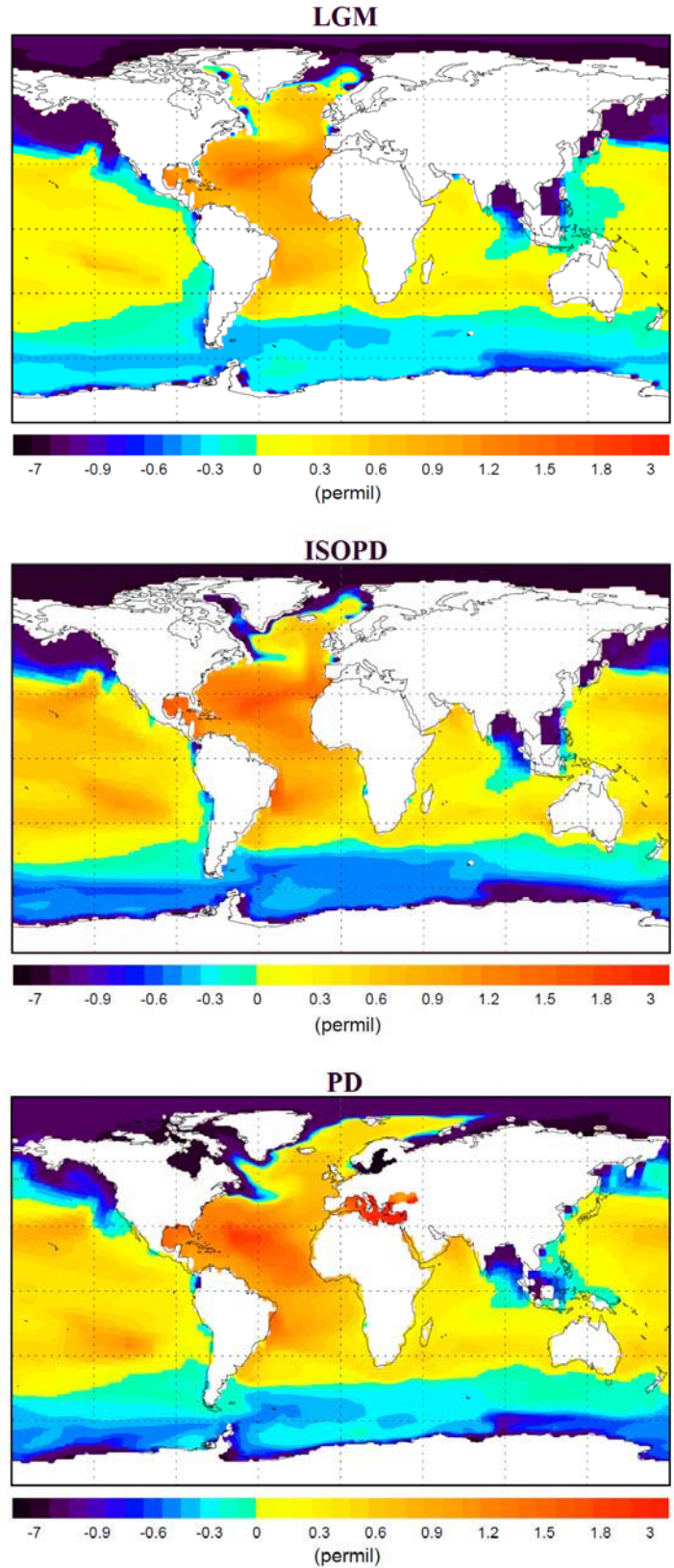


Figure 5.12 Annual mean $\delta^{18}\text{O}_w$ at ocean surface modelled in the LGM, ISOPD, and PD experiments. 1‰ is subtracted from the LGM and ISOPD isotope values to account for the prescribed total LGM ice volume effect.

As illustrated in Figure 5.11, the LGM and ISOPD experiments simulate higher $\delta^{18}\text{O}_w$ values at most latitudes than PD results, which predominantly fall within the range of -3‰ to +1.5‰ and -4‰ to +2‰, respectively. In general, the variation of $\delta^{18}\text{O}_w$ south of 30°N as modelled by ISOPD is almost parallel to the PD distribution. The LGM $\delta^{18}\text{O}_w$ also falls within the range of the other two simulations south of 30°N, but exhibits slightly higher values in the Southern Ocean. In both LGM and ISOPD results, the largest deviations from PD are found in northern mid-to-high latitudes, where an abrupt increase in $\delta^{18}\text{O}_w$ occurs around 60°N followed by a sharp decrease. Despite the increase around 60°N, similar to PD the simulated LGM $\delta^{18}\text{O}_w$ obeys the latitudinal decrease trend that mainly results from the temperature decrease. The slight enrichment of the water isotope composition in the subtropics in comparison to the equatorial regions indicates relative excess in evaporation over subtropical oceans at LGM. The most enriched area, both at LGM and present day, is located around 30°N. The zonal mean LGM $\delta^{18}\text{O}_w$ values reach almost +1.6‰ there. At LGM, the most depleted regions are found north of 75°N, with $\delta^{18}\text{O}_w$ values less than -2‰.

For further illustration, the simulated global $\delta^{18}\text{O}_w$ distributions at sea surface under LGM, PD, and ISOPD boundary conditions are shown in Figure 5.12. With the exclusion of the additional glacial +1‰ prescribed $\delta^{18}\text{O}_w$ in the initial isotopic conditions (for LGM and ISOPD, only), there are no substantial changes of isotopic spatial patterns simulated for the LGM climate, especially at mid-to-low latitudes. In the LGM results, the Atlantic Ocean between 30°S and 40°N shows much enriched isotopic values, especially in the Northern Hemisphere ($\delta^{18}\text{O} > 1.5‰$), in contrast to the Pacific Ocean. The northward transport of these enriched waters by the North Atlantic Drift only reaches the Greenland Sea, while in the PD run they approach further north. Extremely depleted values are seen in the marginal areas of the Arctic Ocean (-4‰ to -8‰, Figure 5.12).

The surface $\delta^{18}\text{O}$ distributions in LGM and ISOPD display rather similar characteristics. The enriched surface water is mainly located in tropical to subtropical region in both cases, but these waters are more enriched in the ISOPD simulation than in the LGM one. The isotope values in the Arctic Ocean under the present day

isotopic forcing are more depleted and homogenous. In addition, the depleted Pacific eastern boundary is more pronounced in the LGM simulation than in the ISOPD experiment. In general, estuaries constitute the most depleted regions because of influx of depleted waters discharged by rivers.

In order to further examine the isotopic changes due to the hydrological variations at LGM, the $\delta^{18}\text{O}_w$ differences between LGM and ISOPD, between ISOPD and PD, as well as the anomaly between LGM and PD (Figure 5.13) are calculated. In these calculations, the additional 1‰ is also subtracted from the ISOPD-PD and LGM-PD differences. Under the LGM ocean circulation condition, the differences introduced by the isotopic fluxes in the Southern Ocean and the India Ocean are around $\pm 0.2\text{‰}$. (Figure 5.13, top) The depletion in the (sub-)tropical Atlantic Ocean ($< -0.4\text{‰}$) is less than in the Pacific Ocean (up to -0.8‰) due to the isotopic fluxes. Noticeable increase in $\delta^{18}\text{O}$ values are found in the Arctic Ocean and the Baffin Bay, where the anomalies are more than $+1\text{‰}$. If we prescribe present-day isotopic composition of precipitation and evaporation, the LGM changes in circulation and topography result in greater variations north of 30°N ($> \pm 0.4\text{‰}$, Figure 5.13, middle panel). The $\delta^{18}\text{O}$ values in the northern North Pacific are around -0.6‰ lower under the LGM circulation, and the North Atlantic Drift is slightly enriched ($\sim 0.2\text{‰}$). The LGM circulation and runoff path cause strong depletion (more than -2‰) in the Arctic Ocean. Combining the fluxes and circulation factors (Figure 5.13, bottom), the sea surface isotopic composition at LGM is more depleted by up to -1‰ in most basins when compared with PD. These depletions are much less in the Southern Atlantic and Indian Oceans, where the anomalies range between -0.2‰ and 0‰ . Significant decrease is seen in the Arctic Ocean, where $\delta^{18}\text{O}$ values are around 1‰ to 2‰ lower compared with present day. In contrast to northern high latitudes, the Southern Ocean is slightly enriched at LGM. In the Northern Atlantic, slight enrichment is shown between 45°N and 60°N . There is distinct increase in $\delta^{18}\text{O}$ values in the Labrador Sea and the Baffin Bay, where the isotopic enrichment rises by up to $+2\text{‰}$.

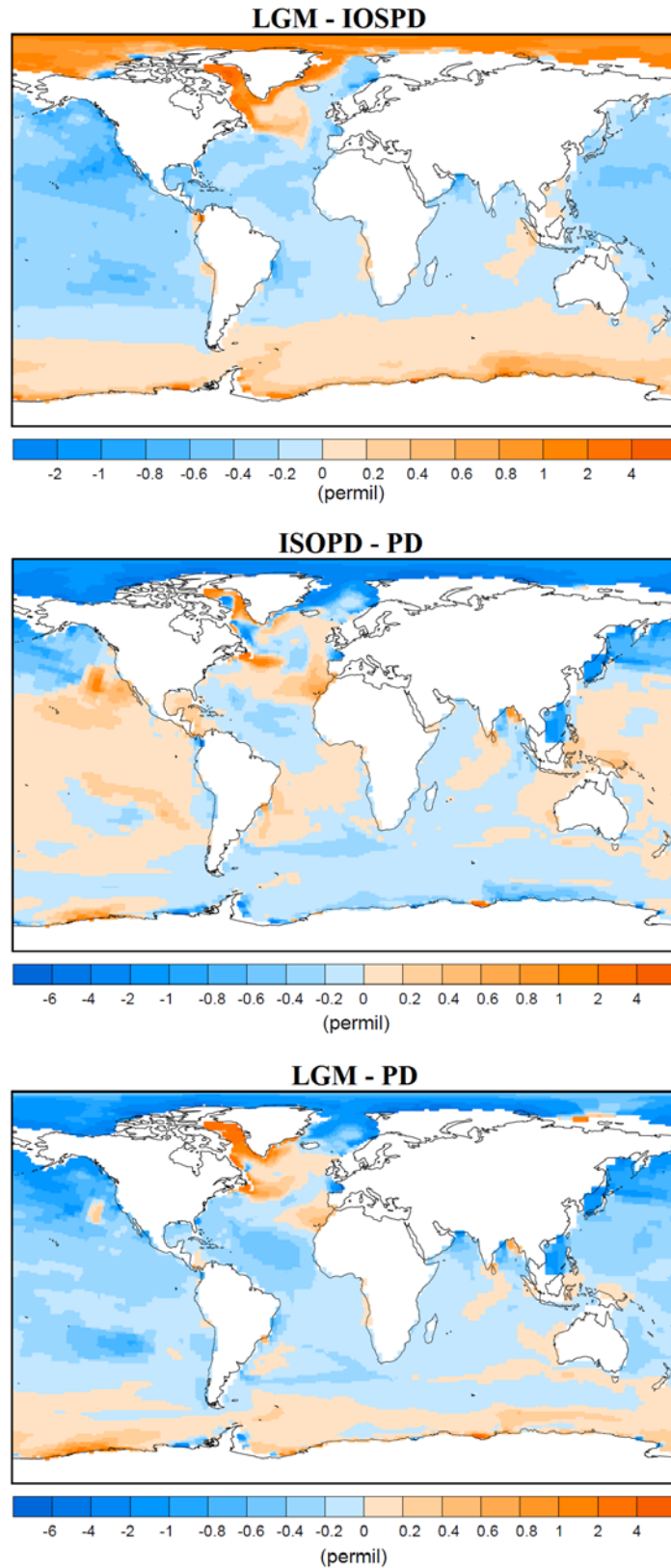


Figure 5.13 The sea surface $\delta^{18}O_w$ anomalies between different model experiments (LGM, ISOPD, and PD). 1‰ is subtracted from the ISOPD-PD and LGM-PD differences to account for the prescribed total LGM ice volume effect.

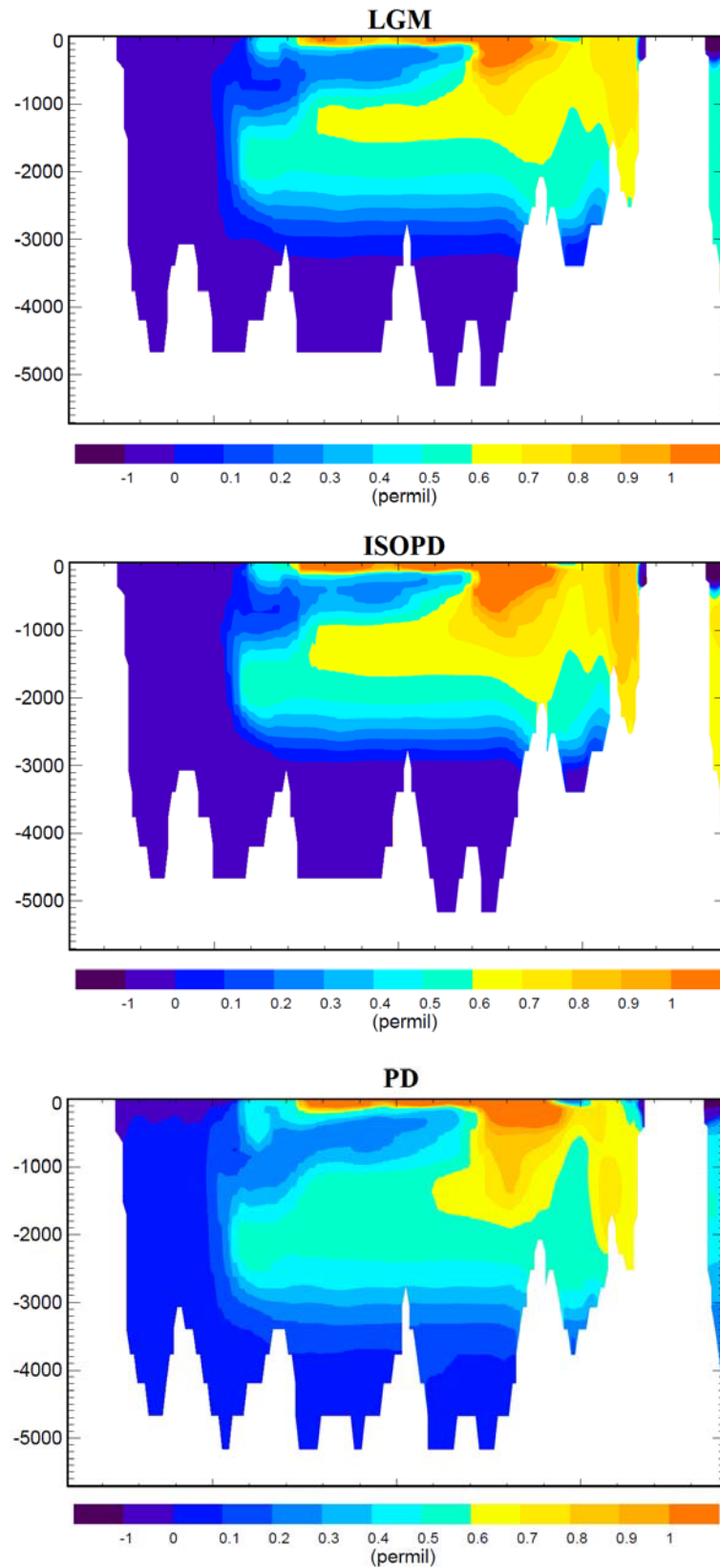


Figure 5.14 The annual zonal mean $\delta^{18}\text{O}_w$ of the Atlantic basin from the LGM, ISOPD, and PD simulations. 1‰ is subtracted from the LGM and ISOPD isotope composition to account for the prescribed total ice volume effect.

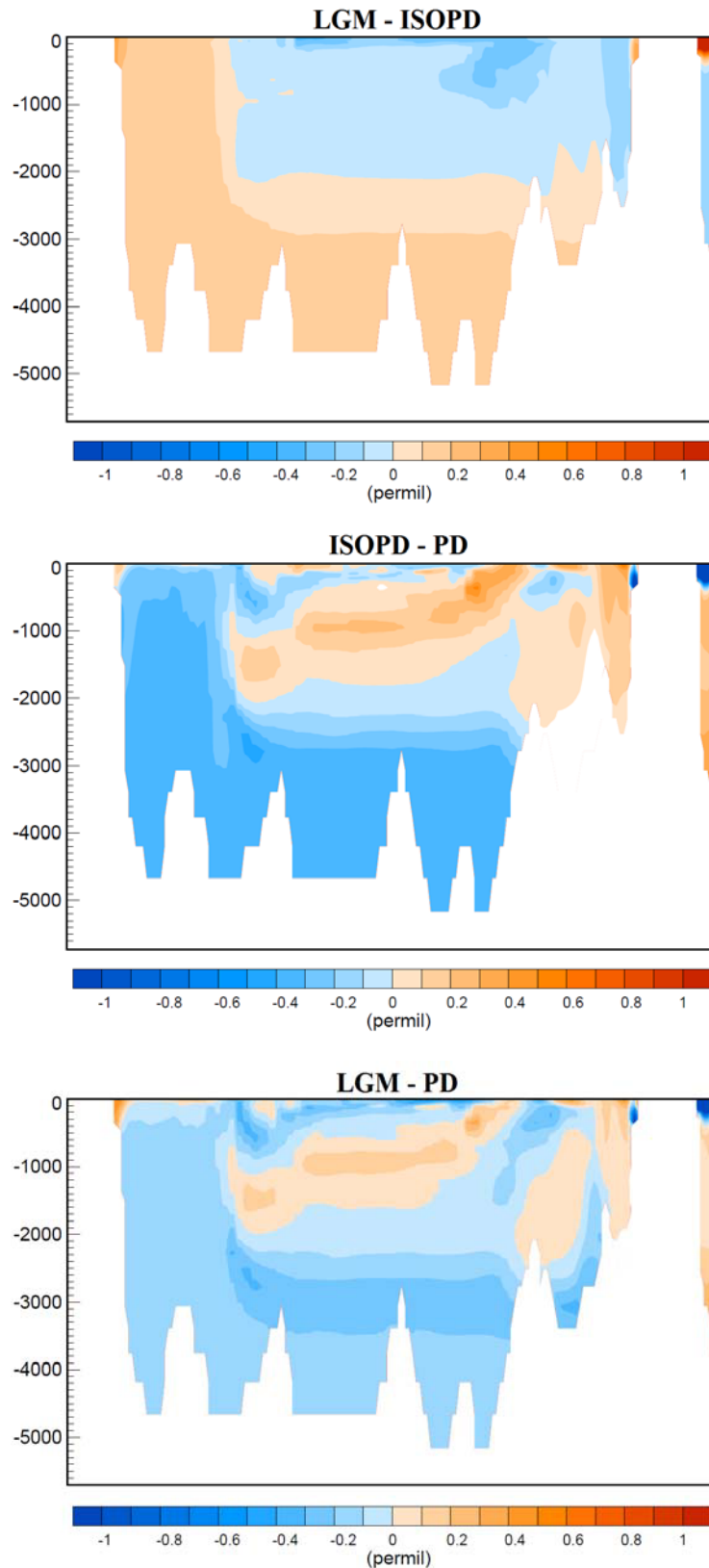


Figure 5.15 The zonal mean $\delta^{18}\text{O}_w$ anomalies in the Atlantic basin between different model experiments (LGM, ISOPD, and PD). 1‰ is subtracted from the ISOPD-PD and LGM-PD differences to account for the prescribed total LGM ice volume effect.

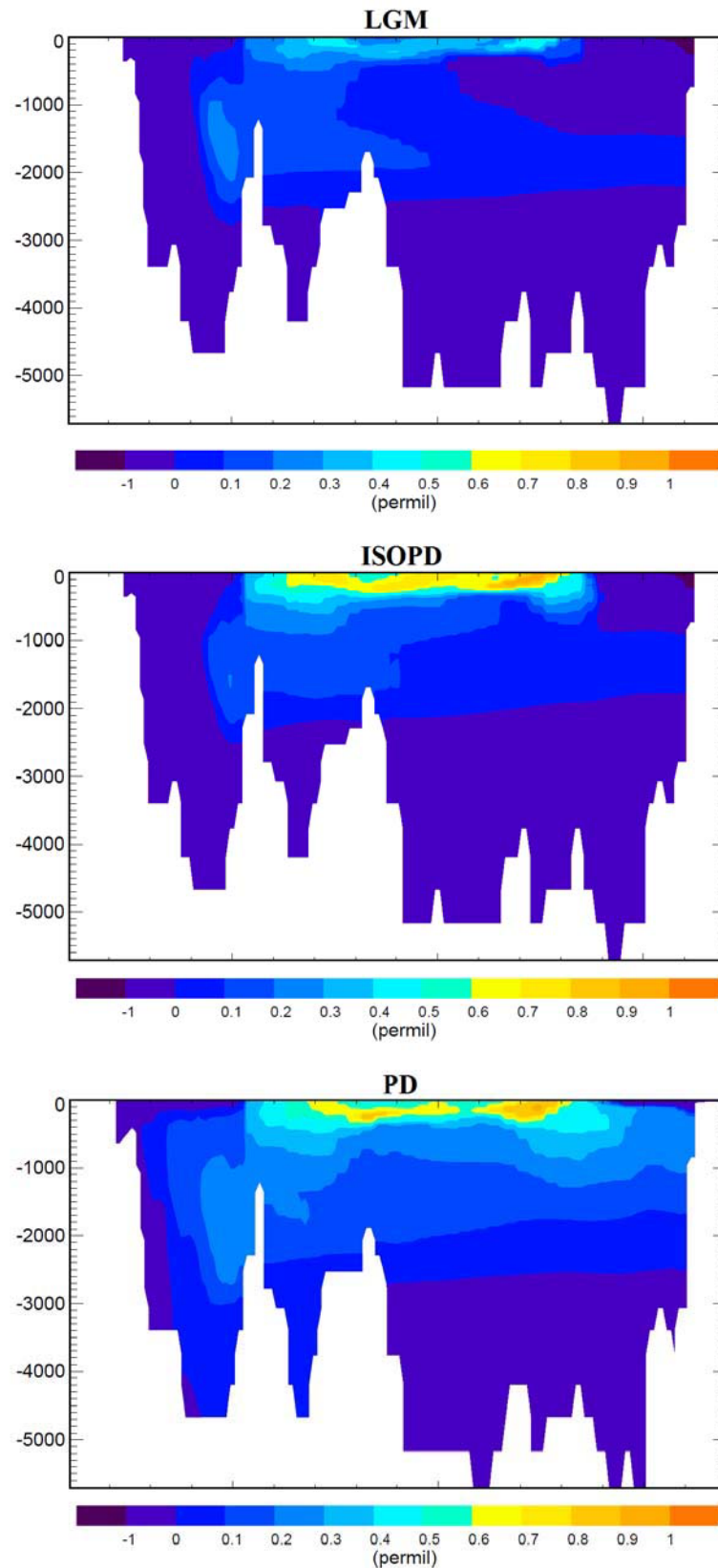


Figure 5.16 The annual zonal mean $\delta^{18}\text{O}_w$ of the Pacific basin from the LGM, ISOPD, and PD simulations. 1‰ is subtracted from the LGM and ISOPD isotope composition to account for the prescribed total LGM ice volume effect.

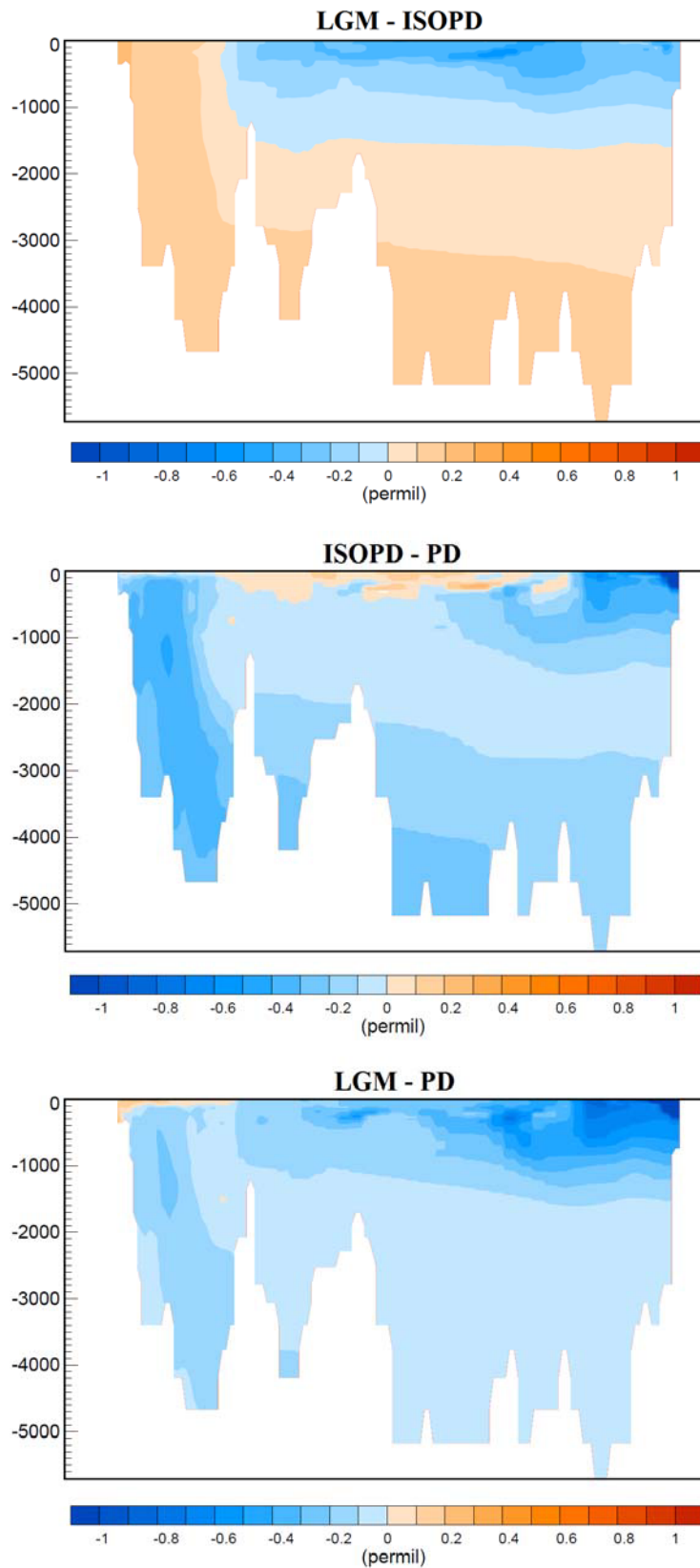


Figure 5.17 The zonal mean $\delta^{18}\text{O}_w$ anomalies in the Pacific basin between different model experiments (LGM, ISOPD, and PD). 1‰ is subtracted from the ISOPD-PD and LGM-PD differences to account for the prescribed total LGM ice volume effect.

The same set of analyses is applied to the subsurface and deep waters in the Atlantic and Pacific Ocean. As seen in Figure 5.14, a meridional cross-section of LGM $\delta^{18}\text{O}_w$ values in the Atlantic basin reveals a similar pattern as seen in the PD simulation, but shallower $\delta^{18}\text{O}_w$ -enriched waters are found in the North Atlantic. The enriched North Atlantic surface water that sinks to about 1km water depth makes the most enriched water mass in the Atlantic section. Below 2.5 km, the comparably depleted Antarctic Bottom Water dominates. The vertical isotopic patterns in the Atlantic are quite alike in the LGM and ISOPD simulation and only slight differences in the $\delta^{18}\text{O}_w$ values can be seen in the enriched upper branch and the depleted lower branch. Differences are depicted in greater detail in Figure 5.15. In comparison to the modern isotopic fluxes, the LGM conditions show slightly depleted ($\sim -0.1\text{‰}$) waters from the surface to 2km depth, where the North Atlantic Deep Water (NADW) dominates. The bottom water, which originates from the Southern Ocean, however, is around 0.2‰ enriched under the LGM isotopic forcing. The result of the ISOPD experiment for the Atlantic cross-section is also compared with the PD simulation. In this case, for the same isotopic fluxes, the changes of the vertical isotopic distribution are reversed. The LGM circulation enriched most of the NADW by around 0.1~0.2‰, but the $\delta^{18}\text{O}_w$ values in the bottom water show a decrease of approximately 0.4‰. In general, the variations in the Atlantic subsurface and deep waters due to the changes of isotopic boundary conditions and circulation are smaller (-0.3‰ to $+0.3\text{‰}$) when compared with the total glacial ice volume effect ($+1\text{‰}$).

The isotopic distribution in the Pacific section is distinct from the Atlantic basin (Figure 5.16). In the LGM simulation, the relatively enriched water mass originates from 40°S-20°S, and has a subsurface extension up to the equator. There is a clear branch of relatively depleted water starting from north of 40°N that sinks to 1km. The isotopic composition in the Pacific basin is lower than the Atlantic basin at LGM. The ISOPD result presents almost same distribution, but more enriched subsurface water. In these two cases, the depletion of bottom water is pronounced. Comparisons between the different simulations are illustrated in Figure 5.17. The variations along the Pacific basin are well stratified in the LGM-ISOPD comparison. The LGM

isotopic forcing produces more depleted waters in the upper 1.5km. The changes in the $\delta^{18}\text{O}_w$ values vary from -0.1‰ to -0.4‰ between surface and 1.5km depth. Below 1.5km, the $\delta^{18}\text{O}_w$ values are slightly higher (0.1‰ ~ 0.2‰), with a clear origin of these enriched water masses in the Southern Ocean. From the ISOPD-PD comparison, we infer that the ocean circulation under the LGM climate condition leads to a depletion at most depths. Only the subsurface waters at tropical and subtropical regions are slightly enriched (0.1‰). The decreases in the $\delta^{18}\text{O}_w$ values in the Southern Ocean are up to 0.4‰. There is a distinct depleted tongue that originates in the North Pacific Ocean, and penetrates southward. The isotopic fluxes and circulation effects together make a large depletion in the upper North Pacific, but compared with PD the variations in most areas at LGM are less than -0.2‰.

5.3.3 Simulated relations between H_2^{18}O and salinity

A positive relationship between salinity (S) and oxygen isotope ($\delta^{18}\text{O}$) is simulated under present day condition. Because of the same mechanism, similar relation between S and $\delta^{18}\text{O}$ is expected in the LGM oceans.

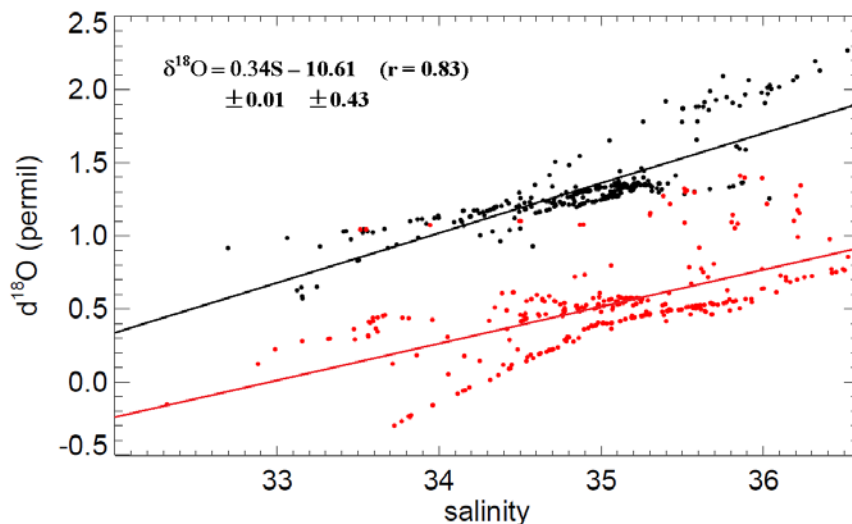


Figure 5.18 Relationship between $\delta^{18}\text{O}$ and salinity S for simulated LGM and present day surface waters in tropical oceans. Black: LGM; red: present day. The regression is calculated from LGM simulation results, the corresponding present day regression is provided in the text.

There are no direct measurements of both sea surface salinity and isotopic composition at LGM. Therefore, we only compare here the simulated LGM $\delta^{18}\text{O}$ -S relations with the present day model results.

There is no dramatic change in the relation between $\delta^{18}\text{O}$ and salinity in the LGM tropical oceans. The isotopic concentration of LGM tropical oceans is higher than present day by considering the global ice volume effect, which shifts the $\delta^{18}\text{O}$ -S regression up. As illustrated in Figure 5.18, the modelled LGM $\delta^{18}\text{O}$ -S slope at tropical oceans is $\sim 0.34\text{‰/PSU}$, which is steeper than the present day slope ($\sim 0.25\text{‰/PSU}$). This steepness induces a more depleted end member, where the LGM $\delta^{18}\text{O}$ value (-10.61‰) is around 2‰ lower than present day. In general, the LGM $\delta^{18}\text{O}$ -S data points are less scattered, which reflects higher correlation between $\delta^{18}\text{O}$ and salinity at tropical oceans.

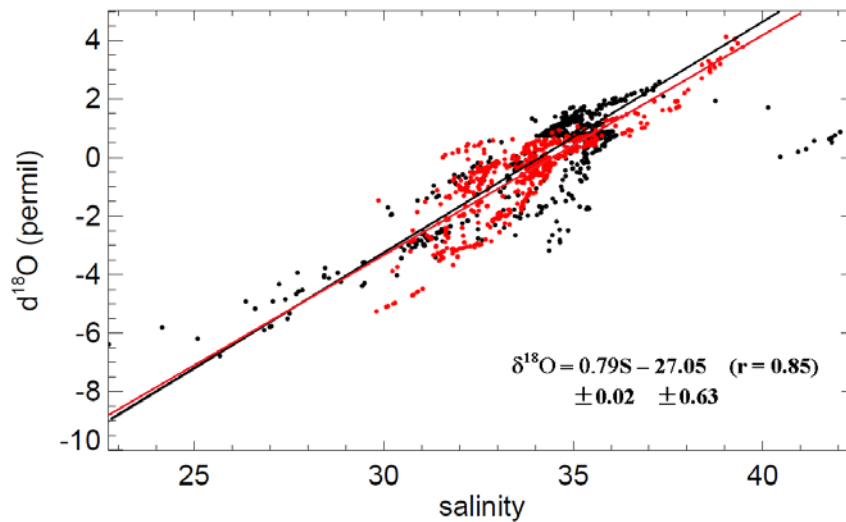


Figure 5.19 Relationship between $\delta^{18}\text{O}$ and salinity S for simulated LGM and present day surface waters in extra-tropical oceans. Black: LGM; red: present day. The regression is calculated from LGM simulation results, the corresponding present day regression is given in text.

For the extra-tropical oceans, the LGM relation between $\delta^{18}\text{O}$ and salinity is strikingly similar to present day (Figure 5.19). The slope (LGM: $\sim 0.79\text{‰/PSU}$, present day: 0.74‰/PSU) is slightly steeper than present day, and end member (LGM: -27.05‰ ,

present day: -25.73‰) is relatively depleted. The LGM $\delta^{18}\text{O}$ -S slopes also follow the general latitudinal trends, with a steeper meridional gradient in high latitudes than in tropical surface waters.

5.4 Discussion

In our LGM results, a cooling of the global oceans is represented. Compared to present day, the decrease of global mean SST is analogous to glacial SST changes estimated from proxy data (Waelbroeck et al., 2009). The strong thermal gradient in the Northern Hemisphere is well simulated at around 40 ~ 45°N. Another region of strong decrease in temperature that extends from the eastern of Iceland to the Eastern Nordic Sea is comparable to the paleo-reconstruction (de Vernal et al., 2006; Kucera et al., 2005). In our simulation, a segment of ocean in the east of the Nordic Sea is perennially frozen; this region is indicated as sea-ice free area in GLAMAP and some recent reconstructions (de Vernal et al., 2006; Kucera et al., 2005). In general, previous reconstructions suggest a 0 – 3°C decrease in most tropical regions during LGM (Ballantyne et al., 2005; Barrows and Juggins, 2005; Waelbroeck et al., 2009), our model results (3 – 4°C) overestimate this tropical cooling. In the southern oceans, the strong cooling around 45°S indicates a northward shift of the polar front during the LGM, increasing the extent of sea-ice concentrations in the Southern Ocean (Gersonde et al., 2005).

In general, our sea surface salinity is comparable to the GLAMAP (Schäfer-Neth and Paul, 2003) reconstruction between 40°S and 40°N, but relatively less saline water in the central subtropical gyre. The robust higher salinity in the Antarctic Ocean is well represented, which is due to the intensive sea ice formation in the Southern Ocean during LGM (Crosta et al., 1998). In the northern counter-part, the increase in salinity is consistent with the sea ice coverage. The fresher water along the Scandinavian margins may be because of the melting from the ice sheet (de Vernal et al., 2000), which is treated as runoff in our simulation. This may also be used to explain the low salinity in the Arctic marginal seas. In the LGM simulation, the Atlantic is flooded by waters of a Southern Ocean origin, in agreement with the measurements of passive

tracer fields (Duplessy et al., 1988; Boyle, 1992; Sarnthein et al., 1994) and the radiocarbon age difference between surface and deep waters (Shackleton et al., 1988; Adkins and Boyle, 1997). The reversed salinity gradient at the deep Atlantic is supported by the saltiest deep Southern Ocean during LGM, which is in line with the pore fluid estimations (Adkins et al., 2002; Boyle, 2002; Adkins and Schrag, 2003).

Widely different Atlantic circulation scenarios are produced by different model studies. Some show a stronger and slightly deeper overturning cell (Kitoh et al., 2001) or uniform vertical extent (Hewitt et al., 2003); while others show a weaker and shallower overturning (Shin et al., 2003; Otto-Bliesner et al., 2006). In response to the simulated hydrological conditions, the behavior of the AMOC in our MPI-OM LGM run generally agrees with a robust AMOC scenario, which is constrained by observations (Lynch-Stieglitz et al., 2007). Therefore we rate our modelled LGM simulation results as a reasonable glacial circulation, suitable for our isotope studies.

The variation of the surface $\delta^{18}\text{O}$ distribution during LGM is mainly caused by the change in continental ice storage and atmospheric isotope fluxes at the air-ocean interface (Juillet-Leclerc et al., 1997). Since we prescribe this ice sheet effect in our experiment, the variation in the model results mainly represent the local changes introduced by the different surface isotope fluxes and the glacial ocean circulation.

During the LGM, the influences from the surface fluxes and the circulation vary in different regions as we see from the different model results. The LGM surface isotope distributions in the Pacific and in the (sub)tropical Atlantic (40°S - 40°N) are similar to modern conditions, which suggests comparable surface current pattern in these regions in the two climate states. This result is in agreement with proxy reconstructions (LeGrande and Lynch-Stieglitz, 2007; Ortiz et al., 1997) and other model simulation (Clauzet et al., 2007). Therefore the simulated changes of surface $\delta^{18}\text{O}_w$ in these areas are dominated by the glacial variations in the isotopic fluxes. The decrease in $\delta^{18}\text{O}_w$ is possibly due to less evaporation during the LGM, which is consistent with the lower surface temperatures during glacial climates. In contrast, the significant changes in the topography and surface currents in the northern North Atlantic and northern polar region overwhelm the influences introduced by the

surface fluxes. During the LGM, the closed Canadian Arctic Archipelago prevents the depleted Arctic water from entering Baffin Bay, which induces a further enrichment of Baffin Bay and Labrador Sea water masses. As a consequence, the Labrador Current brings relatively high $\delta^{18}\text{O}$ water to the Atlantic. The North Atlantic Current has only a narrow northeasterly branch (Watkins et al., 2007) feeding the enriched waters to the eastern Nordic Seas. The glacial northward transport of enriched waters into the polar region is therefore much weaker than the present one. In addition, the presence of large ice sheets over North America and North Europe at the LGM had a strong impact on the river pathways and their discharge into the Arctic Ocean (Alkama et al., 2008). These changes enabled a strongly depleted river discharge to reach the central Arctic, which in combination with the weak northward transport of enriched water masses produced highly depleted surface waters in the Arctic during the LGM.

In contrast to the surface ocean, the variation of vertical $\delta^{18}\text{O}_w$ distribution is mainly caused by the different meridional overturning circulation during the LGM. The isotope distribution in the Atlantic section is in line with the AMOC condition at the LGM. In the North Pacific, there is a zone of intense subsurface water formation, possibly due to a relatively strong cooling in that area. Overall, in most regions the simulated isotopic variations caused by the changes in glacial surface isotope fluxes and ocean circulation are less than the estimated global mean ice sheet impact of +1‰, especially in the deep oceans.

Because past surface salinity and $\delta^{18}\text{O}$ distributions can not be measured directly, previous studies on the salinity- $\delta^{18}\text{O}$ relationships are based on model simulations (Wadley et al., 2002; Roche et al., 2004). However, there is no agreement on the characteristics of the salinity- $\delta^{18}\text{O}$ relation during the LGM. Our simulation shows that there is no drastic change in this relationship from present day, which confirms the results of Roche et al. (2004). This outcome may also support the application of present day salinity- $\delta^{18}\text{O}$ relation in paleo-reconstructions, especially in extra-tropical oceans. However, the surface salinity restoring in the ocean stand alone model can introduce unphysical freshwater fluxes creating uncertainties in the salinity- $\delta^{18}\text{O}$ relation. Such aberrations can be overcome by using a coupled atmosphere-ocean

model.

Chapter 6

$\delta^{18}\text{O}$ composition reconstruction in the biogenic carbonate

After successful implementation of water isotope into the oceanic simulations as described and discussed in the previous chapters, in this chapter we present the simulations of oxygen isotope composition in foraminiferal calcite ($\delta^{18}\text{O}_c$). Three methods are used to calculate the oxygen isotope composition in the shells of planktic foraminifera. The first $\delta^{18}\text{O}_c$ simulation is based on the model results of Chapter 5, the simulated SST and marine oxygen isotope composition ($\delta^{18}\text{O}_w$) are used in the empirical paleo-temperature equation to simulate the sea surface $\delta^{18}\text{O}_c$ under different climate conditions. In the second method, in addition to SST and oceanic $\delta^{18}\text{O}_w$ composition, the seawater carbon chemistry influence on the oxygen isotope partitioning in foraminifera is included. Apart from SST, oceanic $\delta^{18}\text{O}_w$, and seawater carbonate chemistry effects, the modification of the ambient carbonate chemistry by the life processes of foraminifera ('vital effect') are included in the third method. Finally, the $\delta^{18}\text{O}_c$ compositions simulated by these three methods are evaluated by comparing them with the observational data.

6.1 Experiment setup

The oceanic simulation setups are same as the PD and LGM experiment in Chapter 5. In addition, the HAMOCC (Six and Maier-Reimer, 1996) is switched on in the MPI-OM simulation, with the prescribed LGM and present day CO_2 concentration of 185ppm and 278ppm. The required monthly mean dust deposition fluxes for the HAMOCC are obtained from a 9 years simulation of the dust cycle model (Werner et al., 2002).

Following the expression in Zeebe (2007), the overall oxygen isotope fractionation between the sum of DIC and seawater is calculated from the carbonate species ($[\text{CO}_2]$, $[\text{HCO}_3^-]$, and $[\text{CO}_3^{2-}]$) composition in seawater and the individual fractionation factor between them and water. These individual fractionation factors are

temperature-dependent, and are deduced from the measurements in fresh water (Beck et al., 2005).

The FORAM model is a species-based diffusion-reaction model, it needs prescribed vital effects for different planktic foraminifers. In our experiments, we select *Globigerinoides sacculifer* as the simulated species, and only consider two sizes (400 μ m, 800 μ m) for simplicity. This specie has a tropical to temperate distribution, and its salinity and temperature limits are 24 - 47 and 14° - 31°C, respectively. The C fluxes during life processes applied in the model are from the lab measurements (Table 6.1). These fluxes are obtained either in dark or light conditions. The values are not exactly representative of real conditions, but they can provide a range of the carbonate system conditions in the microenvironment of living planktic foraminifera.

Species	Calcification rate (nmol C h ⁻¹)	Respiration rate (nmol C h ⁻¹)	Photosynthesis rate (nmol C h ⁻¹)
<i>G. sacculifer</i> – dark	0.4	2.7	0
<i>G. sacculifer</i> – light	3.25	3.0	12.7

Table 6.1 Measured C fluxes during the life processes of planktic foraminifers *G. sacculifer* (Erez, 1983; Anderson and Faber, 1984; Jørgensen et al., 1985).

6.2 Dust conditions in LGM and present day simulation

Monthly mean dust deposition at the ocean surface is needed to drive the biogeochemical model HAMOCC. It is used to calculate dissolved iron in the surface layer defined by a fixed weight percentage of iron and a constant solubility. According to marine, terrestrial and ice-core records, the dust cycle during LGM is different from present day (Kohfeld and Harrison, 2001). It is characterized as a relatively more active dust cycle, which has greater mineral dust deposition than the present day cycle (Kohfeld and Harrison, 2001). The LGM and present day dust deposition rates applied in our simulations are presented in Figure 6.1.

In the present day simulation, the largest dust deposition fluxes are close to source

regions in the Sahara, Asia and Australia (Figure 6.1a). The Asian dust is transported eastwards into the Pacific, while the Saharan dust is mainly transported over the tropical Atlantic. Most of the Australian dust is carried northwestwards into the Indian Ocean, while small amounts spread in the opposite direction and reach New Zealand.

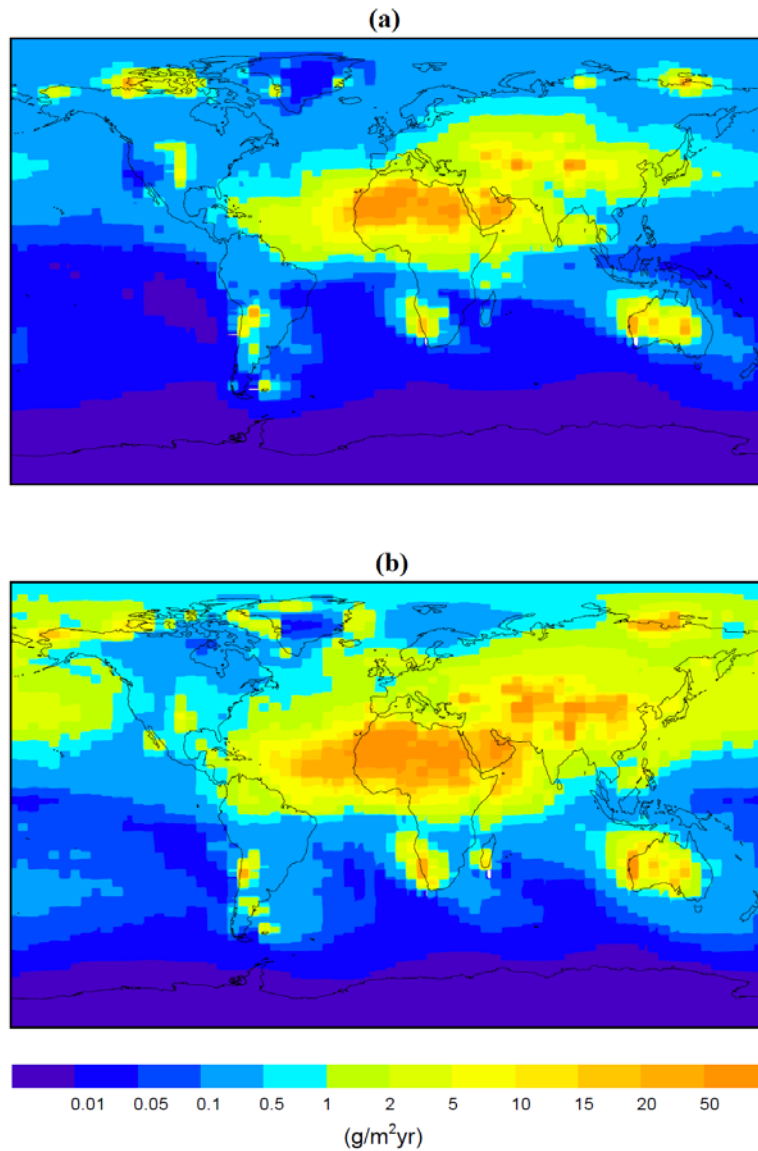


Figure 6.1 Simulated annual mean dust deposition fluxes for (a) present day climate and (b) LGM climate by the dust cycle model (Werner et al., 2002). These fluxes are used as input of the HAMOCC simulation.

Under the LGM climate, the dust deposition rates are around 2 times higher than present day (Figure 6.1b). There are large increases in deposition fluxes over Asia,

which are consistent with the increased emissions from these regions. Due to the stronger wind, the eastward transport of the Asian dust is enhanced, which makes a much higher dust deposition over the North Pacific Ocean. In addition, increased dust depositions are also simulated downwind of other source regions.

6.3 Observational data

For the late Holocene, a global planktonic foraminifera oxygen isotope dataset has been assembled within the MARGO project (Waelbroeck et al., 2005). Assuming that late Holocene and present-day conditions of the ocean are very similar, we will use these data (Figure 6.2) to evaluate our PD $\delta^{18}\text{O}_c$ simulation. The dataset is composed of over 2100 data from recent sediments with thorough age control that has been checked for internal consistency.

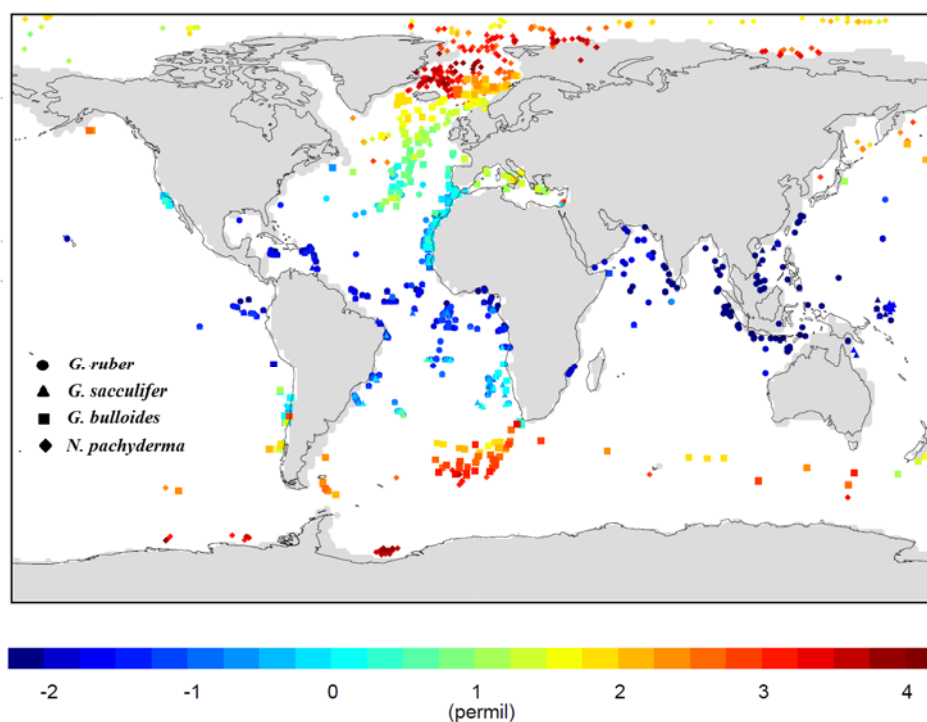


Figure 6.2 MARGO planktonic $\delta^{18}\text{O}_c$ late Holocene (LH) and core top (CT) data for four different species.

The LGM observational data is obtained from the reconstructions based on the glacial sediments in past decades. The details of the oxygen isotope data are listed in the

following Tables.

Core no.	Latitude	Longitude	Water depth(m)	$\delta^{18}\text{O}_{\text{PDB}}$	reference
DGKS9603	28.15	127.27	1100	-0.88	Li et al. (2001)
EN32-PC6	26.95	-91.35	2280	-0.15	Leventer et al. (1982)
GC 4	-12.17	121.56	2069	-1.36	Müller and Opdyke (2000)
GC 5	-12.22	122.12	1462	-1.38	Müller and Opdyke (2000)
GeoB1008-3	-6.58	10.32	3124	-0.23	Schneider et al. (1995)
GeoB1016-3	-11.77	11.68	3411	-0.31	Schneider et al. (1995)
GeoB1028-5	-20.10	9.19	2209	1.27	Schneider et al. (1995)
GeoB1031-4	-21.88	7.10	3105	0.82	Wefer et al. (1996)
GeoB1032-3	-22.92	6.04	2505	0.89	Wefer et al. (1996)
GeoB1105-4	-1.67	-12.43	3225	-0.06	Hale and Pflaumann (1999)
GeoB1112-4	-5.78	-10.75	3125	-0.34	Wefer et al. (1996)
GeoB1220-1	-24.03	5.31	2265	0.66	Wefer et al. (1996)
GeoB1417-1	-15.54	-12.71	2845	0.13	Meinecke (1992)
GeoB1701-4	1.95	3.55	4162	-0.13	Hale and Pflaumann (1999)
GeoB3104-1	-3.67	-37.72	767	-0.25	Arz et al. (1998)
GeoB3117-1	-4.30	-37.09	800	-0.31	Arz et al. (1999)
GeoB3176-1	-7.01	-34.44	1385	-0.12	Arz et al. (1999)
GIK12328-5	21.15	-18.57	2798	1.02	Sarnthein et al. (1994)
GIK16017-2	21.25	-17.80	812	0.12	Sarnthein et al. (1994)
GIK16415-1	9.57	-19.11	3841	0.46	Sarnthein et al. (1994)
GIK16458-2	5.34	-22.06	3518	-0.52	Sarnthein et al. (1994)
GIK16867-2	-2.20	5.10	3891	-0.3	Sarnthein et al. (1994)
GIK17939-2	19.97	117.46	2474	-1.05	Wang et al. (1999)
GIK17940-2	20.12	117.38	1727	-1.18	Wang et al. (1999)
KNR31 GPC-5	33.69	-57.62	4583	0.67	Keigwin and Jones (1989b)
M12-309	26.50	-15.06	2820	1.45	Zahn (1986)
M12-328	21.08	-18.34	2778	0.84	Zahn (1986)
M12-347	15.50	-17.52	2576	1.16	Zahn (1986)
M12-379	23.08	-17.44	2136	1.25	Zahn (1986)
M13-289	18.04	-18.01	2490	0.99	Zahn (1986)
M15-637	27.00	-18.59	3849	1.51	Zahn (1986)
M15-672	34.51	-8.07	2455	1.85	Zahn (1986)
M16-004	29.58	-10.38	1512	1.81	Zahn (1986)
M16-006	29.14	-11.29	796	1.84	Zahn (1986)
M16-030	21.14	-18.03	1500	0.49	Zahn (1986)
M35003-4	12.09	-61.24	1299	-0.38	Rühlemann et al. (1999)
MD76-125	8.35	75.20	1877	-0.78	Sirocko (1989)
MD76-131	15.32	72.34	1230	-0.37	Duplessy (1982)

MD76-135	14.27	50.31	1895	-0.20	Sirocko (1989)
MD77-169	10.13	95.03	2360	-1.13	Duplessy (1982)
MD77-171	11.46	94.09	1760	-1.16	Duplessy (1982)
MD77-194	10.28	75.14	1222	-0.80	Sirocko (1989)
MD77-202	19.13	60.41	2427	-0.07	Sirocko (1989)
MD77-203	20.42	59.34	2442	0.02	Sirocko (1989)
MD79-254	-17.88	38.67	1934	-0.68	Van Campo (1990)
MD90-963	5.04	73.53	2446	-0.83	Bassinot (1994)
MD97-2141	8.80	121.30	3633	-1.60	Dannenmann et al. (2003)
MD98-2162	-4.69	117.90	1855	-1.51	Visser et al. (2003)
MD98-2181	6.30	125.83	2114	-0.93	Stott et al. (2002)
ODP124-769A	8.79	121.29	3656	-1.81	Linsley and Thunell (1990)
ODP 806B	0.32	159.38	2520	-1.30	Lea et al. 2000
PC17	21.36	-158.19	503	-0.82	Lee et al. 2001
PC20	21.34	-158.17	640	-1.20	Lee et al. 2001
RC8-102	-1.42	-86.85	2180	-0.45	Koutavas and Lynch-Stieglitz (2003)
RC11-238	-1.52	-85.82	2573	-0.29	Koutavas and Lynch-Stieglitz (2003)
RC13-140	2.87	-87.75	2246	-0.96	Koutavas and Lynch-Stieglitz (2003)
TR163-19	2.26	-90.95	2348	-0.66	Lea et al. 2000
V19-27	-0.47	-82.00	1373	-0.67	Koutavas and Lynch-Stieglitz (2003)
V19-28	-2.37	-84.65	2720	-0.27	Koutavas and Lynch-Stieglitz (2003)
V21-40	-5.52	-106.77	3182	-0.48	Koutavas and Lynch-Stieglitz (2003)

Table 6.2 Cores used for studies of the LGM oxygen isotope ratios in *G. ruber*.

Core no.	Latitude	Longitude	Water depth(m)	$\delta^{18}\text{O}_{\text{PDB}}$	reference
EN66-10	6.65	-21.90	3527	0.16	Mix and Ruddiman (1985b)
ERDC-92	-2.23	157.00	1598	-0.41	Palmer and Pearson (2003)
GeoB1041-3	-3.48	-7.60	4033	0.61	Wolff (1998)
GeoB1105-4	-1.67	-12.43	3225	0.53	Wolff (1998)
GeoB1112-4	-5.78	-10.75	3125	0.48	Meinecke (1992)
GeoB1501-4	-3.68	-32.01	4257	0.27	Dürkoop et al. (1997)
GeoB1503-1	2.31	-30.65	2306	-0.10	Dürkoop et al. (1997)
GeoB1508-4	5.33	-34.03	3682	0.32	Dürkoop et al. (1997)
GeoB1515-1	4.24	43.67	3129	0.10	Rühlemann et al. (1996)

GeoB1523-1	3.83	-41.62	3292	0.50	Mulitza et al. (1998)
GeoB1701-4	1.95	3.55	4162	0.52	Dürkoop et al. (1997)
GeoB2109-1	-27.91	-45.88	2504	0.53	Dürkoop et al. (1997)
GeoB2117-1	-23.04	-36.65	4045	0.47	Dürkoop et al. (1997)
GeoB2125-1	-20.82	-39.86	1503	0.64	Dürkoop et al. (1997)
GeoB2202-4	-8.20	-34.27	1156	-0.05	Dürkoop et al. (1997)
GeoB2204-2	-8.53	-34.02	2072	0.11	Dürkoop et al. (1997)
GeoB2215-10	0.01	-23.50	3711	0.57	Wolff (1998)
GeoB3104-1	-3.67	-37.72	767	0.20	Arz et al. (1998)
GeoB3117-1	-4.30	-37.09	800	0.32	Arz et al. (1999)
GeoB3176-1	-7.01	-34.44	1385	0.18	Arz et al. (1999)
GIK13521-1	3.02	-22.03	4504	0.26	Sarnthein et al. (1994)
GIK16457-1	5.39	-21.72	3291	0.48	Sarnthein et al. (1994)
GIK16458-1	5.34	-22.05	3518	0.59	Sarnthein et al. (1994)
GIK16458-2	5.34	-22.06	3518	0.65	Sarnthein et al. (1994)
GIK16772-2	-1.35	-11.96	3912	0.75	Sarnthein et al. (1994)
MD98-2181	6.30	125.83	2114	-0.63	Stott et al. (2002)
ODP130-805C	1.23	160.53	3188	-1.10	Berger et al. (1993)
RC8-102	-1.42	-86.85	2180	-0.29	Koutavas and Lynch-Stieglitz (2003)
RC10-131	-14.53	157.97	2933	-0.32	Anderson et al. (1989)
RC11-238	-1.52	-85.82	2573	-0.09	Koutavas and Lynch-Stieglitz (2003)
RC12-109	-25.88	157.87	2930	0.08	Anderson et al. (1989)
RC12-113	-24.88	163.52	2454	0.20	Anderson et al. (1989)
RC13-140	2.87	-87.75	2246	-0.50	Koutavas and Lynch-Stieglitz (2003)
V15-168	0.20	-39.90	4219	0.26	Mix and Ruddiman (1985b)
V19-27	-0.47	-82.00	1373	-0.35	Koutavas and Lynch-Stieglitz (2003)
V19-28	-2.37	-84.65	2720	-0.21	Koutavas and Lynch-Stieglitz (2003)
V21-29	-1.00	-89.35	712	-0.49	Koutavas and Lynch-Stieglitz (2003)
V21-30	-1.22	-89.68	617	-0.32	Koutavas and Lynch-Stieglitz (2003)
V21-40	-5.52	-106.77	3182	-0.13	Koutavas and Lynch-Stieglitz (2003)
V22-38	-9.55	-34.25	3797	0.10	Mix and Ruddiman (1985b)
V22-177	-7.75	-14.62	3290	0.25	Mix and Ruddiman (1985b)
V22-182	-0.55	-17.27	3776	0.40	Mix and Ruddiman (1985b)
V23-110	17.63	-45.87	3746	-0.34	Mix and Ruddiman (1985b)
V24-157	-14.95	147.92	1212	-0.24	Anderson et al. (1989)

V24-161	-18.20	151.45	1670	-0.19	Anderson et al. (1989)
V24-166	-16.52	150.78	781	-0.52	Anderson et al. (1989)
V24-170	-13.52	146.88	2243	-0.58	Anderson et al. (1989)
V24-184	-12.87	146.2	2992	-0.56	Anderson et al. (1989)
V25-56	-3.55	-35.23	3512	0.04	Mix and Ruddiman (1985b)
V25-59	1.37	-33.48	3824	0.20	Mix and Ruddiman (1985b)
V25-60	3.28	-34.83	3749	-0.03	Mix and Ruddiman (1985b)
V25-75	8.58	-53.17	2743	-0.07	Mix and Ruddiman (1985b)
V29-144	-0.20	6.05	2685	0.10	Mix and Ruddiman (1985b)
V30-36	5.35	-27.32	4245	0.07	Mix and Ruddiman (1985b)
V30-40	-0.20	-23.15	3706	0.34	Mix and Ruddiman (1985b)
V30-49	18.43	-21.08	3093	0.54	Mix and Ruddiman (1985b)

Table 6.3 Cores used for studies of the LGM oxygen isotope ratios in *G. sacculifer*.

Core no.	Latitude	Longitude	Water depth(m)	$\delta^{18}\text{O}_{\text{PDB}}$	reference
6706-2	42.16	124.94	1120	2.79	Ortiz et al. (1997)
DSDP 594	-45.52	174.95	1204	3.70	Nelson et al. (1993)
GeoB1008-3	-6.58	10.32	3124	1.03	Schneider et al. (1995)
GeoB1016-3	-11.77	11.68	3411	0.61	Schneider et al. (1995)
GeoB1028-5	-20.10	9.19	2209	1.33	Schneider et al. (1995)
GIK17045-3	52.43	-16.67	3663	2.94	Sarnthein et al. (1994)
GIK17049-6	55.26	-26.73	3331	2.89	Jung (1996)
GIK17050-1	55.47	-27.89	2795	2.72	Jung (1996)
GIK17051-3	56.16	-31.99	2295	2.77	Jung (1996)
GIK23419-8	54.96	-19.76	1487	2.69	Jung (1996)
K 119	50.42	167.73	2440	2.98	Gorbarenko (1996)
KET80-03	38.49	14.30	1900	3.67	Paterne et al. (1986)
KET80-04	39.40	13.34	2909	3.71	Paterne et al. (1986)
KET80-11	39.10	15.05	2111	3.78	Paterne et al. (1986)
KET80-22	40.35	11.43	2430	3.46	Paterne et al. (1986)
KN708-1	50.00	-23.75	4053	3.09	Ruddiman and McIntyre (1981)
M12-309	26.50	-15.06	2820	1.32	Zahn (1986)
M12-328	21.08	-18.34	2778	1.53	Zahn (1986)
M12-347	15.50	-17.52	2576	1.23	Zahn (1986)
M12-379	23.08	-17.44	2136	1.55	Zahn (1986)
M13-289	18.04	-18.01	2490	1.40	Zahn (1986)
M15-637	27.00	-18.59	3849	1.88	Zahn (1986)
M15-672	34.51	-8.07	2455	2.31	Zahn (1986)
M16-004	29.58	-10.38	1512	1.83	Zahn (1986)

M16-006	29.14	-11.29	796	1.56	Zahn (1986)
M16-030	21.14	-18.03	1500	1.44	Zahn (1986)
MD97-2120	-45.53	174.93	1210	2.06	Pahnke et al. (2003)
ODP167-1014	32.83	-119.98	1166	2.30	Hendy and Kennett (2000)
ODP 893	34.29	-120.04	575	2.80	Hendy and Kennett (1999)
PAR87A-01	54.42	-149.43	3480	2.72	Zahn et al. (1991)
PAR87A-10	54.36	-148.47	3664	2.99	Zahn et al. (1991)
SU81-18	37.77	-10.18	3135	2.09	Duplessy et al. (1992)
SU90-03	40.05	-32.00	2475	2.50	Chapman and Shackleton (1998)
TG7	-17.2	-78.11	3120	0.82	Calvo et al. (2001)
W8709A-01BC	41.54	131.96	3680	2.19	Ortiz et al. (1997)
W8709A-13PC	42.12	125.75	2717	2.97	Ortiz et al. (1997)
W8809A-21GC	42.14	126.91	2799	2.70	Ortiz et al. (1997)
W8809A-29GC	41.80	129.00	3136	2.28	Ortiz et al. (1997)
W8809A-31GC	41.68	130.01	3136	2.67	Ortiz et al. (1997)
W8809A-53GC	42.75	126.26	2408	3.16	Ortiz et al. (1997)
W8809A-57GC	41.58	130.62	3330	2.52	Ortiz et al. (1997)
W8809A-08PC	42.26	127.68	3111	2.81	Ortiz et al. (1997)
W8909A-48GC	41.33	132.67	3670	1.82	Ortiz et al. (1997)

Table 6.4 Cores used for studies of the LGM oxygen isotope ratios in *G. bulloides*.

Core no.	Latitude	Longitude	Water depth(m)	$\delta^{18}\text{O}_{\text{V-PDB}}$	reference
BOFS 5k	50.68	-21.87	3345	4.17	Maslin (1992)
BOFS 8k	52.50	-22.04	4045	4.21	Maslin (1992)
BOFS 14k	58.62	-19.44	1756	3.94	Maslin (1992)
BOFS 16k	59.28	-23.14	2502	4.26	Vogelsang (1990)
BOFS 17k	58.00	-16.50	1150	4.17	Maslin (1992)
CH 67-19	45.75	-3.95	1982	3.57	Labeyrie and Duplessy (1985)
CH 69-12	46.02	-4.69	3642	3.65	Duplessy et al. (1991)
CH 69-32	45.40	-5.18	4777	3.56	Duplessy et al. (1991)
CH 72-101	47.47	-8.56	2428	3.51	Labeyrie and Duplessy (1985)
CH 72-104	46.90	-8.08	4590	3.25	Labeyrie and Duplessy (1985)
CH 73-108	58.08	-10.73	2032	4.18	Duplessy et al. (1991)
CH 73-110	59.50	-8.93	1365	4.00	Weinelt (1993)
CH 73-116	55.75	-14.47	2201	4.18	Keigwin and Boyle (1989a)
CH 73-139	54.63	-16.35	2209	3.99	Bard et al. (1987)
CH 73-141	52.86	-16.52	3489	4.00	Duplessy et al. (1991)
CH 77-07	66.60	-10.52	1487	4.62	Ruddiman and McIntyre (1981)

DSDP 609	50.00	-24.00	3884	4.25	Bond et al. (1993)
E11-2	-56.00	-115.00	3109	3.65	Ninnemann and Charles (1997)
ENAM 93-21	62.74	-4.00	1020	4.48	Rasmussen et al. (1996)
FRAM 1/4	84.50	-8.95	3820	4.41	Zahn et al. (1985)
FRAM 1/7	83.88	-6.96	2990	4.61	Zahn et al. (1985)
GC-11	53.52	178.85	3060	3.54	Gorbarenko (1996)
GC-36	50.42	167.73	3300	3.61	Gorbarenko (1996)
GGC-15	48.61	150.43	1980	3.52	Keigwin (1998)
GIK16396-1	61.87	-11.24	1145	4.07	Sarnthein (1995)
GIK16397-2	61.87	-11.18	1145	4.03	Sarnthein (1995)
GIK17045-3	52.43	-16.67	3663	4.01	Sarnthein et al. (1994)
GIK17049-6	55.26	-26.73	3331	4.36	Jung (1996)
GIK17051-3	56.16	-31.99	2295	4.35	Jung (1996)
GIK17724-2	76.00	8.33	2354	4.62	Weinelt (1993)
GIK17725-2	77.46	4.58	540	4.31	Weinelt (1993)
GIK23056-2	68.50	3.83	2665	4.73	Vogelsang (1990)
GIK23065-2	68.50	0.83	2804	4.72	Vogelsang (1990)
GIK23071-3	67.09	2.91	1308	4.49	Vogelsang (1990)
GIK23074-1	66.67	4.91	1157	4.47	Vogelsang (1990)
GIK23262-3	72.23	14.42	1131	4.23	Weinelt (1993)
GIK23294-4	72.38	-10.59	2215	4.71	Weinelt (1993)
GIK23351-1	70.36	-18.21	1672	4.34	Völker (1999)
GIK23354-6	70.33	-10.63	1747	4.50	Völker (1999)
GIK23415-9	53.18	-19.15	2472	4.30	Weinelt (2003)
GIK23419-8	54.96	-19.76	1487	3.91	Jung (1996)
GIK23519-5	64.80	-29.60	1893	4.55	Millo (2006)
HM 25-09	63.05	4.79	600	4.49	Jansen and Erlenkeuser (1985)
HM 31-33	63.63	4.78	1580	4.44	Jansen and Erlenkeuser (1985)
HM 31-36	64.25	0.53	2620	4.75	Jansen and Erlenkeuser (1985)
HM 52-43	64.25	0.73	2781	4.51	Veum et al. (1992)
HM 57-07	68.25	-13.53	1668	4.48	Sarnthein et al. (1995)
HM 71-12	68.43	-13.87	1547	4.69	Sarnthein et al. (1995)
HM 71-14	69.98	-18.08	1624	4.65	Sarnthein et al. (1995)
HM 71-19	69.48	-9.51	2210	4.81	Vogelsang (1990)
HM 80-30	71.78	1.60	2821	4.57	Sarnthein et al. (1995)
HM 80-42	72.25	-9.23	2416	4.44	Sarnthein et al. (1995)
HM 80-60	68.90	-11.86	1869	4.69	Sarnthein et al. (1995)
HM 94-13	71.63	-1.62	1946	4.66	Sarnthein et al. (1995)
HM 94-18	74.50	5.70	2469	4.58	Sarnthein et al. (1995)
HM 94-25	75.60	1.32	2469	4.68	Sarnthein et al. (1995)
HM 94-34	73.77	-2.54	3004	4.71	Sarnthein et al. (1995)
HM 100-7	61.67	-4.72	1125	4.39	Sarnthein et al. (1995)

HU73-031-7	42.98	-55.25	4055	3.16	Keigwin and Jones (1995)
HU87-033-008	62.65	-53.88	2424	4.42	Hillaire-Marcel et al. (1994)
HU90-013-013	58.21	-48.37	3380	4.60	Hillaire-Marcel et al. (1994)
J 11	40.12	134	1150	1.21	Gorbarenko and Southon (2000)
K 11	71.78	1.60	2900	4.66	Ruddiman and McIntyre (1981)
KN708-1	50.00	-23.75	4053	4.11	Ruddiman and McIntyre (1981)
KN708-6	51.57	-29.57	2469	4.46	Keigwin and Boyle (1989a)
KN714-15	58.77	-25.78	2598	4.23	Keigwin and Boyle (1989a)
M 17045	52.43	-16.65	3663	4.01	Winn et al (1991)
M 17048	54.30	-18.16	1859	4.02	Sarnthein et al. (1995)
M 17049	55.28	-26.73	3331	4.29	Jung (1996)
M 17051	56.17	-31.98	2300	4.34	Jung (1996)
M 17701	68.53	11.68	1421	4.34	Sarnthein et al. (1995)
M 17719	72.15	12.57	1823	4.46	Sarnthein et al. (1995)
M 17724	76.00	8.33	2354	4.63	Weinelt (1993)
M 17725	77.47	4.58	2580	4.41	Weinelt et al. (1996)
M 17728	76.52	3.95	2485	4.69	Sarnthein et al. (1995)
M 17730	72.05	7.31	2769	4.60	Weinelt (1993)
M 17732	71.62	4.23	3103	4.75	Sarnthein et al. (1995)
M 23041	68.68	0.22	2258	4.70	Sarnthein et al. (1995)
M 23043	70.27	-3.35	2133	4.56	Sarnthein et al. (1995)
M 23055	68.42	4.10	2311	4.76	Vogelsang (1990)
M 23056	68.50	3.83	2665	4.68	Weinelt et al. (1996)
M 23057	68.40	3.31	3157	4.70	Sarnthein et al. (1995)
M 23059	70.30	-3.12	2283	4.72	Vogelsang (1990)
M 23062	68.73	0.16	2244	4.73	Vogelsang (1990)
M 23063	68.75	0.00	2299	4.76	Vogelsang (1990)
M 23064	68.67	0.33	2571	4.66	Sarnthein et al. (1995)
M 23065	68.50	0.81	2804	4.72	Vogelsang (1990)
M 23068	67.83	1.50	2230	4.74	Vogelsang (1990)
M 23071	67.08	2.93	1308	4.73	Vogelsang (1990)
M 23074	66.67	4.92	1157	4.62	Vogelsang (1990)
M 23254	73.12	9.63	2273	4.70	Sarnthein et al. (1995)
M 23256	73.18	10.95	2061	4.73	Sarnthein et al. (1995)
M 23258	75.00	13.98	1768	4.52	Sarnthein et al. (1995)
M 23259	72.03	9.25	2518	4.68	Weinelt (1993)
M 23260	72.13	11.46	2089	4.71	Weinelt (1993)
M 23261	72.17	13.11	1628	4.60	Weinelt (1993)
M 23262	72.23	14.43	1130	4.33	Weinelt (1993)
M 23269	71.45	0.68	2872	4.83	Weinelt (1993)

M 23294	72.37	-10.59	2224	4.71	Weinelt (1993)
M 23323	67.77	5.93	1286	4.42	Sarnthein et al. (1995)
M 23351	70.36	-18.21	1672	4.40	Völker (1999)
M 23354	70.33	-10.63	1747	4.50	Völker (1999)
M 23415	53.17	-19.20	2472	4.13	Jung (1996)
M 23419	54.97	-19.74	1491	3.96	Jung (1996)
M 23519	64.80	-29.60	1893	4.53	Hohnemann (1996)
MD80-304	-51.04	67.44	1930	4.47	Labeyrie and Duplessy (1985)
MD84-527	-43.49	51.19	3262	3.48	Pichon et al. (1992)
MD88-769	-46.07	90.11	3420	3.35	Rosenthal et al. (1995)
MD2010	66.68	4.56	1226	4.61	Dokken and Jansen (1999)
MD2011	66.97	7.64	1048	4.42	Dreger (1999)
MD2012	72.15	11.43	2094	4.58	Dreger (1999)
MD2284	62.37	-0.98	1500	4.34	Jansen and Meland (2001)
MG 123	79.27	0.81	3050	4.65	Morris (1988)
NA 87-22	55.50	-14.57	2161	4.06	Duplessy et al. (1992)
NO 77-14	62.45	-20.42	1531	4.65	Duplessy et al. (1991)
NO 79-06	54.52	-36.89	2734	4.45	Labeyrie and Duplessy (1985)
NO 79-25	46.98	-27.28	2826	4.10	Duplessy et al. (1992)
NP 90-12	78.41	9.42	628	4.65	Dokken (1995)
NP 90-36	77.62	9.94	1360	4.60	Dokken (1995)
NP90-39	77.26	9.90	2119	4.48	Dokken (1995)
OD 41:4:1	84.03	11.24	3344	4.76	Nørgaard-Pedersen et al. (2003)
ODP 883	51.20	167.77	2385	3.69	Kiefer et al. (2001)
ODP 893	34.29	-120.04	575	2.56	Hendy and Kennett (1999)
ODP 980	55.48	-14.70	2179	4.10	McManus et al. (1999)
PAR87A-01	54.42	-149.43	3480	3.37	Zahn et al. (1991)
PAR87A-10	54.36	-148.47	3664	3.18	Zahn et al. (1991)
PS 1171	68.20	-18.07	935	4.49	Lackschewitz et al. (1994)
PS 1230	78.86	-4.78	1235	4.28	Nørgaard-Pedersen et al. (2003)
PS 1294	78.00	5.37	2668	4.75	Hebbeln and Wefer (1997)
PS 1295	78.00	2.43	3112	4.63	Jones and Keigwin (1989)
PS 1308	80.02	-4.83	1444	3.95	Nørgaard-Pedersen et al. (2003)
PS 1314	80.00	4.50	1382	4.22	Nørgaard-Pedersen et al. (2003)
PS 1388-3	-68.03	-5.92	2526	4.79	Mackensen et al. (1989)
PS 1390-3	-69.63	-6.43	2726	4.62	Grobe and Mackensen (1992)
PS 1394-4	-70.10	-6.85	1700	4.60	Grobe and Mackensen (1992)
PS 1431-1	-69.82	-6.59	2457	4.08	Grobe and Mackensen (1992)
PS 1481-3	-70.84	-13.93	2505	4.72	Grobe and Mackensen (1992)

PS 1498-2	-73.49	-35.51	2818	4.80	Melles (1991)
PS 1533	82.03	15.18	2030	4.60	Köhler (1992)
PS 1535	78.75	1.85	2557	4.60	Köhler (1992)
PS 1591-1	-70.83	-14.55	2361	5.19	Grobe et al. (1990)
PS 1606-3	-73.50	-34.03	2943	4.65	Melles (1991)
PS 1613-4	-74.24	-36.69	1542	4.97	Melles (1991)
PS 1648-1	-69.74	-6.52	2519	4.71	Grobe and Mackensen (1992)
PS 1730	70.12	-17.7	1617	4.29	Stein et al. (1996)
PS 1894	75.81	-8.30	1975	4.39	Nørgaard-Pedersen et al. (2003)
PS 1919	75.00	-11.90	1876	4.39	Stein et al. (1996)
PS 1922	75.00	-8.77	3350	4.40	Stein et al. (1996)
PS 1927	71.50	-17.12	1734	4.35	Stein et al. (1996)
PS 1951	68.84	-20.82	1481	4.48	Stein et al. (1996)
PS 2122	80.39	7.55	705	4.20	Knies (1994)
PS 2123	80.17	9.86	571	4.43	Knies (1994)
PS 2129	81.37	17.47	861	4.68	Knies (1994)
PS 2206	84.28	-2.51	2993	4.60	Stein et al. (1994)
PS 2208	83.64	4.60	3681	4.60	Stein et al. (1994)
PS 2210	83.04	10.70	3702	4.65	Stein et al. (1994)
PS 2212	82.07	15.85	2550	4.26	Vogt (1997)
PS 2423	80.04	-5.45	829	3.80	Notholt (1998)
PS 2424	80.04	-5.74	445	4.20	Notholt (1998)
PS 2613	74.18	-0.48	3259	4.71	Völker (1999)
PS 2644	67.87	-21.77	778	4.50	Völker (1999)
PS 2837	81.23	2.38	1023	4.72	Nørgaard-Pedersen et al. (2003)
PS 2876	81.91	-9.43	1976	4.55	Nørgaard-Pedersen et al. (2003)
PS 2887	79.60	-4.61	1411	3.33	Nørgaard-Pedersen et al. (2003)
PS 16396	61.87	-11.25	1145	4.08	Sarnthein et al. (1995)
PS 16397	61.87	-11.18	1145	4.00	Sarnthein et al. (1995)
PS 21291	78.00	8.70	2400	4.54	Weinelt (1993)
PS 21736	74.33	-5.17	3460	4.65	Jünger (1993)
PS 21842	69.45	-16.52	982	4.44	Sarnthein et al. (1995)
PS 21900	74.53	-2.32	3538	4.45	Jünger (1993)
PS 21906	76.93	-2.15	2990	4.25	Nørgaard-Pedersen et al. (2003)
PS 21910	75.62	1.32	2454	4.50	Weinelt (1993)
PS 23199	68.38	5.24	1968	4.76	Vogelsang (1990)
PS 23205	67.62	5.76	1411	4.62	Vogelsang (1990)
PS 23243	69.38	-6.54	2715	4.71	Vogelsang (1990)

PS 23246	69.40	-12.86	1858	4.58	Vogelsang (1990)
RC 9-225	54.89	-15.40	2334	3.99	Keigwin and Boyle (1989a)
SO 82-5	59.18	-30.90	1416	4.43	van Kreveld et al. (2000)
SU 90-32	61.78	-22.42	2200	3.98	Sarnthein et al. (1995)
SU 90-33	60.57	-22.08	2370	4.22	Cortijo et al. (1997)
SU 90-39	52.57	-21.93	2900	4.25	Cortijo (1995)
SU 90-106	59.98	-39.45	1615	4.40	Weinelt et al. (1996)
SU 90-107	63.08	-28.08	1625	4.17	Sarnthein et al. (1995)
V 23-23	56.80	-44.55	3292	4.34	Mix and Fairbanks (1985a)
V 23-42	62.18	-27.92	1514	4.52	Keigwin and Boyle (1989a)
V 23-81	54.03	-16.14	2393	3.82	Jansen and Veum (1990)
V 23-82	52.59	-21.93	3974	4.34	Keigwin and Boyle (1989a)
V 23-83	49.87	-24.26	3971	4.31	Keigwin and Boyle (1989a)
V 27-17	50.08	-37.31	4054	4.42	Keigwin and Boyle (1989a)
V 27-19	52.10	-38.79	3466	4.46	Keigwin and Boyle (1989a)
V 27-60	72.17	8.58	2525	4.72	Labeyrie and Duplessy (1985)
V 27-86	66.60	1.12	2900	4.72	Labeyrie and Duplessy (1985)
V 27-114	55.05	-33.07	2532	4.42	Keigwin and Boyle (1989a)
V 27-116	52.83	-30.33	3202	4.52	Keigwin and Boyle (1989a)
V 28-14	64.78	-29.58	1855	4.60	Shackleton (1974)
V 28-38	69.38	-4.40	3411	4.82	Keigwin and Boyle (1989a)
V 28-56	68.03	-6.12	2941	4.67	Kellogg et al. (1978)
V 29-180	45.30	-23.87	3049	3.80	Keigwin and Boyle (1989a)
V 29-183	49.14	-25.50	3629	4.10	Keigwin and Boyle (1989)
V 29-206	64.90	-29.28	1624	4.37	Keigwin and Boyle (1989)
V 30-108	56.10	-32.50	3171	4.52	Keigwin and Boyle (1989)
V 30-164	69.83	8.97	2901	4.83	Duplessy et al. (1991)
V 34-90	48.80	150.50	1984	3.30	Gorbarenko et al. (2002)
V 34-98	50.10	153.20	1984	3.62	Gorbarenko et al. (2002)
Vino GGC-17	53.71	165.01	3960	3.80	Keigwin (1998)
Vino GGC-37	50.42	167.73	3300	3.46	Keigwin (1998)

Table 6.5 Cores used for studies of the LGM oxygen isotope ratios in *N. pachyderma*.

6.4 Results: Implications for $\delta^{18}\text{O}$ of the foraminiferal carbonates

Planktonic foraminifera mainly reflect the upper ocean conditions, and have application in the surface ocean reconstruction. Our analyses of results, therefore, mainly focus on sea surface. After running the MPIOM-HAMOCC for 2000 years into a quasi-steady state in the upper ocean, the mean state of the last 100 simulation years is used in the analyses.

6.4.1 $\delta^{18}\text{O}_c$ reconstruction by $\delta^{18}\text{O}_w$ and SST

Using the SST and $\delta^{18}\text{O}_w$ values from the PD and LGM simulation, we simulate the zonal mean sea surface $\delta^{18}\text{O}_c$ at present day and LGM (Figure 6.3) by applying the following empirical ‘paleo-temperature’ equation (Shackleton, 1974):

$$\delta^{18}\text{O}_c = 21.9 + \delta^{18}\text{O}_w - \sqrt{310.61 + 10 * T}$$

where T is in °C.

In Figure 6.3a, the modelled $\delta^{18}\text{O}_c$ at the ocean surface and the bottom of the euphotic zone at approx. 100m (equal to the 8th model layer in MPI-OM) in the present day simulation are compared with a recent compilation of late Holocene $\delta^{18}\text{O}_c$ data from different foraminifera species (Waelbroeck et al., 2005). The modelled annual zonal mean $\delta^{18}\text{O}_c$ values ranges from -4‰ to 4‰ in the upper ocean with low values at tropical to subtropical latitudes and high values at high latitudes. In general, the simulated $\delta^{18}\text{O}_c$ values from the PD simulation resemble the measured $\delta^{18}\text{O}_c$ distribution. Considering the longitudinal variability in modelled surface $\delta^{18}\text{O}_c$, most late Holocene data lie within the spread (shaded area).

For the LGM, the general trend of zonal mean $\delta^{18}\text{O}_c$ mirrors the present day simulation, with $\delta^{18}\text{O}_c$ values increasing towards high latitudes. The simulated $\delta^{18}\text{O}_c$ values vary between -2‰ and +6‰ (with the global ice sheet effect of +1‰ included). But an abrupt decrease occurs around 60°N in the LGM simulation, which is absent in the PD experiment. In general, the LGM $\delta^{18}\text{O}_c$ values are higher than the present-day ones, indicating a colder climate during LGM. The simulation results are comparable with the observational data from LGM sediment cores, especially in tropical to subtropical areas. Most data are within the range of $\delta^{18}\text{O}_c$ estimated by the model (shaded area). The largest model-data difference is located in high northern latitudes, where the simulated abrupt LGM $\delta^{18}\text{O}_c$ depletion is absent from the observations.

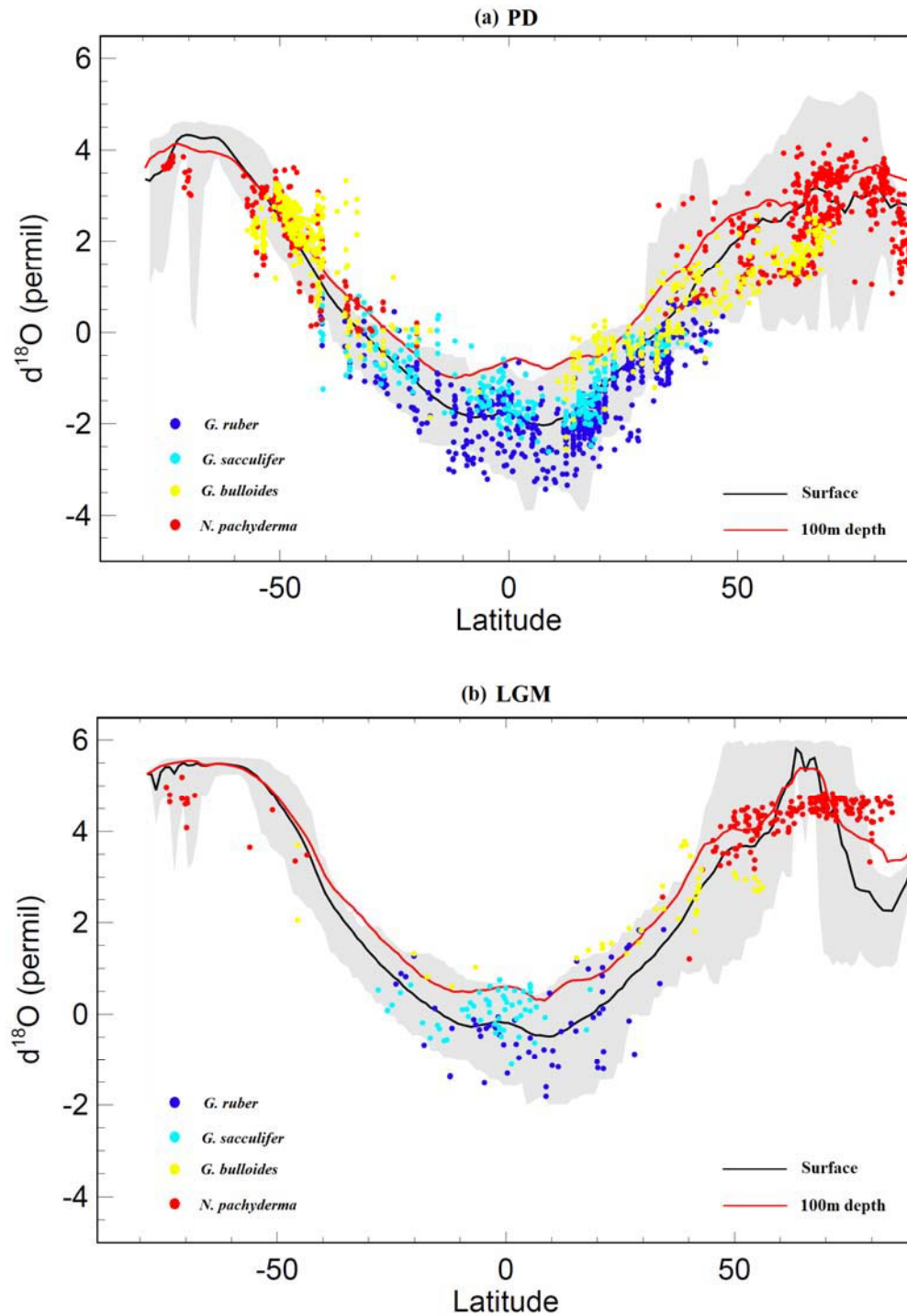


Figure 6.3 Simulated zonal mean $\delta^{18}\text{O}_c$ for the ocean surface (0 – 10m, black line) and bottom of the euphotic zone (~100m, red line) in the PD and LGM simulations. The range of longitudinal variations in $\delta^{18}\text{O}_c$ at the ocean surface is presented as grey shading. The equation used to calculate these lines and shading is taken from Shackleton (1974). The dots indicate observational $\delta^{18}\text{O}_c$ data in the corresponding time period.

In order to examine the model simulation in more detail, a cell-by-cell comparison between observations and model results is made. All observations within a specific grid cell are averaged and compared with the corresponding MPIOM-wiso result. Figure 6.4 shows the comparison for different planktic foraminifera species for the PD simulation. Most of the results scatter around the 1:1 lines, with a slight upper shift for all species. The correlation (*G. ruber*: 0.91, *G. sacculifer*: 0.82, *G. bulloides*: 0.84, *N. pachyderma*: 0.67) and normalized root mean square errors NRMSE (*G. ruber*: 14.0%, *G. sacculifer*: 15.7%, *G. bulloides*: 15.4%, *N. pachyderma*: 22.0%) between model results and observations indicate a good and significant agreement between them. Except *N. pachyderma* ($r = 0.77$ at 100m depth), other species exhibit a higher correlation between model and observation at the surface layer than the 100m depth.

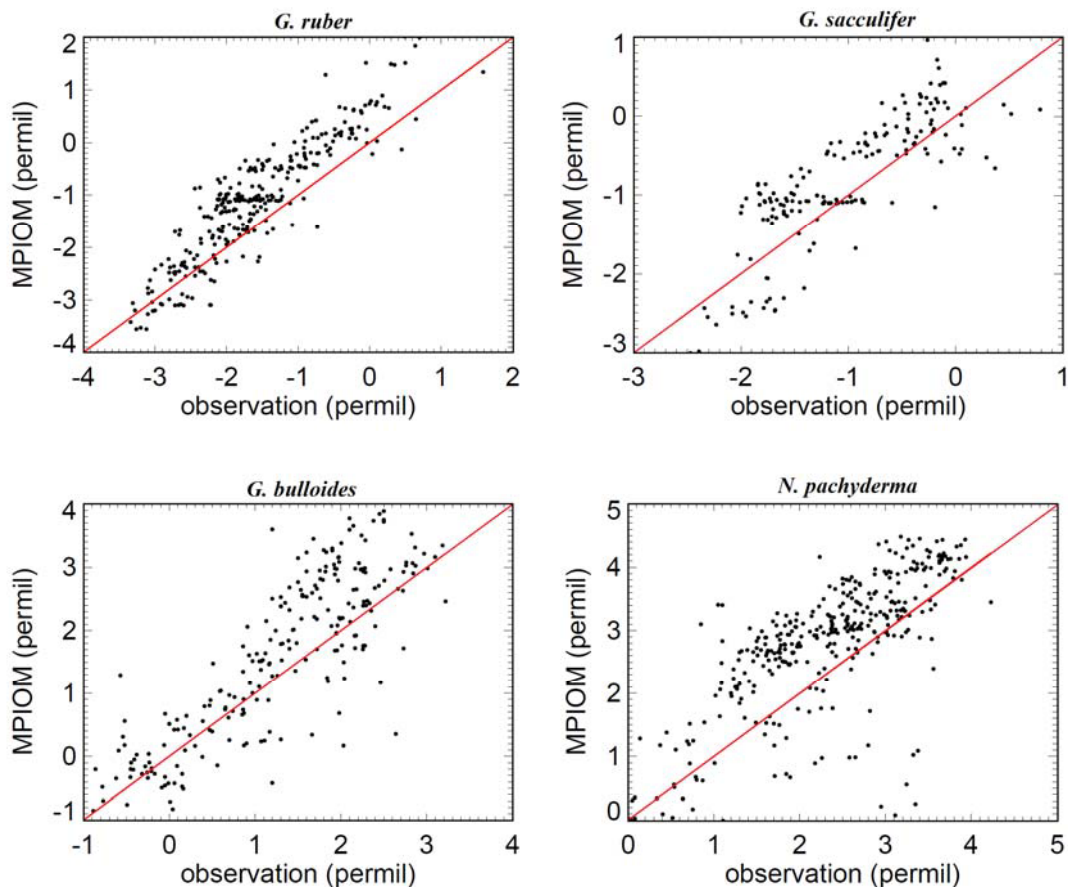


Figure 6.4 Comparison of observed $\delta^{18}O_c$ (averaged onto the MPIOM model grid) versus modelled surface $\delta^{18}O_c$ values for the present day climate. The 1:1 line is colored in red.

The same analyses are applied to the LGM simulation to test the correspondence between the modeled and observed glacial $\delta^{18}\text{O}_c$ values. As shown in Figure 6.5, the simulated $\delta^{18}\text{O}_c$ values for *G. ruber*, *G. sacculifer*, and *N. pachyderma* are comparable with the observations. They are well correlated with the sediment data (*G. ruber*: 0.89, *G. sacculifer*: 0.75, *N. pachyderma*: 0.71), and the corresponding NRMSE are 17.1%, 22.2%, and 22.1% respectively. For *G. ruber* and *N. pachyderma* most simulated $\delta^{18}\text{O}_c$ values are relatively higher than the observed values. The highest $\delta^{18}\text{O}_c$ values reach up to +6‰ in the simulation for *N. pachyderma*, while the observation range between +3‰ and +5‰. As with the present day simulation, only *N. pachyderma* shows a slightly higher correlation (0.73) at 100m depth. For *G. bulloides* the deviations between observed and modelled $\delta^{18}\text{O}_c$ values show a larger spread with a NRMSE of 39.1% than for the other foraminifera species.

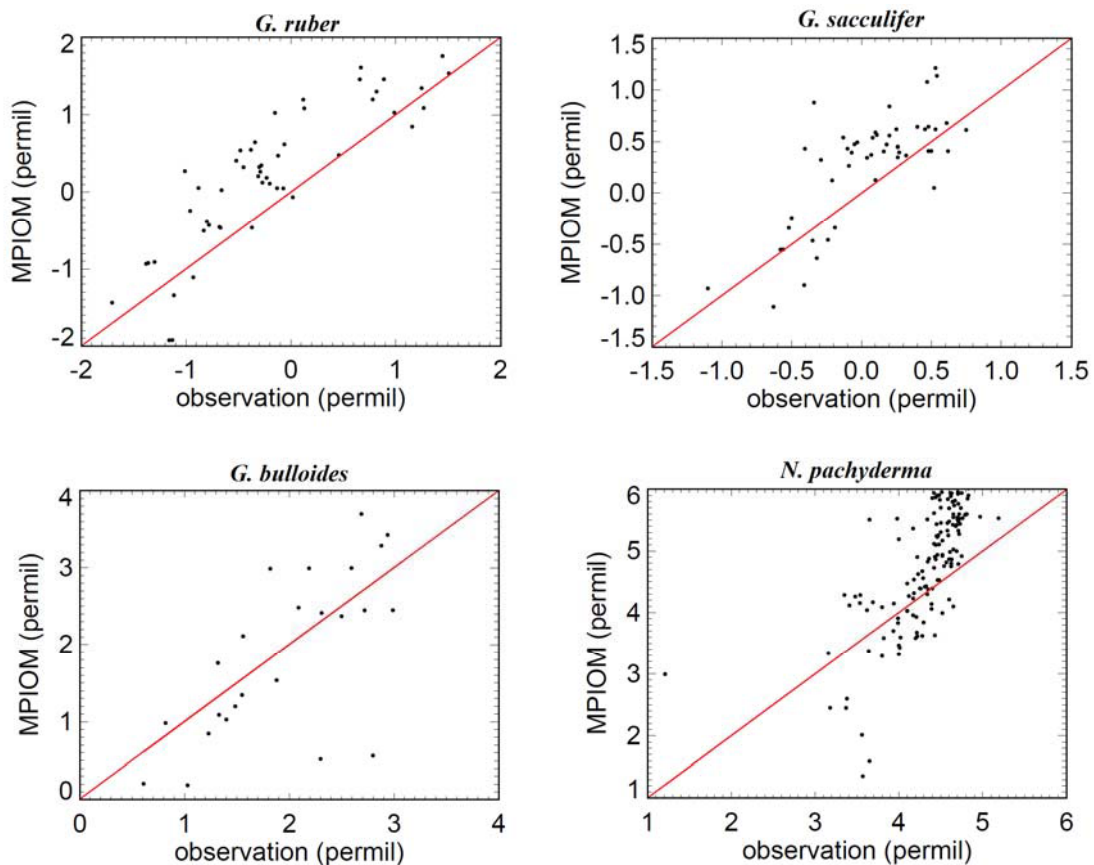


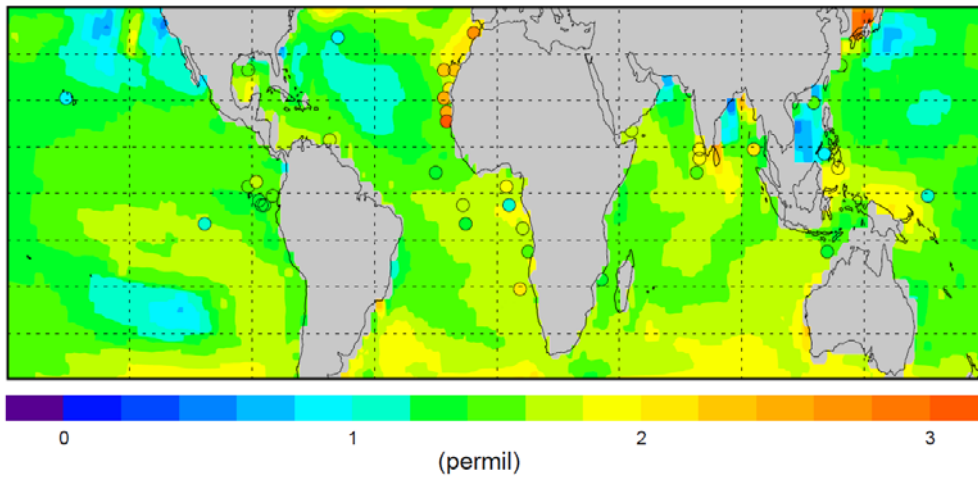
Figure 6.5 Comparison of observed $\delta^{18}\text{O}_c$ (averaged onto the MPIOM model grid) versus modelled surface $\delta^{18}\text{O}_c$ values for the LGM climate. The 1:1 line is colored in red.

Next, we compare the simulated LGM-PD $\delta^{18}\text{O}_c$ differences with the observations. Because the main LGM observations are located in tropical to subtropical regions and the northern North Atlantic, we only show the LGM-PD $\delta^{18}\text{O}_c$ differences between 40°S and 40°N (Figure 6.6), as well as north of 40°N in the North Atlantic (Figure 6.7). *G. ruber*, *G. sacculifer*, and *G. bulloides* are used to evaluate the modelled $\delta^{18}\text{O}_c$ differences between 40°S and 40°N, while *N. pachyderma* $\delta^{18}\text{O}_c$ changes depict the variations north of 40°N in the Atlantic. Again, all $\delta^{18}\text{O}_c$ differences derived from different observations within a specific grid cell are averaged for this comparison.

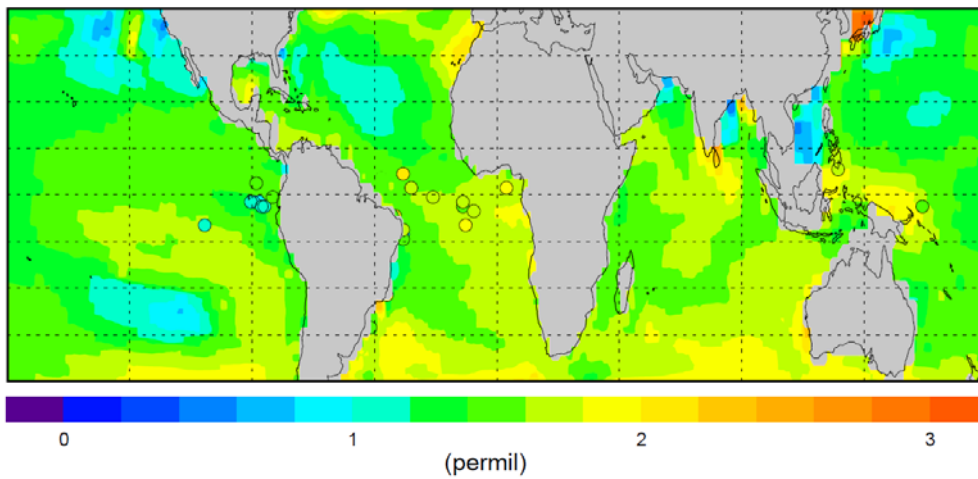
As seen in Figure 6.6, the simulated $\delta^{18}\text{O}_c$ differences between LGM and PD vary from +1‰ to +2‰ in tropical to subtropical ocean (the ice sheet effect is included), and most values fall into the range +1.4‰ to +1.8‰. For all foraminifera species shown in Figure 6.6, our model results agree with the majority of observations, and the slight overestimate of $\delta^{18}\text{O}_c$ in the simulation is less than 0.2‰ in most areas. Distinct disagreement between model results and measurements is seen in the South China Sea, where the observed increase in $\delta^{18}\text{O}_c$ (> 1.4‰) is more pronounced than the simulated changes (< 1‰).

In the northern North Atlantic, the largest glacial increase in $\delta^{18}\text{O}_c$ (> 3‰) occurs at strongly cooled regions as seen in Figure 5.6. The simulated LGM-PD $\delta^{18}\text{O}_c$ differences in most regions agree reasonable well with the observations. Our model simulates a larger increase in $\delta^{18}\text{O}_c$ in the eastern Nordic Sea as compared with the western basin, which is also in agreement with the observations. But the model results show a decrease in $\delta^{18}\text{O}_c$ along the Eastern Greenland Current and north of 80°N, which deviates from the measurements.

G. ruber



G. sacculifer



G. bulloides

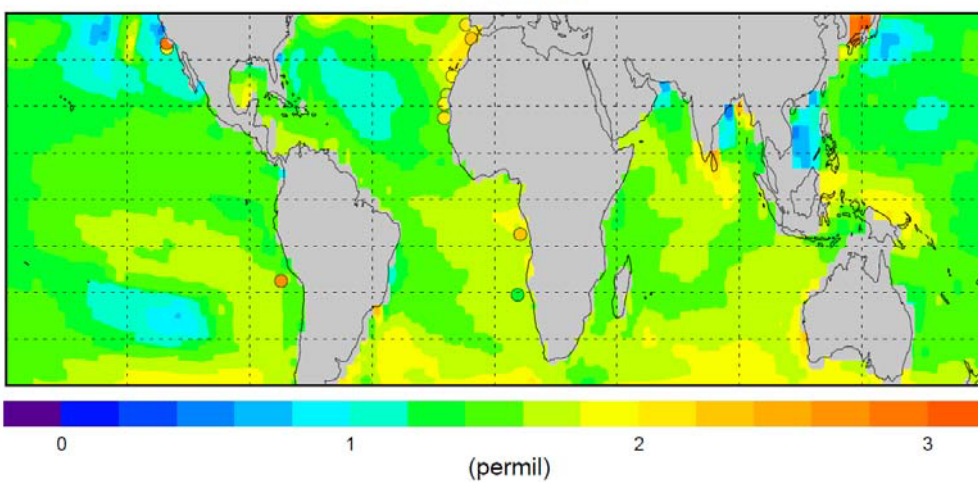


Figure 6.6 Modelled $\delta^{18}\text{O}_c$ differences between LGM and PD in tropical and subtropical sea surface waters. The circles show the LGM-PD differences from the observations (*G. ruber*, *G. sacculifer*, and *G. bulloides*).

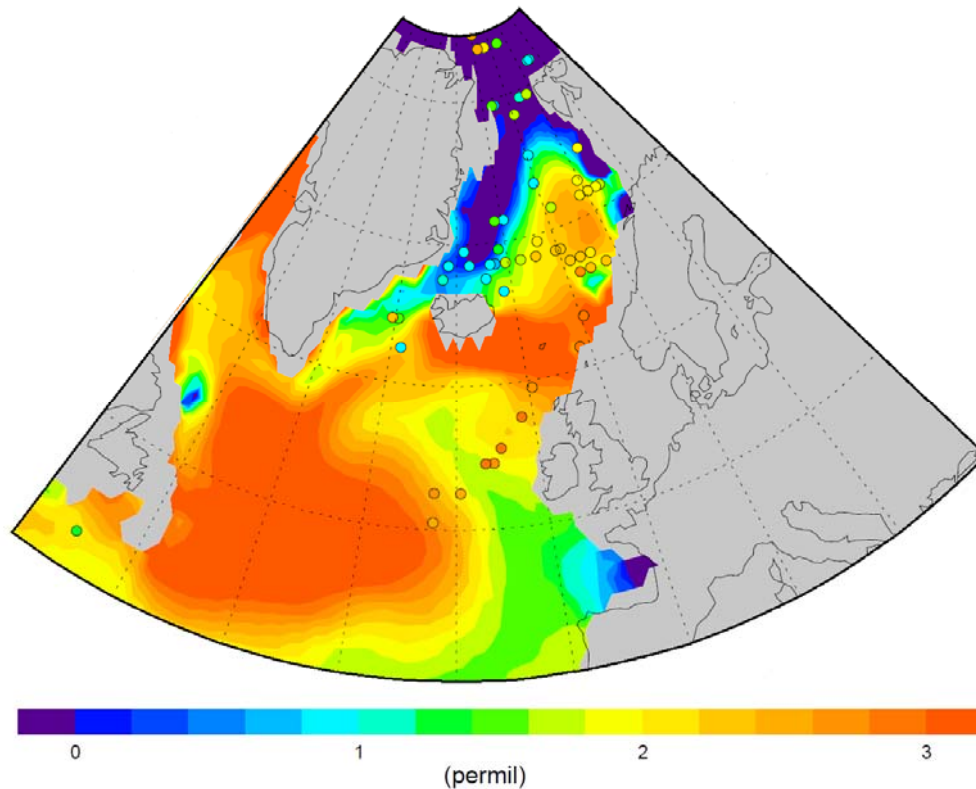
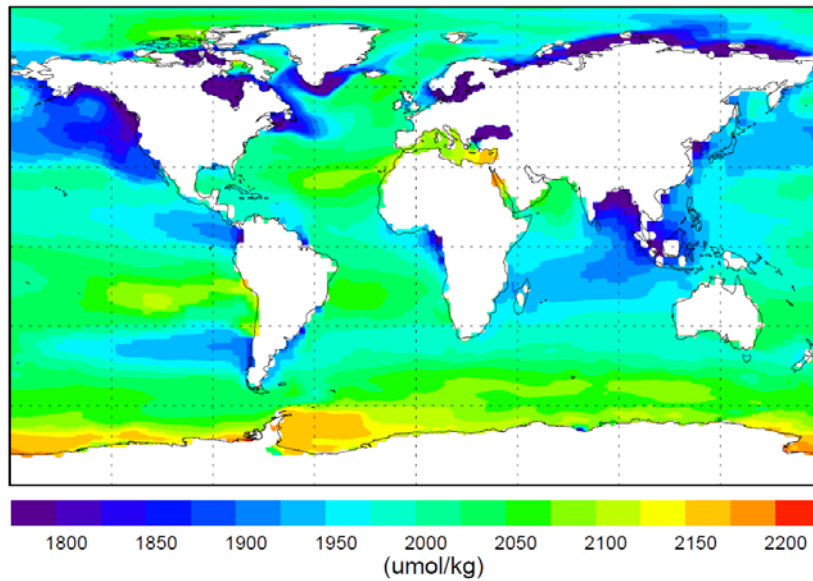


Figure 6.7 Modelled $\delta^{18}\text{O}_c$ differences between LGM and PD in the North Atlantic (north of 40°N). The circles show the LGM-PD differences from the observations (*N. pachyderma*).

6.4.2 $\delta^{18}\text{O}_c$ reconstruction from $\delta^{18}\text{O}_w$, SST and seawater carbonate chemistry conditions

In the last decade, the culture experiments with living foraminifera have demonstrated that the seawater carbonate chemistry is an important factor affecting stable oxygen isotope partitioning in foraminifera. These experiments showed development of isotopically lighter planktic foraminifera shells in the water with a higher CO_3^{2-} concentration (Spero et al., 1997; Bijma et al., 1999). A comprehension of the effect of seawater carbonate chemistry suggested that the calcium carbonate formed from a mixture of the carbonate species (H_2CO_3 , HCO_3^- , and CO_3^{2-}) in proportion to their relative contribution to the dissolved inorganic carbon (Zeebe, 1999).

HAMOCC



GLODAP

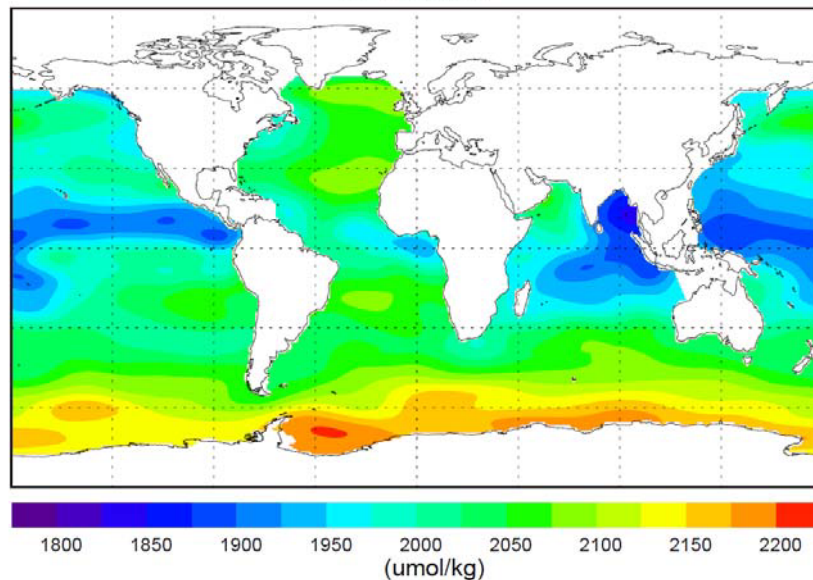
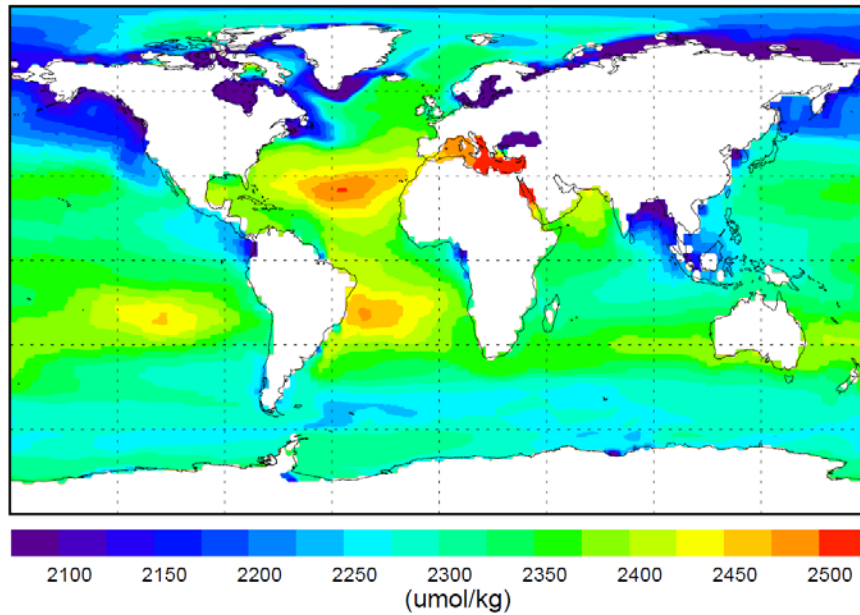


Figure 6.8 The present day annual mean sea surface DIC distributions (in micromol/kg) from the HAMOCC simulation and data compilations taken from the Global Ocean Data Analysis Project (GLODAP, Key et al., 2004). The Nordic Sea and Arctic Ocean has missing values in bottom panel.

The biogeochemical tracers, DIC and alkalinity are governed by physical, chemical and biological processes. As illustrated in Figure 6.8 and Figure 6.9, the present day sea surface distribution of DIC and total alkalinity in general are consistent with the observed patterns. Because the factors that control salinity also influence DIC and

total alkalinity, the surface distribution of DIC and total alkalinity shows features similar to salinity. The high values of DIC and total alkalinity are located in the subtropical regions of the Atlantic Ocean. The highest values found in our simulation are in the Southern Ocean, which are in agreement with the observations, but are smaller than the values in the reanalysis data.

HAMOCC



GLODAP

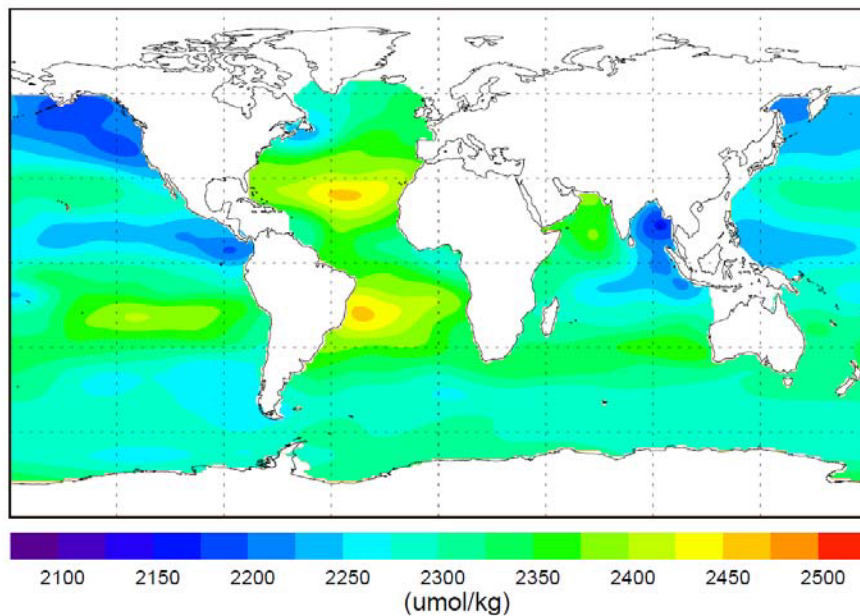


Figure 6.9 The present day annual mean sea surface total alkalinity distributions (in $\mu\text{mol/kg}$) from the HAMOCC simulation and data compilations taken from the Global Ocean Data Analysis Project (GLODAP, Key et al., 2004)

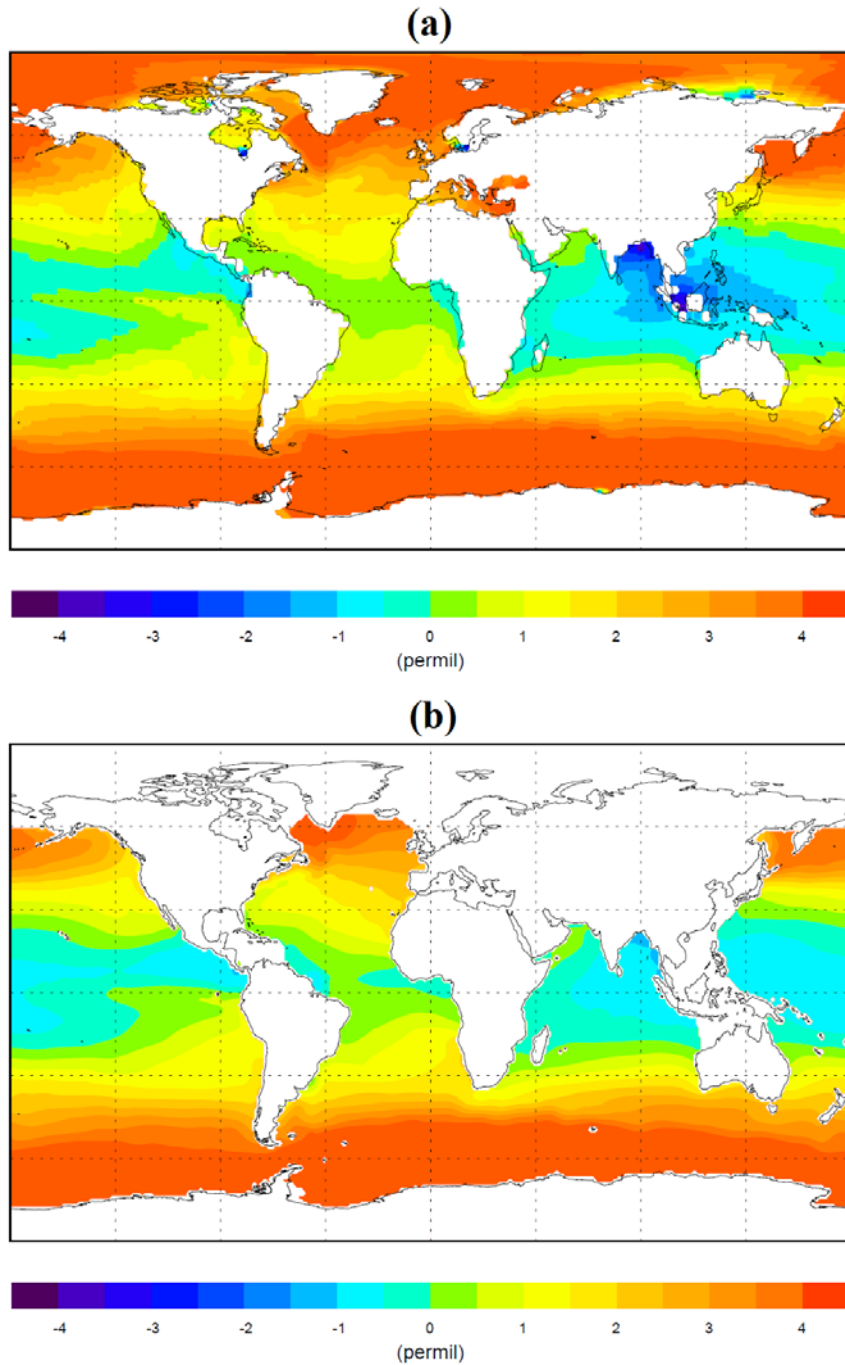


Figure 6.10 The present day annual mean $\delta^{18}\text{O}_c$ calculated from the surface temperature, $\delta^{18}\text{O}_w$ and carbon chemistry conditions (a) from the model simulation; (b) from the reanalysis data GLODAP (DIC and total alkalinity) and WOA09 (temperature and salinity).

Since any parameter of the seawater carbonate system can be estimated if two out of the six parameters (pCO_2 , HCO_3^- , CO_3^{2-} , DIC, alkalinity, and pH) in addition to

salinity, temperature and depth are known (Zeebe and Wolf-Gladrow, 2001), the sea surface DIC, alkalinity, salinity and temperature distributions simulated by the MPIOM-HAMOCC are used to calculate the composition of individual dissolved carbonate species.

Hereafter, the overall oxygen isotope fractionation factor between the sum of DIC and water at sea surface is calculated by using the individual dissolved carbonate species fractionation factor and their concentration in accordance with the given marine temperature (Zeebe, 2007). This overall fractionation factor is used to calculate the oxygen isotope composition in calcite. The same method is also applied on the GLODAP and WOA09 data to obtain the reconstructed $\delta^{18}\text{O}_c$ shown in Figure 6.10b. As seen in Figure 6.10, both reconstructions show the meridional increase in $\delta^{18}\text{O}_c$ concentrations due to the decrease in temperature across latitudes. The reconstruction from the model results is comparable to the reconstruction based on observations; however, in both cases the $\delta^{18}\text{O}_c$ compositions in foraminiferal calcite are overestimated when compared with the observed compositions of foraminifera shells in the Late Holocene sediments.

The simulated oceanic carbon chemistry conditions under LGM climate are depicted in Figure 6.11. It shows features at northern high latitudes that are distinctly in contrast with the present distributions. In general, the surface DIC and total alkalinity concentrations in the glacial oceans are higher than present day, and are around $100\mu\text{mol/kg}$ larger at LGM. Both DIC and total alkalinity concentration in the southern ocean and the Arctic Ocean exhibit obvious increase. Similar to the present day distribution, the large values are also located in the subtropical regions of the Atlantic Ocean. In our simulations, the sea surface DIC, total alkalinity, temperature, and salinity under the LGM conditions indicate 0.05 – 0.1 unit and around 0.1 unit increase in pH values in the Pacific and the northern North Atlantic, respectively. In the remaining areas of the Atlantic and Indian Ocean, the changes in pH values are relatively small (± 0.02 unites).

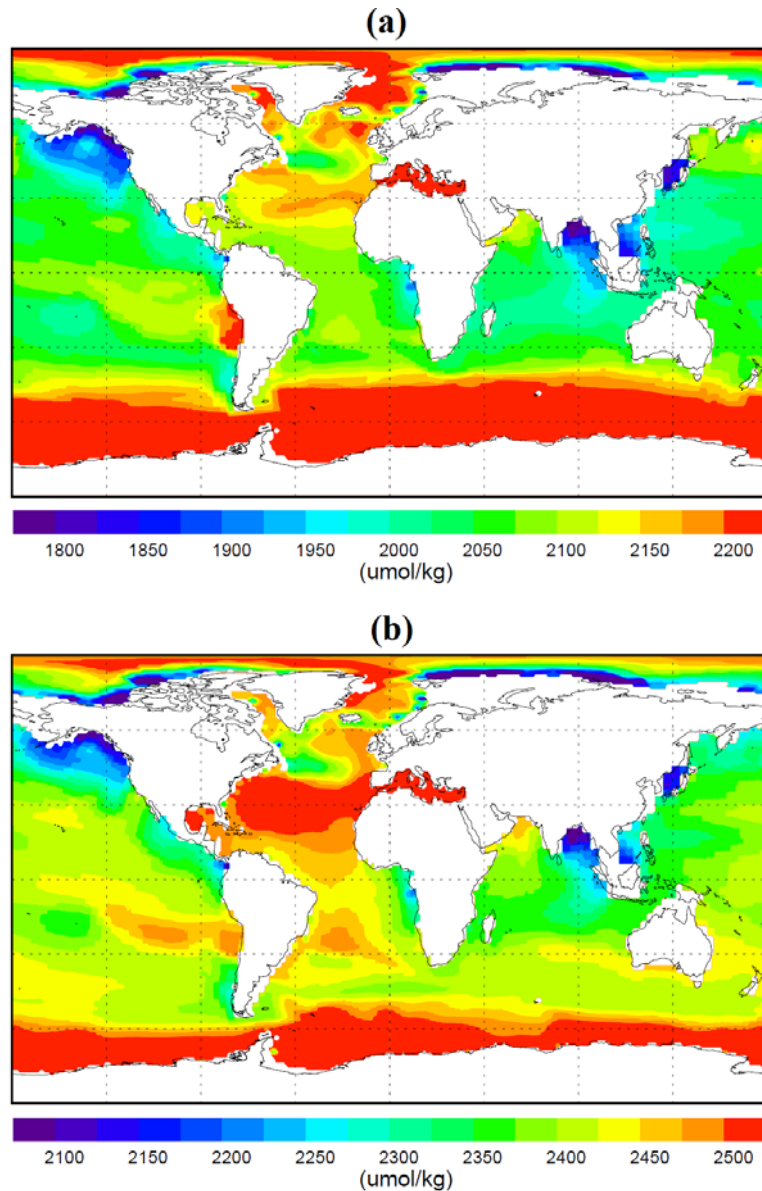


Figure 6.11 The LGM annual mean DIC (a) and total alkalinity (b) distribution at sea surface from model simulation.

The method used in present day $\delta^{18}\text{O}_c$ reconstruction (Figure 6.10) is applied to the LGM conditions. As shown in Figure 6.12, the $\delta^{18}\text{O}_c$ distribution thus achieved has the same trend of increasing values across the latitudes that is characteristic of present day distribution as well, but most basins are relatively more enriched due to the cold climate. Although the simulated patterns are similar to the observations, the reconstructed LGM $\delta^{18}\text{O}_c$ concentration is also more enriched than the foraminiferal data from sediment cores.

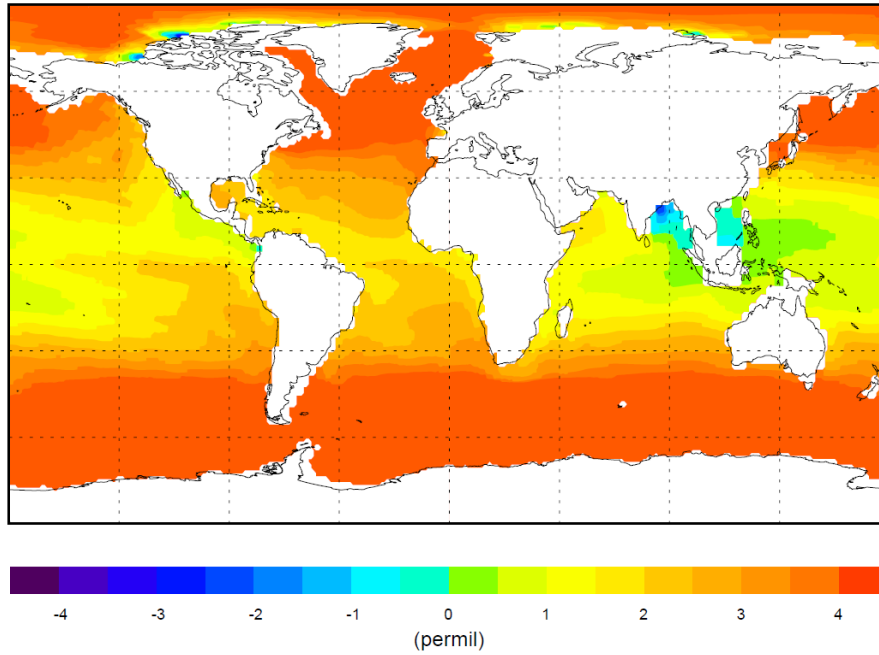


Figure 6.12 The LGM annual mean $\delta^{18}\text{O}_c$ calculated from the surface temperature, $\delta^{18}\text{O}_w$ and carbon chemistry conditions from the model simulation.

Further on, we have obtained the differences between the LGM and PD $\delta^{18}\text{O}_c$ calculated in this subsection. These LGM-PD differences are illustrated in Figure 6.13 together with the LGM-PD $\delta^{18}\text{O}_c$ differences calculated by using the paleo-temperature equation. As seen in Figure 6.13, both methods demonstrate more enriched foraminiferal shells during LGM in most basins except the Arctic Ocean. The absolute values of $\delta^{18}\text{O}_c$ simulated by applying the fractionation factor between the sum of DIC to the marine carbon chemistry and water isotope conditions are overestimated in comparison with the observations at both PD and LGM, however, the $\delta^{18}\text{O}_c$ differences between LGM and PD exhibit reasonable ranges as seen in subsection 6.4.1. In addition, the differences between Figure 6.13a and Figure 6.13b are relatively small compared with the absolute values shown in these Figures. In the (sub)tropical Atlantic and the Indian Ocean, the LGM-PD $\delta^{18}\text{O}_c$ difference variation raised by seawater carbonate chemistry changes is only around 0.03‰. The $\delta^{18}\text{O}_c$ difference between LGM and PD is approximately 0.1‰ smaller in the Pacific Ocean due to the sea surface carbon chemistry changes in this region.

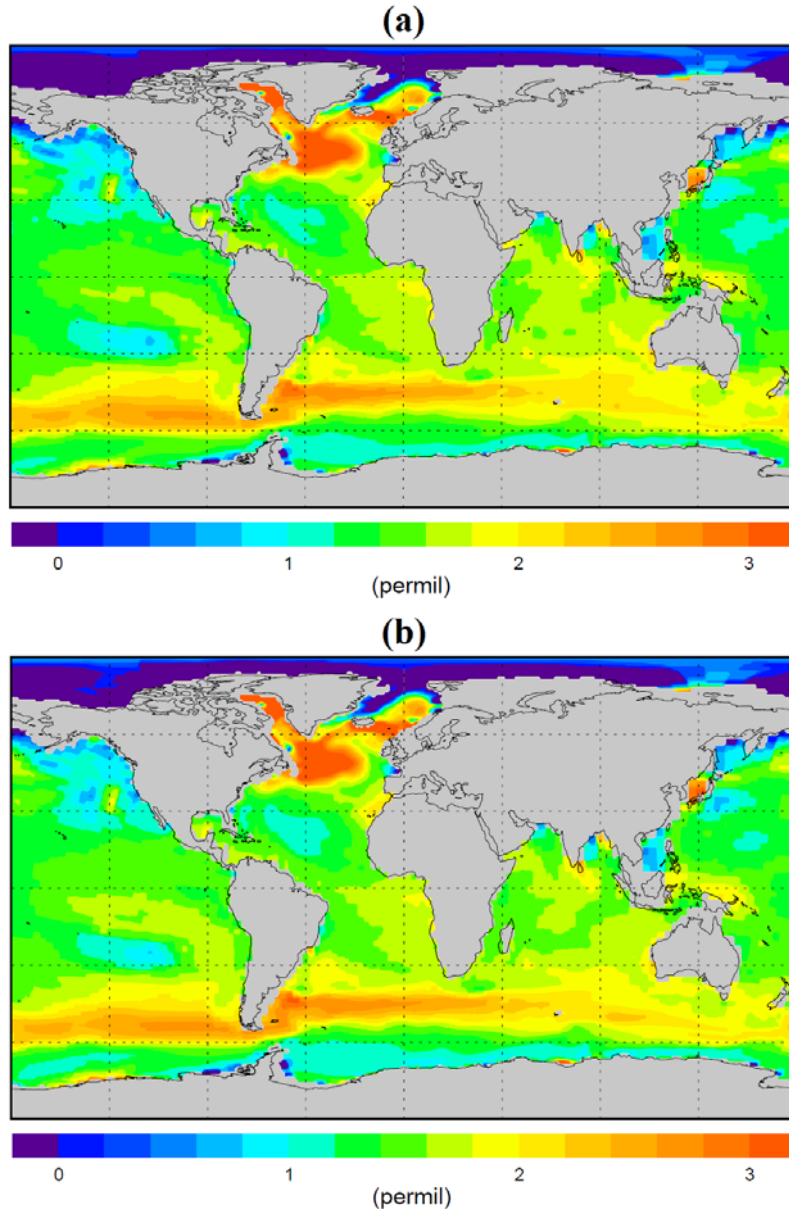


Figure 6.13 Reconstructed $\delta^{18}\text{O}_c$ differences between LGM and PD from (a) the modelled surface temperature, $\delta^{18}\text{O}_w$, and carbonate chemistry; (b) the modelled surface temperature and $\delta^{18}\text{O}_w$.

6.4.3 $\delta^{18}\text{O}_c$ reconstruction from $\delta^{18}\text{O}_w$, SST and DIC conditions in the microenvironment of *G. sacculifer*

Previous studies proposed that the life processes of planktic foraminifera such as calcification, respiration, and photosynthesis of the symbiotic algae (known as ‘vital effect’) have mediate effects on the isotope fractionation via their impact on the

ambient carbonate chemistry (Spero et al., 1997; Bijma et al., 1999). The later model studies (Wolf-Gladrow et al., 1999) also demonstrate the different influences that the ‘vital effect’ has in modifying the ambient concentration of individual carbonate species (CO_2 , HCO_3^- , and CO_3^{2-}).

Here, the same mathematical model (Wolf-Gladrow et al., 1999) is applied to calculate the modified carbonate species concentration within the foraminiferal microenvironment due to the life processes of *G. sacculifer*. The present day $\delta^{18}\text{O}_c$ compositions in *G. sacculifer* shells of different size are reconstructed under dark and light conditions (Figure 6.14). Because *G. sacculifer* is a tropical-subtropical species, only the region within 40°S - 40°N is presented in the figure. There are no significant changes in the $\delta^{18}\text{O}_c$ values for different shell sizes under same life processes, but the depletion under light condition is around 1‰ compared to the dark condition. The reconstructions based on the ambient carbon chemistry without the effects from the ‘vital effects’ show similar patterns for both dark and light conditions, while the dark condition is more enriched and the light condition depleted when compared with the simulations (see Figure 6.10a). In both dark and light conditions, these simulated $\delta^{18}\text{O}_c$ values are more enriched than the observed values obtained from the Late Holocene sediment cores.

Applying the same model and analysis under the LGM conditions, the LGM $\delta^{18}\text{O}_c$ compositions in *G. sacculifer* shells are also calculated for two different sizes under the dark and light conditions. As seen in Figure 6.15, the *G. sacculifer* shell is more enriched at the LGM compared with the present day simulation. Similar to the distributions seen in the modelled results for present day, the differences in the $\delta^{18}\text{O}_c$ values induced by the light conditions are much larger than due to the size differences. Compared to the reconstruction in Figure 6.12, the dark condition presents isotopically heavier shells, and the light condition shows isotopically lighter shells.

Comparisons between the simulated oxygen isotope compositions of *G. sacculifer* in different sizes at LGM and present day are calculated for the dark and light conditions (Figure 6.16). The deviation in the LGM-PD difference because of the dark and light conditions is very small in most areas. There are only very slight LGM-PD

differences in the northern North Pacific and the eastern South Pacific ($< 0.2\text{‰}$) under light conditions. These differences between light and dark conditions are much less obvious than the differences seen in Figure 6.14 and Figure 6.15. In addition, the LGM-PD $\delta^{18}\text{O}_c$ differences calculated by the reconstruction, which included the ‘vital effect’ impacts, are quite similar to the results acquired without considering the life processes (Figure 6.13a). *G. sacculifer* $\delta^{18}\text{O}_c$ differences between LGM and present day obtained from the sediment cores are plotted in Figure 6.16. In general, the simulated $\delta^{18}\text{O}_c$ differences are in agreement with most observations.

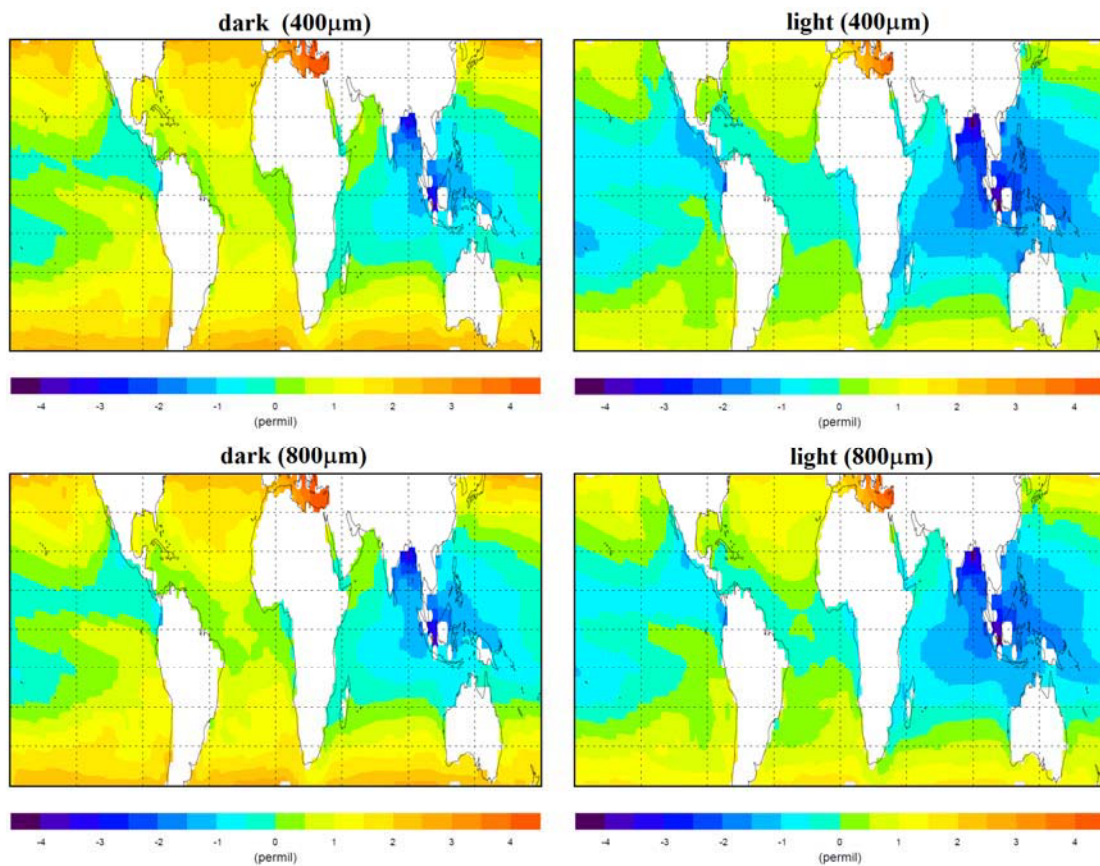


Figure 6.14 The reconstructed present day oxygen isotope compositions in the shell of *G. sacculifer* with two different sizes (400µm and 800µm) under the dark and light conditions.

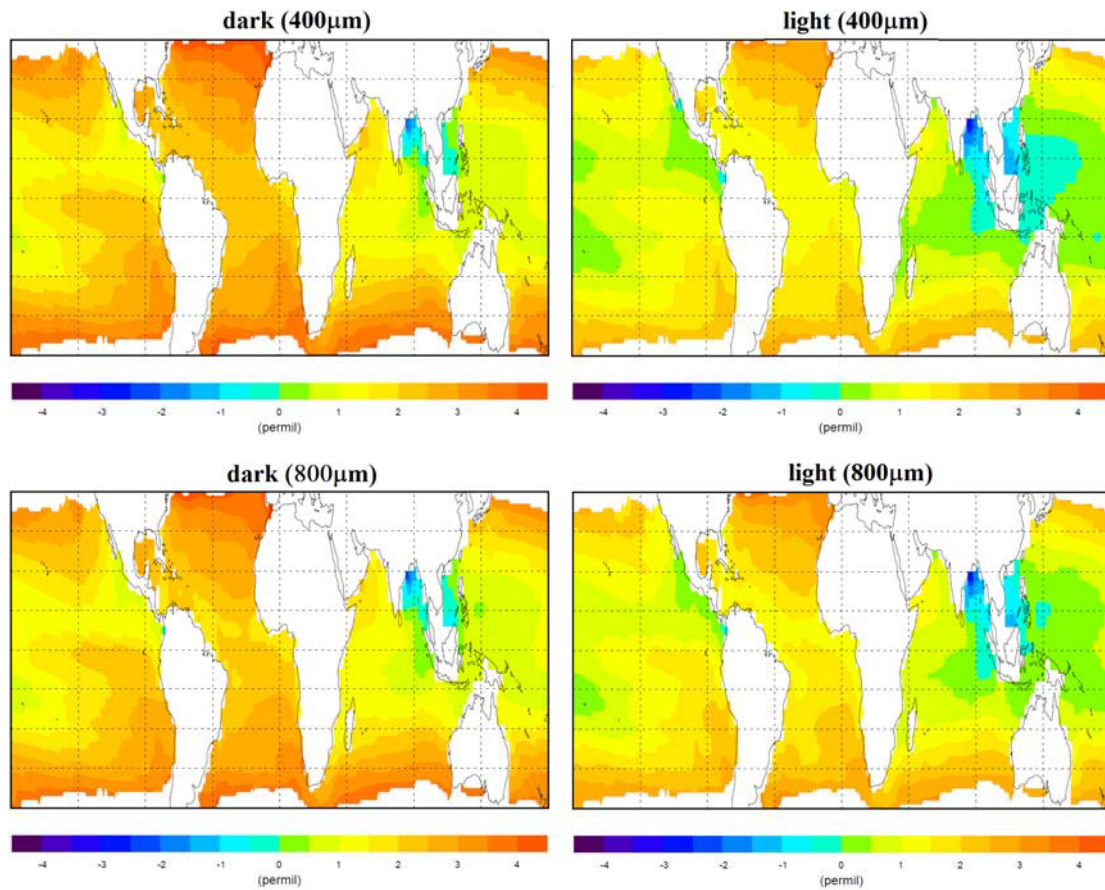


Figure 6.15 The reconstructed LGM oxygen isotope compositions in the shell of *G. sacculifer* with two different sizes (400 μm and 800 μm) under the dark and light conditions.

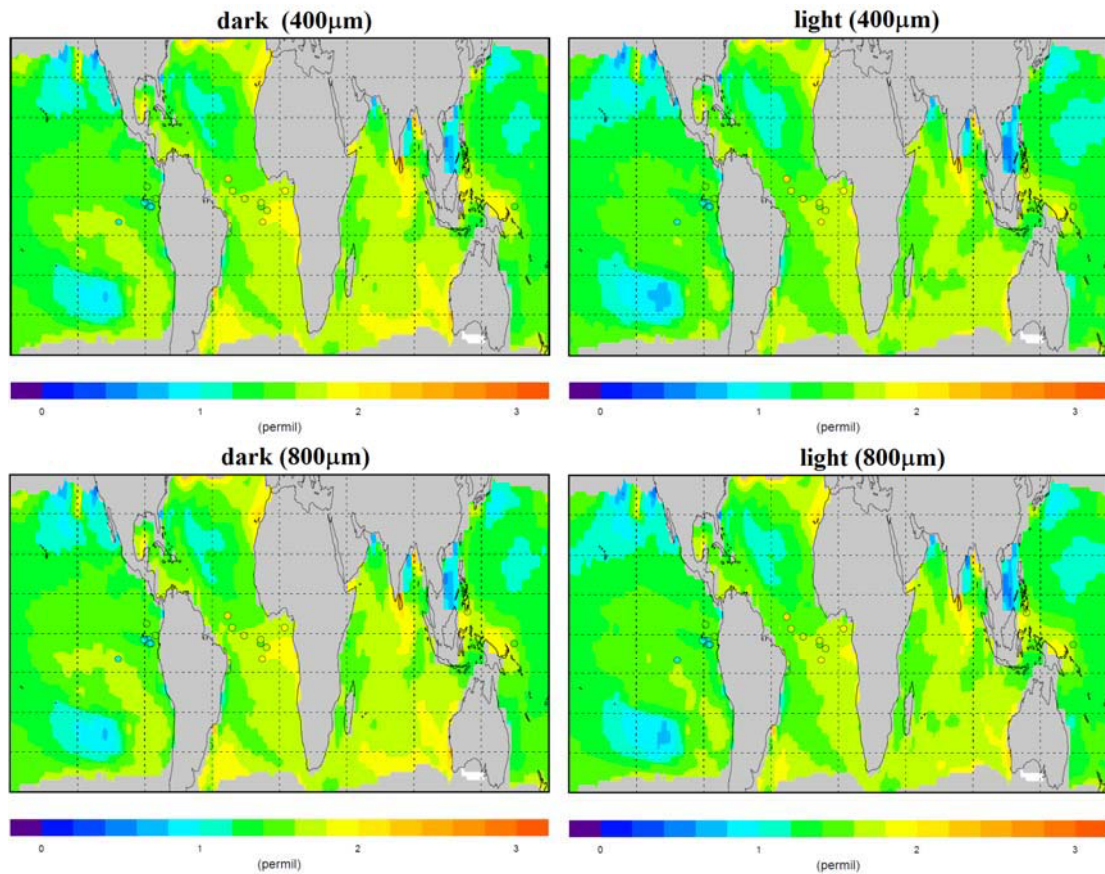


Figure 6.16 The reconstructed LGM-PD differences of oxygen isotope compositions in the shell of *G. sacculifer* with two different size (400µm and 800µm) under the dark and light conditions. The filled circles represent LGM-PD differences from the observed values of *G. sacculifer* that are averaged into the model grid.

6.5 Discussion

No direct measurements of the LGM sea surface waters' isotopic composition exist, which makes it difficult to validate the related model results. However, the simulated $\delta^{18}\text{O}_c$ values derived from the modelled sea surface fields (e.g. SST, $\delta^{18}\text{O}_w$, and seawater carbonate chemistry) enable a model-data comparison. Applying different methods to calculate the oxygen isotope composition in the foraminiferal shell gives us a chance to examine the effects from different factors.

As seen in the results calculated by the temperature and $\delta^{18}\text{O}_w$ depended empirical equation, the simulated surface $\delta^{18}\text{O}_c$ distributions are consistent with the $\delta^{18}\text{O}_c$ measurements at both present day and glacial time. The simulation for (sub)tropical regions agree with $\delta^{18}\text{O}_c$ measurements from *G. ruber* and *G. sacculifer* in both zonal

mean and cell-to-cell comparisons for the PD and LGM simulation. At high latitudes, the slight upper shift of the model-data scatter plot for *N. pachyderma* in the present-day comparison indicates a bit lower sea surface temperature at these regions in our PD simulation. Extremely high $\delta^{18}\text{O}_c$ values ($> 6\text{‰}$) are mainly simulated in the eastern Nordic Sea at LGM, which is approximately 1‰ higher than the observed $\delta^{18}\text{O}_c$ of *N. pachyderma*. This overestimate may indicate colder sea surface temperatures in our LGM simulation than the real glacial conditions in the eastern Nordic Sea. For *G. bulloides*, many LGM measurements are obtained from coastal upwelling regions, which are not well captured by the model simulation. This may be the reason for the large divergence in *G. bulloides* $\delta^{18}\text{O}_c$ between the LGM simulation and the measurements.

As an increase of $\delta^{18}\text{O}_w$ enhances the oxygen isotope composition in the foraminiferal calcite, the simulated decrease in $\delta^{18}\text{O}_w$ due to the glacial boundary condition and circulation dampens the positive ice sheet effect of $\delta^{18}\text{O}_w$. As a consequence, in those (sub)tropical regions, where the isotopic forcing and circulation conditions have a strong impact on the sea surface isotope composition, the overall glacial increase in $\delta^{18}\text{O}_c$ is relatively small. In general, the simulated $\delta^{18}\text{O}_c$ increase at LGM is only slightly higher than the observations, which may indicate a small overestimation of the simulated tropical sea surface cooling. In the eastern Nordic Sea, although the modelled LGM $\delta^{18}\text{O}_c$ compositions are much higher than the observed values, the LGM-PD differences in $\delta^{18}\text{O}_c$ are similar to the measurements. There may be two different interpretations for this discrepancy. Because our PD $\delta^{18}\text{O}_c$ values at northern high latitudes are overestimated in the simulation, it indicates colder surface temperatures than in reality. A comparably realistic decrease in surface temperature therefore introduces too cold glacial SST as compared to the reconstruction. The other way to look at this point is that either the prescribed global mean ice sheet effect in this region is underestimated, or the local isotopic decrease due to fluxes and circulation is overvalued. In this case, the $\delta^{18}\text{O}_c$ increase by the overestimated temperature decrease compensates the effect of $\delta^{18}\text{O}_w$ underestimation. Further distinct differences between model results and observations are found for the Eastern

Greenland Current and polar seas, where the simulated LGM $\delta^{18}\text{O}_c$ is smaller than the observed values. In these areas, the depletion of sea surface waters by the isotopic surface fluxes and ocean circulation overwhelms the enrichment due to the global ice sheet increase, and combined with a small temperature difference, a depletion in $\delta^{18}\text{O}_c$ is simulated. In our experimental set up, river runoff is calculated by considering a closed mass balance, which means that all the precipitation falling over the Northern Hemisphere ice sheets will discharge into the Arctic Ocean. This assumption, which excludes any temporal storage of glacial precipitation on the ice sheets, may introduce unrealistic river discharge into the polar seas, leading to highly depleted waters in this region.

In the second method, the influence of the seawater carbonate chemistry is involved. The simulated $\delta^{18}\text{O}_c$ maintains the meridional increasing trend as seen in the reconstruction using the paleo-temperature equation, which indicates temperature has an important effect on the isotopic concentration in the planktic foraminifera. The overall oxygen isotope fractionation factor between seawater and the dissolved inorganic carbon used in the second method is calculated from the individual dissolved carbonate species fractionation factor. However, these temperature dependent individual fractionation factors are examined in fresh water (Beck et al., 2005; Brenninkmeijer et al., 1983); this application may introduce uncertainties in calculations, and possibly be the reason for the overestimation in the $\delta^{18}\text{O}_c$ values derived from this method when compared with the measurements. The simulated $\delta^{18}\text{O}_c$ for both LGM and present day using the second method are more enriched than the observations, but the differences between LGM and present day show the similar magnitude as seen in the simulation obtained from the paleo-temperature equation and the sediment core data. Therefore the oxygen isotope fractionation factor between individual dissolved carbonate species and fresh water may be relatively larger than the fractionation factor between them and the sea water; this overestimate in the fractionation factor raises the isotopic composition calculated by this method. Since the temperature dependent equations used to calculate the fractionation factor are same in the LGM and present day reconstruction, and the overestimate in the

fractionation factor is counterbalanced when we calculate the differences, the uncertainty may therefore mainly be due to the intercepts in the temperature related equations. There is no obvious deviation between the LGM-PD difference constructed by the paleo-temperature equation and the second method, suggesting that the seawater carbon chemistry has secondary effect on the isotope composition in contrast to temperature and seawater isotope concentration. Boron isotope measured from planktic foraminifera suggest 0.15 ± 0.05 unit increase in sea surface pH value during glacial time (Hönisch and Hemming, 2005), which is equivalent to approximately $100 \mu\text{mol/kg}$ higher carbonate iron concentration. For estimations based on proxy data, the increase in carbonate iron may decrease the $\delta^{18}\text{O}_c$ value by around 0.2‰ (Spero et al., 1997). In our simulation, the increase in sea surface pH values at LGM is smaller than the estimation by proxy data, therefore the decrease in $\delta^{18}\text{O}_c$ due to the increase of carbonate iron is insignificant in most basins. However, in the Pacific Ocean, the increase in pH at sea surface is larger than that in other regions. Consequently, there is less increase in the LGM $\delta^{18}\text{O}_c$ when compared with the LGM $\delta^{18}\text{O}_c$ calculated by the paleo-temperature equation, and the rate of $\delta^{18}\text{O}_c$ decrease due to the increase in pH value agrees with the observations in culture experiments (Spero et al., 1997).

The ‘vital effect’ due to the life processes of planktic foraminifera is considered in the third method. Calcification, respiration, and photosynthesis processes of symbiont barren planktic foraminiferal species affect the oxygen isotope compositions in the shell by modifying the carbonate chemistry of the ambient conditions. In this method, the $\delta^{18}\text{O}_c$ values simulated under dark condition (calcification and respiration only) are always higher than the values calculated for the light condition (calcification, respiration, and photosynthesis are all involved). It is known that higher the carbonate iron concentration or pH values of water, more depleted will be the shells formed by the foraminifera living in that environment. Therefore, the calcification and respiration processes in general decrease the pH values of the water surrounding the shells, while the photosynthesis on the contrary increases it. For the species we have selected (*G. sacculifer*), its dark condition has higher $\delta^{18}\text{O}_c$ values than the reconstruction made in the second method, and the light condition is relatively

depleted. It suggests that the calcification of *G. sacculifer* and the respiration from *G. sacculifer*-symbiont system induce a lower pH value of the water in the microenvironment compared with the bulk value, while the increase in pH values by the symbiont photosynthesis overwhelms the calcification and respiration effect. In reality, the rate of these life processes should be between rates of the dark condition and light condition. And the $\delta^{18}\text{O}_c$ values should be therefore also between the reconstruction under the dark and light conditions. The size difference in *G. sacculifer* does not cause any obvious dissimilarity in the isotope composition of shells. However, these life processes are different for different species, so changes in the micro-environmental carbonate chemistry may vary, and for other species the shell size may also have important impacts. Therefore full knowledge of the species related respiration, calcification, and photosynthesis (symbiont) rates under different oceanic conditions is essential in order to quantify the impacts of life processes on the calcite isotope composition. The symbiont bearing species can increase the pH value of surrounding water by symbiont photosynthesis, and hence this effect must also be considered when applying the pH reconstruction for ambient water. In general, the LGM-PD difference calculated by the third method is similar to the results from the first method. And, in comparison with temperature and $\delta^{18}\text{O}_w$ the 'vital effects' have less influence on the isotopic composition of foraminiferal calcite.

Chapter 7

Conclusions and Outlook

In this study, the water isotope tracers H_2^{18}O and HDO have been successfully implemented into the ocean GCM MPI-OM to explicitly simulate the water isotope composition of seawater under present day and last glacial maximum climate conditions. The oxygen isotope concentration in the planktic foraminifera is also reconstructed based on our modelled sea surface temperature, oxygen isotope concentration in seawater, and seawater carbonate chemistry.

In the present-day simulation, oxygen and hydrogen isotopic composition of seawater are calculated. In addition, a second-order isotope parameter, the deuterium excess of sea surface water, has been analyzed on a basin scale. Our model captures the observed basin-scale features and meridional gradients of surface ocean water. The model simulates a more enriched Atlantic in comparison to the Pacific Ocean, the Mediterranean Sea as the most enriched oceanic basin, and the Arctic estuaries as the isotopically most depleted regions. Regional deficiencies apparent in certain marginal seas are related to relatively coarse horizontal resolution of the model setup. Our model also successfully simulates the observed vertical distribution and water-isotopic composition of Atlantic water masses. Moreover, the simulated *d-excess*- $\delta^{18}\text{O}$ relations are in agreement with the observations, showing an increase of the d-excess for water masses highly depleted in $\delta^{18}\text{O}$. A reverse relationship is detected at high latitudes, where the δD - $\delta^{18}\text{O}$ relations show a steeper slope (>8). The simulated $\delta^{18}\text{O}$ -salinity relationships of tropical and extra-tropical oceans are also in good agreement with the observations, with a flatter $\delta^{18}\text{O}$ -S slope at low latitudes and steeper slope at high latitudes. The modelled δD -salinity relationship shows similar features as $\delta^{18}\text{O}$.

The good performance of the isotope enhanced MPI-OM under present climate (Xu et al., 2012) enables the simulation of oceanic oxygen-isotope composition under LGM climate. In addition, we also analyzed the impacts of isotope fluxes and ocean

circulation on the oceanic isotope distribution respectively. Our modelled LGM sea surface temperature, sea ice extents, as well as general ocean circulation are in agreement with the available proxy data. From these findings we argue that our simulated oceanic $\delta^{18}\text{O}_w$ provides a reasonable distribution for the LGM. In general, the glacial $\delta^{18}\text{O}_w$ distribution does not show distinct differences from the present day condition, apart from large changes in the northern North Atlantic. The comparison between our different experiments suggests that the ice sheet impact dominates the $\delta^{18}\text{O}_w$ content variations from surface to bottom in most regions except the northern high latitudes. In these areas, the LGM changes in topography and circulation also have an important effect on $\delta^{18}\text{O}_w$. Based on the outcome of the sensitivity experiment, the variation of isotope fluxes mainly modifies the local isotopic composition of seawater, while the changes in ocean circulation influence the patterns of isotopic distribution. The simulated LGM $\delta^{18}\text{O}$ -S relationships have similar slope and intercept as seen in the present day simulation for extra-tropical regions. This result may support the application of present $\delta^{18}\text{O}$ -S relationship in the paleo-studies.

We also simulated the $\delta^{18}\text{O}_c$ distribution by combining the sea surface temperature and $\delta^{18}\text{O}_w$ from the model results. These $\delta^{18}\text{O}_c$ values are in good agreement with the observed $\delta^{18}\text{O}_c$ data derived from different foraminiferal species at both PD and LGM, indicating an overall adequate modelled representation of the oceanic and isotopic conditions. Minor LGM-PD $\delta^{18}\text{O}_c$ differences point to a slight overestimation of the SST cooling in the tropical oceans in our simulation. Additionally, the polar seas may be too depleted due to the overestimated river discharge calculated in the model. The agreement between the simulated and observed LGM-PD $\delta^{18}\text{O}_c$ differences in the eastern Nordic Sea suggests that the strong cooling simulated in this region may be realistic.

Furthermore, the reconstructions of $\delta^{18}\text{O}_c$ by considering the seawater carbonate chemistry and ‘vital effects’ show more enriched shells than as seen in the reconstruction from the observed data due to the uncertainty in the oxygen isotope fractionation factor between individual dissolved carbonate species and water. In order to reconstruct more precise $\delta^{18}\text{O}_c$, we still need further understanding of the

fractionation processes between the seawater and the sum of dissolved inorganic carbon. The LGM-PD $\delta^{18}\text{O}_c$ differences calculated by including the seawater carbonate chemistry and foraminiferal ‘vital effect’ impacts are similar to those reconstructed from the paleo-temperature equation. It indicates that the temperature and seawater isotope composition changes constitute the most important controls on the $\delta^{18}\text{O}_c$ differences in the foraminiferal shells. So, before even knowing more about the species depended ‘vital effects’ and the fractionation processes between DIC and seawater, the use of paleo-temperature equation may provide us with the most realistic reconstruction.

The first application of the newly developed stable water isotope module within the MPI-OM ocean model has been focused on the present-day and LGM climate conditions. As a logical next step, the model will be applied to different paleoclimatic conditions in a fully coupled setup to improve our understanding of past marine isotopic changes and its use for paleo-climate reconstructions.

Acknowledgement

I would like first to sincerely appreciate my supervisors Prof. Dr. Gerrit Lohmann and Prof. Dr. Jelle Bijma, giving me the opportunity to undertake this PhD project. Thank you for always supporting me and advising me throughout my PhD study.

The "Earth System Science Research School (ESSReS)", an initiative of the Helmholtz Association of German research centres (HGF) at the Alfred Wegener Institute for Polar and Marine Research is acknowledged for funding this research. Special thank goes to Dr. Klaus Grosfeld for organizing helpful lectures and soft-skill trainings during the last three years, which expand my knowledge in the Earth system science and enable me to improve my scientific performance for reviewing this dissertation.

I am greatly thankful to my colleagues Dr. Martin Werner, Dr. Martin Butzin, who are always ready to answer the research problems I met and the fruitful discussion on the publication, Prof. Dr. Dieter A. Wolf-Gladrow and Dr. Christoph Völker for the helpful discussion on the HAMOCC and FORAM model setups, my officemate Wei Wei, Barbara Hase, and Madlene Pfeiffer for the kindly help in my work and life, and all the other colleagues in Paleoclimate Dynamics group, at AWI, with your accompany, I enjoyed my PhD study here.

I would also like to thank all the Chinese colleagues and friends at Bremerhaven. We shared a lot of nice moments in the past 3 years.

Bibliography

- Adkins, J. F. and Schrag, D. P.: Reconstructing Last Glacial Maximum bottom water salinities from deep-sea sediment pore fluid profiles, *Earth. Planet. Sc. Lett.*, 216, 109-123, 2003.
- Adkins, J. F., McIntyre, K., Schrag, D. P.: The salinity, temperature, and $\delta^{18}\text{O}$ of the glacial deep ocean, *Science*, 298, 1769-1773, 2002.
- Adkins, J. F. and Boyle, E. A.: Changing atmospheric $\Delta^{14}\text{C}$ and the record of deep water paleoventilation ages, *Paleoceanography*, 12, 337-344, 1997.
- Aharon, P. and Chappell, J.: Oxygen isotopes, sea-level changes and temperature history of a coral-reef environment in New Guinea over the last 10^5 years, *Palaeogeogr. Palaeoclimatol. Palaeoecol.*, 56, 337-379, 1986.
- Aharon, P.: 140,000-yr isotope climatic record from raised coral reef in New Guinea, *Nature*, 304, 720-723, 1983.
- Alkama, R., Kageyama, M., Ramstein, G. Marti, O., Ribstein, P., and Swingedouw, D.: Impact of a realistic river routing in coupled ocean-atmosphere simulations of the Last Glacial Maximum climate, *Clim. Dynam.*, 30, 855-869, 2008.
- Anderson, D. M., Prell, W. L., and Barratt, N. J.: Estimates of sea surface temperature in the Coral Sea at the Last Glacial Maximum, *Paleoceanography*, 4, 615-627, 1989.
- Anderson, O. R. and Faber, W. W.: An estimation of calcium carbonate deposition rate in a planktonic foraminifer *Globigerinoides sacculifer* using ^{45}Ca as a tracer: A recommended procedure for improved accuracy, *J. Foram. Res.*, 14, 303-308, 1984.
- Arakawa, A. and Lamb, V. R.: Computational design of the basic dynamical processes of the UCLA general circulation model, *Methods. Comput. Phys.*, 17, 173-265, 1977.
- Arz, H. W., Pätzold, J., and Wefer, G.: Climatic changes during the last deglaciation recorded in sediment cores from the northeastern Brazilian Continental Margin, *Geo-Marine Letters*, 19, 209-218, doi:10.1007/s003670050111, 1999.
- Arz, H. W., Pätzold, J., and Wefer, G.: Correlated millennial-scale changes in surface hydrography and terrigenous sediment yield inferred from last-glacial marine deposits off northeastern Brazil, *Quaternary Research*, 50, 157-166, doi:10.1006/qres.1998.1992, 1998.
- Baertschi, P.: Absolute ^{18}O of standard mean ocean waters, *Earth Planet. Sci.*, 31, 341-344, 1976.
- Ballantyne, A. P., Lavine, M., Crowley, T. J., Liu, J., and Baker, P. B.: Meta-analysis of tropical surface temperatures during the Last Glacial Maximum, *Geophys. Res. Lett.*, 32, L05712, 2005.
- Bard, E., Arnold, M., Maurice, P., Duprat, J., Moyes, J., and Duplessy, J. C.: Retreat velocity of the North Atlantic polar front during the last deglaciation determined by ^{14}C accelerator mass spectrometry, *Nature*, 328, 791-794.
- Barrows, T. T. and Juggins, S.: Sea-surface temperatures around the Australian margin and Indian ocean during the last glacial maximum, *Quaternary Sci. Rev.*, 24, 1017-1047, 2005.
- Bassinot, F. C., Labeyrie, L. D., Vincent, E., Quidelleur, X., Shackleton, N. J., and

Lancelot, Y.: The astronomical theory of climate and the age of the Brunhes-Matuyama magnetic reversal, *Earth and Planetary Science Letters*, 126, 91-108, doi:10.1016/0012-821X(94)90244-5, 1994.

Bauch, D., Schlosser, P., and Fairbanks, R. G.: Freshwater balance and the sources of deep and bottom waters in the Arctic Ocean inferred from the distribution of ^{18}O , *Prog Oceanogr*, 35, 53-80, 1995.

Beck, W. C., Grossman, E. L., and Morse, J. W.: Experimental studies of oxygen isotope fractionation in the carbonic acid system at 15, 25, and 40 (degrees) C, *Deochim. Cosmochim. Ac.*, 69, 3493-3503, 2005.

Berger, W. H., Bickert, T., Schmidt, H., Wefer, G., and Yasuda, M. K.: Quaternary oxygen isotope record of pelagic foraminifers: Site 805, Ontong Java Plateau, In: Berger, W. H., Kroenke, L.W., Mayer, L. A. (eds.), *Proceedings of the Ocean Drilling Program, Scientific Results*, College Station, TX (Ocean Drilling Program), 130, 363-379, doi:10.2973/odp.proc.sr.130.032.1993, 1993.

Berger, W. H.: Planktonic foraminifera: basic morphology and ecologic implications, *J. Paleontology*, 43, 1369-1384, 1969.

Bé, A. W. H., Hemleben, C., Anderson, O. R., Spindler, M., Hacunda, J., and Tuntivate-Choy, S.: Laboratory and field observations of living planktonic foraminifera, *Micropaleontology* 23, 155-179, 1977.

Bemis, B. E., Spero, H., Bijma, J., and Lea, D. W.: Reevaluation of the oxygen isotopic composition of planktonic foraminifera: experimental results and revised paleotemperature equations, *Paleoceanography*, 13, 150-160, 1998.

Bijma, J., Spero, H. J. And Lea, D. W.: Reassessing foraminiferal stable isotope geochemistry: Impact of the oceanic carbonate system (experimental results), In *Use of Proxies in Paleoceanography-Examples from the South Atlantic*, edited by G. Fischer and G. Wefer, Springer, Berlin, Heidelberg, 489-512, 1999.

Bijma, J., Erez, J., and Hemleben, C.: Lunar and semi-lunar reproductive cycles in some spinose planktonic foraminifera, *J. Foram. Res.*, 20, 117-127, 1990a.

Bijma, J., Faver, W. W. Jr., Hemleben, C.: Temperature and salinity limits for growth and survival of some planktonic foraminifers in laboratory cultures, *Journal of Foraminiferal Research*, 20, 95-116, 1990b.

Bond, G., Broecker, W. S., Johnsen, S., McManus, J., Labeyrie, L., Jouzel, J., Bonani, G.: Correlations between climate records from North Atlantic sediments and Greenland ice, *Nature*, 365, 143-147, 1993.

Boyle, E.: Oceanic salt switch, *Science*, 298, 1724-1725, 2002.

Boyle, E. A.: Cadmium and delta-C-13 paleochemical ocean distributions during the stage-2 glacial maximum, *Annu. Rev. Earth Pl. Sc.*, 20, 245-287, 1992.

Brenninkmeijer, C. A. M., Kraft, P., and Mook, W. G.: Oxygen isotope fractionation between CO_2 and H_2O , *Isotope Geosci.*, 1, 181-190, 1983.

Broecker, W. S. and Henderson, G. M.: The sequence of events surrounding Termination II and their implications for the cause of glacial-interglacial CO_2 changes, *Paleoceanography*, 13, 353-364, 1998.

Broecker, W. S.: Oxygen isotope constrains on surface ocean temperatures, *Quat Res*, 26, 121-134, 1986.

Bryan, K.: A numerical method for the study of the circulation of the world ocean, *J Comput Phys*, 4, 347-376, 1969.

Calvo, E., Pelejero, C., Herguera, J. C., Palanques, A., and Grimalt, J. O.: Insolation dependence of the southeastern Subtropical Pacific sea surface temperature over the last 400 Kyrs, *Geophysical Research Letter*, 28, 2481-2484, 2001.

Cappa, C. D., Hendricks, M., DePaolo, D. J., and Cohen, R. C.: Isotopic fractionation of water during evaporation, *J Geophys Res*, 108, 4525, 2003.

Chapman, M. R. and Shackleton, N.: Millennial-scale fluctuations in North Atlantic heat flux during the last 150,000 years, *Earth and Planetary Science Letters*, 159, 57-70, 1998.

Ciais, P., Jouzel, J., Petit, J. R., Lipenkov, V., and White, J. W. C.: Holocene temperature variations inferred from six Antarctic ice cores, *Ann Glaciol*, 20, 427-436, 1994.

Clauzet, C., Wainer, I., Lazar, A., Brady, E., and Otto-Bliesner, B.: A numerical study of the south atlantic circulation at the Last Glacial Maximum, *Palaeogeogr. Palaeoclimatol.*, 253, 509-528, 2007.

CLIMAP: Seasonal reconstruction of the Earth's surface at the Last Glacial maximum, *Map Chart Series MC-36*, 1981.

Cole, J. E., Rind, D., and Fairbanks, R. G.: Isotopic responses to interannual climate variability simulated by an atmospheric general circulation model, *Quaternary Science Reviews*, 12, 387-406, 1993.

Coplen T. B., Kendall, C., and Hopple, J.: Comparison of stable isotope reference samples, *Nature*, 320, 236-238, 1983.

Cortijo, E., Labeyrie, L., Vidal, L., Vautravers, M., Chapman, M. R., Duplessy, J. C., Elliot, M., Arnold, M., Turon, J. L., and Auffret, G.: Changes in sea surface hydrology associated with Heinrich event 4 in the North Atlantic Ocean between 40° and 60°N, *Earth and Planetary Science Letters*, 146, 29-45, 1997.

Cortijo, E.: La variabilité climatique rapide dans l'Atlantique Nord depuis 128 000 ans: relations entre les calottes de glace et l'océan de surface, Ph.D. Thesis, University of Paris, France, 1995.

Craig, H. and Gordon, L. I.: Deuterium and oxygen-18 variations in the ocean and the marine atmosphere, in *Stable Isotopes in Oceanographic Studies and Paleotemperatures*, Tongiogi, E. (Eds.), Spoleto, Italy, 9-130, 1965.

Craig, H.: Isotopic variation in meteoric water, *Science*, 133, 1702, 1961.

Craig, H.: Isotopic standards for carbon and oxygen and correction factors for mass spectrometric analysis of carbon dioxide, *Geochim Cosmochim Acta*, 12, 133-149, 1957.

Criss, R.E. (Eds): *Principles of stable isotope distribution*. New York: Oxford University Press, 1999.

Crosta, X., Pichon, J. J., and Burckle, L. H.: Application of modern analog technique to marine Antarctic diatoms: Reconstruction of maximum sea-ice extent at Last Glacial Maximum, *Paleoceanography*, 13, 284-297, 1998.

Dannenmann, S., Linsley, B. K., Oppo, D. W., Rosenthal, Y., Beaufort, L.: East Asian monsoon forcing of suborbital variability in the Sulu Sea during Marine Isotope Stage

- 3: Link to Northern Hemisphere climate, *Geochemistry Geophysics Geosystems*, 4, 1001, doi:10.1029/2002GC000390, 2003.
- Dansgaard, W.: Stable isotopes in precipitation, *Tellus*, 16, 436-468, 1964.
- Dansgaard, W.: The abundance of O¹⁸ in atmospheric water and water vapor, *Tellus*, 5, 461-469, 1953.
- Delaygue, G., Bard, E., Rollion, C., Jouzel, J., Stievenard, M., Duplessy, J. C., and Ganssen, G.: Oxygen isotope/salinity relationship in the northern Indian Ocean, *J. Geophys. Res.*, 106, 4565-4574, 2001.
- Delaygue, G., Jouzel, J., and Dutay, J. C.: Oxygen 18-salinity relationship simulated by an oceanic general circulation model, *Earth and Planetary Sci. Lett.*, 178, 113-123, 2000.
- de Vernal, A., Rosell-Melé, A., Kucera, M., Hillaire-Marcel, C., Eynaud, F., Weinelt, M., Dokken, T., and Kageyama, M.: Comparing proxies for the reconstruction of LGM sea-surface conditions in the northern North Atlantic, *Quaternary Science Reviews*, 25, 2820-2834, 2006.
- de Vernal, A., Hillaire-Marcel, C., Turon, J. L., and Matthiessen, J.: Reconstruction of sea-surface temperature, salinity, and sea-ice cover in the northern North Atlantic during the last glacial maximum based on dinocyst assemblages, *Canadian Journal of Earth Sciences*, 37, 725-750, 2000.
- Dewit, J.C., VanderStraaten, C. M., and Mook, W. G.: Determination of the absolute hydrogen isotopic ratio of V-SMOW and SLAP, *Geostandards Newslett*, 4, 33-36, 1980.
- Dokken, T. and Jansen, E.: Rapid changes in the mechanism of ocean convection during the last glacial period, *Nature*, 401, 458-461, 1999.
- Dokken, T.: Last interglacial/glacial cycle on the Svalbard/Barents Sea margin, Ph.D. thesis, University of Tromsø, Norway, 1995.
- Dreger, D.: Decadal-to-centennial-scale sediment records of ice advance on the Barents shelf and meltwater discharge into the north-eastern Norwegian Sea over the last 40 kyr, Ph.D. Thesis, University of Kiel, Germany, 1999.
- Duplessy, J. C., Labeyrie, L., Arnold, M., Paterne, M., Duprat, J., and van Weering, T. C. E.: Changes of surface salinity of the North Atlantic Ocean during the last glacial deglaciation, *Nature*, 358, 485-488, 1992.
- Duplessy, J. C., Labeyrie, L. D., Juillet-Leclerc, A., Maitre, F., Duprat, J., and Sarnthein, M.: Surface salinity reconstruction of the North Atlantic Ocean during the last glacial maximum, *Oceanol Acta*, 14, 311-324, 1991.
- Duplessy, J. C., Shackleton, N. J., Fairbanks, R. G., Labeyrie, L., Oppo, D., and Kallel, N.: Deepwater source variations during the last climatic cycle and their impact on the global deepwater circulation, *Paleoceanography*, 3, 343-360, 1988.
- Duplessy, J. C.: North Atlantic deep water circulation during the last climate cycle, *Bulletin de l'Institut de Geologie du Bassin d'Aquitaine*, 31, 379-391, 1982.
- Duplessy, J. C.: Isotope studies, Gribbin, J. (Ed.), *Climate Change*, Cambridge, Cambridge Univ. Press, 46-67, 1978.
- Duplessy, J. C.: Note préliminaire sur les variations de la composition isotopique des eaux superficielles de l'Océan Indien: La relation ¹⁸O-salinité, *C. R. Acad. Sci. Paris*,

271, 1075-1078, 1970.

Dürkoop, A., Hale, W., Mulitza, S., Pätzold, J., and Wefer, G.: Late Quaternary variations of sea surface salinity and temperature in the western tropical Atlantic: Evidence from ^{18}O of *Globigerinoides sacculifer*, *Paleoceanography*, 12, 764-772, doi:10.1029/97PA02270, 1997.

Ehhalt, D. H.: On the deuterium-salinity relationship in the Baltic Sea, *Tellus*, 21, 429-435, doi: 10.1111/j.2153-3490.1969.tb00456.x, 1969.

Emiliani, C.: Pleistocene temperatures, *J. Geol.*, 63, 538-578, 1955.

Emiliani, C.: Depth habitats of some species of pelagic foraminifera as indicated by oxygen isotope ratios, *Amer. J. Sci.*, 252, 149-158, 1954.

Epstein, S. and Mayeda, T. K.: Variations of ^{18}O content of waters from natural sources, *Geochimica et Cosmochimica Acta* 4, 213-224, 1953.

Epstein, S., Buchsbaum, R., Lowenstam, H. A., and Urey, H. C.: Revised carbonate-water isotopic temperature scale, *Geol. Soc. Amer. Bull.*, 64, 1315-1325, 1953.

Erez, J.: Calcification rates, photosynthesis and light in planktonic foraminifera, In: Westbroek, P., de Jong, E. W. (Eds), *Biom mineralization and biological metal accumulation*, Reidel, 307-312, 1983.

Fairbanks, R. G.: A 17,000 year glacio-eustatic sea level record: influence of glacial melting rates on Younger Dryas event and deep-ocean circulation, *Nature*, 342, 637-642, 1989.

Friedman, I., Schoen, B., and Harris, J.: The deuterium content in Arctic sea ice, *J. Geophys. Res.*, 66, 1861-1864, 1961.

Friedman, I.: Deuterium content of nature water and other substance, *Geochimica et Cosmochimica Acta*, 4, 89-103, 1953.

Fröhlich, K., Grabczak, J., and Rozanski, K.: Deuterium and oxygen-18 in the Baltic Sea, *Chem. Geol. Isot. Geosci. Sect.*, 72, 77-83, 1988.

Gat, J. R., Shemesh, A., Tziperman, E., Hecht, A., Georgopoulos, D., and Basturk, O.: The stable isotope composition of waters of the eastern Mediterranean Sea, *J. Geophys. Res.*, 101, 6441-6451, 1996.

Gat, J. R., Bowser, C. J., and Kendall, C.: The contribution of evaporation from the Great Lakes to the continental atmosphere: estimate based on stable isotope data. *Geophys. Res. Lett.*, 21, 557-560, 1994.

Gat, J. R. and Gonfiantini, R. (Eds): *Stable isotope hydrology: Deuterium and Oxygen-18 in the water cycle*, Int. At. Energy Agency, Vienna, 1981.

Gates, W. L., Boyle, J.S., Covey, C., Dease, C. G., Doutriaux, C. M., Drach, R. S., Fiorino, M., Gleckler, P. J., Hnilo, J. J., Marlais, S. M., Phillips, T. J., Potter, G. L., Santer, B. D., Sperber, K. R., Taylor, K. E., and Williams, D. N.: An overview of the results of the Atmospheric Model Intercomparison Project (AMIP I), *Bull Amer Meteorol Soc*, 80(1), 29-55, 1999.

Gent, P. R., Willebrand, J., McDougall, T., and McWilliams, J. C.: parameterizing eddy induced tracer transports in ocean circulation model, *J. Phys. Oceanogr.*, 25, 463-474, 1995.

Gersonde, R., Crosta, X., Abelmann, A., and Armand, L. K.: Sea surface temperature

and sea ice distribution of the last glacial Southern Ocean – A circum-Antarctic view based on siliceous microfossil records, *Quat. Sci. Rev.*, 24, 869-896, 2005.

Gorbarenko, S. A., Nürnberg, D., Derkachev, A. N., Astakhov, A. S., Southon, J. R., and Kaiser, A.: Magnetostratigraphy and tephrochronology of the Upper Quaternary sediments in the Okhotsk Sea: implication of terrigenous, volcanogenic and biogenic matter supply, *Marine Geology*, 183, 107-129, 2002.

Gorbarenko, S. A. and Southon, J. R.: Detailed Japan Sea paleoceanography during the last 25kyr: constrains from AMS dating and of planktonic foraminifera, *Palaeogeography, Palaeoclimatology, Palaeoecology*, 156, 177-193, 2000.

Gorbarenko, S. A.: Stable isotope and lithologic evidence of Late-Glacial and Holocene oceanography of the Northwestern Pacific and its marginal seas, *Quaternary Research*, 46, 230-250, 1996.

Gregory, R.T. and Taylor, H.P.: An oxygen isotope profile in a section of Cretaceous oceanic crust, Samail ophiolite, Oman: evidence for $\delta^{18}\text{O}$ -buffering of the oceans by deep ($> 5\text{km}$) seawater-hydrothermal circulation at mid-ocean ridges, *J. Geophys. Res.*, 86, 2737-2755, 1981.

Grobe, H. and Mackensen, A.: Late Quaternary climatic cycles as recorded in sediments from the Antarctic continental margin, In: Kennett, J. P. and Warnke, D. (eds.), *The Antarctic Paleoenvironment: a perspective on Global Change*, Antarctic Research Series, 56, 349-376, hdl:10013/epic.11662.d001, 1992.

Grobe, H., Fütterer, D. K., and Spieß, Volkhard.: Oligocene to Quaternary sedimentation processes on the Antarctic continental margin, ODP Leg 113, Site 693, In: Barker, P. F., and Kennett, J. P. (eds.), *Proceedings of the Ocean Drilling Program, Scientific Results*, College Station, TX (Ocean Drilling Program), 113, 121-131, doi:10.2973/odp.proc.sr.113.193.1990, 1990.

Hagemann R, Nief G, and Roth, E.: Absolute isotopic scale for deuterium analysis of natural waters: Absolute D/H ratio for SMOW, *Tellus*, 22, 712–715, 1970.

Hale, W. and Pflaumann, U.: Sea-surface Temperature Estimations using a Modern Analog Technique with Foraminiferal Assemblages from Western Atlantic Quaternary Sediments, In: Fischer, G. and Wefer, G. (eds.), *Use of Proxies in Paleoceanography - Examples from the South Atlantic*, Springer, Berlin, Heidelberg, 69-90, 1999.

Hebbeln, D. and Wefer, G.: Late Quaternary Paleoceanography in the Fram Strait, *Paleoceanography*, 12, 65–78, 1997.

Hemleben, C., Spindler, M., and Anderson, O. R.: *Modern planktonic foraminifera*. Springer-Verlag, New York, 1989.

Hendy, I. L. and Kennett, J. P.: Stable isotope stratigraphy and paleoceanography of the last 170 k.y.: Site 1014, TAnner BASin, California, In: Lyle, M., Koizumi, I., Richter, C., Moore, T.C., Jr. (eds.), *Proceedings of the Ocean Drilling Program, Scientific Results*, College Station, TX (Ocean Drilling Program), 167, 129-140, doi:10.2973/odp.proc.sr.167.205.2000, 2000.

Hendy, I. L. and Kennett, J. P.: Latest Quaternary North Pacific surface-water responses imply atmosphere-driven climate instability, *Geology*, 29, 291-294, 1999.

Hewitt, C. D., Stouffer, R. J., Broccoli, A. J., Mitchell, J. F. B., and Valdes, P. J.: The effect of ocean dynamics in a coupled GCM simulation of the Last Glacial Maximum,

- Clim. Dynam., 20, 203-218, 2003.
- Hibler, W. D.: A dynamic thermodynamic sea ice model, *J. Phys. Oceanogr.*, 9, 815-846, 1979.
- Hillaire-Marcel, C., de Vernal, A., Bilodeau, G., Wu, G. P.: Isotope stratigraphy, sedimentation rates, deep circulation, and carbonate events in the Labrador Sea during the last c. 200ka, *Canadian Journal of Earth Science*, 31, 63-89, 1994.
- Hoffmann, G., Werner, M., and Heimann, M.: Water isotope module of the ECHAM atmospheric general circulation model: A study on timescales from days to several years, *J. Geophys. Res.*, 103, 16,871-16,896, 1998.
- Hohnemann, C.: Zur Paläoceanographie des südlichen Dänemarkstraße, Unpublished Dipl. Arb. Thesis, University Kiel, Germany, 1996.
- Horibe, Y. and Ogura, N.: Deuterium content as a parameter of water mass in the ocean, *J. Geophys. Res.*, 73, 1239-1249, 1968.
- Hönisch, B. and Hemming, N. G.: Surface ocean pH response to variations in pCO₂ through two full glacial cycles, *Earth Planet Sci Lett*, 236, 305-314, 2005.
- Jansen, E. and Meland, M.: Stratigraphy of IMAGES cores in the Faeroese-Shetland area, Technical Report 01-01, Bjerknes Centre for Climate Research, Bergen, Norway, 2001.
- Jansen, E. and Veum, T.: Evidence for two-step deglaciation and its impact on North Atlantic deep-water circulation, *Nature*, 343, 612-616, 1990.
- Jansen, E. and Erlenkeuser, H.: Ocean circulation in the Norwegian Sea during the last deglaciation: isotope evidence, *Palaeogeography, Palaeoclimatology, Palaeoecology*, 49, 189-206, 1985
- Jones, G. A. and Keigwin, L.: Evidence from Fram Strait (78°N) for early deglaciation, *Nature*, 336, 56-59, 1989.
- Joussaume, J., Sadourny, R., and Jouzel, J.: A general circulation model of water isotope cycles in the atmosphere, *Nature*, 311, 24-29, 1984.
- Jørgensen, B. B., Erez, J., Revsbech, N. P., Cohen, Y.: symbiotic photosynthesis in a planktonic foraminiferan, *Globigerinoides sacculifer* (Brady), studied with microelectrodes, *Limnol. Oceanogr.*, 30, 1253-1267, 1985.
- Juillet-Leclerc, A., Jouzel, J., Labeyrie, L., and Joussaume, S.: Modern and last glacial maximum sea surface δ¹⁸O derived from an Atmospheric General Circulation Model, *Earth. Planet. Sc. Lett.*, 146, 591-605, 1997.
- Jung, S. J. A.: Wassermassenaustausch zwischen NE-Atlantik und Nordmeer während der letzten 300,000-80,000 Jahre im Abbild stablier O- und C-Isotope, Ph.D. thesis, University Kiel, 1996.
- Jünger, B.: Tiefenwassererneuerung in der Grönlandsee während der letzten 340 000 Jahre, Ph.D. Thesis, University of Kiel, Germany, 1993.
- Keigwin, L. D.: Glacial-age hydrography of the far northwest Pacific Ocean, *Paleoceanography*, 13, 323-339, 1998.
- Keigwin, L. D. and Jones, G. A.: The marine record of deglaciation from the continental margin off Nova Scotia, *Paleoceanography*, 10, 973-986, doi:10.1029/95PA02643, 1995.
- Keigwin, L. D., and Boyle, E. A.: Late Quaternary paleochemistry of high-latitude

- surface waters, *Palaeogeography, Palaeoclimatology, Palaeoecology*, 73, 85-106, 1989a.
- Keigwin L. D. and Jones G. A.: Glacial-Holocene stratigraphy, chronology, and paleoceanographic observations on some North Atlantic sediment drifts, *Deep Sea Research*, 36, 845-867, 1989b.
- Kellogg, T. B., Duplessy, J. C., and Shackleton, N. J.: Planktonic foraminiferal and oxygen isotope stratigraphy and paleoclimatology of Norwegian deep-sea cores, *Boreas*, 7, 61–73, 1978.
- Kendall, C. and Coplen, T. B.: Distribution of oxygen-18 and deuterium in river waters across the United States, *Hydrological processes*, 15, 1363-1393, 2001.
- Key, R., Kozyr, A., Sabine, C., Lee, R. W. K., Bullister, J., Feely, R., Millero, F., Mordy, C., and Peng, T. H.: A global ocean carbon climatology: Results from GLODAP, *Global Biogeochem. Cycles*, 19, GB4031, 2004.
- Khaliwala, S. P., Fairbanks, R. G., and Houghton, R. W.: Freshwater sources to the coastal ocean off northeastern North America: Evidence from $H_2^{18}O/H_2^{16}O$, *J Geophys Res*, 104, 18,241-18,255, 1999.
- Kiefer, T., Sarnthein, M., Erlenkeuser, H., Grootes, P. M., and Roberts, A. P.: North Pacific reponse to millennial-scale changes in ocean circulation over the last 60 Kyr, *Paleocenaography*, 16, 179-189, 2001.
- Kitoh, A., Murakami, S., and Koide, H.: A simulation of the last glacial maximum with a coupled atmosphere-ocean GCM, *Geophys. Res. Lett.*, 28, 2221-2224, 2001.
- Klinger, B. A., Marshall, J., and Send, U.: Representation of convective plumes by vertical adjustment, *J. Geophys. Res.*, 101, 18175-18182, 1996.
- Knies, J.: Spätquartäre Sedimentation am Kontinentalhang nordwestlich Spitzbergens, *Der letzte Glazial/Interglazial-Zyklus*, Thesis, Justus-Liebig-University, Giessen, Germany, 1994.
- Kohfeld, K. E. and Harrison, S. P.: DIRTMAP: The geological record of dust, *Earth. Sci. Rev.*, 54, 81-114, 2001.
- Koutavas, A. and Lynch-Stieglitz, J.: Glacial-interglacial dynamics of the eastern equatorial Pacific cold tongue-Intertropical Convergence Zone system reconstructed from oxygen isotope records, *Paleoceanography*, 18, 1089, doi:10.1029/2003PA000894, 2003.
- Köhler, S. E. I.: Spätquartäre paläo-ozeanographische Entwicklung des Nordpolarmeeres und Europäischen Nordmeeres anhand von Sauerstoff- und Kohlenstoffisotopenverhältnissen der planktischen Foraminifere *Neogloboquadrina pachyderma* (sin.), Geomar Research Centre for Marine Geosciences, Kiel, Germany, 1992
- Kucera, M., Weinelt, Mara., Kiefer, T., Pflaumann, U., Hayes, A., Weinelt, M., Chen, M. T., Mix, A. C., Barrows, T. T., Cortijo, E., Duprat, J., Juggins, S., and Waelbroeck, C.: Reconstruction of sea-surface temperatures from assemblages of planktonic foraminifera: multi-technique approach based on geographically constrained calibration data sets and its application to glacial Atlantic and Pacific Oceans, *Quaternary Science Reviews*, 24, 951-998, 2005.
- Labeyrie, L. D., Duplessy, J. C., and Blanc, P. L.: Variations in the mode of formation

and temperature of oceanic deep waters over the past 125,000 years, *Nature* 327, 477-482, 1987.

Labeyrie, L., and Duplessy, J. C.: Changes in the oceanic $^{13}\text{C}/^{12}\text{C}$ ratio during the last 140,000 years: high-latitude surface water records, *Palaeogeography, Palaeoclimatology, Palaeoecology*, 50, 217-240, 1985.

Lackschewitz, K. L., Dehn, J., and Wallrabe-Adams, H. J.: Volcaniclastic sediments from mid-oceanic Kolbinsey Ridge, north of Iceland: Evidence for submarine volcanic fragmentation processes, *Geology*, 22, 975-978, 1994.

Lea, D. W., Pak, D. K., Spero, H. J.: Climate impact of late Quaternary Equatorial Pacific Sea surface temperature variations, *Science*, 289, 1719, doi:10.1126/science.289.5485.1719, 2000.

Lee, J. E., Fung, I., DePaolo, D. J., and Otto-Bliesner, B.: Water isotopes during Last Glacial Maximum: New general circulation model calculations, *J. Geophys. Res.*, 113, D19109, 2008.

Lee, K. E., Slowey, N. C., and Herbert, T. D.: Glacial sea surface temperatures in the subtropical North Pacific: A comparison of U^k_{37} and foraminiferal assemblage temperature estimates, *Paleoceanography*, 16, 268-279, 2001.

LeGrande, A. N. and Lynch-Stieglitz, J.: Surface currents in the western North Atlantic during the Last Glacial Maximum, *Geochem. Geophys. Geosys.*, 8, 1, 2007.

LeGrande, A. N. and Schmidt, G. A.: Global gridded data set of the oxygen isotopic composition in seawater, *Geophys. Res. Lett.*, 33, L12604, 2006.

Lehmann, M. and Siegenthaler, U.: Equilibrium oxygen-Isotope and Hydrogen-Isotope Fractionation between Ice and Water, *J Glaciol*, 37, 23-26, 1991.

Leventer, A., Williams, D. F., and Kennett, P.: Dynamics of the Laurentide ice sheet during the last deglaciation: evidence from the Gulf of Mexico, *EPSL*, 59, 11-17, 1982.

Li, T.G., Liu, Z. X., Hall, M. A., Berne, S., Saito, Y., Cang, S. X., and Cheng, Z. B.: Heinrich event imprints in the Okinawa Trough: evidence from oxygen isotope and planktonic foraminifera, *Palaeogeography, Palaeoclimatology, Palaeoecology*, 176, 133-146, 2001.

Linsley, B. K. and Thunell, R. C.: The record of deglaciation in the Sulu Sea: evidence for the Younger Dryas event in the tropical western Pacific, *Paleoceanography*, 5, 1025-1039, doi:10.1029/PA005i006p01025, 1990.

Lynch-Stieglitz, J., Adkins, J. F., Curry, W. B., Dokken, T., Hall, I. R., Herguera, J. C., Hirschi, J. J. M., Ivanova, E. V., Kissel, C., Marchal, O., Marchitto, T. M., McCave, I. N., McManus, J. F., Multiza, S., Ninnemann, U., Peeters, F., Yu, E. F., and Zahn, R.: Atlantic Meridional Overturning Circulation during Last Glacial Maximum, *Science*, 316, 66-69, 2007.

Macdonald, R. W., Carmack, E. C., Mclaughlin, E. C., Falkner, K. K., and Swift, J. H.: Connections among ice, runoff and atmospheric forcing in the Beaufort Gyre, *Geophys. Res. Lett.*, 26, 2223-2226, 1999.

Macdonald, R. W., Paton, D. W., Carmack, E. C., and Omstedt, A.: The fresh water budget and under-ice spreading of Mackenzie River water in the Canadian Beaufort Sea based on salinity and $^{18}\text{O}/^{16}\text{O}$ measurements in water and ice, *Journal of*

Geophysical Research, 100, 895-919, 1995.

Mackensen, A., Grobe, H., Hubberten, H. W., Spieß, V., and Fütterer, D. K.: Stable isotope stratigraphy from the Antarctic continental margin during the last one million years, *Marine Geology*, 87, 315-321, doi:10.1016/0025-3227(89)90068-6, 1989

Maier-Reimer, E. and Hasselmann, K.: Transport and storage of CO₂ in the ocean – an inorganic ocean-circulation carbon cycle model, *Climate Dynamics*, 2, 63-90, 1987.

Majoube, M.: Fractionnement en oxygene 18 et en deuterium entre l'eau et sa vapeur, *Journal de Chimie et Physique*, 68, 1423-1436, 1971.

MARGO Project Members: Constraints on the magnitude and patterns of ocean cooling at the Last Glacial Maximum, *Nature Geosci.*, 2, 127-132, 2009.

Marsland, S.J., Haak, H., Jungclaus, J. H., Latif, M., and Roeske, F.: The Max Planck Institute global ocean/sea-ice model with orthogonal curvilinear coordinates, *Ocean. Modell.*, 5, 91-127, 2003.

Maslin, M.: A study of the paleoceanography of the N.E. Atlantic in the late Pleistocene, Ph.D. thesis, University of Cambridge, England, 1992.

Masson-Delmotte, V., Jouzel, J., Landais, A., Stievenard, M., Johnsen, S. J., White, J. W. C., Werner, M., Sveinbjornsdottir, A., and Fuhrer, K.: 2005. GRIP deuterium excess reveals rapid and orbital-scale changes in Greenland moisture origin, *Science*, 309, 118-121, 2005.

McCrea, J. M.: On the isotopic chemistry of carbonates and paleotemperature scale, *J. Chem. Phys.*, 18, 849-857, 1950.

McManus, J. F., Oppo, D. W., and Cullen, J. L.: A 0.5-million-year record of millennial-scale climate variability in the North Atlantic, *Science*, 283, 971, 1999.

Meinecke, G.: Spätquartäre Oberflächenwassertemperaturen im östlichen äquatorialen Atlantik, Ph.D. Thesis, University of Bremen, Germany, 1992.

Meland, M. Y., Jansen, E., and Elderfield, H.: Constraints on SST estimates for the northern North Atlantic/Nordic Seas during the LGM, *Quaternary Sci Rev*, 24, 835-852, 2005.

Melles, M.: Paläoglazologie und Paläozeanographie im Spätquartär am Kontinentalrand des südlichen Weddellmeeres, *Antarktis, Berichte zur Polarforschung*, 81, 190, 1991.

Meredith, M. P., Heywood, K. J., Frew, R. D., and Dennis, P. F.: Formation and circulation of the water masses between the Southern Indian Ocean and Antarctic: Results from $\delta^{18}\text{O}$, *J. Mar. Res.*, 57, 449-470, 1999.

Millo, C., Sarnthein, M., Völker, A., and Erlenkeuser, H.: Variability of the Denmark Strait Overflow during the Last Glacial Maximum, *Boreas*, 35, 50-60, doi:10.1111/j.1502-3885.2006.tb0112.x, 2006.

Mix, A. C. and Fairbanks, R. G.: North Atlantic surface-ocean control of Pleistocene deepocean circulation, *Earth and Planetary Science Letters*, 73, 231–243, 1985a.

Mix, A. C. and Ruddiman, W. F.: Structure and timing of the last deglaciation: Oxygen-isotope evidence, *Quaternary Science Reviews*, 4, 59-108, 1985b.

Morris, T. H.: Stable isotope stratigraphy of the Arctic Ocean Fram Strait to Central Arctic, *Palaeogeography, Palaeoclimatology, Palaeoecology*, 64, 201–219, 1988.

Mulitza, S., Rühlemann, C., Bickert, T., Hale, W., Pätzold, J., and Wefer, G.: Late

- Quaternary ^{13}C gradients and carbonate accumulation in the western equatorial Atlantic, *Earth and Planetary Science Letters*, 155, 237-249, doi:10.1016/S0012-821X(98)00012-0, 1998.
- Mulitza, S., Dürkoop, A., Hale, W., Wefer, G., and Niebler, H. S.: Planktonic foraminifera as records of past surface-water stratification, *Geology*, 25, 335-338, 1997.
- Müller, A. and Opdyke, B. N.: Glacial-interglacial changes in nutrient utilization and paleoproductivity in the Indonesian Throughflow sensitive Timor Trough, easternmost Indian Ocean, *Paleocenography*, 15, 85-94, 2000.
- Nelson, C. S., Cooke, P. J., Hendy, C. H., and Cuthbertson, A. M.: Oceanographic and climatic changes over the past 160,000 years at Deep Sea Drilling Project Site 594 off southeastern New Zealand, southwest Pacific Ocean, *Paleoceanography*, 8, 435-458, doi: 10.1029/93PA01162, 1993.
- Ninnemann, U. S. and Charles, C. D.: Regional differences in Quaternary Subantarctic nutrient cycling: Link to intermediate and deep water ventilation, *Paleoceanography*, 12, 560-567, 1997.
- Notholt, H.: The implication of the “North East Water”—Polynya on the sedimentation by NE-Greenland and late Quaternary paleo-oceanic investigations, Alfred Wegener Institute for Polar and Marine Research, Bremerhaven, Germany, 1998.
- Nørgaard-Pedersen, N., Spielhagen, R. F., Erlenkeuser, H., Grootes, P. M., Heinemeier, J., Knies, J.: Arctic Ocean during the Last Glacial Maximum Atlantic and polar domains of surface water mass distribution and ice cover, *Paleoceanography*, 18, 1063, 2003.
- O’Neil, J. R.: Hydrogen and oxygen isotope fractionation between ice and water, *J. Phys. Chem.*, 72, 3683-3684, 1968.
- Ortiz, J., Mix, A., Hostetler, S., and Kashgarian, M.: The California current of the last glacial maximum: Reconstruction at 42 degree N based on multiple proxies, *Paleoceanography*, 12, 191-205, 1997.
- Otto-Bliesner, B. L., Brady, E. C., Clauzet, G., Tomas, R., Levis, S., Kothavala, Z.: Last Glacial Maximum and Holocene climate in CCSM3, *J. Climate*, 19, 2526-2544, 2006.
- Östlund, H. G. and Hut, G.: Arctic Ocean water mass balance from isotope data, *J Geophys Res*, 89, 6373-6381, 1984.
- Östlund, H. G., Craig, H., Broecker, W. S., and Spender, D.: GEOSECS Atlantic, Pacific and Indian Ocean expeditions: Shorebased Data and graphics, vol. 7, Tech. rep., National Science Foundation, Washington, D.C., 1987.
- Pahnke, K., Zahn, R., Elderfield, H., and Schulz, M.: 340,000-Year Centennial-Scale Marine Record of Southern Hemisphere, *Science*, 301, 948-952, doi:10.1126/science.1084451, 2003.
- Palmer, M. R. and Pearson, P. N.: A 23,000-year record of surface water pH and PCO₂ in the western equatorial Pacific Ocean, *Science*, 300, 480-482, doi:10.1126/science.1080796, 2003.
- Paluszkiwicz, T. and Romea, R. D.: A one-dimensional model for the

parameterization of deep convection in the ocean, *Dyn. Atmos. Oceans*, 26, 95-130, 1997.

Paterne, M., Guichard, F., Labeyrie, J., Gillot, P. Y., Duplessy, J. C.: Tyrrhenian Sea tephrochronology of the oxygen isotope record for the past 60,000 years, *Marine Geology*, 72, 259-285, doi:10.1016/0025-3227(86)90123-4, 1986.

Paul, A., Mulitza, S., Pätzold, J., and Wolff, T.: Simulation of oxygen isotopes in a global ocean model, in *Use of Proxies in Paleoceanography: Examples From the South Atlantic*, Fischer, G. and Wefer, G. (Eds), Springer, New York, 655-686, 1999.

Pichon, J. J., Labeyrie, L. D., Bareille, G. F., Labracherie, M., Duprat, J., and Jouzel J.: Surface water temperature changes in the high latitudes of the southern hemisphere over the last glacial-interglacial cycle, *Paleoceanography*, 7, 289-318, doi:10.1029/92PA00709, 1992.

Price, J. F. and Baringer, M.: Outflows and deep water productions by marginal seas, *Prog. Oceanogr.*, 25, 162-200, 1994.

Rasmussen, T. L., Thomsen, E., van Weering, T. C. E., and Labeyrie, L.: Rapid changes in surface and deep water conditions at the Faeoe Margin during the last 58,000 years, *Paleocenaography*, 11, 757-771, 1996.

Roche, D., Paillard, D., Ganopolski, A., and Hoffmann, G.: Oceanic oxygen-18 at the present day and LGM: equilibrium simulations with a coupled climate model of intermediate complexity, *Earth. Planet. Sc. Lett.*, 218, 317-330, 2004.

Roeckner, E., Bäuml, G., Bonaventura, L., Brokopf, R., Esch, M., Giorgetta, M., Hagemann, S., Kornbluh, L., Schlese, U., Schulzweida, U., Kirchner, I., Manzini, E., Rhodin, A., and Tompkins, A.: The atmospheric general circulation model ECHAM5. Part I: Model description, Max Planck Institute for Meteorology Rep. 349., 2003.

Rosman, J. R. and Taylor, P. D.: Isotopic composition of the elements (technical report): commission on atomic weights and isotopic abundances, *Pure Appl Chem*, 70, 217-235, 1998.

Rosenthal, Y., Boyle, E. A., Labeyrie, L. D., and Oppo, D. W.: Glacial enrichments of authigenic Cd and U in Subantarctic sediments: A climatic control on the elements' oceanic budget?, *Paleoceanography*, 10, 395-414, doi:10.1029/95PA00310, 1995.

Ruddiman, W. F., and McIntyre, A.: The North Atlantic during the last deglaciation, *Palaeogeography, Palaeoclimatology, Palaeoecology*, 35, 145-214, 1981.

8,000 years, *Paleocenaography*, 11, 757-771, 1996.

Rühlemann, C., Mulitza, S., Müller, P. J., Wefer, G., and Zahn, R.: Warming of the tropical atlantic Ocean and slowdown of thermohaline circulation during the last deglaciation, *Nature*, 402, 511-514, doi:10.1038/990069, 1999.

Rühlemann, C., Frank, M., Hale, W., Mangini, A., Mulitza, S., Müller, P. J., and Wefer, G.: Late Quaternary productivity changes in the western equatorial Atlantic: Evidence from ²³⁰Th-normalized carbonate and organic carbon accumulation rates, *Marine Geology*, 135, 127-152, doi:10.1016/S0025-3227(96)00048-5, 1996.

Sarnthein, M., Jansen, E., Weinelt, M., Arnold, M., Duplessy, J. C., Erlenkeuser, H., Flatoy, A., Johannessen, G., Johannessen, T., Jung, S. J. A., Koç, N., Labeyrie, L. D., Maslin, M. A., Pflaumann, U., Schulz, H.: Variations in Atlantic surface ocean paleoceanography, 50°-80°N: a time-slice record of the last 30,000 years,

Paleoceanography, 10, 1063-1094, doi:10.1029/95PA01453, 1995.

Sarnthein, M., Winn, K., Jung, S. J. A., Duplessy, J. C., Labeyrie, L., Erlenkeuser, H., and Ganssen, G.: Changes in East Atlantic Deep-Water circulation over the last 30,000 years – 8 time slice reconstructions, *Paleoceanography*, 9, 209-267, 1994.

Sarnthein, M., Jansen, E., Arnold, M., Duplessy, J. C., Erlenkeuser, H., Flatory, A., Veum, T., Vogelsang, E., Weinelt, M. S.: $\delta^{18}\text{O}$ time-slice reconstruction of meltwater anomalies at termination 1 in the North Atlantic between 50 and 80°N, Bred, E. and Broecker, W. S. (Eds), in *The last deglaciation: Absolute and radio-carbon chronologies*, Springer, New York, 182-200, 1992.

Savin, S. M. and Yeh, H. W.: Stable isotopes in ocean sediments, In *The Sea*, 7, Emiliani, C., Wiley, J. and Sons (Eds), New York, pp. 1521-1554, 1981.

Schäfer-Neth, C. and Paul, A.: The Atlantic Ocean at the Last Glacial Maximum: 1. objective mapping of the GLAMAP sea-surface conditions, Wefer, G., Multiza, S., Ratmeyer, V. (eds), *The South Atlantic in the last Quaternary Reconstruction of Material Budgets and Current Systems*, Springer-Verlag, Berlin, 531-548, 2003.

Schmidt, G. A., LeGrande, A. N., and Hoffmann, G.: Water isotope expressions of intrinsic and forced variability in a coupled ocean-atmosphere model, *J. Geophys. Res.*, 112, D10103, 2007.

Schmidt, G. A., Hoffmann, G., Schindell, D. T., and Hu, Y.: Modelling atmospheric stable water isotopes and the potential for constraining cloud processes and stratosphere–troposphere water exchange, *J. Geophys. Res.*, 110, 021314, 2005.

Schmidt, G. A.: Forward modeling of carbonate proxy data from planktonic foraminifera using oxygen isotope tracers in a global ocean model, *Paleoceanography*, 14, 482-497, 1999a.

Schmidt, G. A., Bigg, G. R., and Rohling, E. J.: Global Seawater Oxygen-18 Database, <http://data.giss.nasa.gov/o18data/>, NASA Goddard Inst. of Space Sci., New York, 1999b.

Schmidt, G. A.: Oxygen-18 variations in a global ocean model, *Geophys. Res. Lett.*, 25, 1201-1204, 1998.

Schneider, R. R., Müller, P. J., and Ruhland, G.: Late Quaternary surface circulation in the east-equatorial South Atlantic: evidence from alkenone sea surface temperatures, *Paleoceanography*, 10, 197-220, doi:10.1029/94PA03308, 1995.

Schrag, D. P., Adkins, J. F., McIntyre, K., Alexander, J. L., Hodell, D. A., Charles, C. D., and McManus, J. F.: The oxygen isotopic composition of seawater during the Last Glacial Maximum, *Quaternary. Sci. Rev.*, 21, 331-342, 2002.

Shackleton, N. J., Duplessy, J. C., Arnold, M., Maurice, P., Hall, M. A., and Cartledge, J.: Radiocarbon age of last glacial Pacific Deep-Water, *Nature*, 335, 708-711, 1988.

Shackleton, N. J.: Oxygen isotopes, ice volume and sea-level, *Quaternary Science Review*, 6, 183-190, 1987.

Shackleton, N. J.: Attainment of isotopic equilibrium between ocean water and the benthonic foraminifera genus *Uvigerina*: isotopic changes during the last glacial, *Cent. Nat. Rech., Sci. Colloq. Int.*, 219, 203-209, 1974.

Sharp, Z.: *Principles of stable isotope geochemistry*, Pearson Education Inc., Upper Saddle River, New Jersey, 2007.

- Shin, S. I., Liu, Z., Otto-Bliesner, B., Brady, E. C., Kutzbach, J. E., and Harrison, S. P.: A simulation of the last glacial maximum climate using the NCAR-CCSM, *Clim. Dynam.*, 20, 127-151, 2003.
- Signes, M., Bijma, J., Hemleben, C., and Ott, R.: A model for planktic foraminiferal shell growth, *Paleobiology*, 19, 71-91, 1993.
- Sirocko, F.: Zur Akkumulation von Staubsedimenten im nördlichen Indischen Ozean; *Anzeiger der Klimageschichte Arabiens und Indiens, Berichte-Reports, Geologisch-Paläontologisches Institut der Universität Kiel*, 27, 185, 1989.
- Six, K. D. and Maier-Reimer, E.: Effects of plankton dynamics on seasonal carbon fluxes in an ocean general circulation model, *Global. Biogeochem. Cycles*, 10, 559-583, 1996.
- Sowers, T. and Bender, M.: Climate records covering the last deglaciation, *Science*, 269, 210-214, 1995.
- Spero, H. J. and Parker, S. L.: Photosynthesis in the symbiotic planktonic foraminifera *Orbulina universa*, and its potential contribution to oceanic primary productivity, *J. Foram. Res.*, 15, 273-281, 1985.
- Spero, H. J., Bijma, J., Lea, D. W., and Bemis, B. E.: Effect of seawater carbonate concentration on foraminiferal carbon and oxygen isotopes, *Nature*, 390, 497-500, 1997.
- Spindler, M., Hemleben, C., Bayer, U., Bé, A. W. H., and Anderson, O. R.: Lunar periodicity of reproduction in the planktonic foraminifera *Hastigerina pelagica*, *Mar. Ecol. Prog. Ser.*, 1, 61-64, 1979.
- Steele, M., Morley, R., and Emold, W.: PHC: A Global Ocean Hydrography with a High-Quality Arctic Ocean, *J. Climate*, 14, 2079-2087, 2001.
- Stein, R., Nam, S., Grobe, H., and Hubberten, H.: Late Quaternary glacial history and short-term ice rafted debris fluctuations along the East Greenland continental margin, In: Andrews, J. T., Austin, W. E. N., Bergsten, H., Jennings, A. E. (Eds.), *Late Quaternary Paleoceanography of the North Atlantic Margins*, Geological Society Special Publication, The Geological Society, Oxford, UK, 135-152, 1996.
- Stein, R., Schubert, C., Vogt, C., and Fütterer, D.: Stable isotope stratigraphy, sedimentation rates and paleosalinity in the latest Pleistocene to Holocene Central Arctic Ocean, *Marine Geology*, 119, 333-355, 1994.
- Stenni, B., Masson-Delmotte, V., Selmo, E., Oerter, H., Meyer, H., Röthlisberger, R., Jouzel, J., Cattani, O., Falourd, S., Fischer, H., Hoffmann, G., Lacumin, P., Johnsen, S. J., Minster, B., Udisti, R.: The deuterium excess records of EPICA Dome C and Dronning Maud Land ice cores (East Antarctica), *Quaternary Science Reviews*, 29, 146-159, 2010.
- Stott, L., Poulsen, C., Lund, S., and Thunell, R.: Super ENSO and global climate oscillations at millennial time scales, *Science*, 297, 222, doi:10.1126/science.1071627, 2002.
- Tindall, J., Flecker, R., Valdes, P., Schmidt, D. N., Markwick, P., and Harris, J.: Modelling the oxygen isotope distribution of ancient seawater using a coupled ocean-atmosphere GCM: Implication for reconstructing early Eocene climate, *Earth Planet. Sci. Lett.*, 292, 265-273, 2010.

- Toggweiler, J. R. and Samuels, B.: Effect of sea ice on the salinity of Antarctic bottom waters, *J Phys Oceanogr*, 25, 1980-1997, 1995.
- Uemura, R., Matsui, Y., Yoshimura, K., Motoyama, H., and Yoshida, N.: Evidence of deuterium excess in water vapor as an indicator of ocean surface conditions, *J Geophys Res*, 113, D19114, 2008.
- UNESCO: Algorithms for computation of fundamental properties of seawater, UNESCO Technical Papers in Marine Science, 44, 1983.
- Urey, H. C., Epstein, S., McKinney, C., and McCrea, J.: Method for measurement of paleotemperature, *Bulletin of the Geological Society of American* (abstract), 59, 1359-1360, 1948.
- Urey, H. C., Brickwedde, F. G., and Murphy, G. M.: A hydrogen isotope of mass 2 and its concentration, *Phys. Rev.*, 40, 1, 1932.
- Van Campo, E., Duplessy, J. C., Prell, W. L., Barratt, N., and Sabatier, R.: Comparison of terrestrial and marine temperature estimates for the past 135kyr off southeast Africa: a test for GCM simulations of Palaeoclimate, *Nature*, 348, 209-212, doi:10.1038/348209a0, 1990.
- Van Kreveld, S., Sarnthein, M., Erlenkeuser, H., Grootes, P. M., Jung, S. J. A., Nadeau, M. J., Pflaumann, U., and Voelker, A. H.: Potential links between surging ice sheets, circulation changes, and the Dansgaard–Oeschger cycles in the Irminger Sea, *Paleoceanography*, 15, 425–442, 2000.
- Veum, T., Arnold, M., Beyer, I., Duplessy, J. C.: Water mass exchange between the North Atlantic and the Norwegian Sea during the last 28,000 years, *Nature*, 356, 783-785, 1992.
- Vimeux, F., Masson, V., Jouzel, J., Petit, J. R., Steig, E. J., Stievenard, M., Vaikmae, R., and J.W.C. White, J. W. C.: Holocene hydrological cycle changes in the southern hemisphere documented in East Antarctic deuterium excess records, *Clim Dyn*, 17, 503-513, 2001.
- Visser, K., Thunell, R., and Stott, L.: Magnitude and timing of temperature change in the Indo-Pacific warm pool during deglaciation, *Nature*, 421, 152-155, 2003.
- Vogelsang, E: Paläo-Ozeanographie des Europäischen Nord-meeres an Hand stabiler Kohlenstoff-und Sauerstoffisotope, Ph.D. Thesis, University of Kiel, Germany, 1990.
- Vogt, C.: Zur Paläozeanographie und Paläoklima im spätquartären Arktischen Ozean: Zusammensetzung und Flux terrigener und biogener Sedimentkomponenten auf dem Morris Jesup Rise und dem Yermak Plateau, *Berichte Polarforschung*, 251, Alfred Wegener Institute, Bremerhaven, Germany, 1997.
- Völker, A.: Zur Deutung der Dansgaard-Oeschger Ereignisse in ultra-hochauflösenden Sedimentprofilen aus dem Europäischen Nordmeer, *Berichte-Reports*, Institute für Geowissenschaften, University Kiel, 9, 278, doi:10.2312/reports-ifg.1999.9, 1999.
- Wadley, M. R., Bigg, G. R., Rohling, E. J., and Payne, A. J.: On modeling present-day and last glacial maximum oceanic $\delta^{18}\text{O}$ distributions, *Global and Planetary Change*, 32, 89-109, 2002.
- Wang, L. J., Sarnthein, M., Erlenkeuser, H., Grimalt, J. O., Grootes, P. M., Heilig, S., Ivanova, E. V., Kienast, M., Pelejero, C., and Pflaumann, U.: East-Asian monsoon

- climate during the Late Pleistocene: high-resolution sediment records from the South China Sea, *Marine Geology*, 156, 245-284, doi:10.1016/S0025-3227(98)00182-0, 1999.
- Wanninkhof, R.: Relationship between wind speed and gas exchange over the ocean, *J. Geophys. Res.*, 97, 7373-7382, 1992.
- Watkins, S. J., Maher, B. A., and Bigg, G. R.: Ocean circulation at the Last Glacial Maximum: A combined modeling and magnetic proxy-based study, *Paleoceanography*, 22, PA2204, 2007.
- Wefer, G., Berger, W. H., Bijma, J., Fischer, G.: Clues to ocean history: A brief overview of proxies, Fisher, G. and Wefer, G. (Eds), in *Use of Proxies in Paleoceanography: Examples from the South Atlantic*, Springer, Berlin, 1-68, 1999.
- Wefer, G., Berger, W. H., Bickert, T., Donner, B., Fischer, G., Kemle-von Mücke, S., Pätzold, J., Meinecke, G., Müller, P. J., Mulitza, S., Niebler, H. S., Schmidt, H., Schneider, R. R., and Segl, M.: Late Quaternary surface circulation of the South Atlantic: The stable isotope record and implications for heat transport and productivity, In: Wefer, G., Berger, W. H., Siedler, G., and Webb, D. (eds.), *The South Atlantic: Present and Past Circulation*, Springer, Berlin, Heidelberg, 461-502, 1996.
- Wei, W., Lohmann, G., and Dima, M.: Distinct modes of internal variability in the Global Meridional Overturning Circulation associated to the Southern Hemisphere westerly winds, *J. Phys. Oceanogr.*, 42, 785-801, 2012.
- Wei, W. and Lohmann, G.: Simulated Atlantic Multidecadal Oscillation during the Holocene, *J. Climate*, doi:10.11275/JCU-D-11-00667.1, 2012.
- Weinelt, M., Rosell-Melé, A., Plaumann, U., Sarnthein, M., Kiefer, T.: Zur Rolle der Produktivität im Nordostatlantik bei abrupten Klimaänderungen in den letzten 80,000 Jahren, *Zeitschrift der Deutschen Geologischen Gesellschaft*, 154, 47-66, 2003.
- Weinelt, M., Sarnthein, M., Plaumann, U., Schulz, H., Jung, S. J. A., and Erlenkeuser, H.: Ice-free Nordic Sea during the Last Glacial Maximum? Potential sites of deepwater formation, *Paleoclimates* 1, 283-309, 1996.
- Weinelt, M.: Veränderungen der Oberflächenzirkulation im Europäischen Nordmeer während der letzten 60,000 Jahre – Hinweise aus stablen Isotopen, Ph.D. Thesis, University of Kiel, Germany, 1993.
- Weiss, R. F., Östlund, H. G., and Craig, H.: Geochemical studies of the Weddell Sea, *Deep Sea Res. Part A*, 26, 1093-1120, 1979.
- Werner, M., Langebroek, P. M., Carlsen, T., Herold, M., and Lohmann, G.: Stable water isotopes in the ECHAM5 general circulation model: Toward high-resolution isotope modeling on global scale. *J. Geophys. Res.*, 116, D15109, doi: 10.1029/2011JD015681, 2011.
- Werner, M., Tegen, I., Harrison, S. P., Kohfeld, K. E., Prentice, I. C., Balkanski, Y., Rodhe, H., and Roelandt, C.: Seasonal and interannual variability of the mineral dust cycle under present and glacial climate conditions, *J. Geophys. Res.-Atmos.*, 107, 4744, 2002.
- Wetzel, P.: Interannual and decadal variability in the air-sea exchange of CO₂ – a model study, PhD thesis, Hamburg University, 2004.
- Williams, D. F. And Healy-Williams, N.: Oxygen isotopic-hydrographic relationships

- among recent planktonic foraminifera from the Indian Ocean, *Nature*, 283, 848-852, 1980.
- Winn, K., Sarnthein, M., Erlenkeuser, H.: stratigraphy and chronology of Kiel sediment cores from the East Atlantic, *Berichte-Reports*, 45, department of Geology and Paleontology, University Kiel, Germany, 1991.
- Wolff, T.: Mixed layer characteristics in the equatorial Atlantic during the late Quaternary as deduced from planktonic foraminifera, Ph.D. thesis, University of Bremen, Germany, 1998.
- Wolf-Gladrow, D. A., Bijma, J., Zeebe, R. E.: Model simulation of the carbonate chemistry in the microenvironment of symbiont bearing foraminifera, *Marine Chemistry*, 64, 181-198, 1999.
- Wolf-Gladrow, D. A. and Riebesell, U.: Diffusion and reactions in the vicinity of plankton: A refined model for inorganic carbon transport, *Marine Chemistry*, 59, 17-34, 1997.
- Xu, X., Werner, M., Butzin, M., and Lohmann, G.: Water isotope variations in the global ocean model MPI-OM, *Geosci Model Dev*, 5, 809-818, 2012.
- Yobbi, D. K.: Effects of tidal stage and ground-water levels on the discharge and water quality of springs in coastal Citrus and Hernando countries, Florida, Tech. Rep. Water Resources Investigations Report 92-4096, U.S. Geol. Surv., 1992.
- Zachos, J. C., Stott, L. D., and Lohmann, K. C.: Evolution of Early Cenozoic Marine Temperatures, *Paleoceanography*, 9, 353-387, 1994.
- Zahn, R., Pedersen, T. F., Bornhold, B. D., and Mix, A. C.: Water mass conversion in the glacial subarctic Pacific (54°N, 148°W): physical constraints and the benthic-planktonic stable isotope record, *Paleoceanography*, 6, 543-560, doi:10.1029/91PA01327, 1991.
- Zahn, R.: Spätquartäre Entwicklung von Küstenauftrieb und Tiefenwasserzirkulation in Nordost-Atlantik. Rekonstruktion anhand stabiler Isotope kalkschaliger Foraminiferen, Ph.D. thesis, Univ. of Kiel, Germany, 1986.
- Zahn, R., Markussen, B., Thiede, J.: Stable isotope data and depositional environments in the late Quaternary, *Nature*, 314, 433-435, 1985.
- Zeebe, R. E.: An expression for the overall oxygen isotope fractionation between the sum of dissolved inorganic carbon and water, *Geochem. Geophys. Geosy.*, 8, Q09002, 2007.
- Zeebe, R. E. and Wolf-Gladrow, D. A.: *CO₂ in seawater: Equilibrium, Kinetics, Isotopes*, Elsevier, 2001.
- Zeebe, R. E.: An explanation of the effect of seawater carbonate concentration on foraminiferal oxygen isotopes, *Geochim Cosmochim Acta*, 63, 2001-2007, 1999.